Free surface flow simulation in estuarine and coastal environments : numerical development and application on unstructured meshes

Andrea Gilberto Filippini

THÈSE

PRÉSENTÉE À

L'UNIVERSITÉ DE BORDEAUX

ÉCOLE DOCTORALE DE MATHÉMATIQUES ET D'INFORMATIQUE

par **Andrea Gilberto Filippini**

POUR OBTENIR LE GRADE DE

DOCTEUR

SPÉCIALITÉ : Mathématiques Appliquées

Free surface flow simulation in estuarine and coastal environments: numerical development and application on unstructured meshes

---

Préparée à INRIA Bordeaux Sud-Ouest (équipe CARDAMOM)

Directeur de thèse : Mario RICCHIUTO

Co-directeur de thèse : Philippe BONNETON

Soutenue le : 14 Décembre 2016

Après avis des rapporteurs :

Michel BENOIT	Professeur des Universités, IRPHE and École centrale de Marseille
Eleuterio TORO	Professeur des Universités, DICAM Università of Trento .....

Devant la commission d'examen composée de :

Riadh ATA	Chargé de recherche, LHSV	Examinateur
Michel BENOIT	Professeur des Universités, IRPHE	Rapporteur
Philippe BONNETON	Directeur de recherche, EPOC - CNRS	Examinateur
David LANNES	Directeur de recherche, IMB	Président
Rodrigo PEDREROS .	Chargé de recherche, BRGM	Examinateur
Mario RICCHIUTO ..	Directeur de recherche, INRIA	Examinateur
Lisl WEYNANS	Maître de conférences, IMB	Examinateur

– 2016 –

Dedicated to my parents

Abstract : Over the last decades, there has been considerable attention in the accurate mathematical modeling and numerical simulations of free surface wave propagation in near-shore environments. A physical correct description of the large scale phenomena, which take place in the shallow water region, must account for strong nonlinear and dispersive effects, along with the interaction with complex topographies. First, a study on the behavior in nonlinear regime of different Boussinesq-type models is proposed, showing the advantage of using fully-nonlinear models with respect to weakly-nonlinear and weakly-dispersive models (commonly employed). Secondly, a new flexible strategy for solving the fully-nonlinear and weakly-dispersive Green-Naghdi equations is presented, which allows to enhance an existing shallow water code by simply adding an algebraic term to the momentum balance and is particularly adapted for the use of hybrid techniques for wave breaking. Moreover, the first discretization of the Green-Naghdi equations on unstructured meshes is proposed via hybrid finite volume/ finite element schemes. Finally, the models and the methods developed in the thesis are deployed to study the physical problem of bore formation in convergent alluvial estuary, providing the first characterization of natural estuaries in terms of bore inception.

Résumé : Ces dernières décennies, une attention particulière a été portée sur la modélisation mathématique et la simulation numérique de la propagation de vagues en environnements côtiers. Une description physiquement correcte des phénomènes à grande échelle, qui apparaissent dans les régions d'eau peu profonde, doit prendre en compte de forts effets non-linéaires et dispersifs, ainsi que l'interaction avec des bathymétries complexes. Dans un premier temps, une étude du comportement en régime non linéaire de différents modèles de type Boussinesq est proposée, démontrant l'avantage d'utiliser des modèles fortement non-linéaires par rapport à des modèles faiblement non-linéaires et faiblement dispersifs (couramment utilisés). Ensuite, une nouvelle approche flexible pour résoudre les équations fortement non-linéaires et faiblement dispersives de Green-Naghdi est présentée. Cette stratégie permet d'améliorer un code "shallow water" existant par le simple ajout d'un terme algébrique dans l'équation du moment et est particulièrement adapté à l'utilisation de techniques hybrides pour le déferlement des vagues. De plus, la première discrétisation des équations de Green-Naghdi sur maillage non structuré est proposée via des schémas hybrides Volume Fini/Élément Fini. Finalement, les modèles et méthodes développés dans la thèse sont appliqués à l'étude du problème physique de la formation du mascaret dans des estuaires convergents et alluviaux. Cela a amené à la première caractérisation d'estuaire naturel en terme d'apparition de mascaret.

Keywords : Boussinesq-type models, Serre-Green-Naghdi equations, Fully nonlinear and weakly dispersive, Wave breaking, Finite Volume, Finite Ele-

ment, Dispersion error, Tidal bore, Alluvial estuaries, Scaling analysis

Mots-clés : Modèle de type Boussinesq, équations de Serre-Green-Naghdi, Fortement non-linéaire et faiblement dispersif, Déferlement des vagues, Volume Fini, Élément Fini, Error de dispersion, Mascaret, Estuaires, Analyse dimensionnelle

Laboratoire d'accueil : INRIA Bordeaux Sud-Ouest - Équipe CARDAMOM, 200 avenue de la vieille tour, 33405 Talence Cedex

Résumé substantiel

Dans les dernières décennies, la modélisation numérique de la propagation des vagues en environnements côtiers a de plus en plus remplacé les expériences en laboratoire dans l'ingénierie côtière. Cela a été possible grâce à la constante augmentation de la puissance des plates-formes informatiques, la parallélisation et le développement des algorithmes de calculs, ainsi que les progrès dans l'analyses numérique des PDEs. Tout ceci a contribué à construire un outil fondamental pour la compréhension et la description du phénomène étudié, exploité par l'ingénierie côtière dans le design des structures côtières, la prévention de l'impact des tsunamis ou de l'inondation due aux mascarets.

Les vagues se propageant près des côtes subissent d'importantes transformations dues à la nature fortement non linéaire et dispersive des phénomènes qui se produisent suite à l'interaction avec des bathymétries complexes (réfractions, diffractions, dispersions des fréquences, shoaling, déferlement, ...). Le systèmes d'équations d'Euler incompressible est le plus adapté pour fournir une description complète et précise du phénomène à toutes ses échelles caractéristiques. Cependant, ce travail a comme objectif de développer un outil permettant une bonne prédiction du problème des vagues à larges échelles (de $\mathcal{O}(m)$ à $\mathcal{O}(km)$), pour lequel l'utilisation de ce système d'équations est très onéreux. C'est pourquoi, des modèles asymptotiques sont couramment utilisés dans l'ingénierie côtière. Ces modèles sont dérivés sous l'hypothèse d'eau peu profonde en utilisant la méthode des perturbations par rapport a un petit paramètre $\mu = h_0/\lambda$ (avec h_0 et λ respectivement la profondeur et longueur horizontale caractéristiques), introduite initialement par Boussinesq [1872]. Le plus simple et populaire de ces modèles est le système d'équations non linéaires de Saint-Venant . Ce système donne une simulation correcte de la propagation des vagues quand le rapport entre la profondeur d'eau h et la longueur d'onde λ est suffisamment petit et fournit une représentation simple et efficace du run-up des vagues. Néanmoins, ce modèle est inadapté pour reproduire les effets de shoaling et de dispersion des fréquences qui ont lieu near-shore. Des modèles non-hydrostatiques sont alors nécessaires. Ceux-ci introduisent des termes de dispersion dans les équations, augmentant le niveau de complexité de leurs résolutions. Plusieurs modèles ont été développés dans les dernières années sous les hypothèses de faible non-linéarité et faible dispersion (*cf.* Peregrine [1967];

Abbott *et al.* [1978]; Beji et Nadaoka [1996]; Madsen et Sørensen [1992]; Nwogu [1994]; ...). Les propriétés d'élaboration de ces modèles reposent souvent sur la relation de dispersion linéaire et le coefficient de shoaling linéaire, qui doivent être aussi proche que possible de ceux de la théorie linéaire des vagues (Airy theory). Cependant, ces modèles sont fréquemment utilisés hors de leur domaine d'application (*e.g.* en s'approchant de la condition de déferlement), là où il serait préférable d'utiliser des modèles fortement non-linéaires comme le système d'équations de Green et Naghdi [1976]. Le domaine de validité de ce modèle requiert seulement une faible dispersion mais n'impose aucune restriction sur la non-linéarité. Néanmoins, il partage les mêmes propriétés de dispersion linéaire du modèle de Peregrine [1967]. C'est pourquoi, Chazel *et al.* [2011] ont proposé un modèle équivalent avec des propriétés de dispersion améliorées qui fait l'objet d'étude de ce travail. Comme tous les modèles de type Boussinesq, les équations de Green-Naghdi ne peuvent pas représenter les effets de dissipation de l'énergie associés au déferlement des vagues. Pour inclure ces effets dans le modèle, un mécanisme de *wave-breaking* doit être incorporé dans les équations: pour détecter et traiter les vagues déferlantes dans le domaine computationnel.

Ce manuscrit présente, dans un premier temps, la dérivation des modèles de type Boussinesq les plus connus de la littérature et l'analyse de leurs propriétés de dispersion et de shoaling dans les régimes linéaire et non-linéaire. Cette analyse met en lumière dans le régime non-linéaire, une connexion entre les performances des modèles faiblement non-linéaires et faiblement dispersifs et la forme des termes dispersifs présents dans les équations. En particulier, nous montrons que pour un couple donné, relation de dispersion linéaire-coefficient de shoaling linéaire, deux systèmes de PDEs non-linéaires peuvent être dérivés, différenciés par la forme de leurs opérateurs dispersifs. Ces opérateurs peuvent être formulés à travers des dérivés de la vitesse ou des dérivés du flux. Nous parlons dans le premier cas de la forme *amplitude-velocity* du modèle et dans le deuxième de la forme *amplitude-flux* et nous montrons que, lorsque la vague s'approche des conditions de déferlement, seul la forme *amplitude-velocity* ou *amplitude-flux* des équations détermine le comportement du modèle (*e.g.* aspect et hauteur des vagues calculés).

Dans une deuxième partie, notre but est d'évaluer une nouvelle stratégie, pour résoudre le système d'équations fortement non-linéaire et faiblement dispersif de Green-Naghdi, qui puisse être facilement généralisée sur un maillage non structuré dans le cas multidimensionnel. Nous considérons une approche hybride (*e.g.* Bonneton *et al.* [2011b]; Kazolea *et al.* [2014]) utilisant le système de Green-Naghdi pour la propagation et le shoaling des vagues, en revenant au système de Saint-Venant pour modéliser la dissipation de l'énergie dans les régions déferlantes. Nous réécrivons les équations de Green-Naghdi en sé-

parant la partie hyperbolique et elliptique du problème à travers la définition d'une nouvelle variable auxiliaire. Donc, nous considérons une procédure de résolution à deux étapes: une phase elliptique dans laquelle un terme source est calculé en inversant l'opérateur associé aux effets dispersifs; une phase hyperbolique dans laquelle les variables du problème évoluent en résolvant les équations de Saint-Venant, contenant le terme source calculés dans la phase précédente. Cette approche est extrêmement flexible dans le sens où elle permet l'utilisation du schéma numérique le plus approprié pour chaque phase de sa résolution. De plus, elle permet d'améliorer un code existant, qui résout le système d'équations de Saint-Venant, en ajoutant simplement un terme purement algébrique à l'équation du moment prenant en compte les effets dispersifs. Concernant la discrétisation numérique de ces deux étapes, nous appliquons des méthodes adaptées à l'utilisation sur maillages arbitrairement non-structurés. Plus spécifiquement, nous nous servons d'une méthode d'éléments finis (EF) standard (Galerkin C^0 avec une approximation linéaire P1) pour la partie elliptique, tandis que deux options sont étudiées pour la partie hyperbolique: une méthode des volumes finis (VF) d'ordre élevé et une méthode d'éléments finis stabilisée. Les propriétés de dispersion associées aux schémas de discrétisation en espace sont étudiés et optimisés par rapport a la relation de dispersion du modèle, en montrant une erreur de phase très proche à celle d'une méthode différences finies d'ordre 4. La technique de résolution proposée est ainsi étendue au cas bi-dimensionnel en utilisant une approche hybride similaire EF/VF. Les modèles discrets obtenus sont minutieusement testés sur des cas de référence concernant la dispersion des vagues, le déferlement et le run-up, en montrant un potentiel prometteur pour la simulation de la dynamique des vagues en environnements côtiers.

La dernière partie de la thèse concerne l'investigation de mécanismes à large échelle qui mènent à la formation d'un mascaret dans des estuaires alluviaux convergents. En utilisant les équations de Saint-Venant, nous développons une analyse dimensionnel qui introduit un nouveau jeu de paramètres sans dimension qui gouverne la dynamique estuarienne, dépendant du forçage de la marée et des propriétés géométriques à large échelle du canal. Nous définissons un critère pour la détection du mascaret basé sur les observations expérimentales *in situ* (*cf.* Bonneton *et al.* [2015]) et nous effectuons une investigation systématique, basée sur 225 simulations numériques dans un canal idéalisé, pour identifier les conditions physiques qui mènent à la génération du mascaret. De cette façon, nous déterminons dans l'espace des paramètres une courbe critique divisant les estuaires en fonction de l'apparition du mascaret. Nous montrons que ce phénomène est contrôlé par la compétition entre deux processus physiques: la distorsion et la dissipation de la vague des marées, respectivement favorable et non-favorable à la formation du mascaret. De plus, nous mettons en évidence le fait que l'amplification de la vague des marées due à la

convergence topographique n'est pas une condition nécessaire pour la génération du mascaret et qu'il existe des estuaires caractérisés par la génération du mascaret avec une dissipation de la vague des marées. Ce travail représente donc la première étude focalisée sur ce sujet, qui a été aussi validé par un jeu de données d'estuaires réels.

Acknowledgements

This part of the thesis is dedicated to express my thanks to all people that have collaborated with me in these years, giving important contributions to the concrete realization of this work, and to everyone that, being on my side, has always believed in me, sustained me and pushed me in doing always better. This work is also yours!
At this point, some of the readers have probably already noticed that what follows is written in Italian. I know that the acknowledgements are usually one of the most read part of a thesis manuscript and I hope you will excuse me for having decided to use here my mother language. I'm sure that there is nothing you will not be able to understand using a good translator.

La prima persona a cui vanno i miei ringraziamenti non può essere che il supervisore del mio lavoro: grazie Mario! Tu mi hai dato la possibilità di intraprendere il viaggio che mi ha portato fino a qui. Seguendomi costantemente, passo dopo passo, trovando sempre la risposta alle mie domande, insegnandomi tanto, e non solo sul piano lavorativo, hai completato la mia formazione e sei stato una fonte costante di ispirazione per fare sempre meglio. Mi hai permesso di instaurare con te un rapporto che va al di là della pura collaborazione scientifica. Spero di essere stato abile a sfruttare al meglio tutto quanto mi hai offerto.

Grazie inoltre a Philippe, il co-supervisore di questo lavoro, per aver potuto approfittare dei suoi consigli e la sua esperienza. Il suo aiuto non si è limitato al lavoro svolto insieme nell'ambito della fluidodinamica negli estuari, ma mi ha fornito una maggiore comprensione fisica dei fenomeni di studio e valorizzazione del lavoro svolto.

Un enorme grazie lo devo a Maria, Luca, Nikos e Stevan, che hanno contribuito concretamente col loro tempo e le loro conoscenze a realizzare parti importanti di questo lavoro. Questo manoscritto porta il mio nome, ma sicuramente anche il vostro avrebbe dovuto figurare accanto al mio. Insieme abbiamo affrontato le difficoltà che ogni volta ci erano poste di fronte e questo ha anche contribuito a maturare tra noi una stretta amicizia di cui mi sento fortunato.

Il mio grazie si estende ulteriormente verso i molti membri dell'équipe CARDAMOM, ciascuno dei quali ha contribuito a creare un ambiente di lavoro sempre motivante e vivace. Grazie per questi anni trascorsi insieme. Colgo l'occasione per scusarmi con quanti tra di voi sono stati disturbati dal mio volume di voce spesso non controllato! Credo che un po' vi mancherò!

In questi tre anni, l'INRIA è stato il luogo di incontro di molte persone ai quali mi sento oggi legato da sentimenti di amicizia. Grazie per tutti i momenti passati insieme, le serate e soprattutto per la gita fuoriporta che abbiamo compiuto insieme in Italia, assolutamente da riorganizzare! Sto pensando in particolare a Andrea, Carlo, Cristoforo, Hicham, Jonathan, Leo, Ulisse, Umberto.

Non posso non fare un ringraziamento speciale alla banda di amici di BINOUZE : Antoine, Axel, Brice, Cam, Charlotte, John, Lulu, Onno, Pablo, Thomas. Ci siamo conosciuti non tanto tempo fa, ma mi avete da subito accolto nella vostra pazza famiglia con un calore unico! Mi sento fortemente legato a ciascuno di voi e sento il bisogno di ringraziarvi per l'amicizia che mi dimostrate e per il vostro sostegno!

Citare tutti quelli che negli anni ho conosciuto e con cui ho condiviso la passione per uno sport (la pallanuoto), l'attaccamento a dei colori (VON e USB Bordeaux), la gioia della vittoria e l'amarezza della sconfitta farebbe raddoppiare il numero di pagine di questo manoscritto. Preferisco dunque ringraziarvi cosi, con un finto anonimato che vi racchiude un po' tutti, pallanuotisti di vecchia e nuova data. Voi rappresentate per me una famiglia estesissima, dalla quale fatico a distaccarmi anche ora che festeggio la ventesima stagione in attivo. Il mio impegno per questo sport ha subito una battuta d'arresto per finalizzare questo lavoro, ma non tarderò a tornare in acqua insieme a voi!

Ultimi, ma non per ordine di importanza, i ringraziamenti più sentiti sono verso la mia famiglia : papà e mamma, nonno, Silvia e Gigi e (da poco) Sofia. Nonostante la distanza geografica che ci ha separato in questi anni, voi avete saputo starmi vicino più di ogni altro, manifestandomi tutto il vostro amore in ogni occasione. Questo risultato raggiunto è merito anche dei vostri sforzi di tutta una vita trascorsa insieme. Grazie di cuore! Spero che questo lavoro possa aver contribuito a rendervi ancora più orgogliosi di me.

Per finire : Mathilde, tu sei stata in questi anni di dottorato il risultato più inatteso, ma anche quello più bello e importante. Sei entrata improvvisamente nella mia vita e l'hai cambiata per sempre con la tua impronta, caricandola di nuovi stimoli grazie alla tua positività e solarità e dandole un significato tutto

nuovo e magnifico. Sono fiero di te, della persona che sei e dell'amore così naturale che ci lega e che si è recentemente concretizzato nella piccola Alice. Grazie per essere stata al mio fianco nei momenti più delicati e stressanti della redazione e finalizzazione di questo lavoro. Ti devo tanto!

Contents

Introduction

With the advent of a significantly increased computing power in the last decades, the accurate numerical simulation of free surface flows in realistic environments has started to play a major role in coastal engineering, largely replacing laboratory experiments in the design of coastal structures and providing a comprehensive picture of the phenomenon under consideration. The reasons of an increasing interest in the field are multiple: the prevention of the impact of tsunami waves and of inundations due to tidal bores (*e.g.* figure 1), the study of the sediment transport and of the coastal and river banks erosion process, the exploitation of renewable resources for energy production (*e.g.* tidal and wind wave energy), the management of coastal human activities (*e.g.* commercial, tourism, sport etc.). Performing an accurate numerical simulation of wave propagation in near-shore zones means providing a physically correct description of water wave dynamics from deep waters, through the near-shore region, up to the shoreline giving a precise prediction of local wave direction, height, speed and strength. In order to accomplish this goal, a set of numerical issues has to be faced as the transition between sub and super-critical flows, frequency dispersion, interaction with natural complex topographies and wetting/drying processes.

Mathematical modeling

In this work we want to achieve a good prediction of the water wave problem on large scales, from $\mathscr{O}(m)$ to $\mathscr{O}(km)$. The use of systems of asymptotic depth averaged equations on this task is quite common, since they lead to numerical models that are of practical use in coastal engineering, compared to the ones produced by more complicated mathematical systems, like the Euler equations. Depth averaged models have thus gained a lot of attention and popularity and significant research efforts have been made in the last 20 years in the development of systems of depth averaged equations which correctly reproduce the effects of wave propagation in the near-shore region including wave shoaling, refraction, diffraction, run-up and breaking.
The Nonlinear Shallow Water (NLSW) equations are one of the most widely used models belonging to this category. They are applied in many works in

Figure 1: Motivational examples: (Left) undular tidal bore propagation in the Garonne river (from Bonneton *et al.* [2015]); (Right) the Sumatra 2004 tsunami wave approaching the coast of Thailand (from Madsen *et al.* [2008]).

literature (*cf.* Munchow et Garvin [1991]; Titov et Synolakis [1998]; Hubbard et Dodd [2002]; Lanzoni et Seminara [1998]; Toffolon *et al.* [2006]; Bonetton [2007]; Marche *et al.* [2007]; Ricchiuto et Bollermann [2009]; Nikolos et Delis [2009] among the others) to describe long wave hydrodynamics when the vertical acceleration of water particles can be neglected, assuming the flow to be nearly horizontal. The NLSW model is a hyperbolic system of balance laws, particularly well suited to represent wave run-up on beaches and breaking wave energy dissipation in the form of propagating bores. However it is inappropriate for the description in deep(er) waters, where the effects related to frequency dispersion become more significant.
The main tool for performing studies in the context of dispersive waves have been pioneered by Boussinesq [1872], which derived a system of equations under the assumption that nonlinearity and dispersion are weak and of the same order of magnitude. Peregrine [1967] derived the first set of Boussinesq-type (BT) equations for variable bathymetry. However, the Peregrine BT model provides a linear dispersion description which rapidly diverges from that given by the linear theory of waves (or Airy theory) as the ratio between water depth and wavelength increases. In the 90s, several enhanced set of weakly nonlinear and weakly dispersive BT equations have been developed using the linear dispersion relation and shoaling coefficient as design properties to improve the original model of Peregrine and pushing towards deep(er) waters the range of applicability of these equations (*cf.* Madsen et Sørensen [1992]; Nwogu [1994]; Beji et Nadaoka [1996] are only the most known). Each of these models is different in the form and arrangement of the dispersive terms inside the equations. Such terms take the form of higher order derivatives (∂_{xxx} or ∂_{xxt}) of the unknowns of the problem. These models are adapted to describe wave propa-

gation and transformation in intermediate waters, but are often used outside their range of applicability, attending the wave breaking point in conditions of increased nonlinearity. Even though the results provided can be satisfactory, fully nonlinear models should instead be used in these cases. Green et Naghdi [1976] (GN) derived a set of fully nonlinear and weakly dispersive BT equations which has gained a lot of attention in the recent past. Its range of validity requires only the dispersion parameter to be small (long wave or shallow water hypothesis) but does not impose any restriction to nonlinearity. However, the GN system share the same linear dispersion properties of the Peregrine model. Chazel *et al.* [2011]; Bonneton *et al.* [2011b] proposed an equivalent model with improved dispersion properties, which will be the subject of study of this work.

Like all the BT models, the GN equations are unable to represent the energy dissipation effects associated to wave breaking. To actually include these effects in the model, a wave breaking mechanism has to be incorporated to the equations in order to track and handle breaking waves in the computational domain. Several approaches have been developed among the years, which mainly reduced to either including *ad-hoc* viscosity terms in the governing equations, or coupling the BT model with the NLSW equations creating a hybrid BT/NLSW model, which suppress the dispersive terms in breaking regions.

Even after the choice of the more suitable mathematical model, the overall numerical simulation of water waves propagating in coastal environments has to deal with many challenges and numerical issues. The problem is time-dependent. Nonlinear and dispersive processes have to be accurately simulated, which implies limiting the dissipation and the dispersion error of the numerical schemes. Rolling breaking waves cannot be represented with 2D models, however the abrupt decrease of averaged wave height and the dissipation/transformation of the wave potential energy in breaking waves can be represented by shocks. Therefore, shock-capturing capabilities are demanded to the schemes, which have to be also positivity-preserving and to respect the well-balancedness/C-property in order to treat dry states and wet/dry fronts inside the computational domain. Moreover, simulations on complex topographies and with moving fronts requires dealing with un-structured meshes. Finally, to solve the equations on physical close domains, boundary conditions are required. For dispersive models the use of wave generation and sponge layers have to be considered in order to either produce incoming waves or to dissipate the outgoing ones. These techniques are far from being optimal and need to be reiteratively tuned with respect to the model used and to the characteristics of the wave that want to be created/dissipated.

The work discussed in the thesis will, thus, deal with all these numerical aspects describing the strategies adopted to face the above issues.

Numerical approaches

From the numerical point of view BT equations have been discretized using different numerical techniques like Finite Differences (FD), Finite Elements (FE) and Finite Volume (FV) approaches. The major challenges that need to be dealt with are the approximation of the complex higher order derivative terms present in all the non-hydrostatic depth-averaged models, in respect of the accuracy requirements on the schemes in terms of low dispersion errors.
FD discretizations have been the firsts applied to solve BT equations. Their initial popularity is due to the ease with which higher order derivatives can be discretized (*cf.* Beji et Nadaoka [1996]; Fuhrman et Bingham [2004]; Wei et Kirby [1995]; Nwogu [1994] to cite a few). Higher order schemes have been realized mixing fourth and second order centered difference formula (*cf.* Wei et Kirby [1995]). The main drawback of the finite difference approach is the need of structured spatial meshes, even for irregular domains, and poor local mesh adaptivity potential (even tough hierarchical block structured multi-level approaches do exist, see *e.g.* Berger et Leveque [1998]). Moreover, high order discretizations need sensibly enlarged stencil and these schemes have also revealed to be noisy in practice near shorelines and in locations with rapidly changing solutions, such as breaking wave crest.
Fully unstructured solvers, allowing for adaptive mesh refinement, have been proposed based either on the FV, or on the FE approach. FV methods still represent the vast majority of the existing schemes of the literature, exploiting the fact that the robustness of the numerical schemes developed for the NLSW equations (*cf.* Toro [2001]; LeVeque [2002]) carries over to the Boussinesq application. Moreover the shock capturing capabilities of these codes, when applied to the NLSW equations, have motivated the use of hybrid BT/NLSW models to take over and control the wave breaking process.
On the other hand, the FE approximation gives a framework to naturally introduce higher order polynomial representation of the unknowns and of their derivatives, simply by handling these as auxiliary variables. The work of Eskilsson et Sherwin [2006]; Engsig-Karup *et al.* [2006] on discontinuous Galerkin approximations of enhanced BT models shows the potential in terms of accuracy of the finite element approach. Continuous Galerkin discretizations of Boussinesq models have been discussed in Walkley [1999]; Walkley et Berzins [2002]; Ricchiuto et Filippini [2014], while the use of an upwind stabilized Galerkin scheme, known as Streamline Upwind Petrov Galerkin scheme (SUPG) of Hauke [1998]; Hughes et Brook [1982]; Hughes *et al.* [2010], is presented in Ricchiuto et Filippini [2014]. These contributions show results at least as good as those obtained by means of finite difference schemes, with the additional flexibility of a natural unstructured mesh formulation. Moreover, the SUPG scheme have shown very high potential in handling the NLSW, both in terms of preservation of physically relevant steady equilibrium (well-balancedness), and

Figure 2: Illustration of a tidal bore propagating in the Garonne River. Aerial photograph taken at Podensac on September 10, 2010. Tidal wave amplitude at the estuary mouth $a_0 = 2.5$ [m] and freshwater discharge $q_0 = 128m3/s$ (from Bonneton *et al.* [2016]).

in terms of a stable approximation of moving shorelines Ricchiuto et Bollermann [2009]; Ricchiuto [2011]; Hauke [1998]; Brufau et Garcia-Navarro [2003]. An hybrid BT/NLSW model based on the SUPG scheme of Ricchiuto et Filippini [2014] has been discussed in Bacigaluppi *et al.* [2014a,b]. For purely hyperbolic problems, it is known that, compared to finite differences, finite element schemes have improved dispersion characteristics, due to the presence of a mass matrix.

For what concerns the GN equations, several discretization approaches have been explored. We refer to Antunes do Carmo *et al.* [1993]; Cienfuegos *et al.* [2006, 2007]; Chazel *et al.* [2011]; Bonneton *et al.* [2011b]; Marche et Lannes [2015]; Li *et al.* [2014]; Mitsotakis *et al.* [2014]; Duran et Marche [2014] among others. In Cienfuegos *et al.* [2006, 2007], the authors derive a higher order FV scheme in one dimension. In Chazel *et al.* [2011]; Bonneton *et al.* [2011b] a hybrid FV/FD splitting approach is used, while Marche et Lannes [2015] follows the same idea for the solution of a new class of two-dimensional GN equations on structured meshes. In Li *et al.* [2014] a coupled discontinuous Galerkin and Continuous Galerkin is developed in one dimension but using only flat bottom topographies. Most of them are also really hard to extend in two dimensions. Up to now, the only known work of the literature involving the solution of the fully nonlinear GN equations on 2D unstructured meshes is the approach of Duran et Marche [2016] using a discontinuos Galerkin method.

Estuarine dynamics

Over the last decade there has been an increasing interest in estuarine dynamics, producing an increasing understanding of the complex mechanisms which rule their fluid dynamic and morphodynamic processes. The research in the field is motivated by the important impact of estuaries to the global surrounding environment and to human activities which exploit river estuaries as important trade routes. An estuary is the transition between two distinct water bodies: a river and a sea. The alternance of the tidal forcing on the river mouth is responsible for the harmonic pumping of into and out of the estuary with an erosive power that finds its natural morphological equilibrium only if the banks converge at an exponential rate. The discharge of the river provides fresh water and sediments to the estuary system. These are transported downstream by the residual downstream flux, which is result of a combination of the harmonic tidal flow and the downward river flow. Under particular conditions of tidal forcing, river discharge, estuary convergence rate and bottom friction the original tidal wave can experience strong phenomena of distortion and amplification/dissipation which may lead, in some case, to the formation of a bore.

Tidal bores are an intense nonlinear wave phenomenon which has been observed in many convergent alluvial estuaries world-wide (see example in figure 2). Up until the beginning of the 21^{st} century, tidal bore characterization in natural environments was based essentially on qualitative observations (*cf.* Lynch [1982]; Bartsch-Winkler et Lynch [1988]). In the last decade several quantitative field studies have been focused on small-scale bore processes, devoted to the analysis of wave, turbulent and sediment processes associated with tidal bores (*e.g.* Simpson *et al.* [2004]; Wolanski *et al.* [2004]; Bonneton *et al.* [2011c, 2012]; Furgerot *et al.* [2013] and references therein). Most of these studies focused on well-developed tidal bores and small scale processes for some specific estuaries, but not on the tidal-bore occurrence conditions for any given alluvial estuaries. The basic conditions for tidal bore formation are well-known (*cf.* Bartsch-Winkler et Lynch [1988]): a large tidal range, a shallow and convergent channel, and low freshwater discharge. Yet, estuarine classification in terms of tidal bore occurrence cannot be established from simple criteria based on these hydrodynamic and geometric conditions. Nevertheless, bore formation criteria based on the tidal range, Tr, has been published (*cf.* Bartsch-Winkler et Lynch [1988]; Chanson [2012]), but the empirical criteria used for these estimations are not clearly defined and numerous observations on tidal bores in the Gironde/Garonne estuary (*cf.* Bonneton *et al.* [2015]), Seine estuary (*cf.* Bonneton *et al.* [2012]) or Sée estuary (*cf.* Furgerot *et al.* [2013]) do not support them. These examples prove that such a simple criterion, based on a dimensional flow variable, cannot be relevant to determine tidal bore occurrence. A systematic study on the physical parameters control-

ling tidal bore formation has not been addressed yet.

Thesis contributions

This thesis is the result of a transversal research on BT models. In the first part of the work, we consider the derivation of some widely used systems of BT equations, including both weakly-nonlinear weakly dispersive systems and fully-nonlinear weakly-dispersive ones, focusing in particular on the analysis of their dispersive and shoaling properties in both the linear and nonlinear regimes. The BT models are often designed optimizing their linear properties with respect to Airy theory, however understanding their behavior in the nonlinear conditions is of paramount importance for practical applications. The analysis performed has put in light a connection between models performances in the nonlinear regime and the form of the dispersive terms included in the equations. For a given couple linear dispersion relation-linear shoaling parameter, we show that is possible to derive two systems of nonlinear PDEs differing in the form of the linear dispersive operators. In particular, within the same asymptotic accuracy, these operators can either be formulated by means of derivatives of the velocity, or in terms of derivatives of the flux. In the first case we speak of *amplitude-velocity* form of the model, in the second of *amplitude-flux* form. We show examples of these couples for some known linear relations. We then show, both analytically and by numerical nonlinear shoaling tests, that while for small amplitude waves the accuracy of the dispersion and shoaling relations is fundamental, when approaching breaking conditions it is only the amplitude-velocity or amplitude-flux form of the equations which determines the behaviour of the model, and in particular the shape and the height of the waves. In this regime we thus find only two types of behaviours, whatever the form of the linear dispersion relation and shoaling coefficient.

In the second part of the manuscript, our aim is to evaluate a strategy that can be easily generalized on arbitrary unstructured meshes in the multidimensional case for the solution of fully nonlinear, weakly dispersive free surface waves. For this reason we consider the hybrid approach, used *e.g.* in Bonneton *et al.* [2011b] and Kazolea *et al.* [2014] using the GN partial differential equations for propagation and shoaling, while locally reverting to the NLSW equations to model energy dissipation in breaking regions. Starting from the form of the GN equations proposed in Bonneton *et al.* [2011b] and Chazel *et al.* [2011], we consider a two steps solution procedure: an elliptic phase in which a source term is computed by inverting the coercive operator associated to the dispersive effects; an hyperbolic phase in which the flow variables are evolved by solving the NLSW equations, with all non-hydrostatic effects accounted for by the source computed in the elliptic phase. For the numerical discretization

of these two steps in one dimension, we consider methods which can be easily generalized on arbitrary unstructured meshes in the multidimensional case. In particular, we focus on the use of a standard C^0 Galerkin finite element method for the elliptic phase, while high order finite volume (FV) and stabilized finite element (FE) methods are used independently in the hyperbolic phase. The discrete dispersion properties of the fully coupled methods thus obtained are studied and optimized with respect to the model dispersion relation, showing phase accuracy very close to that of a fourth order finite difference method. In addition, we will exploit the two steps solution procedure to obtain a robust embedding of wave breaking. We evaluate two strategies: one based on simply neglecting the non-hydrostatic contribution in the hyperbolic phase; the second involving a tighter coupling of the two phases, with a wave breaking indicator embedded in the elliptic phase to smoothly turn off the dispersive effects. The solution strategy proposed is then extended to the two-dimensional case, using a similar FE/FV hybrid approach. The discrete models obtained are thoroughly tested on benchmarks involving wave dispersion, breaking and run-up, showing a very promising potential for the simulation of complex near shore wave physics.

The last part of the thesis deals with the investigation of the large scale mechanism of tidal bore formation in convergent alluvial estuaries. Using the Saint Venant (or NLSW) equations, we develop a scaling analysis of the global tidal wave transformation as a function of both the tidal forcing at the estuary mouth and the large-scale geometric properties of the channel, introducing a new set of dimensionless parameters. Using a criterion for bore detection based on experimental observations *in situ* (*cf.* Bonneton *et al.* [2015]), we perform extensive numerical simulations (225 runs) on an idealized channel to identify the physical conditions that lead to tidal bore generation. In the space of parameters, we determine a critical curve which divides estuaries according to tidal bore occurrence. We show that bore formation is controlled by the competition between two physical processes: a) the knee-shaped distortion of the tidal wave, with flood dominance and eventually bore inception; b) the dissipation of the tidal wave, which is unfavourable to bore formation. We also provide evidence that amplification due to topographic convergence is not a necessary condition for tidal bore generation and that there exist estuaries which display both wave damping and bore development. The work represents the first systematic study focusing on this scope, which is also validated using some real estuaries data collection. The validity of the results has been also assessed in presence of freshwater river discharge, showing that, for low river discharge, its effect on estuarine dynamics can be neglected.

These contributions have produced the following series of scientific publications and talks in workshops and conferences:

Publications:

- Ricchiuto, M. and Filippini, A.G. (2014), Upwind residual discretization of enhanced Boussinesq equations for wave propagation over complex bathymetries, *J.Comput.Phys., 271, 306-341.*
- Filippini, A.G., Bellec, S., Colin, M. and Ricchiuto, M. (2015), On the nonlinear behavior of Boussinesq type models: amplitude-velocity vs amplitude-flux forms, *Coast.Eng., 99, 109-123.*
- Filippini, A.G., Kazolea, M. and Ricchiuto, M. (2016), A flexible genuinely nonlinear approach for nonlinear wave propagation, breaking and run-up, *J.Comput.Phys., 310, 381–417.*
- Bonneton, P., Filippini, A.G., Arpaia, L., Bonneton, N. and Ricchiuto, M. (2016) Conditions for tidal bore formation in convergent alluvial estuaries, *Estuar.Coast.Shelf S., 172, 121-127.*
- Arpaia, L., Filippini, A.G., Bonneton, P. and Ricchiuto, M. *in preparation* Modelling analysis of tidal bore formation in convergent estuaries.
- Filippini, A.G., Kazolea, M. and Ricchiuto, M. *in preparation*, A fully nonlinear and weakly dispersive approach for wave propagation, breaking and run-up on unstructured meshes.

Conferences and Workshops:

- ECMI 2014: On nonlinear shoaling properties of enhanced Boussinesq models; Taormina (Italy), 9-13 June 2014.
- Tidal Bore Workshop 2015: Modeling analysis of tidal bore formation on convergent estuaries; Caen (France), 18-20 May 2015.
- IAHR 2015: Modeling analysis of tidal bore formation on convergent estuaries; The Hague (Nederlands), 28 June - 3 July 2015.
- Boundary Conditions Workshop: Boundary conditions for coastal wave models: hyperbolic systems; Bordeaux (France), 17-20 November 2015.

Outline of the thesis

The thesis is organized as follows. Chapter 1 is dedicated to the mathematical modeling of free surface flows in the domain of the asymptotic depth averaged BT models. We show the main steps for the derivation of the most known and used BT model of the literature from the original Euler system. The dispersive and shoaling property of each model are discussed and compared with respect

to the results given by the Airy theory in the linear regime. The behaviour of the different type of PDEs in the nonlinear contest is also compared and analyzed. The chapter ends introducing the fully nonlinear weakly dispersive system of GN, and its enhanced variant of Chazel *et al.* [2011]; Bonneton *et al.* [2011b], which will be the subject of study in the second part of the work.
The solution strategy proposed for the one dimensional GN system of equations is introduced in chapter 2. The equations are re-written obtaining an elliptic-hyperbolic decoupling and the details of the discretization strategies are presented: a continuous C^0 Galerkin scheme for the elliptic part; a high order FV and SUPG schemes for the hyperbolic part. The dispersive properties of the schemes are investigated and optimized in the time-continuous case. The description of the basic discretizations is completed with a discussion on the time integration schemes along with boundary condition and wet/dry treatment and friction. Two alternative ways of embedding wave breaking are proposed. Suitable numerical tests in one spatial dimension are implemented in chapter 3 to validate the schemes implemented, highlight their different performances and compare the results to experimental data.
In chapter 4, we apply the solution strategy to the two-dimensional case. The 2D GN system of equations is discretized by means of a hybrid FE/FV method and all the arguments discussed for the one-dimensional case are extend to the multi-dimensional. The scheme is then validated and tested against analytical solutions and experimental data for standard benchmark of the field and on unstructured meshes in chapter 5.
Finally, chapter 6 is dedicated to the numerical investigation of the physical conditions leading to tidal bore formation in convergent alluvial estuaries. We introduce the governing equations and define the dimensionless parameters emerging from the scaling analysis. Using real estuaries data, collected from the literature, we identify the space of parameters suitable to perform our study. We provide the definition of the idealized case of study and introduce a criterion for bore detection based on experimental observation *in situ*. We discuss the implementation of the boundary conditions for the simulation, validating the implemented ones using previous numerical results from the literature. Then, at last, we show the results of the numerical investigation and we account for the effect of water river discharge on bore formation.

Chapter 1

The Physical Models

Contents

The accurate mathematical modeling and numerical simulation of water wave propagation in near-shore regions has received considerable attention in the last decades, since they have largely replaced laboratory experiments in the coastal engineering community. In the classical fluid-mechanics framework, a free surface flow can be described using the three dimensional Navier-Stokes (NS) system of equations, assuming the fluid to be Newtonian, viscous and incompressible. The solution of the NS system of equations in practical application is extremely costly. For this reason, despite the modern ever increasing computing power, less computational demanding models have been developed and are now widely used in the engineering community, especially in large scale approximation as *e.g.* tsunami propagation or storm surge simulations at global or regional scales. In shallow water conditions, the classical approach is based on a perturbation method with respect to a small parameter $\mu = h_0/\lambda$ (with h_0 and λ the characteristic water depth and horizontal scale) in order to reduce the three-dimensional equation system to a two-dimensional one. This method, initially introduced by Boussinesq [1872], allows to derive several system of depth averaged shallow water equations, which are named Boussinesq-type equations.

The simpler and most popular depth-averaged model is the Nonlinear Shallow Water (NLSW) system of equations. This set of equations performs a correct simulation of the wave propagation where the ratio between water depth h and wavelength λ is sufficiently small, it gives a good description of energy dissipation in wave breaking as shocks and is simple and efficient to represent the wave run-up on beaches. However, the NLSW model is unable to reproduce the effects of shoaling and frequency dispersion which take place in the near-shore region, before the waves reach the surf zone. These phenomena are the main causes which determine the height of the waves reaching the beach together with the instant and location of wave breaking. For these reasons, even if the interest in coastal applications is mainly focused on the *on-shore zone*, where the human activities are concentrated, it is of primary importance to be able to accurate simulate the whole process of wave transformation from the deep ocean, up to the coast. Many other models have, thus, been developed, based on Boussinesq-type (BT) equations, trying to extend the range of validity of the NLSW system and to optimize its dispersion properties with respect to the so-called Airy theory, directly obtained from the three-dimensional Euler equations.

BT models explicitly introduce dispersion terms in the equations, which, therefore, are more suitable in waters where dispersion effects start to have a relevant influence on the free surface deformation. They have become an increasingly important predictive tool in coastal engineering. However, they have to be used with much care. Quite often, weakly-nonlinear variants of these

models, such as those proposed in Abbott *et al.* [1978]; Beji et Nadaoka [1996]; Madsen et Sørensen [1992]; Nwogu [1994]; Peregrine [1967], are used outside of their range of applicability, *e.g.* when reaching breaking conditions. In these cases fully-nonlinear models should, instead, be used Grilli *et al.* [1994]. Moreover, to actually include the energy dissipation effects associated to wave breaking, either *ad-hoc* viscosity terms are included, or a coupling with the NLSW equations is introduced Tonelli et Petti [2011]; Tissier *et al.* [2012]; Brocchini [2014]; Kazolea *et al.* [2014]. Despite of the fact that they are theoretically well adapted only for small amplitude waves, in practice these models seem to provide good results even when they are used outside they domain of validity Roeber et Cheung [2012]; Brocchini [2014]; Kazolea *et al.* [2014].

One of the keys of the successfull application of these systems of equations is the use of a properly designed wave breaking model. Such a model includes a breaking detection criterion and a dissipation mechanism. The challenge for a correct capturing of these fronts is the understanding of the genuinely nonlinear physics underlying breaking, as well as the behavior of the underlying dispersive wave propagation model, and in particular the wave shoaling when approaching the nonlinear regime. Accounting for genuinely nonlinear effects is thus a research topic of high priority Brocchini [2014]. While the linear properties of the models can be thoroughly studied analytically Dingemans [1997], in the nonlinear case some properties, such as *e.g.* the shoaling behavior, must be studied numerically.

There exist several types of weakly nonlinear BT models. These all provide different approximations of the nonlinear wave (or Euler) equations. The design properties of these models are often the linear dispersion relation and shoaling coefficients, which should be as close as possible to those of the linear wave theory in the range of wave numbers relevant for the applications sought. Given a linear dispersion relation and linear shoaling coefficient, it is known that two nonlinear set of Partial Differential Equations (PDEs) can be formulated, both degenerating to the same linearized system. Denoting by a the wave amplitude, h_b the mean water level, and λ the wavelength, these two models are alternate forms within the same asymptotics in terms of the nonlinearity $\varepsilon = a/h_b$ and dispersion $\mu = h_b/\lambda$ parameters. The main difference is in the nature of the higher order derivatives, which can either be applied to the velocity u, or to the flux $q = hu$, h denoting the water depth. These formulations are referred here to as *amplitude-velocity*, and *amplitude-volume flux* forms. Examples of such couples for some dispersion relations are given in Dingemans [1997].

1.1 The Euler system of equations

Before showing the governing equations for the water waves problem, we present the general notation used in this work. In order to simplify the notation, all the models and their asymptotic developments will be shown in two-dimensions (in the vertical plane (x, z)), however the procedure is absolutely general and can be performed in the three dimensional case (x, y, z) (*cf.* Lannes [2013]). As shown in figure 1.1, a Cartesian coordinate system is adopted, with horizontal and vertical directions x and z respectively. We denote the velocity vector by $\mathbf{u} = (u, w)^T$. The free surface elevation is the main unknown of the problem. It is denoted by $\eta(x, t)$ and measured with respect to its rest state represented by h_0. The bathymetry $b(x)$ is a time-independent and sufficiently regular function. The total water depth can be thus expressed by:

$$h(t, x) = h_0 + \eta(t, x) - b(x) = \eta(t, x) + h_b(x) \ ,$$

where h_b represents the water depth at rest, defined by $h_b(x) = h_0 - b(x)$.

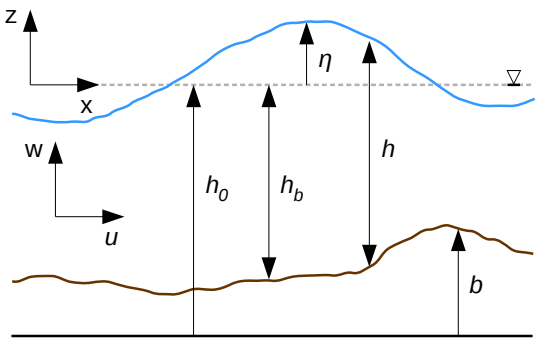

Figure 1.1: Sketch of the free surface flow problem, main parameters description.

Using the hypothesis of constant density ρ of the fluid, bathymetry $b(x)$ independent from time, and neglecting the effects due to the surface tension and viscosity, the water wave problem can be described using the incompressible Euler's equations. Following the notation just introduced, denoting with p the pressure and g the gravity, this system, valid for $z \in [b(x), h_0 + \eta(x, t)]$, takes the form:

$$u_t + uu_x + wu_z + \frac{p_x}{\rho} = 0 \ , \tag{1.1}$$

$$w_t + uw_x + ww_z + \frac{p_z}{\rho} + g = 0 \ , \tag{1.2}$$

$$u_x + w_z = 0 \ , \tag{1.3}$$

where $(\cdot)_x$ and $(\cdot)_z$ indicate respectively the derivatives with respect to x and z of the quantity $(\cdot)$. The system is composed by two equations of momentum conservation, in the x (1.1) and z (1.2) Cartesian directions respectively, written in convective form, and by the incompressible equations (1.3).
The equation for the vorticity $\boldsymbol{\omega} = \nabla \wedge \mathbf{u}$ of a two-dimensional free surface and inviscid flow reads:

$$\boldsymbol{\omega}_t + \big(\mathbf{u} \cdot \nabla\big)\boldsymbol{\omega} = 0 \ . \tag{1.4}$$

Due to the fact that the viscous effects have been neglected, there are no source terms in equation (1.4), so an irrotational initial state will remain irrotational. For water wave propagation, irrotationality is quite well verified. The effects of the viscous boundary layer (ocean floor) and shear layer (water-air) are very small in the propagation phase. We can, thus, include into the previous system (1.1)-(1.3) the irrotational condition:

$$u_z - w_x = 0 \ . \tag{1.5}$$

Two boundary conditions have to be added to the irrotational and incompressible Euler system in order to solve it. The free surface is the interface between the water and the air. It is defined by the property that the fluid particles cannot cross this interface and it is characterized by the equation $f(x, z, t) = 0$. Due to the fact that the two fluids are immiscible all the particles belonging to the surface interface will remain on it and the velocity components, of the fluid and of the surface, normals to the interface must equal. Given the free surface velocity vector $\mathbf{u_s}$ and the unitary vector normal to the interface $\mathbf{n} = \frac{\nabla f}{\|\nabla f\|}$, it follows that:

$$\mathbf{u} \cdot \mathbf{n} = \mathbf{u_s} \cdot \mathbf{n} \ ,$$

hence:

$$\mathbf{u} \cdot \nabla f = \mathbf{u_s} \cdot \nabla f \ .$$

Deriving with respect to time the free surface relation $f(x, z, t) = 0$, we obtain:

$$\frac{df}{dt} = \frac{\partial f}{\partial t} + \frac{\partial f}{\partial x}\frac{dx}{dt} + \frac{\partial f}{\partial z}\frac{dz}{dt} \ ,$$

that, by means of the $\mathbf{u}_s$ definition, becomes:

$$\frac{df}{dt} = f_t + \mathbf{u}_s \cdot \nabla f = 0 \ ,$$

from which:

$$f_t + \mathbf{u} \cdot \nabla f = 0 \ .$$

Considering the free surface definition: $f(x, z, t) = z - (h_0 + \eta(x, t))$, we thus obtain $\nabla f = (-\eta_x, 1)^T$ and, finally, the cinematic condition at the free surface $z = h_0 + \eta(x, t)$:

$$w = \eta_t + u\eta_x \ . \tag{1.6}$$

Following the same procedure, but taking into account the fact that the bed does not change along the time, we can obtain the slip condition at the bottom boundary $z = b(x)$:

$$w = ub_x \ . \tag{1.7}$$

1.2 On near-shore wave transformation

Waves propagating in near-shore regions undergo deep transformations in both phase and energy. Shoaling, dispersion and breaking deeply affect the incoming wave, such that a description of the flow field can be said accurate only if all these playing actors are well reproduced by the model, used for the numerical simulation. In particular, the right time instant and space location of breaking are caught only if the wave shoaling and dispersion processes are well set out. For this reason, the correct choice of the most suitable model for the specific application considered is essential.

Wave shoaling is a transformation process experienced by waves entering shallower waters. In particular, water depth reduction acts on the incoming wave increasing its steepness and height, augmenting its initial wavenumber k_0 and decreasing its celerity.
Figure 1.2 shows, instead, the effects of frequency dispersion acting on a monochromatic wave, propagating over a submerged bar. The original signal propagates undisturbed until the bar is reached. The abrupt change of the bed, with initial reduction of water depth, causes the wave to shoal, changing its original amplitude and its spectrum adding higher frequencies, and causes the fragmentation of the original wave signal into a complex train of waves also including higher harmonics. Each of them start to travel with an own characteristic celerity speed, such that they originate an intricate process of

wave interactions which give a seemingly chaotic texture to the water free surface. This example may induce to think that dispersion is mainly related to nonlinear waves and to interactions with bed variations. However, a simple analysis on the linear theory of waves (or Airy wave theory) tells us that this is not the case, and that dispersion is present also in the linear regime and for flat bathymetry.

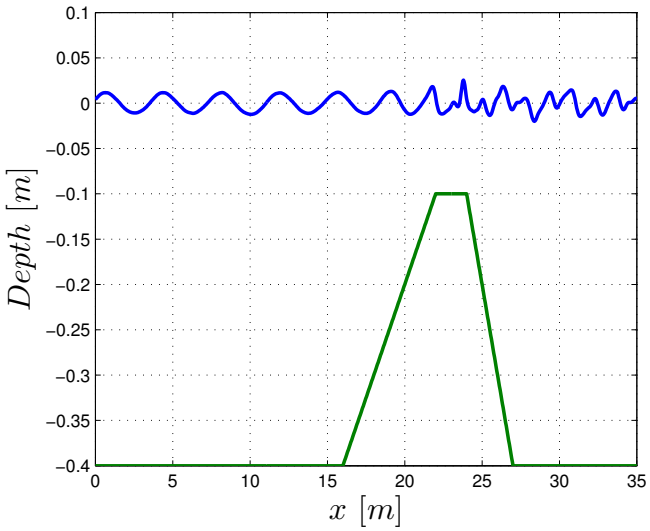

Figure 1.2: Monochromatic wave propagating over a submerged bar: numerical computation using the Madsen and Sørensen model (1.93).

Giving the most accurate possible description to these phenomena has become the guideline in the derivations of the several depth-averaged models that, within the limits of different asymptotic approximations of the Euler model, have been developed to avoid the cost and complexity of using system (1.1)-(1.5) in practical coastal application. In particular, it has become a common use in the literature to validate (or invalidate) simplified systems of equations by studying their linear dispersion characteristics and, in particular, evaluating the error made with respect to the results of the linear Airy theory. We will, thus, pursue the same strategy in the following sections, in which we are going to introduce and discuss some well known depth-averaged models. We will start by recalling the linear wave theory in the next section.

1.3 Airy wave theory

The linear theory of waves can be derived by linearizing the Euler equations (1.1)-(1.3) together with (1.5) . In order to perform this linearization, we first

use the irrotational condition (1.5) to rewrite the first two equations of the system as:

$$\begin{aligned} u_t + uu_x + ww_x + \frac{p_x}{\rho} &= 0 \ , \\ w_t + uu_z + ww_z + \frac{p_z}{\rho} + g &= 0 \ . \end{aligned}$$

Than, we observe that, as a consequence of incompressibility and irrotationality of the flow, the velocity can be derived from a potential Φ, whose derivatives with respect to the Cartesian directions represent the two components of the velocity vector: $u = \Phi_x$ and $w = \Phi_z$. Introducing the potential Φ in the equations, we obtain:

$$\begin{aligned} \Phi_{xt} + \Phi_x\Phi_{xx} + \Phi_z\Phi_{xz} + \frac{p_x}{\rho} &= 0 \ , \\ \Phi_{zt} + \Phi_x\Phi_{zx} + \Phi_z\Phi_{zz} + \frac{p_z}{\rho} + g &= 0 \ , \end{aligned}$$

that can be also written introducing the gradient operator $\nabla(\cdot)$ as:

$$\nabla\Big(\Phi_t + \frac{1}{2}\big((\Phi_x)^2 + (\Phi_z)^2\big) + \frac{p}{\rho} + gz\Big) = 0 \ .$$

Integrating the last expression and redefining the flow potential in order to include in it the constant coming from the integration $\Phi := \Phi + \int C(t)dt$, we get:

$$\Phi_t + \frac{1}{2}\big((\Phi_x)^2 + (\Phi_z)^2\big) + \frac{p}{\rho} + gz = 0 \ . \tag{1.8}$$

Note that equation (1.8) is also known as the non-stationary Bernoulli equation in $b(x) \leq z \leq h_0 + \eta$. We can obtain a new formulation of system (1.1)-(1.5) evaluating (1.8) at the free surface $z = h_0 + \eta$. The pressure appears in the Euler system only through its gradient. It can be thus redefined up to an arbitrary constant value, giving us the possibility to assign $p = 0$ at the free surface. The final form we get is the following:

$$\Phi_t + \frac{1}{2}\big((\Phi_x)^2 + (\Phi_z)^2\big) + g\eta = 0 \quad at \quad z = h_0 + \eta(x,t) \ , \tag{1.9}$$

$$\Phi_{xx} + \Phi_{zz} = 0 \quad at \quad b \leq z \leq h_0 + \eta(x,t) \ , \tag{1.10}$$

$$\Phi_z = \eta_t + \Phi_x\eta_x \quad at \quad z = h_0 + \eta(x,t) \ , \tag{1.11}$$

$$\Phi_z = -(h_b)_x\Phi_x \quad at \quad z = b(x) \ . \tag{1.12}$$

The system is now ready to be linearized around the rest state $h(x) = h_0$ and $u = w = 0$, giving what we can call the Airy system of equations:

$$\Phi_t + g\eta = 0 \quad at \quad z = h_0 \ , \tag{1.13}$$

$$\Phi_{xx} + \Phi_{zz} = 0 \quad at \quad b \leq z \leq h_0 \ , \tag{1.14}$$

$$\Phi_z = \eta_t \quad at \quad z = h_0 \ , \tag{1.15}$$

$$\Phi_z = -(h_b)_x \Phi_x \quad at \quad z = b(x) \ . \tag{1.16}$$

Dispersion Properties: It is common use, in the literature, to evaluate the dispersion characteristics of a model by means of a Fourier analysis on a horizontal bottom, looking for signals of the type $u(x,t) = u_0 \exp^{j(\omega t - kx)}$, with ω the angular frequency and k the corresponding wave number of the signal. Such analysis allows to obtain an expression for the phase velocity C described by the model. The phase velocity of a wave is the rate at which the phase of the wave propagates in space, meaning the velocity at which the phase of any frequency component of the wave travels. It is generally defined by the following relation:

$$C = \frac{\omega}{k} \ . \tag{1.17}$$

Another quantity used to measure the wave dispersion, which is related to C, is the group velocity C_g. This represents the velocity of propagation of the energy in a wave train and is defined as:

$$C_g = \frac{\partial \omega}{\partial k} \ , \tag{1.18}$$

having denoted with $\partial(\cdot)/\partial k$ the partial derivative of $(\cdot)$ with respect to the variable k. Using the phase velocity definition (1.17), it emerges the relation:

$$C_g = C + k\frac{\partial C}{\partial k} \ . \tag{1.19}$$

In order to find the expression for C given by the Airy theory, we first rewrite system (1.13)-(1.16) using a constant value of bathymetry $b(x) = b$. Moreover, the variable η can be eliminated by substituting (1.15) into (1.13), previously derived with respect to time. This, finally, gives:

$$\Phi_{tt} + g\Phi_z = 0 \quad at \quad z = h_0 \ , \tag{1.20}$$

$$\Phi_{xx} + \Phi_{zz} = 0 \quad at \quad b \leq z \leq h_0 \ , \tag{1.21}$$

$$\Phi_z = -(h_b)_x \Phi_x \quad at \quad z = b \ . \tag{1.22}$$

We, than, introduce in equation (1.21) a solution of the form $\Phi(x,z,t) = B(z)\exp^{j(\omega t - kx)}$, with j the imaginary unit, obtaining the Ordinary Differential Equation (ODE):

$$B_{zz} - k^2 B = 0 \ .$$

The solutions of this ODE are written in the form:

$$B(z) = \alpha \cosh\big(kz\big) + \beta \cosh\big(kz\big) \ .$$

Using the condition (1.22) to find the constants, we deduce that:

$$\Phi(x,z,t) = \alpha \cosh\big(kz\big) \exp\Big(j(\omega t - kx)\Big) \ . \tag{1.23}$$

with α a real number that will not play any role in the rest of the derivation. In fact, substituting (1.23) into (1.20) leads to:

$$-\omega^2 \alpha \cosh\big(kh_0\big) \exp\Big(j(\omega t - kx)\Big) + g\alpha k \sinh\big(kh_0\big) \exp\Big(j(\omega t - kx)\Big) = 0 \ ,$$

and, finally, rearranging:

$$C_{Airy}^2 = \frac{\omega^2}{k^2} = g h_0 \frac{\tanh(\varphi_0)}{\varphi_0} \ , \tag{1.24}$$

having introduced the variable:

$$\varphi_0 = k h_0 = 2\pi h_0/\lambda = 2\pi\mu \ ,$$

with $\mu = h_0/\lambda$.
Relation (1.24) states that the phase velocity of a wave is function of its wavenumber k, meaning that any wave travels at a different speed depending on its frequency causing dispersion. This result has been found using the linear theory of Airy and making the hypothesis of flat bathymetries, meaning that, dispersion is an effect inherent to wave propagation and it is not introduced by the bathymetry. However, the effects of dispersion become quantitatively important only for increasing values of the parameter kh_0 or $\frac{h_0}{\lambda}$.
The group velocity can be evaluated using the relation (1.19). This gives:

$$C_{g,Airy} = \frac{C_{Airy}}{2}\left(1 + \frac{2\varphi_0}{\sinh(2\varphi_0)}\right) \ . \tag{1.25}$$

Shoaling Properties: To characterize wave shoaling in the linear case, one introduces the shoaling coefficient s which relates the rate of change in wave amplitude to the rate of change in water depth $h = h(x)$:

$$\frac{a_x}{a} = -s\frac{h_x}{h} \ . \tag{1.26}$$

The procedure to compute explicit expressions for the coefficient s is described in many papers and textbooks, see *e.g.* Dingemans [1997]; Beji et Nadaoka [1996]; Madsen et Sørensen [1992]; Kazolea [2013]; Lee *et al.* [2003]. Here we retrace the main steps to recover the shoaling gradient expression for the Airy theory. We start by considering the so-called conservation relation of the energy flux (*cf.* Dingemans [1997]):

$$\left(a^2 C_g\right)_x = 0 \ , \tag{1.27}$$

from which straightforward manipulations lead to:

$$\frac{1}{a^2 C_g}\left(a^2 C_g\right)_x = \frac{a_x}{a} + \frac{1}{2C_g}\left(C_g\right)_x = 0 \ . \tag{1.28}$$

From equation (1.25), introducing $\varphi = kh$, we note that $C_{g,Airy} = C_{Airy}F(\varphi)$. This means:

$$\frac{1}{C_{g,Airy}}\left(C_{g,Airy}\right)_x = \frac{1}{C_{Airy}}\left(C_{Airy}\right)_x + \frac{1}{F}F_x \ ,$$

From the phase velocity definition (1.17), we also deduce that:

$$C_x = \left(\frac{\omega}{k}\right)_x = -\frac{\omega}{k^2}k_x \ ,$$

being ω independent of x. Thus:

$$\frac{C_x}{C} = -\frac{k_x}{k} \ ,$$

which transforms the energy flux conservation equation (1.27) as follow:

$$\frac{a_x}{a} + \frac{1}{2}\left(\frac{F_x}{F} - \frac{k_x}{k}\right) = 0 \ . \tag{1.29}$$

The value of F_x/F can be obtained directly from (1.25):

$$\frac{F_x}{F} = \frac{2\varphi\Big(\sinh(2\varphi) - 2\varphi\cosh(2\varphi)\Big)}{\sinh(2\varphi)\Big(\sinh(2\varphi) + 2\varphi\Big)}\left(\frac{k_x}{k} + \frac{h_x}{h}\right) = 0 \ . \tag{1.30}$$

In order to find a relation between h_x/h and k_x/k we rewrite the phase velocity expression (1.24):

$$\frac{\omega^2 h}{g} = \varphi\tanh(\varphi) \ , \tag{1.31}$$

and we derive it with respect to x:

$$\frac{\omega^2}{g}h_x = \Big(\tanh(\varphi) + \varphi\big(1-\tanh^2(\varphi)\big)\Big)\left(\frac{k_x}{k} + \frac{h_x}{h}\right) .$$

Using again (1.31) to substitute ω^2 and rearranging the terms, we obtain the relation between the derivative of h and k:

$$\frac{k_x}{k} = \left(\frac{-2\varphi}{2\varphi + \sinh(2\varphi)}\right)\frac{h_x}{h} . \tag{1.32}$$

Finally we use (1.32) and (1.30) into (1.29), deducing the expression of the shoaling gradient for the linearized wave theory:

$$s_{Airy} = 2\varphi\,\frac{\sinh(2\varphi) + \varphi\big(1-\cosh(2\varphi)\big)}{\big(2\varphi + \sinh(2\varphi)\big)^2} . \tag{1.33}$$

To be able to actually compare the results of the analysis to the results obtained by numerically solving the models, there is a small catch, not often underlined in literature. To explain this, first consider that, for a given variation (usually linear) of the bathymetry, the local wavenumber $k(x)$ can also be obtained by solving an ODE, as (1.32), of the type:

$$\frac{k_x}{k} = -\gamma\frac{h_x}{h} , \tag{1.34}$$

where $h(x)$ is defined by the test set up, and where the expression for γ are dependent on the wave model used (Madsen et Sørensen [1992]; Beji et Nadaoka [1996]; Lee *et al.* [2003] etc). The values of the shoaling parameter, can be thus represented in two ways (*cf.* Filippini *et al.* [2015]). The one which is most classically reported is $s_0 = s(h(x), k_0)$, representing its variation with respect to $k_0 h(x)$, where k_0 is the initial wave number of the incoming wave. This leads to the result reported on the left on figure 1.3. However, the variation shown in the picture is not the actual one obtained in practice. To obtain this variation, one must integrate (1.34) to obtain $k(x)$, and use it to modify $s(h(x), k(x))$ when integrating (1.26) to compute the actual wave amplitudes. The shoaling coefficient can then still be plotted against $k_0 h$, by computing for a given x the corresponding values of $k_0 h(x)$, and the local value of $s(h(x), k(x)) = -a_x(x)h(x)/(a(x)h_x(x))$. This results in the right picture on figure 1.3, similar to the one reported (without any explanation) in Madsen et Sørensen [1992]. Remark that only when including the variation of the wavenumber in the integration of 1.26 the correct amplitudes are obtained.

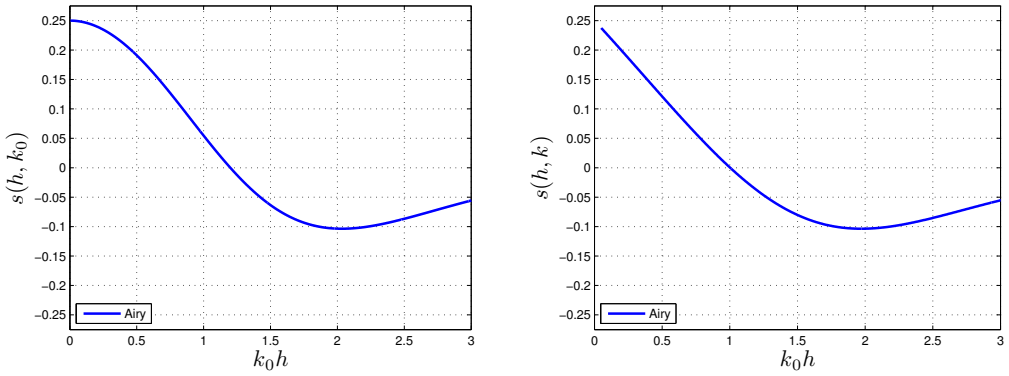

Figure 1.3: Linear shoaling: representation of the linear shoaling coefficient s of the linear wave theory of Airy (1.33). On the left is sketched $s(h(x), k_0)$, thus computing the values of s using the initial wavenumber of the signal k_0. On the right, instead, the variation of $k(x)$ along the domain is considered in the computation of the shoaling coefficient, thus: $s(h(x), k(x))$.

1.4 On modeling dispersion

Before proceeding to the derivation of the asymptotic models for wave propagation, we want to spend some words on what is the mathematical instrument that allows to model the dispersion in a given partial differential equation. This will provide us a better comprehension of the complex structure which characterizes most of the models that we are going to discuss in the following sections.
We consider the simplest PDE represented by a mono-dimensional linear scalar advection equation for the generic variable u:

$$u_t + a u_x = 0 \ , \tag{1.35}$$

where a is the constant velocity of propagation of the information.
Applying the Fourier analysis to (1.35), the following relation for the phase velocity is obtained:

$$jw - jak = 0 \ ,$$

which, using the definition (1.17), leads to:

$$C^2 = a^2 \ .$$

Contrary to what has been pointed out for the Airy equations, the expression for the phase velocity C does not depend on the wavenumber k in this case, meaning that all the information will travel according to the same velocity value, given by a. This can be easily verified since the solution of (1.35)

can be determined analytically through the method of characteristics in all the space-time domain, for a given couple of initial and boundary conditions. It can be thus confirmed that any signal will be transported unchanged to the right or to the left, according with the sign of a, and no frequency dispersion will appear in the simulation.
In the context of the Fourier analysis, used to perform this study, the only way to include wave dispersion in the equations is thus of adding terms containing higher order derivatives (in odd number) of the scalar quantity u. Consider the following PDE:

$$u_t + a u_x - \alpha u_{xxt} = 0 \ , \tag{1.36}$$

with α any real number. The Fourier analysis gives, in this case, the following result:

$$jw - jak - j\alpha w k^2 = 0 \ ,$$

from which it follows:

$$C^2 = \left(\frac{a}{1 - \alpha k^2} \right)^2 .$$

The general idea just presented, finds extensive application in the systems of equations that will be introduced in the following sections. These dispersive models for water wave propagation are, in fact, generally characterized by the occurrence of third order derivatives ($(\cdot)_{xxx}$ and $(\cdot)_{xxt}$) of the variables of the problem. Some models, called *enhanced*, are also characterized by the presence of some tuning parameters. These are real numbers, like α in (1.36), whose value is generally adjusted in order to match as much as possible the linear dispersive properties described by the Airy theory.
Note that equation (1.36) can be rewritten as a system of PDEs, composed by a hyperbolic and a stationary elliptic equation, by introducing a new scalar variable w:

$$w_t + a u_x = 0 \ ,$$

$$u - \alpha u_{xx} = w \ .$$

Reformulating the problem in this way allows to identify a PDE structure involving a first order problem plus an auxiliary elliptic equation. This structure is basically the same of the nonlinear wave system (1.9)-(1.12). This decomposition may be used to apply the more appropriate numerical method to each of the two part which compose the system. This idea is the base of the discretization procedure proposed in this work, and described in chapters 2 and 4, discussing the application of this approach to the Green-Naghdi system of equations (*cf.* Filippini *et al.* [2016, 2017]).

1.5 Asymptotic development

Solving the incompressible and irrotational Euler system for large scale numerical simulations is very computational demanding. The Boussinesq-type models have been developed in the past in order to bypass this obstacle in practical applications. These are depth averaged asymptotic approximation of the original system. Their derivation, in fact, consists of two main steps. Firstly, the velocity u is expressed by an asymptotic development in terms of the depth averaged velocity $\bar{u}$ or in terms of the velocity value u_θ, measured at an arbitrary depth z_θ. Secondly, some hypothesis, involving the order of magnitude of the dimensionless parameters of the problem, are imposed to neglect some terms in the asymptotic development. The physical characteristics scales for propagating waves are the wavelength λ, the wave amplitude a and the still water depth h_0 (considering negligible the variation of the bed). The wave period T is not considered, since it can be obtain from λ and h_0, through the dispersion relation. The wave propagation is, thus, characterized by two dimensionless parameters:

$$\varepsilon = \frac{a}{h_0} \quad \text{and} \quad \mu = \frac{h_0}{\lambda} = \frac{\varphi_0}{2\pi} \ ,$$

where ε characterizes the degree of nonlinearity of the flow and μ characterizes the degree of dispersion of the waves. Some other nondimensional parameters can be obtained through different combinations of ε and μ, and may be used to recover other dimensionless forms of the Euler equations.

Before performing the dimensional analysis of the Euler system, we rewrite the model in order to eliminate the pressure from the unknowns. To this scope we use the irrotational condition (1.5) to rewrite the (1.1) and (1.2) as:

$$\begin{aligned} u_t + uu_x + ww_x + \frac{p_x}{\rho} &= 0 \ , \\ w_t + uu_z + ww_z + \frac{p_z}{\rho} + g &= 0 \ . \end{aligned}$$

We now reintroduce the velocity potential, Φ, such that $u = \Phi_x$ and $w = \Phi_z$. It is thus possible to obtain an expression for the pressure by integrating the second equation from the free surface $h_0 + \eta$ to an arbitrary level z. Such expression can be thus substituted into the first equation and, after some simplifications, the following relation will be obtained:

$$[\Phi_t(h_0+\eta)]_x + g\eta_x + \left[\frac{u^2(h_0+\eta)}{2}\right]_x + \left[\frac{w^2(h_0+\eta)}{2}\right]_x = 0 \ .$$

Using the cinematic boundary condition, we develop the derivative of $\Phi_t(h_0+\eta)$ with respect to x in order to rewrite the equation in terms of the only unknowns η, u and w:

$$[\Phi(h_0+\eta)]_x = \Phi_x(h_0+\eta) + \eta_x\Phi_z(h_0+\eta) \ .$$

In this way, the original Euler system of equations can be rewritten as:

$$\begin{aligned} u_t(h_0+\eta) + \eta_x w_t(h_0+\eta) + g\eta_x + \\ + \left[\frac{u^2(h_0+\eta)}{2}\right]_x + \left[\frac{w^2(h_0+\eta)}{2}\right]_x = 0 \ , \\ u_x + w_z = 0 \ , \\ u_z - w_x = 0 \ , \end{aligned} \tag{1.37}$$

with boundary conditions:

$$w = \eta_t + u\eta_x \qquad \text{at } z = h_0+\eta \ , \tag{1.38}$$

$$w = ub_x \qquad \text{at } z = b \ . \tag{1.39}$$

System (1.37) is now ready to be made dimensionless. At this scope, we introduce the following set of dimensionless quantities:

$$x' = \frac{x}{\lambda} \ , \ z' = \frac{z}{h_0} \ , \ t' = \frac{\sqrt{gh_0}}{\lambda}t \ , \ \eta' = \frac{\eta}{a} \ , \ b' = \frac{b}{h_0} \ , \tag{1.40}$$

$$u' = \frac{h_0}{a\sqrt{gh_0}}u \ , \ w' = \frac{\lambda}{a}\frac{1}{\sqrt{gh_0}}w \ , \ p' = \frac{p}{gh_0\rho} \ . \tag{1.41}$$

Substituting these expressions into (1.37), the dimensionless parameters ε and μ appear in the equations (we drop the primes for the sake of clarity):

$$\begin{aligned} u_t(1+\varepsilon\eta) + \varepsilon\mu^2\ \eta_x w_t(1+\varepsilon\eta) + \eta_x + \\ +\varepsilon\left[\frac{u^2(1+\varepsilon\eta)}{2}\right]_x + \varepsilon\mu^2\left[\frac{w^2(1+\varepsilon\eta)}{2}\right]_x = 0 \ , \end{aligned} \tag{1.42}$$

$$u_x + w_z = 0 \ , \tag{1.43}$$

$$u_z - \mu^2 w_x = 0 \ , \tag{1.44}$$

with the boundary conditions:

$$w = \eta_t + \varepsilon u\eta_x \qquad \text{at } z = 1+\varepsilon\eta \ , \tag{1.45}$$

$$w = ub_x \qquad \text{at } z = b \ . \tag{1.46}$$

We want now to express the horizontal velocity u by means of an asymptotic development in terms of the depth averaged horizontal velocity $\bar{u}$, defined by:

$$\bar{u} = \frac{1}{(1+\varepsilon\eta-b)}\int_b^{1+\varepsilon\eta} u\,dz \ .$$

To this scope, we consider in this part that $\mathscr{O}(\mu^2) \ll 1$, while $\mathscr{O}(\varepsilon) \sim 1$. Integrating the equation (1.44) from $z = 1$ to a general water depth $\tilde{z}$, and neglecting the terms of order $\mathscr{O}(\mu^2)$, we obtain:

$$\tilde{u} = u_0 + \mathscr{O}(\mu^2) \ ,$$

where $\tilde{u}$ and u_0 are the dimensionless horizontal velocities respectively at the arbitrary depth $\tilde{z}$ and at the reference depth $z = 1$. This expression can be used in equation (1.43), which can than be integrated between $z = b$ and $\tilde{z}$, using the boundary condition (1.46), in order to obtain:

$$\tilde{w} = -\Big((\tilde{z}-1)(u_0)_x + (h_b u_0)_x\Big) + \mathscr{O}(\mu^2) \ . \tag{1.47}$$

This can be substituted in (1.44) that, integrated again from $z = 1$ to $\tilde{z}$, provides the asymptotic development of u in terms of u_0, up to the fourth order $\mathscr{O}(\mu^4)$:

$$\tilde{u} = u_0 - \mu^2\left(\frac{(\tilde{z}-1)^2}{2}(u_0)_{xx} + (\tilde{z}-1)(h_b u_0)_{xx}\right) + \mathscr{O}(\mu^4) \ . \tag{1.48}$$

It now remains to express u_0 as function of the depth averaged horizontal velocity $\bar{u}$. We, thus, integrate equation (1.48) from $z = b$ to $z = 1+\varepsilon\eta$. Dividing the result by the water depth $h = 1+\varepsilon\eta-b$ and after some manipulations, the following expression can be obtained:

$$\bar{u} = u_0 - \mu^2\left[\frac{\varepsilon^2\eta^2 - \varepsilon\eta h_b + h_b^2}{6}(u_0)_{xx} + \frac{\varepsilon\eta - h_b}{2}(h_b u_0)_{xx}\right] + \mathscr{O}(\mu^4) \ . \tag{1.49}$$

From (1.49), introducing $h = \varepsilon\eta + h_b$ and isolating u_0, it directly comes:

$$u_0 = \bar{u} + \mu^2\left[\left(\frac{h^2}{6} - \frac{h_b}{2}\Big(h-h_b\Big)\right)(u_0)_{xx} + \left(\frac{h}{2} - h_b\right)(h_b u_0)_{xx}\right] + \mathscr{O}(\mu^4) \ . \tag{1.50}$$

Neglecting the terms of order $\mathscr{O}(\mu^2)$, the previous relation simplifies to:

$$u_0 = \bar{u} + \mathscr{O}(\mu^2) \ ,$$

that can be used inside equation (1.50), to express u_0 as function of $\bar{u}$:

$$u_0 = \bar{u} + \mu^2 \left[\left(\frac{h^2}{6} - \frac{h_b}{2}\big(h - h_b\big) \right) \bar{u}_{xx} + \left(\frac{h}{2} - h_b \right) (h_b \bar{u})_{xx} \right] + \mathscr{O}(\mu^4) \ . \quad (1.51)$$

We can finally replace (1.51) into (1.48):

$$\begin{aligned} \tilde{u} = \bar{u} - \mu^2 \Bigg[& \left(\frac{(\tilde{z}-1)^2}{2} - \frac{h^2}{6} + \frac{h_b}{2}\big(h - h_b\big) \right) \bar{u}_{xx} + \\ & + \left((\tilde{z}-1) - \left(\frac{h}{2} - h_b \right) \right) (h_b \bar{u})_{xx} \Bigg] + \mathscr{O}(\mu^4) \ . \end{aligned} \quad (1.52)$$

Using equation (1.52), we can express the horizontal velocity at an arbitrary level $\tilde{u}$ as an asymptotic development of the depth averaged horizontal velocity $\bar{u}$, truncated at the fourth order $\mathscr{O}(\mu^4)$. This represents the starting point for the derivation of all the asymptotic models treated in this work.
Similarly, we can deduce an asymptotic development for the vertical velocity, by substituting equation (1.51) in (1.47):

$$\tilde{w} = -\Big((\tilde{z}-1)\bar{u}_x + (h_b \bar{u})_x \Big) + \mathscr{O}(\mu^2) \ . \quad (1.53)$$

Before showing how different models can be derived, we remark that an exact equation can be obtained by integrating the incompressibility equation on the depth:

$$\int_b^{h_b+\eta} u_x dz + \int_b^{h_b+\eta} w_z dz = 0 \ .$$

Applying the Leibnitz rule [1] and using the boundary conditions (1.38) and (1.39) to simplify the expression, we get:

$$\eta_t + (h\bar{u})_x = 0 \ . \quad (1.54)$$

This is the so-called continuity equation, equivalent to an equation for volume conservation. Since it comes from the cinematic boundary condition of the Euler equations, it is an exact equation and characterizes all the models having η and $\bar{u}$ as unknowns.

[1] Given three functions $f(x,z)$, $a(x)$ and $b(x)$ such that f and f_x are continuous in x and z, and such that a and b belong to C^1, than:

$$\frac{\partial}{\partial x}\left(\int_{a(x)}^{b(x)} f(x,z)dz \right) = \int_{a(x)}^{b(x)} f_x(x,z)dz + f\big(x,b(x)\big)b'(x) - f\big(x,a(x)\big)a'(x)$$

1.6 The Nonlinear Shallow Water equations

The simplest depth averaged approximation of the Euler equations that can be derived from the asymptotic development (1.52) is the so-called NonLinear Shallow Water system (NLSW). This model is based on the assumptions that $\mathscr{O}(\varepsilon) \sim 1$, while $\mathscr{O}(\mu^2) \ll 1$ and therefore negligible. Because of this, the velocity development (1.52) reduces to the simple relation:

$$\tilde{u} = \bar{u} + \mathscr{O}(\mu^2) \ .$$

Evaluating this relation at the free surface $z = 1 + \varepsilon\eta$, it gives:

$$u(1 + \varepsilon\eta) = \bar{u} + \mathscr{O}(\mu^2) \ ,$$

which can be used in (1.42), obtaining:

$$\bar{u}_t + \varepsilon\bar{u}\bar{u}_x + \eta_x = \mathscr{O}(\mu^2) \ . \tag{1.55}$$

Neglecting the terms of order $\mathscr{O}(\mu^2)$ and coming back to the physical variables, we obtain the one-dimensional NLSW system by coupling equation (1.55) with the continuity equation (1.54):

$$\begin{aligned} \eta_t + (h\bar{u})_x &= 0 \ , \\ \bar{u}_t + \bar{u}\bar{u}_x + g\eta_x &= 0 \ . \end{aligned} \tag{1.56}$$

Considering the two horizontal Cartesian directions (x,y), the system (1.56), written in two-dimensional form, reads:

$$\begin{aligned} \eta_t + \nabla \cdot (h\bar{\mathbf{u}}) &= 0 \ , \\ \bar{\mathbf{u}}_t + (\bar{\mathbf{u}} \cdot \nabla)\bar{\mathbf{u}} + g\nabla\eta &= 0 \ , \end{aligned} \tag{1.57}$$

where the vector $\bar{\mathbf{u}}$ contains the depth averaged velocity components $\bar{u}$ and $\bar{v}$ respectively in the x and y directions, and ∇ represents the gradient operator. The NLSW model (1.56) is a system of nonlinear hyperbolic Partial Differential Equations (PDEs). This particular nature is the key of its great success and large diffusion. It can be numerically solved using many different techniques. To this end, the model should be rewritten in a conservative form, which is more suitable for numerics. To this purpose, a new variable: the volume flux $\bar{q} = h\bar{u}$, has to be introduced. A conservation law can be obtained for this variable by multiplying the first equation of system (1.56) by $\bar{u}$ and adding to it the second equation of (1.56), multiplied by h. Since: $\eta_t(x,t) = \big(\eta(x,t) + h_b(x)\big)_t = h_t(x,t)$, this final one-dimensional conservative formulation is obtained:

$$\begin{aligned} h_t + \bar{q}_x &= 0 \ , \\ \bar{q}_t + \left(\frac{\bar{q}^2}{h}\right)_x + g\left(\frac{h^2}{2}\right)_x + gh(h_b)_x &= 0 \ , \end{aligned} \tag{1.58}$$

which, in two-dimensions, becomes:

$$\begin{aligned} h_t + \nabla \cdot \bar{\mathbf{q}} &= 0 \ , \\ \bar{\mathbf{q}}_t + \nabla \cdot \left(\frac{\bar{\mathbf{q}} \otimes \bar{\mathbf{q}}}{h}\right) + \nabla\left(\frac{gh^2}{2}\right) + gh\nabla h_b &= 0 \ , \end{aligned} \tag{1.59}$$

being $\bar{\mathbf{q}} = h\bar{\mathbf{u}}$ and $\otimes$ denoting the tensor product between two vectors:

$$\mathbf{a} \otimes \mathbf{b} = \begin{bmatrix} a_1 b_1 & a_1 b_2 \\ a_2 b_1 & a_2 b_2 \end{bmatrix} \ ,$$

with $\mathbf{a} = [a_1,\, a_2]^T$ and $\mathbf{b} = [b_1,\, b_2]^T$.

Linear Dispersion Properties : The NLSW system does not contain any dispersive term. According to the fundamentals of wave dispersion modeling, presented in section 1.4, we expect this model to be characterized by a phase velocity which will be completely independent from the wave number k. We thus linearize system (1.56) around the steady state characterized by $h(x) = h_0 = \text{const}$ and $u = 0$:

$$\begin{aligned} \eta_t + h_0 \bar{u}_x &= 0 \ , \\ \bar{u}_t + g\eta_x &= 0 \ . \end{aligned} \tag{1.60}$$

Then, we perform the Fourier analysis on system (1.56), looking for a solution in the form $\eta(x,t) = \eta_0 \exp^{\nu t - jkx}$, $\bar{u}(x,t) = \bar{u}_0 \exp^{\nu t - jkx}$, where $\nu = \xi + j\omega$ (being ξ the dissipation rate and ω the phase shift), ending up on the following system:

$$\begin{aligned} \nu\eta_0 + jkh_0\bar{u}_0 &= 0 \ , \\ \nu\bar{u}_0 + jkg\eta_0 &= 0 \ . \end{aligned}$$

Solving for ν, we get the complex eigenvalue problem:

$$\begin{pmatrix} \nu & jkh_0 \\ jkg & \nu \end{pmatrix} \begin{pmatrix} \eta_0 \\ \bar{u}_0 \end{pmatrix} = 0$$

which simply gives:

$$\begin{aligned} \xi &= 0 \ , \\ \omega^2 &= k^2 g h_0 \ . \end{aligned}$$

Using the definition (1.17), the phase velocity described by the NLSW model appears to be:

$$C_{SW}^2 = gh_0 \ , \tag{1.61}$$

Figure 1.4 shows, in function of the reduced frequency of the wave kh_0, the trend of the error in phase velocity with respect to the Airy theory one, determined by the relation:

$$\text{err} = 100\left(\frac{C - C_{Airy}}{C_{Airy}}\right) \ , \tag{1.62}$$

The figure puts in evidence the lack of accuracy given by the NLSW model in terms of linear dispersion. This will propagate any frequency with the same speed, defined by C_{SW}, hence, its error with respect to the linear wave theory rapidly diverges and becomes greater than 5% already after $kh_0 \simeq 0.6$.

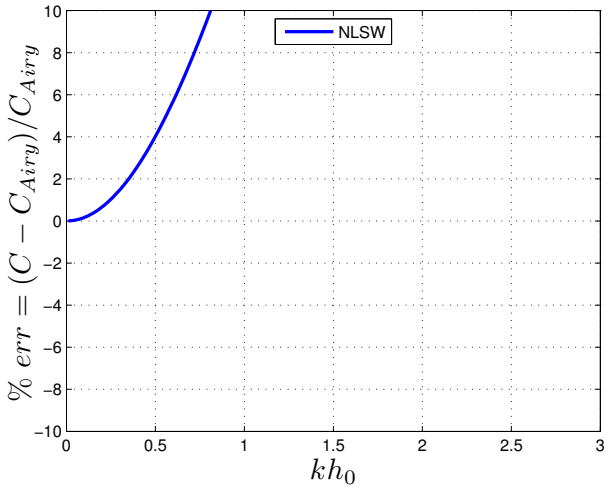

Figure 1.4: Percentage error in phase velocity description with respect to the Airy theory (eq. (1.24)) for the NLSW model (eq. (1.61)).

Linear Shoaling Properties : The expression of the shoaling gradient s for the NLSW model will be obtained using the procedure described in Madsen et Sørensen [1992]. The system of equation is linearized on a mild slope bathymetry, $h(x) = h_b(x)$:

$$\begin{aligned} \eta_t + (h\bar{u})_x &= 0 \ , \\ (h\bar{u})_t + gh\eta_x &= 0 \ . \end{aligned} \tag{1.63}$$

A wave equation, corresponding to system (1.63), is then found by deriving the first equation with respect to time t, deriving the second equation with re-

spect to the horizontal coordinate x and summing up the resulting expression. In this case the result gives:

$$\eta_{tt} - g(h\eta_x)_x = 0 \ . \tag{1.64}$$

A solutions of the form $\eta(x) = a(x)\exp^{j(\omega t - \psi(x))}$, with $\psi_x = k(x)$, is substituted in (1.64), considering the wave amplitude $a(x)$, the water depth $h(x)$ and the wave number $k(x)$ as slowly varying functions of x (so to neglect higher order derivatives and product of derivatives of such quantities). Collecting the terms containing first order derivatives of a, k and c, one ends with:

$$\alpha_1 \frac{a_x}{a} + \alpha_2 \frac{k_x}{k} + \alpha_3 \frac{h_x}{h} = 0 \ .$$

The relation between k_x and h_x emerges from algebraic manipulations on the lowest order terms of (1.64), as detailed in Madsen et Sørensen [1992]. This allows to define the coefficient γ of (1.34) and, in turn, to obtain the final expression of the shoaling gradient coefficient as (see Madsen et Sørensen [1992] for details):

$$s = \frac{\alpha_3 - \alpha_2 \gamma}{\alpha_1} \ . \tag{1.65}$$

For the model considered, we found simply:

$$\alpha_1 = 2 \ , \quad \alpha_2 = 1 \ , \quad \alpha_3 = 1 \ , \quad \gamma = \frac{1}{2} \ ,$$

and, consequently, that the shoaling gradient expression of the NLSW model $s_{SW}(h, k)$ is the constant number:

$$s_{SW} = \frac{1}{4} \ . \tag{1.66}$$

The comparison with respect to the result of Airy theory (1.33), illustrated in figure 1.5 (left for $s(h(x), k_0)$ and right for $s(h(x), k(x))$), shows once more the limitations of this basic model.

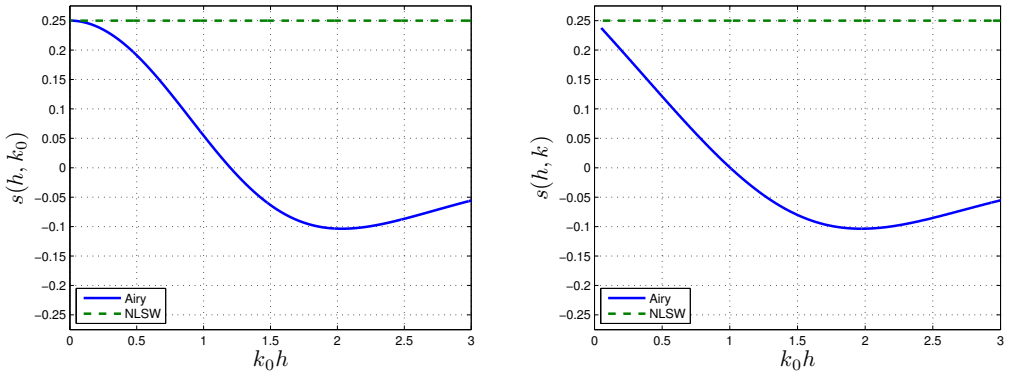

Figure 1.5: Linear shoaling: comparison between the linear shoaling coefficient of the NLSW model s_{SW} (eq. (1.66)) and the one described by the linear wave theory of Airy (eq. (1.33)). On the left is sketched $s(h(x), k_0)$, thus computing the values of s using the initial wavenumber of the signal k_0. On the right, instead, the variation of $k(x)$ along the domain is considered in the computation of the shoaling coefficient, thus: $s(h(x), k(x))$.

Summary : In this section, we have shown how the NLSW model can be recovered by neglecting all the terms of order $\mathscr{O}(\mu^2)$ in the asymptotic development of the horizontal velocity $\tilde{u}$ (1.52). In this sense, the NLSW model represents the least accurate approximation of the Euler system of equations (1.37), or an approximation of order $\mathscr{O}(\varepsilon)$. Despite its poor linear dispersion and shoaling characteristics, it performs accurate description of wave propagating in very shallow waters. Other models should, instead, be used for the region of intermediate waters, when the interaction with the bathymetry becomes more important and the dispersion and shoaling effects are predominant. As mentioned in the introduction, more accurate models have been developed in the last years to tackle this problem. In the following paragraphs we will present some of them, in order of growing degree of accuracy and complexity.

1.7 Weakly nonlinear Boussinesq-type models : amplitude-velocity vs amplitude-flux forms

In this section, we review a certain number of weakly nonlinear Boussinesq-type (BT) models, showing the main passages for their derivation, which is based on the assumptions that:

$$\varepsilon \ll 1 \ , \ \mu^2 \ll 1 \quad \text{and} \quad \varepsilon = \mathscr{O}(\mu^2) \ .$$

This fact implies the Ursell number Ur of the problem to be:

$$Ur = a\lambda^2/h_b^3 = \varepsilon/\mu^2 \sim \mathscr{O}(1) \ .$$

Moreover, the small magnitude of ε gives a weakly nonlinear nature to these models. Because of these assumptions, the BT models are obtained by retaining all the $\mathscr{O}(\varepsilon)$ and $\mathscr{O}(\mu^2)$ terms of the Euler equations, neglecting the $\mathscr{O}(\varepsilon\mu^2)$ and $\mathscr{O}(\mu^4)$ ones. For this reasons, their structure is generally composed by an hyperbolic part, formed by the NLSW system in its conservative (1.58) or non-conservative (1.56) form, plus some elliptic operators containing the higher order dispersive terms. These are the terms of order $\mathscr{O}(\mu^2)$, that have been neglected for the NLSW derivation.
In this section we will show that, within the same asymptotic accuracy, it is possible to construct two nonlinear set of PDEs, characterized by dispersive terms that involve: the free surface elevation and the velocity in one case, the free surface elevation and the volume flux in other. We will thus speak respectively in terms of *amplitude-velocity* and *amplitude-flux* forms. What follows is largely inspired by the published work of Filippini *et al.* [2015], where this theory was applied to four linear relations corresponding to the model of Peregrine Peregrine [1967] and to the enhanced models of Beji and Nadaoka Beji et Nadaoka [1996], Madsen and Sørensen Madsen et Sørensen [1992], and Nwogu Nwogu [1994]. Here, for brevity, the only Peregrine and Madsen-Sørensen models will be discussed. The interested reader can consult Filippini *et al.* [2015] for more details.

1.7.1 The models of Peregrine and Abbott

In order to obtain the model of Peregrine, the terms of order $\mathscr{O}(\varepsilon\mu^2)$ in the asymptotic development (1.52) have to be neglected. The expression resulting from this operation will read:

$$\tilde{u} = \bar{u} - \mu^2\left[\left(\frac{(\tilde{z}-1)^2}{2} - \frac{h_b^2}{6}\right)\bar{u}_{xx} + \left((\tilde{z}-1) - \frac{h_b}{2}\right)(h_b\bar{u})_{xx}\right] + \mathscr{O}(\varepsilon\mu^2, \mu^4) \ . \quad (1.67)$$

Following the same procedure adopted to recover the NLSW system, we evaluate (1.67) at the free surface $z = 1 + \varepsilon\eta$:

$$\tilde{u} = \bar{u} + \mu^2\left(\frac{h_b^2}{6}\bar{u}_{xx} - \frac{h_b}{2}\big(h_b\bar{u}\big)_{xx}\right) + \mathscr{O}(\varepsilon\mu^2, \mu^4) \ .$$

and we use it in (1.42). Once again terms of order $\varepsilon\mu$ have to be neglected, obtaining:

$$\bar{u}_t + \varepsilon\bar{u}\bar{u}_x + \eta_x + \mu^2\left(\frac{h_b^2}{6}\bar{u}_{xxt} - \frac{h_b}{2}\big(h_b\bar{u}\big)_{xxt}\right) = \mathscr{O}(\varepsilon\mu^2, \mu^4) \ . \quad (1.68)$$

Coming back to dimensional variables, the one dimensional Boussinesq model of Peregrine is obtained, reading:

$$\begin{aligned} \eta_t + (h\bar{u})_x &= 0 \ , \\ \bar{u}_t + \bar{u}\bar{u}_x + g\eta_x + \frac{h_b^2}{6}\bar{u}_{xxt} - \frac{h_b}{2}(h\bar{u})_{xxt} &= 0 \ , \end{aligned} \tag{1.69}$$

and in two dimensions:

$$\begin{aligned} \eta_t + \nabla \cdot (h\bar{\mathbf{u}}) &= 0 \ , \\ \bar{\mathbf{u}}_t + (\bar{\mathbf{u}} \cdot \nabla)\bar{\mathbf{u}} + g\nabla\eta + \frac{h_b^2}{6}\nabla\Big(\nabla \cdot \bar{u}_t\Big) - \frac{h_b}{2}\nabla\Big(\nabla \cdot (h\bar{u})_t\Big) &= 0 \ . \end{aligned} \tag{1.70}$$

Multiplying the first equation of (1.69) by $\bar{u}$, the second one by h and summing up the resulting expressions, we can rewrite the Peregrine system in terms of the conservative variables $(h, \bar{q})$, to which we will refer all along this work in terms of the P system:

$$\begin{aligned} h_t + \bar{q}_x &= 0 \ , \\ \bar{q}_t + \left(\frac{\bar{q}^2}{h}\right)_x + gh\eta_x + hP_t(\bar{u}) &= 0 \ . \end{aligned} \tag{1.71}$$

where $P(\cdot)$ is the elliptic operator defined by:

$$P(\cdot) = \frac{h_b^2}{6}(\cdot)_{xx} - \frac{h_b}{2}\big(h(\cdot)\big)_{xx} \ . \tag{1.72}$$

In two-dimensions, system (1.71) becomes:

$$\begin{aligned} h_t + \nabla \cdot (h\bar{\mathbf{u}}) &= 0 \ , \\ \bar{\mathbf{q}}_t + \nabla \cdot \left(\frac{\bar{\mathbf{q}} \otimes \bar{\mathbf{q}}}{h}\right) + gh\nabla\eta + hP_t(\bar{\mathbf{u}}) &= 0 \ , \end{aligned} \tag{1.73}$$

with $P(\cdot)$ now:

$$P(\cdot) = \frac{h_b^2}{6}\nabla\Big(\nabla \cdot (\cdot)\Big) - \frac{h_b}{2}\nabla\Big(\nabla \cdot \big(h_b(\cdot)\big)\Big) \ . \tag{1.74}$$

System (1.71) allows to underline the structure of the Peregrine model, which is obtained by adding to the NLSW equations some $\mathscr{O}(\mu^2)$ dispersive terms expressed by the time derivative of an elliptic linear differential operator applied to the depth-averaged velocity $\bar{u}$.

Focusing on the dimensionless form of the dispersive terms of system (1.71), we can observe that:

$$\left(\varepsilon\eta + h_b\right)\ \mu^2\left(\frac{h_b^2}{6}\bar{u}_{xx} - \frac{h_b}{2}(h_b\bar{u})_{xx}\right) = \mu^2\left(\frac{h_b^3}{6}\left(\frac{\bar{q}}{h_b}\right)_{xx} - \frac{h_b^2}{2}\bar{q}_{xx}\right) + \mathscr{O}(\varepsilon\mu^2, \mu^4)\ . \tag{1.75}$$

As a consequence, an asymptotically equivalent system can be obtained by replacing the dispersive terms of system (1.71) by the right hand side of equality (1.75). The resulting system of equations is known in the literature as the BT model of Abbott (A model), which firstly derived these equations in Abbott *et al.* [1978], and in dimensional variables it reads:

$$\begin{aligned} h_t + \bar{q}_x &= 0\ , \\ Q_t(\bar{q}) + \left(\frac{\bar{q}^2}{h}\right)_x + gh\eta_x &= 0\ , \end{aligned} \tag{1.76}$$

where, once more, there is the appearance of the time derivative of a linear elliptic operator, denoted by $Q(\cdot)$ and defined by :

$$Q(\cdot) = (\cdot) + h_b\left(\frac{h_b^2}{6}\left(\frac{(\cdot)}{h_b}\right)_{xx} - \frac{h_b}{2}(\cdot)_{xx}\right)\ . \tag{1.77}$$

For completeness we report the two-dimensional form of (1.76), which reads:

$$\begin{aligned} h_t + \nabla\cdot(h\bar{\mathbf{u}}) &= 0\ , \\ Q_t(\bar{\mathbf{q}}) + \nabla\cdot\left(\frac{\bar{\mathbf{q}}\otimes\bar{\mathbf{q}}}{h}\right) + gh\nabla\eta &= 0\ , \end{aligned} \tag{1.78}$$

with:

$$Q(\cdot) = (\cdot) + h_b\left(\frac{h_b^2}{6}\nabla\left(\nabla\cdot\left(\frac{(\cdot)}{h_b}\right)\right) - \frac{h_b}{2}\nabla\left(\nabla\cdot(\cdot)\right)\right)\ . \tag{1.79}$$

Linear Dispersion Properties: The two models, just derived, differ from the NLSW one by the presence of the third order derivative terms in the momentum equation, which are $\mathscr{O}(\mu^2)$. As we have shown in section 1.4, these are essential for modeling wave dispersion with a given set of PDEs. We will, now, compute the phase velocity of these models, which share the same linear form. Linearizing around the steady state $h(x) = h_0 = \text{const}$ the one-dimensional systems (1.71) and (1.76), we get:

$$\begin{aligned} \eta_t + h_0\bar{u}_x &= 0\ , \\ \bar{u}_t + g\eta_x - \frac{h_0^2}{3}\bar{u}_{xxt} &= 0\ . \end{aligned} \tag{1.80}$$

The Fourier analysis follows the same procedure shown for the NLSW system and provides the following expression for the phase velocity:

$$C_P^2 = \frac{gh_0}{1 + \frac{\varphi_0^2}{3}} \ . \tag{1.81}$$

The phase velocity just computed is an improvement of (1.61) and is now explicitly dependent from the wavenumber k. Figure 1.6 displays the percentage error with respect to the Airy theory, using the error definition (1.62). We can, thus, observe that the P and A models give a better description to wave dispersion with respect to the NLSW one, even if the error with respect to the linear wave theory rapidly grows moving towards values of kh_0 greater than 1 (err $> 5\%$ for $kh_0 > 1.9$), and hence deeper waters or equivalently shorter waves.

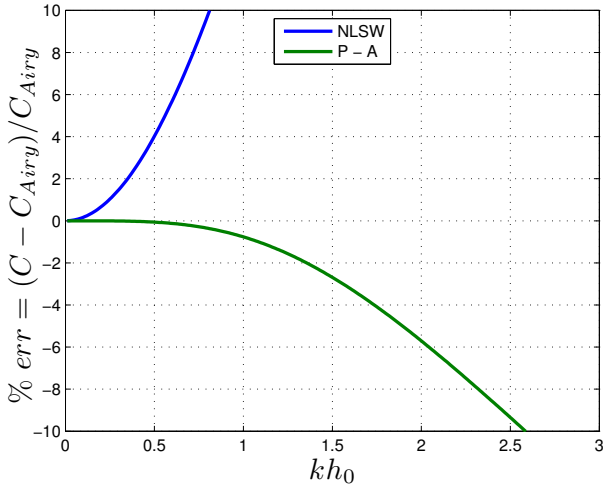

Figure 1.6: Percentage error in phase velocity description with respect to the Airy theory (eq. (1.24)) for the P and A models (eq. (1.81)).

Linear Shoaling Properties: We want now to verify the linear shoaling properties of the P and A models. The starting point consists of the linearized system:

$$\begin{aligned} \eta_t + (h\bar{u})_x &= 0 \ , \\ (h\bar{u})_t + gh\eta_x - \frac{h^2}{3}(h\bar{u})_{xxt} - \frac{hh_x}{3}(h\bar{u})_{xt} &= 0 \ . \end{aligned} \tag{1.82}$$

Note that here, following Madsen et Sørensen [1992], we have used the mild slope approximation, consisting in neglecting both higher derivatives of h_b and $(h_b)_x^2$ terms. Once again, the linear form (1.82) is shared by both the models. The procedure to obtain s is identical to that already described in the previous

section. We limit ourself in reporting the expressions of the coefficients α_1, α_2, α_3 and γ, reading:

$$\alpha_1 = 2 \ , \quad \alpha_2 = 1 \ , \quad \alpha_3 = 1 - \frac{2}{3}\varphi^2 \ , \quad \gamma = -\frac{1}{2}\left(\frac{\varphi^2}{3} - 1\right) \ ,$$

These can be used in (1.65), to obtain:

$$s_P = \frac{1}{4}(1 - \varphi^2) \ . \tag{1.83}$$

As it was for the phase velocity expression, also the linear shoaling gradient appears to be clearly improved with respect to the NLSW one. In Figure 1.7 we can appreciate such improvement. In particular we can see that the linear shoaling description is closer to the Airy one, especially for $k_0 h < 0.5$, however this rapidly diverges from the true behaviour in deeper water, rendering the P and A models invalid in these situations.

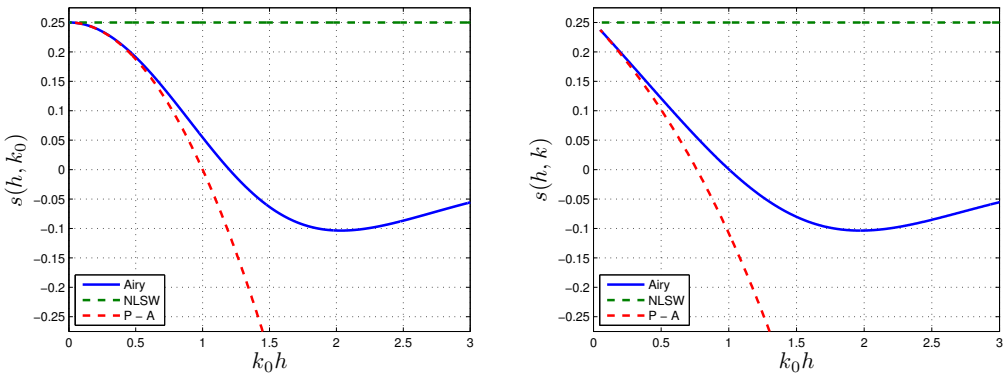

Figure 1.7: Linear shoaling: the linear shoaling coefficient of the NLSW model s_{SW} (eq. (1.66)) and of the P-A ones s_P (eq. (1.83)) are plotted against s_Airy (given by eq. (1.33)). On the left is sketched $s(h(x), k_0)$, thus computing the values of s using the initial wavenumber of the signal k_0. On the right, instead, the variation of $k(x)$ along the domain is considered in the computation of the shoaling coefficient, thus: $s(h(x), k(x))$.

Summary: The models of Peregrine and Abbott allow to improve the results performed by the NLSW model for higher values of μ. In the linearized case, the two models are identical and share the same linear dispersive and linear shoaling characteristics. In the nonlinear case the two systems are both $\mathscr{O}(\varepsilon\mu^2, \mu^4)$ approximations of the Euler equations, however they do differ as the dispersive terms are expressed in terms of the derivatives of $\bar{u}$ in the Peregrine one and in terms of $\bar{q}$ in (1.76). Compared to (1.71), system (1.76) has a more compact and seemingly conservative structure, as it does not involve any

additional non-conservative product w.r.t the NLSW equations. Note however, that the two systems are not just one the equivalent reformulation of the other in terms of a different set of variables. They actually contain different differential terms.
The limited accuracy of systems (1.71) and (1.76), *e.g.* in terms of linear dispersion relations, has pushed the development of the so-called enhanced BT models. These are improved approximations which, while still remaining of order $\mathscr{O}(\varepsilon\mu^2, \mu^4)$ with respect to the Euler equations, provide substantially enhanced approximations of the linearized dispersion relations and shoaling coefficients of the original three-dimensional equations. The dispersion relations of these models are valid up to the deep water limit (correspondent to $h/\lambda = 0.5$ in the literature), increasing their useful range for many practical application. In the following we will recall the derivation and properties of the enhanced BT model originally proposed in Madsen et Sørensen [1992].

1.7.2 The model of Madsen and Sørensen

From the huge family of enhanced Boussinesq-type models, we discuss here the one proposed by Madsen and Sørensen in Madsen et Sørensen [1992]. This model can be obtained from the Abbott equations. First we add and subtract the quantity $\mu^2\beta\bar{q}_{xxt}$, to the non-dimensional form of the momentum equation of system (1.76):

$$\bar{q}_t + \varepsilon\left(\frac{\bar{q}^2}{h}\right)_x + h\eta_x + \mu^2\left(\frac{h_b^3}{6}\left(\frac{\bar{q}}{h_b}\right)_{xxt} - \frac{h_b^2}{2}\bar{q}_{xxt} + \beta\bar{q}_{xxt} - \beta\bar{q}_{xxt}\right) = \mathscr{O}(\varepsilon\mu^2, \mu^4) \ . \tag{1.84}$$

Neglecting the terms of order $\mathscr{O}(\varepsilon)$ and $\mathscr{O}(\mu^2)$, and using the fact that $h = h_b + \mathscr{O}(\varepsilon)$, we deduce that:

$$\bar{q}_t = -h_b\eta_x + \mathscr{O}(\varepsilon, \mu^2) \ .$$

Such expression can be used in (1.84) in order to replace the term $+\beta\bar{q}_{xxt}$ by $-\beta\eta_{xxx}$. The system analyzed in Madsen et Sørensen [1992] is finally obtained by neglecting all terms of order $\mathscr{O}(\varepsilon\sigma^2, \sigma^4)$, and in the mild slope hypothesis by neglecting terms containing $(h_b)_x^2$ and $(h_b)_{xx}$. The resulting dimensional equations are known in the literature as the Madsen and Sørensen (MS) model, and they read:

$$\begin{aligned} h_t + \bar{q}_x &= 0 \ , \\ \hat{Q}_t(\bar{q}) + \left(\frac{\bar{q}^2}{h}\right)_x + gh\eta_x - g\beta h_b\hat{P}(\eta_x) &= 0 \ , \end{aligned} \tag{1.85}$$

where $\hat{P}(\cdot)$ and $\hat{Q}(\cdot)$ are defined by:

$$\hat{P}(\cdot) = h_b^2(\cdot)_{xx} + 2h_b(h_b)_x(\cdot)_x \ , \tag{1.86}$$

$$\hat{Q}(\cdot) = (\cdot) - \left(\frac{1}{3} + \beta\right) h_b^2(\cdot)_{xx} - \frac{h_b}{3}(h_b)_x(\cdot)_x \ . \tag{1.87}$$

We report also the two-dimensional form of the system, which is:

$$\begin{aligned} h_t + \nabla \cdot (h\bar{\mathbf{u}}) &= 0 \ , \\ \hat{Q}_t(\bar{\mathbf{q}}) + \nabla \cdot \left(\frac{\bar{\mathbf{q}} \otimes \bar{\mathbf{q}}}{h}\right) + gh\nabla\eta - g\beta h_b \hat{P}(\nabla\eta) &= 0 \ , \end{aligned} \tag{1.88}$$

where $\bar{\mathbf{q}} = (q^{(1)}\ q^{(2)})^T$, with:

$$\hat{P}(\cdot) = h_b^2 \nabla\Big(\nabla \cdot (\cdot)\Big) + h_b\Big(\mathcal{D}(\nabla\eta) + \nabla h_b\Big(\nabla \cdot (\cdot)\Big)\Big) \ , \tag{1.89}$$

$$\hat{Q}(\cdot) = (\cdot) - \left(\frac{1}{3} + \beta\right) h_b^2 \nabla\Big(\nabla \cdot (\cdot)\Big) - \frac{h_b}{6}\mathcal{D}(\cdot) - \frac{h_b \nabla h_b}{6}\Big(\nabla \cdot (\cdot)\Big) \tag{1.90}$$

$$\tag{1.91}$$

and the operator $\mathcal{D}$ defined by:

$$\mathcal{D} = \begin{pmatrix} (h_b)_x q_x^{(1)} + (h_b)_y q_x^{(2)} \\ (h_b)_x q_y^{(1)} + (h_b)_y q_y^{(2)} \end{pmatrix} \ . \tag{1.92}$$

We will show in the following paragraphs that the free parameter β allows to substantially improve the linear dispersion and shoaling properties with respect to (1.76), at the cost of a more complex and nonconservative structure, due to the term $g\beta d\hat{P}(\eta_x)$. By reason of the same hypothesis on the bathymetry, the MS model reduces exactly to the Abbott one when $\beta = 0$ just in case of constant bathymetries.

The model presented is in *amplitude-flux* form, as the dispersive terms involve derivatives of the depth averaged flux $\bar{q}$ and not of the velocity. An asymptotically equivalent system in wave *amplitude-velocity* form can be obtained by manipulating the P model in a very similar way and applying the mild slope hypothesis (details omitted for brevity). The final form of the model reached is:

$$\begin{aligned} h_t + \bar{q}_x &= 0 \ , \\ \bar{q}_t + \left(\frac{\bar{q}^2}{h}\right)_x + gh\eta_x - h\tilde{P}_t(\bar{u}) - g\beta h\hat{P}(\eta_x) &= 0 \ , \end{aligned} \tag{1.93}$$

where:

$$\tilde{P}(\cdot) = \left(\frac{1}{3} + \beta\right) h_b^2 (\cdot)_{xx} + (1 + 2\beta) h_b (h_b)_x (\cdot)_x \ . \tag{1.94}$$

In two-dimensions, this becomes:

$$\begin{aligned} h_t + \nabla \cdot (h\bar{\mathbf{u}}) &= 0 \ , \\ \bar{\mathbf{q}}_t + \nabla \cdot \left(\frac{\bar{\mathbf{q}} \otimes \bar{\mathbf{q}}}{h}\right) + gh\nabla\eta - h\tilde{P}_t(\bar{\mathbf{u}}) - g\beta h\hat{P}(\nabla\eta) &= 0 \ , \end{aligned} \tag{1.95}$$

with:

$$\tilde{P}(\cdot) = \left(\frac{1}{3} + \beta\right) h_b^2 \nabla\Big(\nabla \cdot (\cdot)\Big) + \left(\frac{1}{6} + \beta\right) h_b \mathcal{D}(\cdot) + \frac{h_b \nabla h_b}{6}\Big(\nabla \cdot (\cdot)\Big) \ . \tag{1.96}$$

System (1.93) reduces to the P model when $\beta = 0$ and the bathymetry is constant, however it has substantially improved linear characteristics with respect to (1.71). In the following we will refer to this model as to the *Madsen-Sørensen-Peregrine* (MSP) system.

Linear Dispersion Properties: Models (1.85) and (1.95) share the same linearized system which reads:

$$\begin{aligned} \eta_t + h_0 \bar{u}_x &= 0 \ , \\ \bar{u}_t + g\eta_x - \left(\frac{1}{3} + \beta\right) \bar{u}_{xxt} - g\beta h_0^2 \eta_{xxx} &= 0 \ . \end{aligned} \tag{1.97}$$

The Fourier analysis, performed on system (1.97), gives the following relation for the phase velocity C of the model:

$$C_{MS}^2 = gh_0 \frac{1 + \beta\varphi_0^2}{1 + \left(\frac{1}{3} + \beta\right)\varphi_0^2} \ , \tag{1.98}$$

where φ_0 has been defined in the previous sections.
Note that (1.98) improves the previous relation of the P model (1.98). This can still be recovered, since for the particular choice of $\beta = 0$ the two expressions collapse into one another. The constant β can assume any real value. This gives the opportunity to arbitrarily improve the linear dispersion properties of the MS and MSP models. In particular, for this couple of models, one can match the Padé approximation of the dispersion relations of the linear wave theory, using $\beta = 1/15$ (following Madsen et Sørensen [1992]). This particular value of β has been used to produce figure 1.8, where it can be observed that

the error in the linear phase representation, committed by using the MS or MSP models instead of the Euler one, is $< 2\%$ in almost all the range of kh_0 considered, pushing in the so called "deep water" region ($kh_0 > \pi$) the limit of applicability of these models.

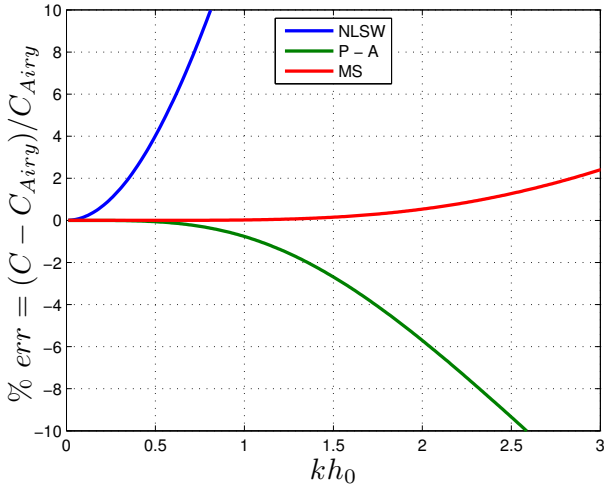

Figure 1.8: Percentage error in phase velocity description with respect to the Airy theory (eq. (1.24)) for the MS and MSP models. The plot has been performed using $\beta = 1/15$ in equation (1.98).

Linear Shoaling Properties: Once more, we complete the linear shoaling coefficient of the models under consideration by applying the procedure described in Madsen et Sørensen [1992]. The models are, thus, linearized assuming a slow varying bathymetry $h(x) = h_b(x)$ for which all higher order derivatives of h_b can be considered small and neglected. The two systems reduce to:

$$\begin{aligned} \eta_t + (h\bar{u})_x &= 0 \ , \\ (h\bar{u})_t + gh\eta_x - \left(\frac{1}{3} + \beta\right) h^2 (h\bar{u})_{xxt} - \frac{hh_x}{3}(h\bar{u})_{xt} + & \\ - g\beta h\big(h^2\eta_{xxx} + 2hh_x\eta_{xx}\big) &= 0 \ . \end{aligned} \tag{1.99}$$

The coefficients α_1, α_2, α_3 and γ, that can be obtained from the analysis of (1.99) and are:

$$
\begin{aligned}
\alpha_1 &= 2\left(1 + 2\beta\varphi^2 + \beta\left(\frac{1}{3} + \beta\right)\varphi^4\right) , \\
\alpha_2 &= 1 + 6\beta\varphi^2 + 5\beta\left(\frac{1}{3} + \beta\right)\varphi^4 , \\
\alpha_3 &= 1 + \left(4\beta - \frac{2}{3}\right)\varphi^2 + \beta\left(\frac{2}{3} + 3\beta\right)\varphi^4 , \\
\gamma &= \frac{1}{2}\left[\frac{1 + (2\beta - \frac{1}{3})\varphi^2 + \beta(\beta + \frac{1}{3})\varphi^4}{1 + 2\beta\varphi^2 + \beta(\frac{1}{3} + \beta)\varphi^4}\right] .
\end{aligned}
\tag{1.100}
$$

These can be used in (1.65) to obtain the expression of the shoaling coefficient $s_{MS}(h,k)$. Figures 1.9 left and right compare the shoaling gradient coefficient of all the models discussed so far to the reference s_{Airy}. The results puts in evidence the great improvement in the linear shoaling description obtaining with the enhanced BT models introduced.

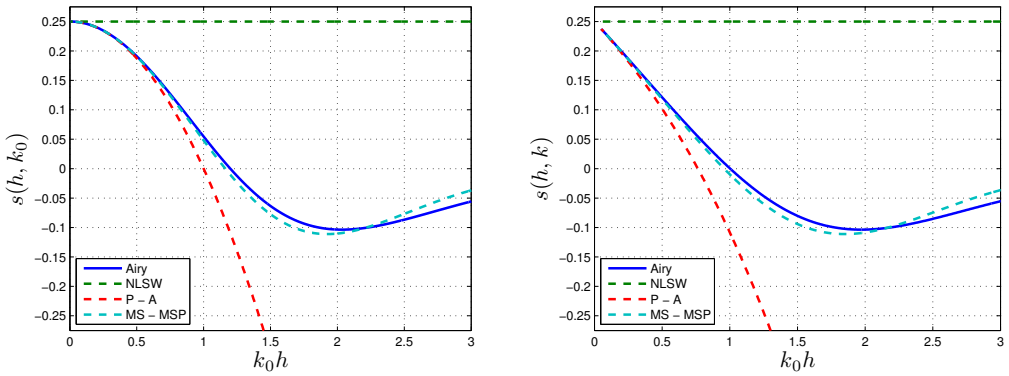

Figure 1.9: Linear shoaling: the linear shoaling coefficients (1.66), (1.83) and s_{MS} are plotted against s_{Airy} (given by eq. (1.33)). On the left is sketched $s(h(x),k_0)$, thus computing the values of s using the initial wavenumber of the signal k_0. On the right, instead, the variation of $k(x)$ along the domain is considered in the computation of the shoaling coefficient, thus: $s(h(x),k(x))$.

Summary: The models discussed in this section are among the most popular enhanced BT models of the literature. They share the linear shoaling coefficient and an improved linear dispersion relation, which matches the Padé approximation of (1.24), when $\beta = 1/15$. However they differ in the composition of their dispersive terms, written in terms of $(\eta,\bar{q})$ in (1.85) and in terms of $(\eta,\bar{u})$ in (1.93). Due to these characteristics, the MS and MSP systems give a more accurate representation of the phase velocity and shoaling in intermediate water, with k_0h up to 3, with respect to the models, discussed in

the previous section. These improved characteristics have been shown for the case of the MS and MSP models but they can be generalized, with different levels of accuracy every time, for all the enhanced BT models proposed in the literature, *e.g.* the ones of Nwogu Nwogu [1994], Beji and Nadaoka Beji et Nadaoka [1996], etc.
However, in practical applications, weakly nonlinear BT models are used, quite often, outside their range of applicability, approaching the nonlinear regime. As we will see shortly, in these conditions, their behaviour is practically independent on their linear dispersion relations and shoaling parameters. In particular, the analysis of the higher harmonics will show that the nonlinear form of the system has a dramatic effect on the amplitudes of the harmonics, which basically depends on whether the model is in *amplitude-velocity* of amplitude-flux form (Filippini *et al.* [2015]), as it will be discussed in the next section.

1.7.3 Nonlinear Dispersion: second order harmonics

In the previous sections we have already used the Fourier analysis on a horizontal bottom to investigate the linear dispersion properties of the models. In this section, our attention focuses on higher-order solutions (in particular the second-order one) that emerge from introducing in the dimensionless form of the models a solution of the form:

$$\eta' = a_1 \cos(\xi) + \varepsilon a_2 \cos(2\xi) \,, \qquad u' = u_1 \cos(\xi) + \varepsilon u_2 \cos(2\xi) \,, \quad (1.101)$$

with $\xi = \omega' t' - k' x'$ and being ω' the dimensionless angular frequency and k' the corresponding dimensionless wave number:

$$\omega' = \frac{\lambda}{\sqrt{g h_0}}\, \omega \,, \quad k' = \lambda k \,.$$

The procedure follow closely the work of Madsen et Schaffer [1998]. Here we show its application just to the Peregrine model, the analysis of the other models is similar with small variations discussed in a final remark.

The linear dispersion properties of the models emerge looking at the first-order solution: substituting (1.101) in system (1.71) and collecting all the terms of $\mathscr{O}(1)$. For the Peregrine equations, one obtains (dropping the primes for sake of clarity):

$$\begin{aligned} -\omega a_1 + k h_0 u_1 &= 0 \,, \\ -\omega u_1 + k a_1 + \mu^2 \omega \frac{k^2 h_0^2}{3} u_1 &= 0 \,, \end{aligned}$$

which can be easily solved, giving:

$$u_1 = \frac{\omega}{kh_0} a_1 \ ,$$
$$\frac{\omega^2}{k^2 h_0} = \frac{1}{1 + \dfrac{\mu^2 \varphi_0^2}{3}} \ , \tag{1.102}$$

where one can identify the expression for the dimensionless phase velocity of the P model obtained earlier.
However, more information on the theoretical behaviour of the models can be extracted looking at the higher harmonics. Collecting all the terms of order $\mathscr{O}(\varepsilon)$ one obtains:

$$-2\omega a_2 + 2kh_0 u_2 + k a_1 u_1 = 0 \ ,$$
$$-2\omega u_2 + 2k a_2 + \frac{k}{2} u_1^2 - \frac{8}{3}\mu^2 k^2 \omega u_2 = 0 \ .$$

Using the first equation of system (1.102), we can write:

$$\begin{pmatrix} m_{11} & m_{12} \\ m_{21} & m_{22} \end{pmatrix} \begin{pmatrix} a_2 \\ u_2 \end{pmatrix} = \frac{a_1^2}{h_0} \begin{pmatrix} F_1 \\ F_2 \end{pmatrix} ,$$

with:

$$m_{11} = 2\omega \ , \quad m_{12} = -2kh_0 \ , \quad m_{21} = -2k \ , \quad m_{22} = 2\omega(1 + 4/3\phi) \ ,$$
$$F_1 = \omega \ , \quad F_2 = \frac{\omega^2}{2h_0 k} \ .$$

Solving the linear system, using the dispersion relation to simplify ω, and passing to dimensional variables, we end up with:

$$a_2 = \frac{3}{4} \frac{a_1^2}{h_0} \frac{1}{\phi^2} \left(1 + \frac{8}{9}\phi^2 \right) \ . \tag{1.103}$$

This value can be compared to the one found with the Stokes theory (Madsen et Schaffer [1998]):

$$a_2^{Airy} = \frac{1}{4} \left(\frac{a_1^2}{h_0} \right) \phi \coth(\phi) (3 \coth^2(\phi) - 1) \ . \tag{1.104}$$

Remark 1.1. *In adapting this procedure to the different BT models discussed, particular attention must be paid for the A and MS systems. For these models the relevant ansatz is:* $q' = q_1 \cos(\xi) + \varepsilon q_2 \cos(2\xi)$. *Subsequently, always dropping the primes:*

$$\varepsilon \frac{q^2}{h_0 + \varepsilon\eta} = \varepsilon \frac{q^2}{h_0} + \mathscr{O}(\varepsilon^2) \ ,$$

which can be used to show:

$$\varepsilon \left(\frac{q^2}{h_0 + \varepsilon\eta} \right)_x = \varepsilon 2k \frac{q_1^2}{h_0} \sin(\xi)\cos(\xi) + \mathscr{O}(\varepsilon^2). \tag{1.105}$$

The analysis of the first and second harmonics can then be performed assembling the proper order linear systems as shown for the Peregrine equations.

The results obtained for the different models are compared on figure 1.10 in terms of the ratio a_2/a_2^{Stokes}. The first obvious remark is that the second harmonic, taking into account the nonlinear behavior of the PDEs, reveals four different behaviours: one for each BT model considered. This is in contrast with the results given by the first order solutions discussed up to now, which where coupling the models on the base of their linear properties.
The most striking result, however, is that only two different trends are observed, which, as anticipated, depend uniquely on whether the model is in *amplitude-velocity* or *amplitude-flux* form. In particular, all the models in *amplitude-flux* form underestimate the wave amplitude: the error is monotonically increasing with an increase of the reduced wavenumber kh_0. On the contrary, all the models in *amplitude-velocity* form give a non-monotone trend, with an initial overestimation of the amplitude, and a peak which is close to $kh_0 = 1$ for the enhanced BT models (Filippini *et al.* [2015]). Moreover, the error obtained with this latter class of models is smaller, being the ratio closer to one.

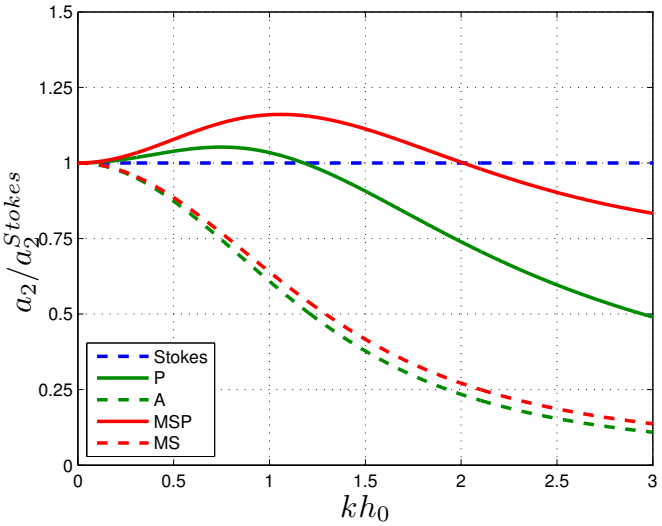

Figure 1.10: Ratio of the second harmonic a_2/a_2^{Stokes} for the models considered. Continuous line : *amplitude-velocity* models. Dashed lines : *amplitude-flux* models.

1.7.4 Nonlinear Shoaling

In this paragraph we use of the test proposed in Grilli *et al.* [1994] to study the wave shoaling characteristics of the discussed models in conditions close to wave breaking. The test consists of a solitary wave of amplitude $a/h_0 = 0.2$ m propagating on a water depth $h_0 = 0.44$ m, and shoaling onto a constant slope of $1:35$. Note that in this test the local values of the nonlinearity parameter are roughly $\varepsilon = a_0/h \in [0.2; 2.2]$, which is clearly in the nonlinear range $\varepsilon \geq 1$. A representation of this test is given below in figure 1.11.

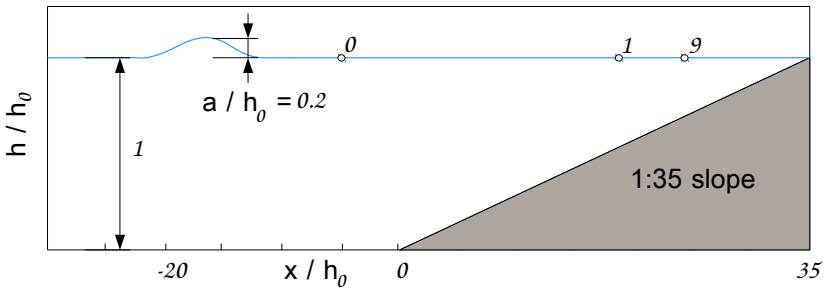

Figure 1.11: Shoaling of a solitary wave; computational configuration and gauges position.

The simulations are performed with a stabilized finite element approach which will be presented in chapter 2. However, note that all the results are grid converged and the curves reported are a genuine representation of the behaviour of the models. Results are discussed for the four weakly nonlinear BT models presented and are compared to the data of the laboratory experiments of Grilli *et al.* [1994]. The data available consist in the values of the free-surface elevations measured in 10 gauges positioned at stations from 0 to 9 (figure 1.11), with gauge 0 positioned just before the toe of the slope and gauge 9 located close to the wave breaking point. We refer to Grilli *et al.* [1994] for the precise description of the setup. In our test, gauge 0 is used to calibrate the phase of the solutions obtained, the semi-analytical solitary waves traveling at a celerity depending on the form of the model. The resulting shoaling wave profiles are compared to the experiments in figures 1.12 and 1.13, while the spatial evolution of the peak height is compared to the experiments in figure 1.14.

In figure 1.12 and 1.13, we can observe that all the models provide results in phase with the experimental data, meaning that the transformation of the phase speed during shoaling is well represented by all of them. Moreover, it appears that, as soon as nonlinear effects start being relevant, the main factor influencing the behavior of the model is its amplitude-velocity or amplitude-flux form, enhanced models giving the same results as Peregrine or Abbott equations. All the models in amplitude-velocity form provide waves with con-

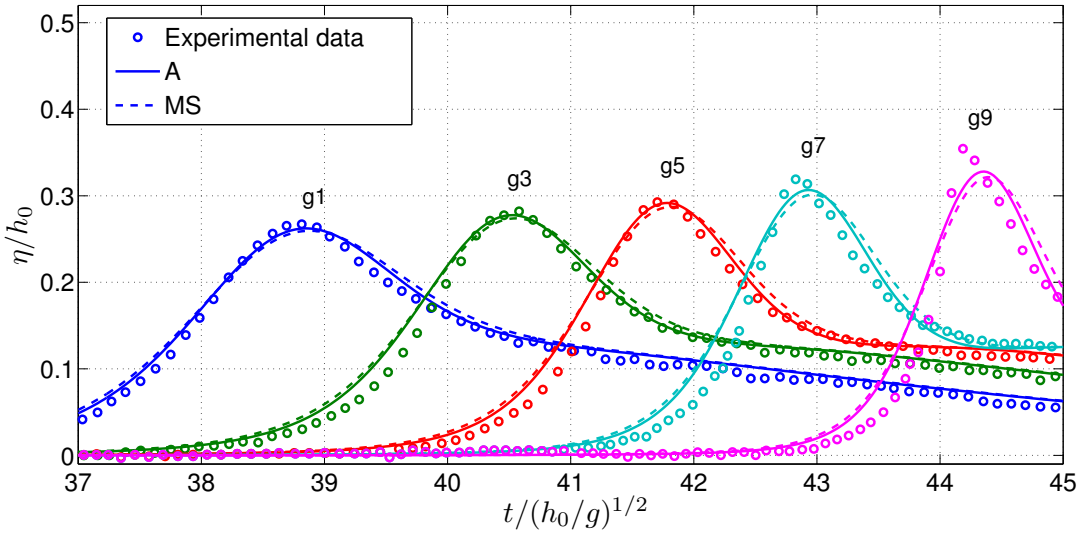

Figure 1.12: Nonlinear shoaling. Comparison between the computed wave heights at gauges 1, 3, 5, 7 and 9 and laboratory data from Grilli *et al.* [1994]; models in amplitude-flux form.

siderably higher peaks and fronts with larger slope compared to the data. On the contrary, all the models in amplitude-flux form give shorter waves with smaller slopes. This independently on the quality of the linearized system.
This result confirms the analytical findings about the study of the propagation of higher harmonics, realized in the previous paragraph, and is extremely important if one is to use these models in conjunction with a breaking detection plus dissipation mechanism. In particular, whether based on the slope of the front, on wave curvature, or on wave height, two distinct parametrizations of the detection criterion are necessary for these two family of models. In fact, looking at gauge 9, which is roughly where wave breaking should be detectable according to the experiments, we can see that: amplitude-velocity models have front slopes and wave heights larger than those of the data; amplitude-flux models give lower amplitudes and, more importantly, much smaller front slopes. For criteria based on the shape of the profiles, such as those discussed *e.g.* in Tissier *et al.* [2012]; Kazolea *et al.* [2014], this might mean that, for a given parametrization of the constants involved in the breaking criterion, amplitude-velocity models might give an early breaking, while amplitude-flux models will most likely give a late breaking, or not break at all. We remark, once more, that this result is independent on the quality of the model in terms of linear phase accuracy, the models of Peregrine and Abbott giving results considerably close to their enhanced versions. Moreover, the outcome is completely general and can be easily extended to the enhanced BT models of Beji-Nadaoka and Nwogu and their respective amplitude-flux formulations, as

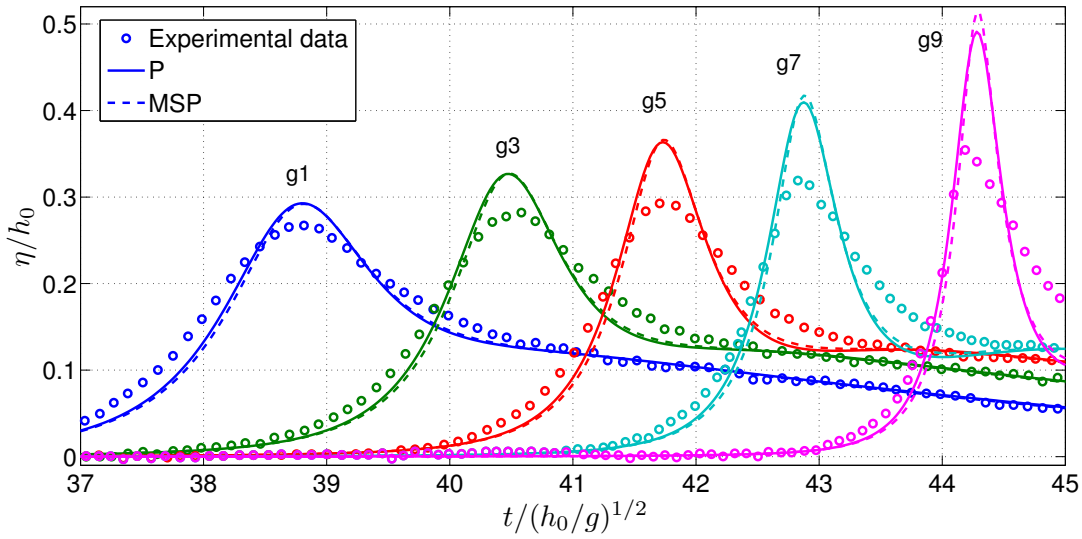

Figure 1.13: Nonlinear shoaling. Comparison between the computed wave heights at gauges 1, 3, 5, 7 and 9 and laboratory data from Grilli *et al.* [1994]; models in amplitude-velocity form.

done in Filippini *et al.* [2015].
To overcome this duality, fully nonlinear models need to be considered. This is the object of the next sections.

1.8 Fully nonlinear Boussinesq-type models : the Serre-Green-Naghdi model

Green et Naghdi [1976] derived a fully non-linear weakly dispersive set of equations for an uneven bottom, which represents a two dimensional extension of the Serre equations Sebra-Santos *et al.* [1987]. They are known as Serre or Green-Naghdi (GN), or fully nonlinear Boussinesq equations. The range of validity of this model may vary as much as far the nonlinearity parameter ε is concerned but it requires the shallowness parameter μ to be small (less than one). The GN model has been fully justified mathematically by Lannes [2013], in the sense that the error between the solutions of the GN system and the Euler equations is small and of size $O(\mu^2)$ and that $u_{GN} \to u_{Euler}$ if $\mu \to 0$. We refer to Lannes [2013]; Lannes et Bonneton [2009] for more details.

In this section, we will briefly review the main steps for the derivation of the GN model. As already mentioned, these equations are based on the assumptions that:

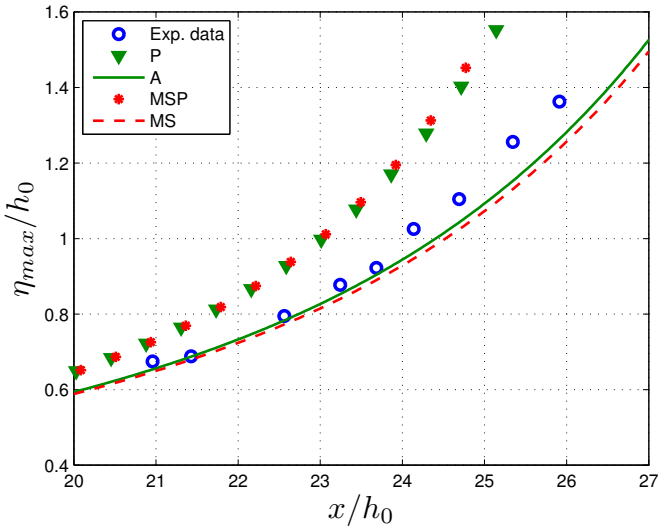

Figure 1.14: Nonlinear shoaling. Comparison between the computed wave peak evolutions in space and laboratory data from Grilli *et al.* [1994] for the models discussed.

$$\varepsilon \sim \mathscr{O}(1) \ , \quad \mu^2 \ll 1 \ .$$

Thus, the GN model can be obtained by pushing on the asymptotic development of the Euler's system up to the order $\mathscr{O}(\mu^4)$, retaining into the equations also the terms of order $\mathscr{O}(\varepsilon\mu^2)$. This will require to find the asymptotic expressions of $u(1+\varepsilon\eta)$, $w(1+\varepsilon\eta)$, $u_t(1+\varepsilon\eta)$ and $w_t(1+\varepsilon\eta)$ in terms of $\bar{u}$ as to be used into (1.42). We start by evaluating (1.67) and (1.53) at the free surface $z = 1+\varepsilon\eta$. This gives:

$$u(1+\varepsilon\eta) = \bar{u} - \mu^2\left(\left(\frac{h^2}{3} - \frac{hh_b}{2}\right)\bar{u}_{xx} + \frac{h}{2}\Big(h_b\bar{u}\Big)_{xx}\right) + \mathscr{O}(\mu^4) \ , \tag{1.106}$$

and:

$$w(1+\varepsilon\eta) = -\Big(\big(h-h_b\big)\bar{u}_x + (h_b\bar{u})_x\Big) + \mathscr{O}(\mu^2) \ . \tag{1.107}$$

Then, we derive (1.67) and (1.53) with respect to time and we evaluate the resulting expression at the free surface:

$$\begin{aligned} u_t(1+\varepsilon\eta) = \bar{u}_t - \mu^2\left(\left(\frac{h^2}{3} - \frac{hh_b}{2}\right)\bar{u}_{xxt} + \frac{h}{2}\Big(h_b\bar{u}\Big)_{xxt}\right) + \\ - \mu^2\left(\left(\frac{2h}{3} - \frac{h_b}{2}\right)h_t\bar{u}_{xx} + \frac{h_t}{2}\Big(h_b\bar{u}\Big)_{xx}\right) + \mathscr{O}(\mu^4) \ , \end{aligned} \tag{1.108}$$

$$w_t(1+\varepsilon\eta) = -\Big(\big(h-h_b\big)\bar{u}_{xt} + (h_b\bar{u})_{xt}\Big) + \mathscr{O}(\mu^2) \ . \tag{1.109}$$

We can now use in (1.42) all the relations just found: (1.106), (1.108), (1.107) and (1.109). Neglecting all the terms of order $\mathscr{O}(\mu^4)$, using also (1.54) to replace h_t by $-(h\bar{u})_x$ and rearranging the final expression, we end with:

$$\begin{aligned} \bar{u}_t + \varepsilon\bar{u}\bar{u}_x + \eta_x - \frac{\mu^2}{h}\left[\left(\frac{h^3}{3} - \frac{h^2h_b}{2}\right)R(\bar{u}) + \frac{h^2}{2}R(h_b\bar{u})\right]_x + \\ + \mu^2(h_b)_x\Big(\big(h-h_b\big)R(\bar{u}) + R(h_b\bar{u})\Big) = \mathscr{O}(\mu^4) \ . \end{aligned} \tag{1.110}$$

with $R(\cdot)$ defined as follows:

$$R(\cdot) = (\cdot)_{xt} + \varepsilon\bar{u}(\cdot)_{xx} - \varepsilon\bar{u}_x(\cdot)_x \ , \tag{1.111}$$

We thus obtain the system of equations of Green-Naghdi by coupling the continuity equation (1.54) with the equation (1.110) just found. In the form used by Bonneton *et al.* [2011b], the GN system in one-dimension finally reads:

$$\begin{aligned} \eta_t + (h\bar{u})_x = 0 \ , \\ (1+\mathcal{T})\left(\bar{u}_t + \bar{u}\bar{u}_x\right) + g\eta_x + \mathcal{Q}_1(\bar{u}) = 0 \ , \end{aligned} \tag{1.112}$$

with:

$$\mathcal{T}(\cdot) = -\frac{1}{3h}\Big(h^3(\cdot)_x\Big)_x - \frac{h}{2}(\cdot)_x b_x + \frac{1}{2h}\Big(h^2 b_x(\cdot)\Big)_x + b_x(\cdot)b_x \ , \tag{1.113}$$

$$\mathcal{Q}_1(\cdot) = \frac{2}{3h}\Big(h^3\big((\cdot)_x\big)^2\Big)_x + h\big((\cdot)_x\big)^2 b_x + \frac{1}{2h}\Big(h^2(\cdot)^2 b_{xx}\Big)_x + (\cdot)^2 b_{xx}b_x \ . \tag{1.114}$$

According to Lannes et Marche [2015] the above formulation does not require the computation of third order derivatives, while this is necessary in the standard formulation of the GN system. Moreover, the presence of the operator $(1+\mathcal{T})$ makes the model very stable with respect to high frequency perturbations, which is of highest interest for numerical computations.
In terms of the conservative variables $(h, \bar{q})$ the system can be rewritten as:

$$\begin{aligned} h_t + \bar{q}_x = 0 \ , \\ (1+T)\left(\bar{q}_t + \left(\frac{\bar{q}^2}{h}\right)_x\right) + gh\eta_x + h\mathcal{Q}_1(\bar{u}) = 0 \ , \end{aligned} \tag{1.115}$$

where:

$$T(\cdot) = h\mathcal{T}\left(\frac{(\cdot)}{h}\right) \ . \tag{1.116}$$

This system of equations differs from the P one only for the nonlinear terms of order $\mathscr{O}(\varepsilon\mu^2)$ that have been retained in the asymptotic development of the velocity. For this reason, the GN model share the same linear dispersion properties of the P model. In, Chazel *et al.* [2011], the authors propose an equivalent model with enhanced linear frequency dispersion and shoaling description with respect to (1.115). This has been recovered by adding some terms of $\mathscr{O}(\mu^2)$ to the momentum equation using a tuning parameter α:

$$\begin{aligned} h_t + \bar{q}_x &= 0 \ , \\ (1+\alpha T)\left(\bar{q}_t + \left(\frac{\bar{q}^2}{h}\right)_x + g\frac{\alpha-1}{\alpha}h\eta_x\right) + \frac{g}{\alpha}h\eta_x + h\mathcal{Q}_1(\bar{u}) &= 0 \ . \end{aligned} \tag{1.117}$$

In this work we will refer to this new system of equation as the enhanced GN system (eGN); note that it is possible to recover the original GN model by simply setting $\alpha = 1$, while the value of α which allows to optimize the linear dispersion properties of the model will be discussed and indicated in the next paragraph.
The two-dimensional forms of systems (1.117) can be written in the following form:

$$\begin{aligned} h_t + \nabla\cdot(h\bar{\mathbf{u}}) &= 0 \ , \\ (I+\alpha T)\left(\bar{\mathbf{q}}_t + \nabla\cdot\left(\frac{\bar{\mathbf{q}}\otimes\bar{\mathbf{q}}}{h}\right) + g\frac{\alpha-1}{\alpha}h\nabla\eta\right) + \frac{g}{\alpha}h\nabla\eta + h\mathcal{Q}_1(\bar{\mathbf{u}}) &= 0 \ , \end{aligned} \tag{1.118}$$

with the operators $T(\cdot)$ and $\mathcal{Q}_1(\cdot)$ now defined by:

$$\begin{aligned} T(\cdot) = &-\frac{1}{3}\nabla\left(h^3\nabla\cdot\left(\frac{(\cdot)}{h}\right)\right) - \frac{h^2}{2}\left(\nabla\cdot\left(\frac{(\cdot)}{h}\right)\right)\nabla b + \\ &+\frac{1}{2}\nabla\left(h^2\nabla b\cdot\left(\frac{(\cdot)}{h}\right)\right) + h\left(\nabla b\cdot\left(\frac{(\cdot)}{h}\right)\right)\nabla b \ , \end{aligned} \tag{1.119}$$

$$\begin{aligned} \mathcal{Q}_1(\cdot) = &\frac{2}{3h}\nabla\left(h^3\left(\nabla(\cdot)_1\cdot\nabla^\perp(\cdot)_2 + \Big(\nabla\cdot(\cdot)\Big)^2\right)\right) + \\ &+ h^2\left(\nabla(\cdot)_1\cdot\nabla^\perp(\cdot)_2 + \Big(\nabla\cdot(\cdot)\Big)^2\right)\nabla b + \\ &+ \frac{1}{2h}\nabla\left(h^2\Big((\cdot)\cdot\Big((\cdot)\cdot\nabla\Big)\nabla b\Big)\right) + \\ &+ \Big((\cdot)\cdot\Big((\cdot)\cdot\nabla\Big)\nabla b\Big)\nabla b \ , \end{aligned} \tag{1.120}$$

where $(\cdot)_1$ and $(\cdot)_2$ indicates respectively the first ans second component of the vector $(\cdot)$, and $\nabla^\perp$ stays for the normal gradient operator. Note that the two-dimensional form of system (1.115) will read exactly as (1.118) when the value $\alpha = 1$ is set.

The operator $T(\cdot)$ plays a key role, as its inversion is necessary to be able to obtain evolution equations for the physical variables. For this reason, following Alvarez-Samaniego et Lannes [2008] it is important to stress that $T(\cdot)$ can be written in compact form involving two operators $S_1(\cdot)$ and $S_2(\cdot)$ and their adjoint $S_1^*(\cdot)$ and $S_2^*(\cdot)$, namely:

$$T(\cdot) = S_1^*\left(hS_1\left(\frac{(\cdot)}{h}\right)\right) + S_2^*\left(hS_1\left(\frac{(\cdot)}{h}\right)\right) , \tag{1.121}$$

where, in multiple space dimensions:

$$S_1(\cdot) = \frac{h}{\sqrt{3}}\nabla\cdot(\cdot) - \frac{\sqrt{3}}{2}\nabla b\cdot(\cdot) , \qquad S_2(\cdot) = \frac{1}{2}\nabla b\cdot(\cdot) ,$$

reducing in one-dimension to:

$$S_1(\cdot) = \frac{h}{\sqrt{3}}(\cdot)_x - \frac{\sqrt{3}}{2}b_x(\cdot) , \qquad S_2(\cdot) = \frac{1}{2}b_x(\cdot) . \tag{1.122}$$

Note that this formulation is essential to show the coercivity of the operator $(I + \alpha T)$, via the corresponding variational form of $T(\cdot)$:

$$a_{\mathrm{T}}(\nu,\phi) = \int_\Omega S_1(\nu)\, h\, S_1\left(\frac{\phi}{h}\right) + \int_\Omega S_2(\nu)\, h\, S_2\left(\frac{\phi}{h}\right) . \tag{1.123}$$

The interested reader can refer to Alvarez-Samaniego et Lannes [2008] for details concerning the coercivity analysis.

Based on this property, a discretization procedure for system (1.117) is proposed in chapter 2, while the spatial discretization in two dimensions is treated in chapter 4. In the remainder of this chapter, we discuss, instead, the dispersion and shoaling properties of these models.

Linear Dispersion Properties: The expression of the phase velocity for the eGN model can be recovered similarly to what already done for the previous models. In this case the linearized eGN system reads:

$$\begin{aligned} \eta_t + h_0\bar{u}_x &= 0 , \\ \bar{u}_t + g\eta_x - \frac{\alpha}{3}h_0^2\bar{u}_{xxt} - g\frac{(\alpha-1)}{3}h_0^2\eta_{xxx} &= 0 , \end{aligned} \tag{1.124}$$

with h_0 the constant still water level. This linearized system is similar to (1.97), except for the form of the tuning coefficients multiplying the dispersive terms. Consequently, also the phase velocity expression has a structure similar to that of C_{MS}:

$$C_{eGN}^2 = gh_0 \frac{1 + \left(\frac{\alpha - 1}{3}\right)\varphi_0^2}{1 + \frac{\alpha}{3}\varphi_0^2} \,. \tag{1.125}$$

Chazel *et al.* [2011] indicate $\alpha = 1.159$ to be the value optimizing the the above relation with respect to the Airy theory. A proof of this is given in figure 1.15, where it is shown the percentage error for the phase velocity, performed by the GN and eGN models with respect to the Airy's theory. In particular, it can be noted that the absolute value of the error never exceeds 1% , in the case of the eGN model, for the whole range of reduced frequencies kh_0 considered, pushing in deeper waters the limit of application of this model. Moreover, the comparison of the linear dispersion relations (1.97) and (1.124) reveals the relation $\alpha = 3\beta + 1$ that provide the same linear dispersion description for the MS and eGN models.

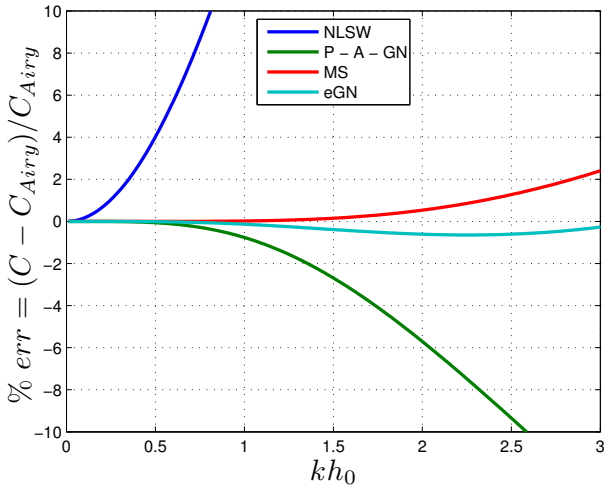

Figure 1.15: Percentage error in phase velocity description with respect to the Airy's theory (eq. (1.24)) for the GN and eGN models. The plot has been performed using the optimized value of $\alpha = 1.159$ given by Lannes et Marche [2015].

Linear Shoaling Properties: To investigate the linear shoaling behaviour, the following system has to be studied:

$$\begin{aligned}
&\eta_t + (h\bar{u})_x = 0 \ , \\
&(h\bar{u})_t + gh\eta_x - \frac{\alpha}{3}h^2(h\bar{u})_{xxt} - \frac{\alpha}{3}hh_x(h\bar{u})_{xt} + \\
&\qquad\qquad - \ g(\alpha-1)h\left(\frac{h^2}{3}\eta_{xxx} + hh_x\eta_{xx}\right) = 0 \ ,
\end{aligned} \tag{1.126}$$

where, as before, the linearization has been performed considering a slow varying bathymetry $h(x) = h_b(x)$ and high order derivatives of this quantity have thus been neglected. Once more, an analogy can be done with system (1.99), observing that in this case any relation between the two parameters β and α would give the same linear shoaling behaviour to the two systems.
The analysis described in Madsen et Sørensen [1992], performed on system (1.126), reveals the following values of the coefficients α_1, α_2, α_3 and γ:

$$\begin{aligned}
\alpha_1 &= 2\left(1 - \frac{\alpha}{3}\frac{P}{Q}\varphi^2 + \frac{4}{3}(\alpha-1)\varphi^4\right) \ , \\
\alpha_2 &= 1 - \frac{\alpha}{3}\frac{P}{Q}\varphi^2 + 2(\alpha-1)\varphi^4 \ , \\
\alpha_3 &= 1 - \alpha\frac{P}{Q}\varphi^2 + 2(\alpha-1)\varphi^4 \ , \\
\gamma &= -\frac{1-\Omega}{\Omega} \ ,
\end{aligned} \tag{1.127}$$

having set $P = 1 + \frac{\alpha-1}{3}$, $Q = 1 + \frac{\alpha}{3}$ and $\Omega = 2\left(1 + \frac{\alpha-1}{3P}\varphi^2 - \frac{\alpha}{3Q}\varphi^4\right)$.
The above relations are used into (1.65) giving the shoaling coefficient expression $s_{eGN}(h,k)$, whose behaviour is plotted in figure 1.16 as function of the quantity k_0h. It can be observed that the eGN trend is, once again, very close to the MS one, diverging from it only for $k_0h > 1.6$, but still remaining a great improvement with respect to the pattern of the GN model which, as well as the P one, rapidly deviates from the Airy's reference curve.

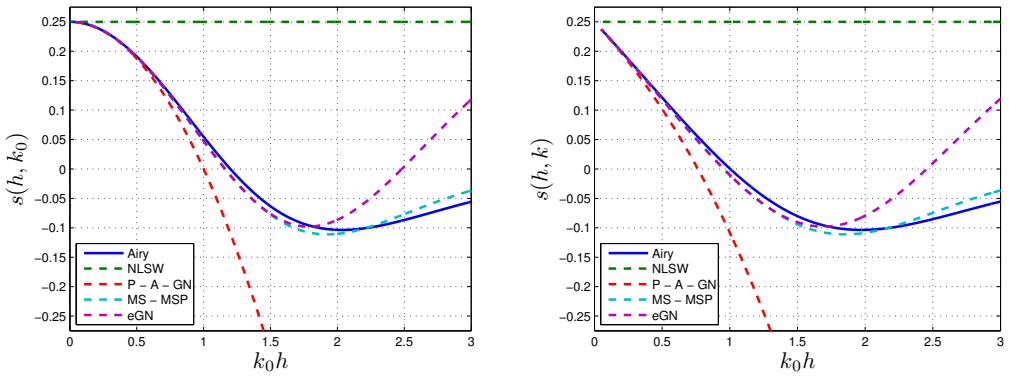

Figure 1.16: Linear shoaling: comparison between the linear shoaling coefficients of the discussed models with respect to the results given from the Airy's theory. On the left is sketched $s(h(x), k_0)$, thus computing the values of s using the initial wavenumber of the signal k_0. On the right, instead, the variation of $k(x)$ along the domain is considered in the computation of the shoaling coefficient, thus: $s(h(x), k(x))$.

Nonlinear Shoaling Properties: After having investigated the linear properties of the fully nonlinear GN and eGN models, finding that these are comparable to those of the weakly nonlinear models presented in the previous section, we now make use of the shoaling test of Grilli *et al.* [1994], already presented, to investigate their behaviour in the nonlinear regime.
As we have done before, we compare the simulations performed using the two models with respect to some gauge signals at different locations along the slope (figure 1.17), in particular gauge 9 is located close to the breaking point of the wave, and to the wave height envelope in space (figure 1.18).

Once again, figure 1.17 shows that the results performed with the two models are well in phase with respect to the laboratory data. But this time, also the wave amplitude is very well described by the simulation. This highlights the fact that, as soon as nonlinear effects start being relevant, the weakly nonlinear models gives an inadequate representation of the phenomenon, which is instead well reproduced by the fully nonlinear GN equations and even better by the eGN ones.

Further Developments: The analysis of the linear and nonlinear properties, just accomplished, show that systems (1.115) and (1.117) are, generally, more accurate than the weakly nonlinear BT models in simulating the water wave propagation problem in the near-shore region. Nevertheless, they are, also, more complicated to solve. In particular, the inversion of the differential operator $\left(1 + \alpha T(\cdot)\right)^{-1}$ at any time step is very computational demanding, especially in two-dimensional problems. Very recently a strategy to tackle this issue has been proposed in Lannes et Marche [2015]. Neglecting some terms

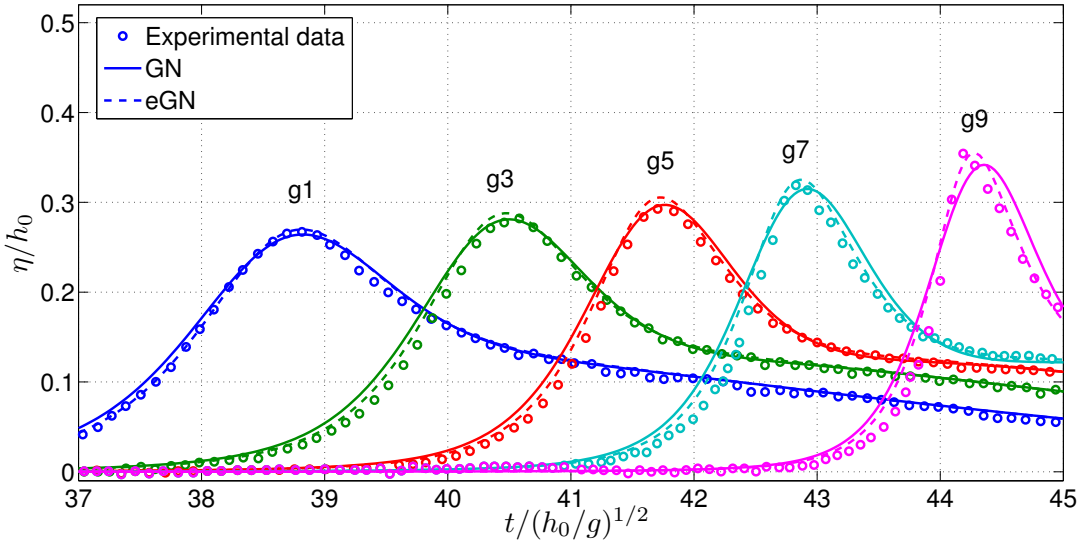

Figure 1.17: Nonlinear shoaling. Comparison between the computed wave heights at gauges 1, 3, 5, 7 and 9 and laboratory data from Grilli *et al.* [1994] for the GN and eGN models.

of order $\mathscr{O}(\mu^4)$, while keeping the same linear properties of the model, they show that it is possible to derive a system of equations in which the operator to be inverted is diagonal with time independent coefficients. We invite the interested reader to consult Lannes et Marche [2015] for more details about the derivation procedure and the mathematical justification of this model. Here we limit ourself in showing its final form, that reads:

$$\begin{cases} h_t + \bar{q}_x = 0 \ , \\ (1+\alpha T_d)\left(\bar{q}_t + \left(\dfrac{\bar{q}^2}{h}\right) + g\dfrac{\alpha-1}{\alpha}h\eta_x\right) + \dfrac{g}{\alpha}h\eta_x + \\ \qquad\qquad + h\Big(\mathcal{Q}_1(\bar{u}) + g\mathcal{Q}_2(\eta)\Big) + g\mathcal{Q}_3(\eta) = 0 \ . \end{cases} \tag{1.128}$$

The several operators appearing in the system are defined as follows:

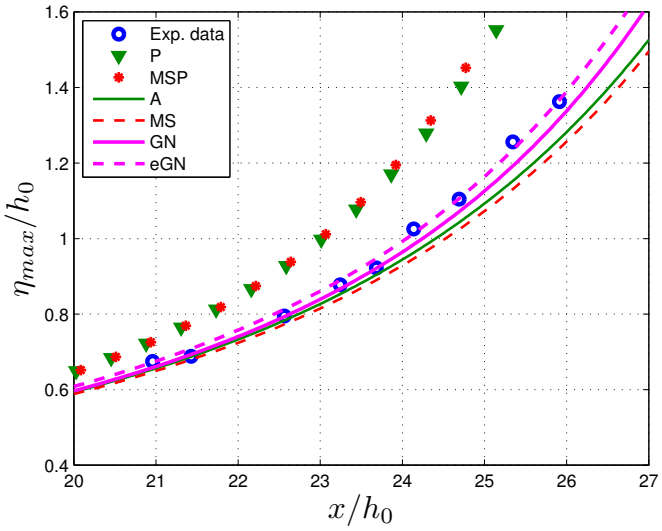

Figure 1.18: Nonlinear shoaling. Comparison between the computed wave peak evolutions in space and laboratory data from Grilli *et al.* [1994] for the models discussed.

$$T_d(\cdot) = h_b \mathcal{T}_d\left(\frac{(\cdot)}{h_b}\right) = -\frac{1}{3}\left(h_b^3\left(\frac{(\cdot)}{h_b}\right)_x\right)_x , \tag{1.129}$$

$$\mathcal{Q}_2(\cdot) = -\frac{1}{2h}\Big(h^2 b_x(\cdot)_x\Big)_x + \left(\frac{h}{2}(\cdot)_x - b_x(\cdot)_x\right)b_x , \tag{1.130}$$

$$\mathcal{Q}_3(\cdot) = -\mathcal{S}\Big(\big(1+\alpha T_b\big)^{-1}\big(h(\cdot)_x\big)\Big) , \tag{1.131}$$

$$\mathcal{S}(\cdot) = -\frac{1}{6}(h^2 - h_b^2)_x(\cdot)_x - \frac{h^2 - h_b^2}{3}(\cdot)_{xx} + \frac{1}{6}(h^2 - h_b^2)_{xx}(\cdot) . \tag{1.132}$$

All along the text we will refer to system (1.128) as the GNd model in the case with $\alpha = 1$, as the eGNd model when, instead, the optimized value of α is used.
If it is true that the inversion of the operator $(1+\alpha T_d)$ allows to achieve a great gain in the computational time, since this operation can be done just ones at the beginning of the simulation and the result stored, it is also true that the GNd and eGNd models represent, in the same asymptotic of the fully nonlinear BT models, two different system of equations respect to respectively the GN and eGN models. Therefore, even if the linear properties of these systems remain the same, there is no point to expect them to behave the same in the nonlinear regime. Indeed, by repeating the nonlinear shoaling test with these models, we found that the envelope in space of the maximum wave elevation is not as well represented as the respective non diagonal models. Moreover, the gauge signals show a large phase lag in time. These results deserve more

attention and further investigations.
In this work we focus on the eGN model (1.117)-(1.118).

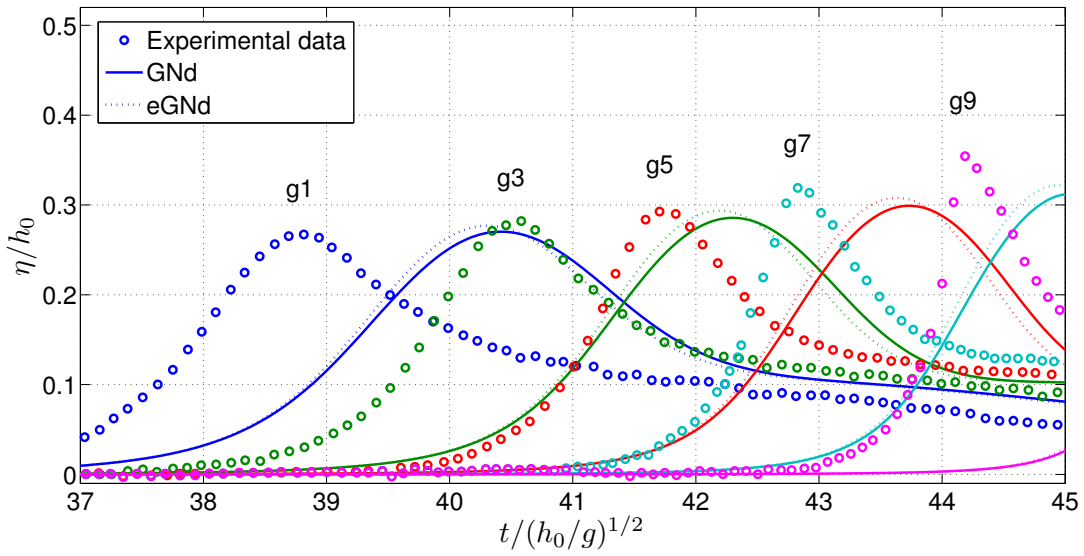

Figure 1.19: Nonlinear shoaling. Comparison between the computed wave heights at gauges 1, 3, 5, 7 and 9 and laboratory data from Grilli *et al.* [1994], using the GNd and eGNd models.

1.9 Modelling wave breaking

Wave breaking is an important phenomenon in near-shore environments. It dissipates wave energy through the generation of turbulence, including substantial air entrainment. As waves shoal, wave fronts become steeper and steeper, until wave crest overturns. Depth averaged models, such as those considered in this work, are unable to describe this phenomenon, limiting the possibility of their application in real coastal environments. A lot of efforts have been made in modern days to overcome this problem and incorporate in the existing models the description of this additional physical effect. To this end, a closure model is necessary to simulate the breaking process numerically. This is composed of two main elements: an energy dissipation mechanism, and a trigger mechanism related to the initiation and possibly the termination of the breaking process.
Concerning the former aspect, the first efforts have been towards the development of roller models (*cf.* Schaffer *et al.* [1993]), vorticity models (*cf.* Veeramony et Svendsen [2000]) or eddy viscosity models (*cf.* Zelt [1991]; Kennedy *et al.* [2000]), these latters still widely used. In eddy viscosity models, the dissipation due to turbulence generated by wave breaking is treated by a diffusion

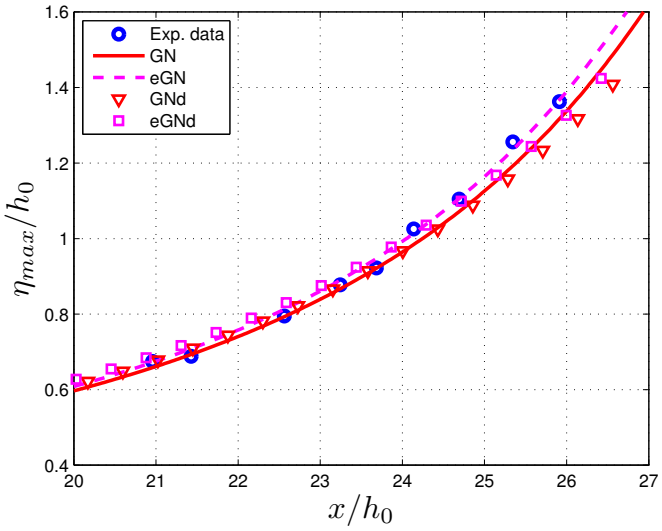

Figure 1.20: Nonlinear shoaling. Comparison between the computed wave peak evolutions in space and laboratory data from Grilli *et al.* [1994] for the several variants of the Green-Naghdi model discussed.

term in the momentum equation . The amount of dissipation is then calibrated through the value of the eddy viscosity coefficient, tuned with respect to some experimental data.
More recently, Bonetton [2004] and Bonetton [2007] have shown the ability of the NLSW equations to accuratly reproduce the celerity of irregular waves propagating over gently sloping beaches and to predict wave distortion and energy dissipation of periodic broken waves in the inner surf zone, validating their results with respect to the experiments conducted by Cox [1995] and Ting et Kirby [1996]. Pictures of figure 1.21 have been taken from Bonetton [2007] and show, for a case of periodic broken wave propagation over a gently sloping beach, computed and measured time series of surface elevation at different locations inside the inner surf zone (on the right), and the spatial evolution of the wave elevation towards the beach (on the left). These results prove that the NLSW model is able to reproduces the nonlinear wave distortion towards the sawtooth shape assumed by the wave profiles in the surf region, and give a good prediction of the wave height decay and dissipation.

Thus, recent progress in the representation of wave breaking has been made using hybrid approaches in which the dispersive effects are turned off when some criteria are satisfied, reducing the model to the NLSW. In such models, breaking waves are threated as discontinuos solutions and the wave energy dissipation, which occurs in breaking, is recovered in moving bores and hydraulic jumps. Such an approach has gained attention by several researchers in the past few years (*cf.* Borthwick *et al.* [2006]; Tonelli et Petti [2009, 2010]; Ka-

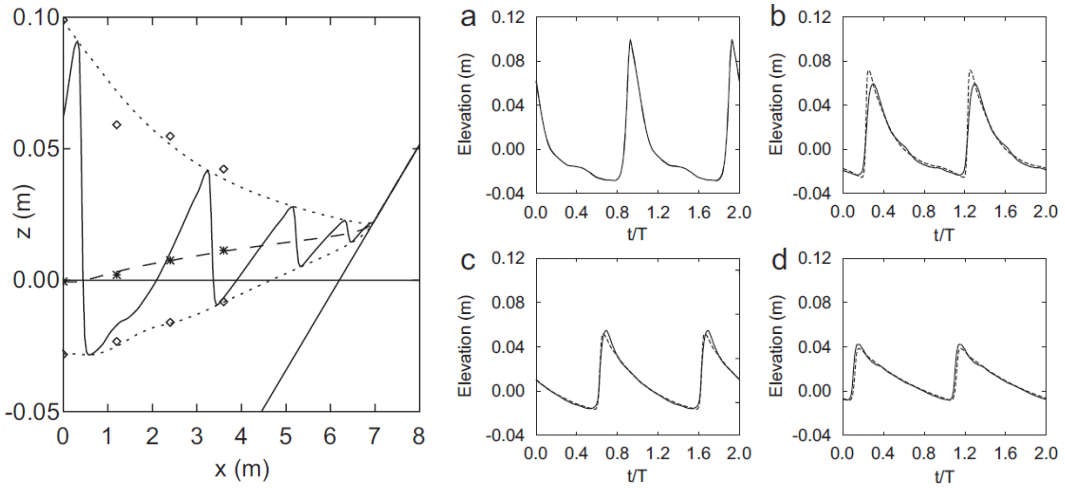

Figure 1.21: Source: Bonetton [2007]. On the left: spatial evolution of wave elevation; (short-dashed lines) computed η_{min} and η_{max}; (long-dashed line) computed $\bar{\eta}$; (solid line) instantaneous surface elevation at a given time $\bar{t}$; ($\diamond$) measured η_{min} and η_{max}; ($*$) measured $\bar{\eta}$. On the right: time series of surface elevation in the inner surf zone; comparison between NLSW numerical model (dashed lines) and experiments by Cox [1995].

zolea et Delis [2013]; Shi *et al.* [2012]; Roeber et Cheung [2012]; Orszaghova *et al.* [2012]; Tissier *et al.* [2012]; Tonelli et Petti [2012]), and goes hand in hand with the adoption of the finite-volume method as the dominant computational technique. These methods have, in fact, been evolved to provide robust shock-capturing capabilities for the NLSW equations (*cf.* Toro [2001]). In this work, we also applied a hybrid approach for energy dissipation in breaking regions, with special reference to the works of Tissier *et al.* [2012]; Kazolea et Delis [2013]; Bacigaluppi *et al.* [2014a]. The additional advantage of the solution procedure proposed, by decomposing the original eGN system in an elliptic and an hyperbolic part, is to allow a direct embedding of wave breaking either by simply neglecting the non-hydrostatic contribution ϕ in the hyperbolic phase, or even with a tighter coupling of the two phases using the breaking indicator to smoothly turn off ϕ in the elliptic phase. More details concerning the detection and triggering of the breaking model and on the coupling between Green-Naghdi and NLSW equations will be discussed in section 2.9.

Chapter 2

Numerical Discretization in One-Dimension

Contents

In this chapter we propose two hybrid strategies for the solution of the one-dimensional enhanced Green-Naghdi system of equations (1.117). We consider a two steps solution procedure composed by: a first step where the non hydrostatic source term is recovered by inverting the elliptic coercive operator associated to the dispersive effects; a second step which involves the solution of the hyperbolic shallow water system with the source term, computed in the previous phase, which accounts for the non-hydrostatic effects. Our objective is to choose numerical methods that can be also generalized on arbitrary unstructured meshes in two dimensions. In particular, we focus on the use of a classical C^0 Galerkin finite element method (described in section 2.2) for the elliptic phase. For the hyperbolic step, we will consider both a third order Finite Volume (section 2.3) and a third order stabilized Finite Element solver (section 2.4). The choice of a continuous finite element approach for the elliptic phase aims at simplifying as much as possible this step, and minimize its cost. As it will be illustrated in section 2.7.2, a second order P^1 approximation already allows to obtain the dispersion properties of a fourth order finite difference scheme (*cf.* Ricchiuto et Filippini [2014]). Moreover, the discrete dispersion properties of the fully coupled schemes obtained are also studied in section 2.7.2, showing accuracy close or better to that of a fourth order finite difference method. The hybrid approach of locally reverting to the nonlinear shallow water equations is used to recover energy dissipation in breaking regions. To this scope, in section 2.9.3, we evaluate two strategies: simply neglecting the non-hydrostatic contribution in the hyperbolic phase; imposing a tighter coupling of the two phases, with a wave breaking indicator embedded in the elliptic phase to smoothly turn off the dispersive effects. The discrete models obtained are thoroughly tested on benchmarks involving wave dispersion, breaking and run-up in chapter 3, showing a very promising potential for the simulation of complex near shore wave physics in terms of accuracy and robustness. The main content of this chapter has appear in Filippini *et al.* [2016].

2.1 Discretization Strategy: elliptic-hyperbolic decoupling

To discretize system (1.117), we apply the idea enunciated at the end of section 1.4. To this scope, the system is recast in the following way (from now on we will leave the notation $\bar{(\cdot)}$ for the depth averaged quantities for simplicity):

$$\begin{aligned} h_t + q_x &= 0 \ , \\ (I + \alpha T)\left[q_t + \left(\frac{q^2}{h}\right)_x + gh\eta_x\right] - T\left(gh\eta_x\right) + h\mathcal{Q}_1(u) &= 0 \ . \end{aligned} \tag{2.1}$$

This allows the operator $(I + \alpha T)$ to be applied to the full shallow water residual. This form suggests a possible splitting of the elliptic part of the problem from the hyperbolic one, which is obtained as follow:

$$
\begin{aligned}
(I + \alpha T)\,\phi &= \mathcal{W} - \mathcal{R}\ , && (2.2)\\
h_t + q_x &= 0\ , && (2.3)\\
q_t + \left(\frac{q^2}{h}\right)_x + gh\eta_x &= \phi\ .
\end{aligned}
$$

having also defined $\mathcal{W} = T(gh\eta_x)$ and $\mathcal{R} = h\mathcal{Q}_1(u)$. Given an initial solution, the system above can now be solved in two independent steps :

1. An elliptic step solving (2.2) for the non-hydrostatic term ϕ ;
2. An hyperbolic step for system (2.3), evolving the flow variables.

Note that this formulation differs from the ones previously proposed in literature (see *e.g.* Duran et Marche [2014]) as it allows the enhancement of an existing shallow water code by the addition of a purely algebraic term to the discrete momentum balance. It has the additional advantage of being a priori able to embed wave breaking effects in the elliptic phase, thus remaining completely non-intrusive with respect to the hyperbolic code. To evaluate this simplified and flexible strategy, we will investigate the accuracy and robustness obtainable when the two steps above are each solved with a different numerical method. The aim is to allow the choice of the method most appropriate and efficient for each step and to provide a simple technique to enhance shallow water codes including genuinely nonlinear dispersive effects.
We have purposely used here the word decoupling and not splitting. Indeed, the elliptic phase does not involve any time derivative, so this is not a splitting method, at least not in the sense used in Bonneton *et al.* [2011b] or in Strang [1968]. In particular, this approach provides an unsplit spatial discretization of:

$$
\begin{aligned}
h_t + q_x &= 0\ ,\\
q_t + \left(\frac{q^2}{h}\right)_x + gh\eta_x &= (I + \alpha T)^{-1}\left[T(gh\eta_x) - h\mathcal{Q}_1(u)\right]\ .
\end{aligned}
$$

This results in systems of ODEs, which can be evolved in time by any of the known high order time integration methods without any other source of error that the truncation of the spatial discretizations involved and of the ODE integrators. Our aim is to evaluate a strategy in which the two steps are each solved with an appropriate numerical method. Many hybrid methods can be

obtained by choosing different hyperbolic methods, such as *e.g.* the discontinous Galerkin method Zhang *et al.* [2012]; Xing *et al.* [2010], or the residual distribution method Ricchiuto [2015]. The interest is to study the potential of a formulation which can be easily generalised on arbitrary unstructured meshes. Here we focus on the use of a standard C^0 Galerkin finite element method for the elliptic phase, using P^1 approximation. High order finite volume (FV) and finite element (FE) methods are, instead, used independently in the hyperbolic phase and the resulting algorithms will be compared in the following sections. These schemes have been preferred to the class of Discontinuous Galerkin (DG) schemes, since the higher number of degrees of freedom in the DGs approaches increases the computational cost of the simulations, augmenting the size of the matrix to invert. Furthermore, the DGs schemes are characterized by CFL restrictions of the computational time-step and the application of boundary conditions breaks the order of the scheme. On the contrary, Wei et Kirby [1995] have proven, in the finite difference framework, to be able to obtain a fourth order accurate method by discretizing the dispersive terms using only second order formulae and Ricchiuto et Filippini [2014] developed a generalization of this, based on a P^1 Galerkin method, showing that it was possible to perform a dispersion description close to that of the fourth order finite difference scheme, by simply using P^1 basis functions.

2.2 Elliptic phase: Continuous Finite Element formulation

Spatial domain discretization and notation: Let Ω denote the spatial domain. We consider a tesselation Ω_h composed by a set of non-overlapping elements, the subscript h denoting the reference mesh size. The generic element K is defined by a set of nodes, *e.g.* in one space dimension $\mathrm{K} \equiv [x_i,\, x_{i+1}]$, with $\mathrm{h}_K = x_{i+1} - x_i$. Unknowns are stored at nodes as time dependent values $\{\eta_i(t)\}_{i\geq 1}$ and $\{q_i(t)\}_{i\geq 1}$. For a generic node i we will also denote by K_i the set of elements containing i as a node. As in the standard P^1 finite element method, nodal values are interpolated by means of piecewise linear continuous shape functions $\varphi_i(x)$, the interpolated values being denoted by η_h, and q_h with:

$$\eta_\mathrm{h}(t,x) = \sum_{i\geq 1} \eta_i(t)\varphi_i(x) = \sum_K \sum_{j\in K} \eta_j(t)\varphi_j(x) \ ,$$

$$q_\mathrm{h}(t,x) = \sum_{i\geq 1} q_i(t)\varphi_i(x) = \sum_K \sum_{j\in K} q_j(t)\varphi_j(x) \ ,$$

with $\varphi_i(x)$ the standard continuous piecewise linear finite element basis functions assuming value 1 in node i and zero in all the other nodes (*cf.* figure

2.1). As discussed in the introduction, in this work we focus on piecewise linear interpolation in order to show the feasibility of the use of compact low order discretizations of the elliptic operator for wave propagation. However all the developments presented, including the general form of the schemes, extend naturally to higher order polynomial approximations.

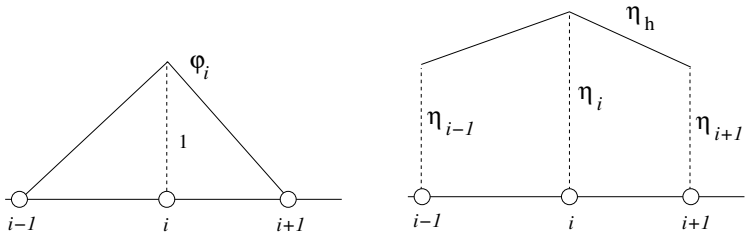

Figure 2.1: P^1 finite element interpolation

In the following subsections we present the schemes studied in the work in the hypothesis that periodic boundary conditions are used. More details concerning boundary conditions and wave generation are given in sections 2.8.3.
For simplicity we assume in the following that the points are equally spaced, so that $x_{i+1} - x_i = \Delta x \ \ \forall i$, but non-uniform meshes can be used with the same methods discussed here with very little modifications. For a given node i, we will also denote by C_i the cell $[x_{i-\frac{1}{2}} \ , \ x_{i+\frac{1}{2}}]$, with $x_{i+\frac{1}{2}} - x_{i-\frac{1}{2}} = \Delta x$.

Continuous Galerkin approximation: The first step for solving system (2.3) is to compute separately the value of the auxiliary variable ϕ from (2.2). In this work we discretize equation (2.2) by means of a standard C^0 Galerkin finite element approach. This discretization strategy passes by the writing of the variational form of the equation. The actual discretization is obtained by evaluating all the integrals by a numerical quadrature over each element of the discretization, with the assumption of piecewise linear variation of all the quantities involved h_h , η_h , b_h , u_h , ϕ_h . Defining $\Phi = [\phi_1(t),\ \phi_2(t),\ ...,\ \phi_N(t)]^T$ and $U = [u_1(t),\ u_2(t),\ ...,\ u_N(t)]^T$, with N the total number of nodes, the final form of the Galerkin approximation of the problem can be written as:

$$(\mathrm{M}^\mathrm{G} + \alpha \mathrm{T})\Phi = \mathrm{W} - \mathrm{R} \ , \tag{2.4}$$

$$\mathrm{W} = \mathrm{T}\ \delta \ , \tag{2.5}$$

$$\mathrm{R} = \mathrm{Q}\,(h, U) \ , \tag{2.6}$$

with δ an approximation of $gh\eta_x$.

The matrix M^G is the Galerkin mass matrix: a symmetric, positive definite and constant matrix whose entries are represented by:

$$\mathrm{M}^{\mathrm{G}}_{i,j} = \int_{\Omega_\mathrm{h}} \varphi_i \, \varphi_j \ . \tag{2.7}$$

The matrix $\mathrm{T}(h_\mathrm{h}, b_\mathrm{h})$ is deduced immediately from the variational form of (1.116), discussed *e.g.* in Lannes [2013]. All computation done, due to the assumed periodic boundary conditions, we obtain (partial derivatives now denoted by $\partial_{(.)}$ for the sake of clarity):

$$\begin{aligned}
\mathrm{T}_{i,j}(h_\mathrm{h}, b_\mathrm{h}) = {} & \frac{1}{3}\int_{\Omega_\mathrm{h}} \partial_x\varphi_i \, h_\mathrm{h}^2 \, \partial_x\varphi_j - \frac{1}{3}\int_{\Omega_\mathrm{h}} \partial_x\varphi_i \, h_\mathrm{h} \, \partial_x h_\mathrm{h} \, \varphi_j \ + \\
& + \frac{1}{2}\int_{\Omega_\mathrm{h}} \varphi_i \, \partial_x b_\mathrm{h} \, \partial_x h_\mathrm{h} \, \varphi_j - \frac{1}{2}\int_{\Omega_\mathrm{h}} \partial_x\varphi_i \, h_\mathrm{h} \, \partial_x b_\mathrm{h} \, \varphi_j \ + \\
& - \frac{1}{2}\int_{\Omega_\mathrm{h}} \varphi_i \, h_\mathrm{h} \, \partial_x b_\mathrm{h} \, \partial_x\varphi_j + \int_{\Omega_\mathrm{h}} \varphi_i \, (\partial_x b_\mathrm{h})^2 \, \varphi_j \ ,
\end{aligned} \tag{2.8}$$

having developed all the derivatives of $1/h_\mathrm{h}$ in order to explicitly remove the singularity with respect to h.
Proceeding similarly we obtain for the operator $\mathrm{Q}(h_\mathrm{h}, u_\mathrm{h}, b_\mathrm{h}, \delta_{b\mathrm{h}})$:

$$\begin{aligned}
\mathrm{Q}_{i,j}(h_\mathrm{h}, u_\mathrm{h}, b_\mathrm{h}, \delta_{b\mathrm{h}}) = {} & -\frac{2}{3}\int_{\Omega_\mathrm{h}} \partial_x\varphi_i \, h_\mathrm{h}^3 \, (\partial_x u_\mathrm{h})^2 + \int_{\Omega_\mathrm{h}} \varphi_i \, \partial_x b_\mathrm{h} \, h_\mathrm{h}^2 \, (\partial_x u_\mathrm{h})^2 \ + \\
& + \int_{\Omega_\mathrm{h}} \varphi_i \, \delta_{b\mathrm{h}} \, h_\mathrm{h}^2 \, u_\mathrm{h} \, \partial_x u_\mathrm{h} + \int_{\Omega_\mathrm{h}} \varphi_i \, \delta_{b\mathrm{h}} \, h_\mathrm{h} \, \partial_x h_\mathrm{h} \, u_\mathrm{h} \ + \\
& + \frac{1}{2}\int_{\Omega_\mathrm{h}} \varphi_i \, \partial_x\delta_{b\mathrm{h}} \, h_\mathrm{h}^2 \, u_\mathrm{h} + \int_{\Omega_\mathrm{h}} \varphi_i \, \partial_x b_\mathrm{h} \, \delta_{b\mathrm{h}} \, h_\mathrm{h} \, u_\mathrm{h} \ .
\end{aligned} \tag{2.9}$$

The arrays δ and δ_b contain nodal values of auxiliary variables introduced to handle the third order derivatives. In particular, we have:

$$(\mathrm{M}^{\mathrm{G}}\delta_\mathrm{h})_i = \int_{\Omega_\mathrm{h}} \varphi_i \, g \, h_\mathrm{h} \ \partial_x\eta_\mathrm{h} \ , \tag{2.10}$$

$$(\mathrm{M}^{\mathrm{G}}\delta_{b\mathrm{h}})_i = -\int_{\Omega_\mathrm{h}} \partial_x\varphi_i \, \partial_x b_\mathrm{h} \ . \tag{2.11}$$

The linear systems (2.10) and (2.11) can be solved very efficiently, being M^{G} symmetric, positive defined and constant. On the contrary, the properties of the matrix $(\mathrm{M}^{\mathrm{G}} + \alpha\mathrm{T})$ cannot be known *a priori*. However, the continuous

finite element formulation, used here, inherits the coercivity property of the corresponding continuous variational form (1.123). This bilinear form has been studied in Lannes [2013] and shown to be coercive, which is enough to guarantee the invertibility of $(\mathrm{M}^{\mathrm{G}} + \alpha \mathrm{T})$.
This inversion, however, remains the most computationally demanding process of our algorithm. In particular, exploiting the tridiagonal structure of the M^{G} and $(\mathrm{M}^{\mathrm{G}} + \alpha \mathrm{T})$ matrices, their inversions have been performed using the DGTSV function of `LAPACK` package, which uses a method based on Gaussian elimination by partial pivoting. For the M^{G} matix, we have stored the constant LU decomposition, reducing the reconstruction of the nodal values $\delta_{\mathrm{h},i}$ and $\delta_{b\mathrm{h},i}$ to a matrix-vector product. This cannot be done for $(\mathrm{M}^{\mathrm{G}} + \alpha \mathrm{T})$, whose decomposition has to be re-computed at each time step.
The kind of discretization performed allows many degrees of freedom in the management of the Galerkin mass matrices M^{G} which appear in it and that can be lumped (or not) always retaining second order of accuracy, as it will be shown in section 2.7.1. The optimization of the linear dispersion properties of the resulting schemes (see section 2.7.2) led us to the choice of not lumping any of the mass matrices appearing in the discretization. In the case of linear system (2.11), the choice does not affect the linear dispersion properties of the scheme, due to the fact that Q is nonlinear, and is motivated by the will to be consistent with (2.10) and the consideration that the cost to solve (2.11) should be payed only once at the beginning of the computation and kept all along the simulation, being b time-independent.

2.3 Hyperbolic phase: Finite Volume Scheme

Setting $\mathbf{U} = [h, q]^T$, we will use the FV scheme to write the equations for averages of $\mathbf{U}$ over the cells C_i, namely for:

$$\mathbf{U}_i(t) = \frac{1}{\Delta x} \int_{C_i} \mathbf{U}(x,t) \ . \tag{2.12}$$

Using (2.2)-(2.3), and following Bermudez et Vazquez [1994]; Brufau *et al.* [2002]; Hubbard et García-Navarro [2000]; Nikolos et Delis [2009], the semi-discrete form of the equations can now be written as:

$$\frac{d}{dt}\mathbf{U}_i = -\frac{1}{\Delta x}\left[\mathbf{F}_{i+\frac{1}{2}} - \mathbf{F}_{i-\frac{1}{2}}\right] + \frac{1}{\Delta x}\Delta\mathbf{S}_{bi} + \overline{\mathbf{\Phi}} \ , \tag{2.13}$$

where $\mathbf{F}_{i\pm\frac{1}{2}}$ and $\Delta\mathbf{S}_{bi}$ are the numerical fluxes at each cell interface and the numerical topography source respectively. The last term is where the link with the elliptic phase is made. In particular, it reads:

$$\overline{\mathbf{\Phi}} = \frac{1}{\Delta x}\int_{C_i}\begin{pmatrix} 0 \\ \phi_{\mathrm{h}} \end{pmatrix} = \frac{1}{8}\begin{pmatrix} 0 \\ \phi_{i-1} + 6\phi_i + \phi_{i+1} \end{pmatrix} \ , \tag{2.14}$$

having integrated exactly over C_i the piecewise linear polynomial ϕ_h obtained from the elliptic phase discussed in the previous section. The numerical fluxes $\mathbf{F}_{i\pm\frac{1}{2}}$ at the cell interfaces can be evaluated by means of an exact or approximate Riemann solver. In this work we used the approximate Riemann solver of Roe [1981] along with an upwind discretization of the topography source Bermudez et Vazquez [1994]. The numerical fluxes in (2.13) are defined as:

$$\begin{aligned}\mathbf{F}_{i+\frac{1}{2}} &= \mathbf{F}_{i+\frac{1}{2}}(\mathbf{U}^L_{i+\frac{1}{2}}, \mathbf{U}^R_{i+\frac{1}{2}}) \;= \\ &= \frac{1}{2}\left(\mathbf{F}(\mathbf{U}^R_{i+\frac{1}{2}}) + \mathbf{F}(\mathbf{U}^L_{i+\frac{1}{2}})\right) - \frac{1}{2}|\mathbf{A}|_{i+\frac{1}{2}}\Delta\mathbf{U}_{i+\frac{1}{2}}\;,\end{aligned} \tag{2.15}$$

where $\Delta(\cdot)_{i+\frac{1}{2}} = (\cdot)^R_{i+\frac{1}{2}} - (\cdot)^L_{i+\frac{1}{2}}$. $\mathbf{A}_{i+\frac{1}{2}}$ is the Roe-averaged Jacobian matrix and is equal to $[\mathbf{X}|\mathbf{\Lambda}|\mathbf{X^{-1}}]_{i+\frac{1}{2}}$, where $\mathbf{X}_{i+\frac{1}{2}}$ and $\mathbf{X}^{-1}_{i+\frac{1}{2}}$ are respectively the left and right eigenvector matrices and $\mathbf{\Lambda}_{i+\frac{1}{2}}$ is the diagonal matrix having the eigenvalues on the main diagonal.

The numerical integration with the upwind scheme presented up to now leads to approximations that are only first order accurate, if a constant distribution is assumed in each computational cell C_i. To achieve higher accuracy we evaluate the left and right states using a third order MUSCL reconstruction scheme (*cf.*Waterson et Deconinck [2007]; Kermani *et al.* [2003]). The reconstruction is performed for the variables $[h,\, u]$ as well as for the topography b. For the $(i+\frac{1}{2})$ interface the reconstructed values of a primitive variable w can be written as:

$$\begin{aligned}w^L_{i+\frac{1}{2}} &= w_i + \frac{\psi(r_i)}{4}\left[(1-\kappa)\Delta w_{i-\frac{1}{2}} + (1+\kappa)\Delta w_{i+\frac{1}{2}}\right]\;, \\ w^R_{i+\frac{1}{2}} &= w_{i+1} - \frac{\psi(r_{i+1})}{4}\left[(1-\kappa)\Delta w_{i+\frac{3}{2}} + (1+\kappa)\Delta w_{i+\frac{1}{2}}\right]\;,\end{aligned} \tag{2.16}$$

where ψ is the limiter function with $r_i = \frac{\Delta h_{i-\frac{1}{2}}}{\Delta h_{i+\frac{1}{2}}}$, and where third order of accuracy in smooth regions is obtained for $\kappa = \frac{1}{3}$. In this work, the widely known MIN-MOD, MC and Van Albada limiter functions are implemented (*cf.* LeVeque [2002]) and used only only in the region of the domain where the NLSW system is solved, *i.e.* the regions where wave breaking is detected. Any other function of the literature can be used, but the study of the influence on the solution is beyond the scopes of this work. The initial Roe scheme may allow non-physical numerical solutions, as expansion shocks (*cf.* Toro [2009]; LeVeque [2002]). The solution to this problem can be achieved by ensuring the numerical solution to respect the so called entropy condition. This problematic, together with the strategy adopted to tackle it, will be discussed in section 2.6.

In the numerical solution, the correct discrete balance between the numerical fluxes and the numerical topography source is very important. A scheme that respects this balance is known in the literature as a well-balanced scheme, while the property is also known as C-property. As it has been shown in Bermudez et Vazquez [1994], an upwind discretization approach should also be used for the bed topography term $\mathbf{S}_b$ to avoid non-physical oscillations in the solution by satisfying the C-property in hydrostatic flow conditions (flow at rest). The choice of a Roe's solver in this work is justified not only by its wide popularity and applicability, but also by the well established numerical treatment of the topography source terms in order to satisfy the C-property, which can be easily incorporated in this solver. To satisfy the exact C-property, the topography source term must be linearized in the same way and evaluated in the same state (Roe-averaged state) as the flux terms and reconstructed as $\partial_x h$. Of course, if an other Riemann solver is employed (*e.g.* HLL, HLLC) for the computation of the numerical fluxes, a different technique should be used, see for example Roeber *et al.* [2010]; Tonelli et Petti [2009]. In this work, following Bermudez et Vazquez [1994]; Hubbard et García-Navarro [2000], the source term in (2.13) contains the following two contributions:

$$\Delta \mathbf{S}_{b,\,i} = \mathbf{S}^{-}_{b,\,i+\frac{1}{2}}(\mathbf{U}^{L}_{i+\frac{1}{2}}, \mathbf{U}^{R}_{i+\frac{1}{2}}) + \mathbf{S}^{+}_{b,\,i-\frac{1}{2}}(\mathbf{U}^{L}_{i-\frac{1}{2}}, \mathbf{U}^{R}_{i-\frac{1}{2}}) \ ,$$

where:

$$\begin{aligned}
\mathbf{S}^{+}_{b\,i+\frac{1}{2}}(\mathbf{U}^{L}_{i+\frac{1}{2}}, \mathbf{U}^{R}_{i+\frac{1}{2}}) &= \frac{1}{2}\Big[\mathbf{X}(\mathbf{I} + \mathbf{\Lambda}^{-1}|\mathbf{\Lambda}|)\mathbf{X}^{-1}\Big]_{i+\frac{1}{2}} \widetilde{\mathbf{S}}_{b\,i+\frac{1}{2}}(\mathbf{U}^{L}_{i+\frac{1}{2}}, \mathbf{U}^{R}_{i+\frac{1}{2}}) \ , \\
\mathbf{S}^{-}_{b\,i+\frac{1}{2}}(\mathbf{U}^{L}_{i+\frac{1}{2}}, \mathbf{U}^{R}_{i+\frac{1}{2}}) &= \frac{1}{2}\Big[\mathbf{X}(\mathbf{I} - \mathbf{\Lambda}^{-1}|\mathbf{\Lambda}|)\mathbf{X}^{-1}\Big]_{i+\frac{1}{2}} \widetilde{\mathbf{S}}_{b\,i+\frac{1}{2}}(\mathbf{U}^{L}_{i+\frac{1}{2}}, \mathbf{U}^{R}_{i+\frac{1}{2}}) \ ,
\end{aligned} \tag{2.17}$$

and with:

$$\widetilde{\mathbf{S}}_{b\,i+\frac{1}{2}}(\mathbf{U}^{L}_{i+\frac{1}{2}}, \mathbf{U}^{R}_{i+\frac{1}{2}}) = \begin{bmatrix} 0 \\ -g\dfrac{h^L + h^R}{2}\left(b^R - b^L\right) \end{bmatrix}_{i+\frac{1}{2}} .$$

For the first order scheme, using the relation above, the discretization of the numerical flux term balances with the one of the topography source term for hydrostatic conditions. This gives in each mesh cell: $u = 0$ and $b^R - b^L = -\left(h^R - h^L\right)$. While this holds for the first order scheme, this is not the case when using higher reconstructions as we do here. In this case, following Hubbard et García-Navarro [2000]; Nikolos et Delis [2009], we include the additional correction term $\mathbf{S}^{\star}_{b}$ for maintaining the correct balance i.e.:

$$\Delta \mathbf{S}_{b\,i} = \mathbf{S}^{-}_{b\,i+\frac{1}{2}} + \mathbf{S}^{+}_{b\,i-\frac{1}{2}} + \mathbf{S}^{\star}_{b}\left(\mathbf{U}^{L}_{i+\frac{1}{2}}, \mathbf{U}^{R}_{i-\frac{1}{2}}\right) \ ,$$

with:

$$\mathbf{S}_b^\star\left(\mathbf{U}_{i+\frac{1}{2}}^L, \mathbf{U}_{i-\frac{1}{2}}^R\right) = \begin{bmatrix} 0 \\ -g\dfrac{h_{i-\frac{1}{2}}^R + h_{i+\frac{1}{2}}^L}{2}\left(b_{i-\frac{1}{2}}^R - b_{i+\frac{1}{2}}^L\right) \end{bmatrix}.$$

2.4 Hyperbolic phase: Upwind Stabilized Finite Element Scheme

2.4.1 Continuous Galerkin approximation:

Two FE methods are considered here. The first is a classical C^0 Galerkin approximation of the two equations (2.3). For an internal node i, the discrete continuous Galerkin (cG) equations are readily obtained by evaluating the integrals of the weak formulation:

$$\begin{aligned} \int_{\Omega_\mathrm{h}} \varphi_i\, \partial_t h_\mathrm{h} - \int_{\Omega_\mathrm{h}} \partial_x \varphi_i\, q_\mathrm{h} = 0 \\ \int_{\Omega_\mathrm{h}} \varphi_i\, \partial_t q_\mathrm{h} - \int_{\Omega_\mathrm{h}} \partial_x \varphi_i \left[\frac{q_\mathrm{h}^2}{h_\mathrm{h}} + g\frac{h_\mathrm{h}^2}{2}\right] - \int_{\Omega_\mathrm{h}} \varphi_i\, \tilde{S}_b - \int_{\Omega_\mathrm{h}} \varphi_i\, \phi_\mathrm{h} = 0\ , \end{aligned} \tag{2.18}$$

with $q_{\mathrm{h},i} = (h_\mathrm{h} u_\mathrm{h})_i$ and $\tilde{S}_b = -gh\partial_x b$.
With the notation of the previous section, the integrals can be approximated as in Ricchiuto et Filippini [2014]:

$$\mathbf{M}^\mathrm{G}\frac{d}{dt}\mathbf{U} = -\frac{1}{2}\left[\mathbf{F}(\mathbf{U}_{i+1}) - \mathbf{F}(\mathbf{U}_{i-1})\right] + \frac{1}{2}\tilde{\mathbf{S}}_{b\,i+\frac{1}{2}} + \frac{1}{2}\tilde{\mathbf{S}}_{b\,i-\frac{1}{2}} + \overline{\mathbf{\Phi}}^\mathrm{G}\ , \tag{2.19}$$

where $\mathbf{M}^\mathrm{G}$ is the Galerkin mass matrix defined in (2.7).
By analogy with (2.13), we use the notation $\overline{\mathbf{\Phi}}$ for the contribution of the non-hydrostatic terms, which in this case is given by:

$$\overline{\mathbf{\Phi}}^\mathrm{G} = \mathbf{M}^\mathrm{G}\mathbf{\Phi}\ . \tag{2.20}$$

As shown in section 2.7.1, scheme (2.19) is fourth order accurate in space on constant Δx meshes, when the shallow water limit is considered.

2.4.2 Stabilized Upwind discretization:

Scheme (2.19) is a centered approximations of the equations and is not well suited for the discretization of the shallow water limit for which some form of

upwinding is necessary to stabilize the system, or to provide positivity corrections in correspondence of moving shorelines and discontinuities (*cf.* Ricchiuto *et al.* [2007]; Ricchiuto et Bollermann [2009]). We thus consider the upwind stabilized method proposed in Ricchiuto et Filippini [2014], Bacigaluppi *et al.* [2014a,b] (see also Hughes *et al.* [2010]). We start by rewriting scheme (2.18) with the short-notation:

$$\mathcal{R}_i^{\mathrm{cG}}(\eta_{\mathrm{h}}, q_{\mathrm{h}}) = 0 \ , \tag{2.21}$$

with $\mathcal{R}_i^{\mathrm{cG}}(\eta, q)$ the array whose components are the left hand sides of the first two equations in (2.18). In order to construct an upwinding operator, we consider now the quasi-linear form of the NLSW equations which can be recast as:

$$\partial_t \begin{pmatrix} \eta \\ q \end{pmatrix} + A \partial_x \begin{pmatrix} \eta \\ q \end{pmatrix} = 0 \ , \quad A = \begin{pmatrix} 0 & 1 \\ c^2 - u^2 & 2u \end{pmatrix} \ ,$$

where $c^2 = g h_0$ is the NLSW celerity (1.61). We recall that matrix A admits a full set of real linearly independent eigenvectors, associated to the two eigenvalues $u \pm c$. Following the SUPG stabilization technique (*cf.* Hughes et Brook [1982]; Hughes *et al.* [2010]; Ricchiuto et Bollermann [2009]; Abgrall [2006]), we define the *stabilized* variant of the continuous Galerkin (2.18) as:

$$\mathcal{R}_i^{\mathrm{cG}}(\eta_{\mathrm{h}}, q_{\mathrm{h}}) + \sum_{\mathrm{K} \in \Omega_h} \int_{\mathrm{K}} A \, \partial_x \varphi_i \, \tau_{\mathrm{K}} \, \mathbf{R}_{\mathrm{h}} = 0 \ , \tag{2.22}$$

where the matrix τ_{K} is the so-called SUPG stabilization parameter, and having denoted by $\mathbf{R}_{\mathrm{h}}$ the local residual value of the eGN equations:

$$\mathbf{R}_{\mathrm{h}} = \begin{pmatrix} \partial_t h_{\mathrm{h}} + \partial_x q_{\mathrm{h}} \\ \partial_t q_{\mathrm{h}} + \partial_x (q_{\mathrm{h}}^2 / h_{\mathrm{h}} + g h_{\mathrm{h}}^2 / 2) - \tilde{S}_b - \phi_{\mathrm{h}} \end{pmatrix} \ , \tag{2.23}$$

obtained by replacing in the continuous equations the discrete approximation of the unknowns. We employ here the definition of the SUPG stabilization parameter allowing to recover the upwind discretization of a first order hyperbolic operator (see *e.g.* Barth [1998]; Deconinck *et al.* [2003] and references therein), namely:

$$\tau_{\mathrm{SU}} = \frac{1}{\sum\limits_{j \in \mathrm{K}} |\partial_x \varphi_j^K|} |A^{\mathrm{K}}|^{-1} \ , \tag{2.24}$$

which in the 1D case becomes, in practice, $\tau_{\mathrm{SU}} = \frac{\Delta x}{2} |A|^{-1}$, with the absolute value $|A|$ computed by means of standard eigenvalue decomposition.
Using the notation of (2.19), the streamline upwind scheme, thus, reads:

$$\mathbf{M}^{\mathrm{G}}\frac{d}{dt}\mathbf{U} = -\frac{1}{2}\left[\mathbf{F}(\mathbf{U}_{i+1}) - \mathbf{F}(\mathbf{U}_{i-1})\right] + \frac{1}{2}\tilde{\mathbf{S}}_{b\,i+\frac{1}{2}} + \frac{1}{2}\tilde{\mathbf{S}}_{b\,i-\frac{1}{2}} + \overline{\mathbf{\Phi}}^{\mathrm{G}} + \\ - \sum_{j=0}^{1}\int_{x_{i+j-1}}^{x_{i+j}} A\,\partial_x\varphi_i\,\tau_{\mathrm{SU}}\,\mathbf{R}_{\Delta x}\ . \tag{2.25}$$

Using definitions (2.23)-(2.24) and the notation of the previous section, the following form can be derived:

$$\mathbf{M}^{\mathrm{SU}}\frac{d}{dt}\mathbf{U} = -\left[\mathbf{F}_{i+\frac{1}{2}}(\mathbf{U}_i,\mathbf{U}_{i+1}) - \mathbf{F}_{i+\frac{1}{2}}(\mathbf{U}_{i-1},\mathbf{U}_i)\right] + \mathbf{S}^{-}_{b\,i+\frac{1}{2}}(\mathbf{U}_i,\mathbf{U}_{i+1}) + \\ + \mathbf{S}^{+}_{b\,i-\frac{1}{2}}(\mathbf{U}_{i-1},\mathbf{U}_i) + \overline{\mathbf{\Phi}}^{\mathrm{SU}}\ , \tag{2.26}$$

where the numerical fluxes and sources have exactly the same expression as in (2.15) and (2.17) respectively, and where the entries of the Streamline Upwind mass matrix now couple the h and q ODEs and depend on the sign of the shallow water flux Jacobian matrix A. In particular:

$$\left[\mathbf{M}^{\mathrm{SU}}(\cdot)\right]_i = \frac{\Delta x}{6}(\cdot)_{i-1} + \frac{2\Delta x}{3}(\cdot)_i + \frac{\Delta x}{6}(\cdot)_{i+1} + \\ + \frac{\Delta x}{4}\mathrm{sign}(A_{i-\frac{1}{2}})\Big((\cdot)_{i-1} + (\cdot)_i\Big) + \\ - \frac{\Delta x}{4}\mathrm{sign}(A_{i+\frac{1}{2}})\Big((\cdot)_{i+1} + (\cdot)_i\Big)\ . \tag{2.27}$$

By analogy with (2.13), we have used the notation $\overline{\mathbf{\Phi}}$ for the contribution of the non-hydrostatic terms, which in this case is given by

$$\overline{\mathbf{\Phi}}^{\mathrm{SU}} = \mathbf{M}^{\mathrm{SU}}\mathbf{\Phi}\ .$$

Because of the coupling of the two equations, caused by the Jacobian matrix, $\mathbf{M}^{\mathrm{SU}}(\cdot)$ results in a sparse matrix with a block structrure which corresponds to the connectivity of the mesh. As a consequence of this, the inversion of this matrix is performed using the ITSOLVE routine ILUT of `SPARSEKIT` (*cf.* Saad [1996]), which uses a preconditioned GMRES algorithm.
As it will be shown later on, the stabilized FE method (2.26) is third order accurate in space when the shallow water limit is considered for constant Δx, and it preserves exactly steady state still flat free surface states, we refer to Ricchiuto et Filippini [2014]; Bacigaluppi *et al.* [2014a,b] for all additional details.

2.4.3 Shock capturing finite element method:

Let us consider again, in this paragraph, the scalar advection equation (1.35). Imagine to have applied our numerical discretization of the PDE and to have now to deal with the linear system:

$$\mathbf{A}\mathbf{U}^{n+1} = \mathbf{B}\mathbf{U}^{n} \ .$$

Consider the case in which the data at time t^n are given by a discontinuity between u_r and u_l, so that $u_r \leq u_i^n \leq u_l \quad \forall i$. We are interested in preserving this condition, in particular in being able to compute $u_r \leq u_i^{n+1} \leq u_l \quad \forall i$ as well. A sufficient condition for this to be true is that the following conditions are simultaneously verified (*cf.* Berman et Plemmons [1979]):

- $B_{ij} \geq 0$,
- $A_{ii} > 0 \quad \text{and} \quad A_{ij} \leq 0$,
- $|A_{ii}| > \sum_{j \neq i} |A_{ij}|$ at least for one i (irreducibly diagonally dominant) .

The first condition is easily satisfied, as the right hand side of the SUPG scheme is the same as that of the first order Roe scheme, which can be guaranteed positive coefficient (or also TVD as *cf.* Harten [1983]; Barth et M. [2004]) under a Δt restriction. The second and third conditions guarantee that $A_{ij}^{-1} \geq 0$, allowing to prove the required bounds on U^{n+1}. In the case of the SUPG scheme, this can be obtained at discontinuities by modifying the method discussed in the previous paragraph by locally introducing a lumping of the mass matrix $\mathbf{M}^{\mathrm{SU}}$, wherever discontinuities occur (*cf.* Bacigaluppi *et al.* [2014a,b]). Handling moving bores and dry areas will thus be possible, by introducing the following nonlinear splitting of the mass matrix ("sc" stands for shock capturing):

$$\begin{aligned}\left[\mathbf{M}^{\text{SU-sc}}(\cdot)\right]_i = \Delta x(\cdot)_i &+ \psi_{i+\frac{1}{2}}\frac{\Delta x}{2}\left[\frac{1}{3}\Big((\cdot)_{i+1} - (\cdot)_i\Big) - \frac{\operatorname{sign}(A_{i+\frac{1}{2}})}{2}\Big((\cdot)_{i+1} + (\cdot)_i\Big)\right] \\ &+ \psi_{i-\frac{1}{2}}\frac{\Delta x}{2}\left[\frac{1}{3}\Big((\cdot)_{i-1} - (\cdot)_i\Big) + \frac{\operatorname{sign}(A_{i-\frac{1}{2}})}{2}\Big((\cdot)_{i-1} + (\cdot)_i\Big)\right] \ .\end{aligned} \tag{2.28}$$

The quantity $\psi_{i\pm\frac{1}{2}}$ in (2.28) is a limiter function.
For $\psi = 0$ the lumping of the matrix is activated and the scheme reduces

to the first order version of Roe's scheme, which is basically the first order version of (2.13). This scheme shows a monotonicity preserving behaviour, also preserving the non-negativity of the depth in flooding areas. Moreover, the lumping of the mass matrix on the Galerkin scheme, in case of the chosen P^1 basis function space, introduces a degree of dissipation, but in general it does not imply a reduction of the asymptotic overall accuracy, which remains second order, as it will be shown in section 2.7.1.
For $\psi = 1$ the third order finite element method (2.26) is recovered. Any function can be used to detect smooth areas and dry or shocked regions. Here, we use the smoothness sensor proposed in Bacigaluppi *et al.* [2014a,b] and based on two different approximation of the curvature of the free surface elevation η:

$$\psi_{i+\frac{1}{2}} = \min(\psi_i, \psi_{i+1}) \,, \qquad \psi_i = \min\left(1,\, \alpha \frac{|\int_\Omega \varphi_i \partial_x \eta_\mathrm{h}|}{|\int_\Omega \partial_x \varphi_i \partial_x \eta_\mathrm{h} + V_i|}\right) \tag{2.29}$$

where V_i is obtained as the fourth order finite difference approximation of $\partial_{xx}\eta_i$, and with $\alpha = \frac{1}{9}$ as in the cited references.

The final form of the scheme, thus, reads:

$$\begin{aligned} \mathbf{M}^{\text{SU-sc}} \frac{d}{dt}\mathbf{U} = &- \left[\mathbf{F}_{i+1/2}(\mathbf{U}_i, \mathbf{U}_{i+1}) - \mathbf{F}_{i+1/2}(\mathbf{U}_{i-1}, \mathbf{U}_i)\right] + \mathbf{S}^-_{b\,i+1/2}(\mathbf{U}_i, \mathbf{U}_{i+1}) + \\ &+ \mathbf{S}^+_{b\,i-1/2}(\mathbf{U}_{i-1}, \mathbf{U}_i) + \overline{\mathbf{\Phi}}^{\text{SU-sc}} \,, \end{aligned} \tag{2.30}$$

where, again, we have made use of the following notation for the non-hydrostatic contribution term:

$$\overline{\mathbf{\Phi}}^{\text{SU-sc}} = \mathbf{M}^{\text{SU-sc}} \mathbf{\Phi} \,.$$

Note that the hybrid technique for the wave breaking treatment, which is the one used in this work, consists in solving smooth wave profiles with the Boussinesq equations, reverting to the NLSW system only when breaking waves are detected. The use of the limiter is thus only active in the region of the domain where the Shallow Water equations are solved, namely the breaking region. Anywhere else, in the Green-Naghdi region, $\psi = 1$ and the third order scheme (2.26).

2.5 Wetting/drying and Mass conservation

In order to treat dry cells we use the technique described in Ricchiuto et Bollermann [2009] and Ricchiuto [2015]. In particular, we introduce two threshold

parameters ϵ_h^{wd} and ϵ_u^{wd}, acting independently on the water height and the velocity respectively. So, if h in a node is less that ϵ_h^{wd}, that node is considered as dry. This parameter is very small, compared to the mesh size (typical values range are between $10^{-9} \div 10^{-6}$). The second parameter is used to avoid division by zero, especially when the velocity values are recovered from q, and is set to:

$$\epsilon_u^{wd} = \frac{\Delta x^2}{L^2} \ ,$$

with L the length of the spatial domain. If in a node $h \leq \epsilon_u^{wd}$, the velocity is set to zero in that node. To avoid loosing mass from this procedure, and guarantee an absolute mass conservation, we follow the treatments proposed in Delis *et al.* [2011]; Brufau *et al.* [2004] and Liang et Borthwick [2009], where the total mass in nodes with $h \leq \epsilon_u^{wd}$ is redistributed uniformly to the rest of the domain.

In the previous section 2.3 we have already spoken about the C-property of a model. The goal is to ensure that the flux and source terms in the upwind are numerically balanced, such to preserve exactly the steady state lake at rest solution (corresponding to $u = 0$ and $\eta = 0$ everywhere) also in presence of bathymetry variations and dry areas. In particular, the presence of dry areas may generate spurious numerical waves, as illustrated in Castro *et al.* [2005]; Kazolea et Delis [2013]; Ricchiuto et Bollermann [2009]. In this case, it is of primary importance to ensure that $\Delta\eta$ is seen to be zero at the dry front. As the value of $\eta = h - h_0 + b$ in the first dry node only depends on the bathymetry, this is not necessarily the case, and an artificial hydrostatic force may be experienced by the scheme, which can induce oscillations or spurious mass flow. To ensure this property, we use a standard technique consisting in redefining the bed elevation at the emerging dry cell (*cf.* Brufau *et al.* [2002, 2004] as:

$$\Delta b = \begin{cases} h^L & \text{if } h^L > \epsilon_h^{wd} \text{ and } h^R \leq \epsilon_h^{wd} \text{ and } b^R < (b^R - b^L) \ , \\ (b^L - b^R) & \text{otherwise} \ , \end{cases} \tag{2.31}$$

when a wet/dry front exists between computational cells with (reconstructed) face values L and R. For both FV and FE schemes this modification is applied in the computation of the source term $\tilde{\mathbf{S}}_b$. A similar treatment holds if R is wet and L dry.
Just for the FV scheme, further modifications have to be done. The higher order MUSCL reconstruction (2.16) is switched off on the wet/dry interface and a first order approximation of the L and R states is performed instead. Moreover, in order to prevent the simulation to display an unphysical flow in

motion over adverse slopes, following Castro *et al.* [2005] and Kazolea et Delis [2013], we impose at the wet/dry interface the condition below:

$$\begin{aligned} &\text{if:} \quad h^L > \epsilon_h^{wd} \ \text{ and } \ h^R \leq \epsilon_h^{wd} \ \text{ and } \ h^L < (b^R - b^L) \ , \\ &\text{then:} \quad u^L = u^R = 0 \ . \end{aligned}$$

Note that the actual velocity is not zero on the wet cell, but only on assumed as such at the interface when computing the numerical flux and the topography source term contributions.

Finally we use the exponential filter proposed in Ricchiuto et Bollermann [2009] and Ricchiuto [2015] to properly detect regions in proximity of dry areas and to recover there the first order scheme. This exponential function is defined by $f_h = e^{-(\frac{10}{N}y)^2}$, where:

$$y = \frac{h_{MAX} - \epsilon_h}{\max\big(\epsilon_h, (h_{min} - \epsilon_h)\big)} \ ,$$

h_{MAX} is computed as the maximum value of water depth in the whole grid, while h_{min} is the minimum water column on a stencil composed by five nodes in one-dimension.

2.6 Entropy fix

Shock capturing methods, such as the FV and SUPG schemes just discussed in the previous sections, must verify a discrete analogous of the Rankine-Hugoniot jump conditions, so that the proper shock speed and strength are obtained. As deeply documented in the literature (*cf.* Roe [1981]; Harten et Hyman [1983]; Toro [2001]; LeVeque [2002] among the others), the Rankine-Hugoniot conditions do not allow, alone, to define a unique weak solution to the Riemann problem. Unphysical shock may, in fact, appear in the expansion region, typically when sonic conditions are reached. In order to find the physically correct solution to the problem, it is generally invoke the concept of entropy conditions, by reference to the second law of thermodynamics. Expansion shocks, in fact, violate the principle which impose the entropy to increase across a shock, and can thus considered as non admissible solutions. The numerical schemes must, thus, be modified in order to account for the only weak solution satisfying the entropy condition; such modification is known as entropy fix. The first proposals for such an entropy fix were put forward in the by Harten et Hyman [1983]. Their approach is quite general: the entropy fix is considered as a means to guarantee that the numerical scheme produces the entropic solution to the hyperbolic problem, defined as the limit of the solution of the

corresponding viscous problem, when the viscosity and the thermal conductivity vanish (vanishing viscosity solution).This can be accomplished by writing the upwind scheme so as to put into evidence its numerical dissipation matrix, and by operating on this matrix to assure a non-zero viscous contribution to the numerical flux.
This viewpoint is not limited to the approximate Riemann solver formulated by Roe, but may be applied to any method written in dissipation form Harten et Hyman [1983]. In our case the absolute value of the Jacobian matrix $|A|$ can be seen as a matrix viscosity. Harten's entropy correction consists in preventing the eigenvalues of this matrix from becoming too small or to vanish. This will allow the discontinuity to be correctly dissipated by the scheme.
In each cell $[a, b]$ of the computational domain, we compute the eigenvalues of the shallow water system: $\bar{\lambda}_{1,2} = \bar{u} \mp \bar{c}$, using the average quantities on the cell:

$$\bar{h} = \frac{h_{i+1} + h_i}{2} \ , \quad \bar{u} = \frac{q_{i+1} + q_i}{h_{i+1} + h_i} \ , \quad \bar{c} = \sqrt{g\bar{h}} \ .$$

The eigenvalues are also computed in the two nodes of the cell, giving $\lambda_{1,2a} = u_a \mp c_a$ and $\lambda_{1,2b} = u_b \mp c_b$. Than, considering the spectral decomposition of the absolute value of the local Jacobian matrix $|A| = R|\Lambda|L$, the eigenvalues matrix $|\Lambda|$ is modified as follows:

$$\Lambda = \begin{bmatrix} \bar{\lambda}_1/v_1 & 0 \\ 0 & \bar{\lambda}_2/v_2 \end{bmatrix} \ ,$$

where $v_{1,2}$ are defined follow Harten et Hyman [1983]:

$$v_{1,2} = \begin{cases} |\bar{\lambda}_{1,2}| & \text{if} \quad |\bar{\lambda}_{1,2}| \geq \epsilon_{1,2} \ , \\ \dfrac{\bar{\lambda}_{1,2}^2}{2\epsilon_{1,2}} + \dfrac{\epsilon_{1,2}}{2} & \text{otherwise} \ , \end{cases}$$

and where the $\epsilon_{1,2}$ are small positve numbers defined by:

$$\epsilon_{1,2} = \frac{1}{2}\max\big(0, \max(\lambda_{1,2a} - \lambda_{1,2b}, \lambda_{1,2b} - \lambda_{1,2a})\big) \tag{2.32}$$

Both the FV and SUPG schemes discussed in sections 2.3 and 2.4.2 share the same Jacobian matrix for the computation of the upwind term. The entropy fix procedure just described is thus applied to both the schemes and tested against Riemann problem cases in section 3.2. The results of the tests performed assess the valdity of the procedure applied.

2.7 Time continuous error analysis

In this section we present a truncation and dispersion error analysis of the schemes introduced. While it is natural to consider the linearized system (1.124) for the dispersion analysis, for simplicity we will consider equations (1.124) for the truncation error as well. The analysis is time-continuous, meaning that we do not take into account time integration, thus allowing to better underline differences between the space discretizations considered. In particular, we will study five different schemes: the three described in sections 2.3 and 2.4, plus the second (FD2) and fourth (FD4) order centered finite difference schemes, used as references for comparison.

Following the work done in Walkley [1999]; Walkley et Berzins [2002]; Eskilsson et Sherwin [2003], we consider the finite difference form of all the schemes and we analyze it with respect to its truncation and dispersion errors. Clearly, this approach is not the standard one for finite element and residual distribution (*cf.* Burman [2010]; Hartmann et Houston [2009]; Abgrall et Roe [2003]; Deconinck et Ricchiuto [2007]); it is only suited in one space dimension and its results cannot be generalized to the multidimensional case, especially on irregular meshes. It does however provide a very good indication of the potential of the schemes, especially when structured, or mildly unstructured, grids can be used in two dimensions.

Equivalent finite difference equations: The expressions obtained when discretizing (1.124) are quite long and reporting them in the body of the manuscript might lead to useless excessive length. The full discrete equations are thus reported in appendix A (equations (A.1), (A.2), (A.3), (A.4), and (A.5) for the FD2, FD4, cG, SUPG and FV schemes respectively). We limit ourselves to a few observations which can be made.

By only considering the discrete form of the FD2 and cG schemes, reported here after:

- FD2:

$$\begin{aligned}
&\frac{d\eta_i}{dt} + \frac{h_0}{2\Delta x}\left(u_{i+1} - u_{i-1}\right) = 0 \ , \\
&\frac{du_i}{dt} + \frac{g}{2\Delta x}\left(\eta_{i+1} - \eta_{i-1}\right) - \frac{\phi_i}{h_0} = 0 \ , \\
&\phi_i - \frac{\alpha h_0^2}{3\Delta x^2}\left(\phi_{i+1} - 2\phi_i + \phi_{i-1}\right) = \\
&\qquad\qquad = \frac{g h_0^3}{6\Delta x^3}\left(-\eta_{i+2} + 2\eta_{i+1} - 2\eta_{i-1} + \eta_{i-2}\right) \ ;
\end{aligned} \tag{2.33}$$

- cG:

$$\begin{aligned}
&\frac{\Delta x}{6}\left(\frac{d\eta_{i+1}}{dt} + 4\frac{d\eta_i}{dt} + \frac{d\eta_{i-1}}{dt}\right) + \frac{h_0}{2}\left(u_{i+1} - u_{i-1}\right) = 0 \ , \\
&\frac{\Delta x}{6}\left(\frac{du_{i+1}}{dt} + 4\frac{du_i}{dt} + \frac{du_{i-1}}{dt}\right) + \frac{g}{2}\left(\eta_{i+1} - \eta_{i-1}\right) \ + \\
&\qquad\qquad - \frac{\Delta x}{6h_0}\left(\phi_{i+1} + 4\phi_i + \phi_{i-1}\right) = 0 \ , \\
&\frac{\Delta x}{6}\left(\phi_{i+1} + 4\phi_i + \phi_{i-1}\right) - \frac{\alpha h_0^2}{3\Delta x}\left(\phi_{i+1} - 2\phi_i + \phi_{i-1}\right) = \\
&\qquad\qquad = \frac{g h_0^3}{6\Delta x^2}\left(-\eta_{i+2} + 2\eta_{i+1} - 2\eta_{i-1} + \eta_{i-2}\right) \ .
\end{aligned} \tag{2.34}$$

It can be observed that the same second order accurate discretization of the hyperbolic fluxes, and of the dissipative and dispersive terms of the elliptic equation, is provided by the FD2 and cG schemes. Concerning the remaining terms of the equations, the FD2 scheme provides a pointwise approximation of the quantities $(\cdot)_i$, while the cG scheme yields a coupling of neighboring nodes via the mass matrices:

$$\frac{1}{6}(\cdot)_{i+1} + \frac{2}{3}(\cdot)_i + \frac{1}{6}(\cdot)_{i-1} \ .$$

The two schemes are otherwise identical. In particular scheme (2.33) can be recovered from (2.34) by simply lumping all the mass matrices.
In addition, we remark that for the FV and SUPG schemes, expression (A.5) and (A.4) respectively, although the upwind stabilization techniques are applied on the hyperbolic part of system (2.2)-(2.3), the elliptic one still remain discretized by means of the centered Continuous Galerkin discretization, namely the third equation of (2.34), in accordance with the solution strategy proposed in section 2.1.

2.7.1 Truncation Error Analysis

The procedure to compute the truncation errors for the schemes in appendix A requires lenghty calculations, here we just report the leading order expressions. We make use, in this section, of the notation $\partial_{(\cdot)^n}$ to indicate the derivative of order n with respect to $(\cdot)$; $c^2 = gh_0$ denotes the square of the linearized Shallow Water celerity (*cf.* (1.61)).

Elliptic phase: Here we report the leading order expressions of the truncation errors of the schemes concerning the discretization of the elliptic part of the system (*cf.* equation (2.2)):

$$\mathrm{TE}^{\phi}_{FD2} = -\frac{\Delta x^2}{4}\partial_{x^2}\left(-\frac{\alpha h_0^2}{9}\partial_{x^2}\phi_i + \frac{g h_0^3}{3}\partial_{x^3}\eta_i\right) + \mathscr{O}(\Delta x^4)\ , \tag{2.35}$$

$$\mathrm{TE}^{\phi}_{FD4} = -\frac{\Delta x^4}{90}\partial_{x^4}\left(\frac{\alpha h_0^2}{3}\partial_{x^2}\phi_i + \frac{7 g h_0^3}{4}\partial_{x^3}\eta_i\right) + \mathscr{O}(\Delta x^6)\ , \tag{2.36}$$

$$\mathrm{TE}^{\phi}_{cG_{ML}} = -\frac{\Delta x^2}{12}\partial_{x^2}\left(-\frac{\alpha h_0^2}{3}\,\partial_{x^2}\phi_i + g h_0^3\,\partial_{x^3}\eta_i\right) + \mathscr{O}(\Delta x^4)\ , \tag{2.37}$$

$$\mathrm{TE}^{\phi}_{cG} = -\frac{\Delta x^2}{12}\partial_{x^2}\left(\left(1 - \frac{\alpha h_0^2}{3}\right)\partial_{x^2}\phi_i + \frac{5 g h_0^3}{3}\,\partial_{x^3}\eta_i\right) + \mathscr{O}(\Delta x^4)\ . \tag{2.38}$$

For the cG scheme proposed in section 2.2, we report the two expressions when the two mass matrices appearing in equations (2.2) and (2.10) are lumped $\mathrm{TE}^{\phi}_{cG_{ML}}$, or not TE^{ϕ}_{cG}. It can be observed, in this way that mass lumping does not change the accuracy of the scheme which remains of $\mathscr{O}(\Delta x^2)$, while instead affecting the linear dispersion of the scheme, as it will be explored in detail in section 2.7.2.

Hyperbolic phase: In this paragraph we report the leading order terms of the truncation errors of the discretization of the hyperbolic step. We compare here the expressions for the three schemes proposed to the ones obtained using the FD2 and FD4 schemes:

- FD2 scheme:

$$\begin{aligned}
\mathrm{TE}^{\eta}_{FD2} &= -\frac{h_0 \Delta x^2}{6}\partial_{x^2}\Big(\partial_x u_i\Big) + \mathscr{O}(\Delta x^4)\ , \\
\mathrm{TE}^{u}_{FD2} &= -\frac{g \Delta x^2}{6}\partial_{x^2}\Big(\partial_x \eta_i\Big) + \mathscr{O}(\Delta x^4)\ ;
\end{aligned} \tag{2.39}$$

- FD4 scheme:

$$\begin{aligned} \mathrm{TE}^{\eta}_{FD4} &= \frac{h_0 \Delta x^4}{30} \partial_{x^4} \Big(\partial_x u_i \Big) + \mathscr{O}(\Delta x^6) \ , \\ \mathrm{TE}^{u}_{FD4} &= \frac{g \Delta x^4}{30} \partial_{x^4} \Big(\partial_x \eta_i \Big) + \mathscr{O}(\Delta x^6) \ ; \end{aligned} \tag{2.40}$$

- cG scheme:

$$\begin{aligned} \mathrm{TE}^{\eta}_{cG} &= \frac{\Delta x^4}{24} \partial_{x^4} \left(\frac{2}{15} \, h_0 \, \partial_x u_i \right) + \mathscr{O}(\Delta x^6) \ , \\ \mathrm{TE}^{u}_{cG} &= \frac{\Delta x^4}{24} \partial_{x^4} \left(\frac{2}{15} \, g \, \partial_x \eta_i \right) + \mathscr{O}(\Delta x^6) \ ; \end{aligned} \tag{2.41}$$

- FV scheme:

$$\begin{aligned} \mathrm{TE}^{\eta}_{FV} &= -\frac{c \Delta x^3}{12} \partial_{x^3} \Big(\partial_x \eta_i \Big) + \mathscr{O}(\Delta x^4) \ , \\ \mathrm{TE}^{u}_{FV} &= -\frac{c \Delta x^3}{12} \partial_{x^3} \Big(\partial_x u_i \Big) + \mathscr{O}(\Delta x^4) \ ; \end{aligned} \tag{2.42}$$

- SUPG scheme:

$$\begin{aligned} \mathrm{TE}^{\eta}_{SUPG} &= -\frac{c \Delta x^3}{12 g} \partial_{x^3} \left(\frac{g}{2} \partial_x \eta_i \right) + \mathscr{O}(\Delta x^4) \ , \\ \mathrm{TE}^{u}_{SUPG} &= -\frac{g \Delta x^3}{12 c} \partial_{x^3} \left(\frac{h_0}{2} \partial_x u_i \right) + \mathscr{O}(\Delta x^4) \ ; \end{aligned} \tag{2.43}$$

A first remark must be done concerning the form of the leading errors just presented. These formulae have been obtained in the classical way by substituting the standard Taylor series expansions in space into equations (A.1), (A.2), (A.3), (A.4), and (A.5). In the procedure we have, thus, considered the exact solution of the term ϕ_i / h_0 in the momentum equations, given by $\phi_i / h_0 = \partial_t u_i + g \partial_x \eta_i$. It should be, thus, not surprising to observe a complete fourth order of accuracy for the cG scheme and a third order one for the FV and SUPG schemes. In fact, the classic results of the literature concerning the leading truncation errors of these schemes (*cf.* Ricchiuto et Filippini [2014]) are recovered by considering that, numerically, the complete coupling of the

three equations will provide a perturbed value of ϕ_i with an $\mathcal{O}(\Delta x^2)$, which may be propagate also in the solution of the hyperbolic system.
After this specification, we can now compare the above expressions, making the following remarks. Concerning the two equations of the hyperbolic system, all the schemes provide higher consistency order with respect to the FD2 scheme. In particular, the FD4 and cG schemes are fourth order accurate in space on constant Δ_x meshes, while SUPG and FV provides an $\mathcal{O}(\Delta x^3)$ approximation of the equations. This, while well known for the FD4 and cG scheme, is an interesting result for the SUPG.
In particular, looking at the form of the truncation error, we can try to guess what the dispersion error of the schemes might be. Indeed, the FD2 scheme contains, in the leading $\mathcal{O}(\Delta x^2)$ truncation error term, third order derivatives which will affect its dispersion relation significantly. In particular, note that these will be active at the same wavenumbers impacted by the physical dispersion, which is also modelled by third order derivatives. On the contrary the FD4 and cG schemes show a truncation error containing only fifth order derivatives, which allows to guess a very good discrete dispersion relation for these methods. Similar considerations can be done for the errors of the FV and SUPG schemes, which do not contain any third order derivative, similar to those contained in the equations, but only fourth and fifth order terms related to higher order dissipation and dispersion. This allow to anticipate good dispersion relations for these schemes. The qualitative observation just made will be quantitatively verified by means of the explicit study of the dispersion error of the schemes, which is the subject of the next section.

2.7.2 Dispersion Error Analysis

The analytical expression of the linear dispersion relation for the enhanced Green-Naghdi model has been given in section 1.8. As already explained, such relation can be recovered by means of a Fourier analysis on a horizontal bottom, performed on the linearized system of equations:

$$
\begin{aligned}
(I + \alpha T_{LIN})\phi &= T_{LIN}(g h_0 \eta_x) \ , && (2.44)\\
\eta_t + h_0 u_x &= 0 \ , && (2.45)\\
h_0 u_t + g h_0 \eta_x &= \phi \ .
\end{aligned}
$$

where h_0 represents the constant water depth and $T_{LIN}(\cdot) = -\frac{1}{3} h_0^2 (\cdot)_{xx}$.
Having a low dispersion error with respect to the model is of paramount importance for any numerical scheme that wants to be applied to the study of near-shore wave propagation. In this section, we will perform an analysis on the discrete dispersion relations of the schemes implemented: continuous finite

element (with and without the upwind stabilization) and finite volume; comparing them and finding the best possible configuration of the discretization which minimizes the dispersion error. We remark that the following analysis is devoted to the optimization of the schemes with respect to the eGN dispersion relation. An other approach may consist in performing this optimization with respect to the Airy dispersion relation, but the investigation of this aspect is left to future works.
We perform our analysis replacing the nodal values of η and u, in each of the finite difference form of the discretized schemes of appendix A, by a propagating Fourier mode $W_i = W_0 e^{\nu_{\Delta x} t + jkx_i}$; where $\nu_{\Delta x} = \xi_{\Delta x} + j\omega_{\Delta x}$ and $\xi_{\Delta x}$ and $\omega_{\Delta x}$ represents respectively the amplification rate and the phase speed, while k is the wave number of the Fourier mode. The algebraic expression obtained in such a way can be easily rewritten in terms of the nodal value W_i, using relations of the type $W_{i\pm1} = e^{\pm jk\Delta x}$. The resulting system of equations constitutes a complex eigenvalue problem whose solution is the dispersion factor $\nu_{\Delta x}$.
The dispersion formula obtained are hard to interpret, so we have chosen to present the results in the form of comparison plots, in which the dispersion error curves of the model are compared among them and with respect to the ones given by second (FD2) and fourth (FD4) order finite difference discretization schemes. For the sake of brevity and clarity, in the following, we will just present the concluding remarks and we invite the reader to consult appendix B, where it is reported the complete definition of the several quantities involved in the following analysis.

Finite element: When also the hyperbolic part is discretized with the centered Galerkin FE scheme described in (2.19), the system obtained has the finite difference form (A.3). For the nodal values of a Fourier mode this becomes:

$$\left(\tilde{\mathrm{M}}^{\mathrm{G}} - \frac{\alpha h_0^2}{3}\tilde{\mathrm{S}}^{\mathrm{G}}\right)\phi_i = -\frac{g h_0^3}{3}\tilde{\mathrm{T}}^{\mathrm{G}}\left(\tilde{\mathrm{M}}^{\mathrm{G}}\right)^{-1}\eta_i \ , \tag{2.46}$$

$$\begin{aligned} \tilde{\mathrm{M}}^{\mathrm{G}}\nu_{\Delta x}\eta_i + h_0\tilde{\mathrm{F}}^{\mathrm{G}}u_i &= 0 \ , \\ \tilde{\mathrm{M}}^{\mathrm{G}}\nu_{\Delta x}u_i + g\tilde{\mathrm{F}}^{\mathrm{G}}\eta_i &= \frac{1}{h_0}\tilde{\mathrm{M}}^{\mathrm{G}}\phi_i \ . \end{aligned} \tag{2.47}$$

While different expressions are obtained for the second and third equations when other schemes are used in the hyperbolic phase, note that the first one remains the same in all the cases considered in this work. The discrete phase $\omega_{\Delta x}$ is computed by imposing that the above linear system admits a non-trivial solution, and hence that the associated matrix has zero determinant.
As first approach, we compute the error performed by the scheme respect to

the NLSW equations. The discretized NLSW linear system can be recast simply setting $\phi = 0$ in (2.47) and the error is displayed in figure 2.2 through the quantity $|\omega_{Scheme} - \omega_{SW}|/\omega_{SW}$, plotted against the inverse of the number of nodes per wavelength N. The relative errors of the FD2 and FD4 finite difference schemes are also reported as a reference (see appendix B for detailed expressions). For the Shallow Water case, the trends displayed are found to be invariant with respect to the choice of kh_0. This is not surprising, since the phase celerity of the NLSW model (1.61) is independent from the wavenumber k, as discussed in section 1.6. The picture show that the centered Galerkin scheme provides a dispersion error which is better than that of the fourth order finite difference method.

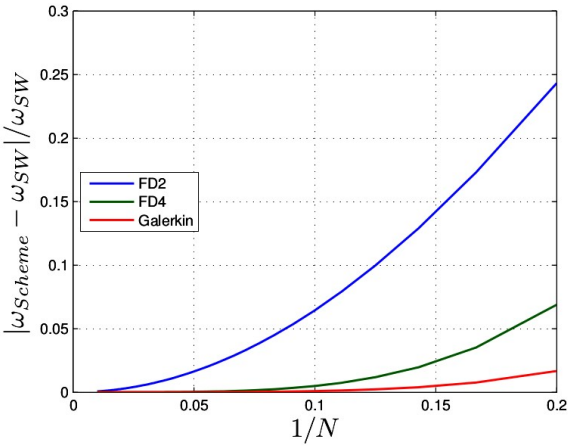

Figure 2.2: Dispersion error for the centered Galerkin FE scheme with respect to the NLSW model (the error is independent from reduced frequency kh_0): comparison with respect to the FD2 and FD4 schemes.

Concerning the eGN system, the results obtained from (2.47) are summarized in figure 2.3. We still consider the relative dispersion error with respect to the exact phase (1.15). The curves are obtained for the two values $kh_0 = 0.5$ and $kh_0 = 2.5$, corresponding to a long and to a short(er) wave (or equivalently to shallow and deep(er) waters) respectively. Also in this case, the pictures show that the centered Galerkin scheme provides a dispersion error which is comparable or better than that of the fourth order finite difference method. Please, note that the value $kh_0 = 2.5$ approaches π, which is considered as the limit between shallow and deep waters for Boussinesq models, due to the estimation of the phase error of the model (*cf.* figure 1.15). Of course, it is more crucial for a numerical scheme to provide a small dispersion error when also the error provided by the model is low.

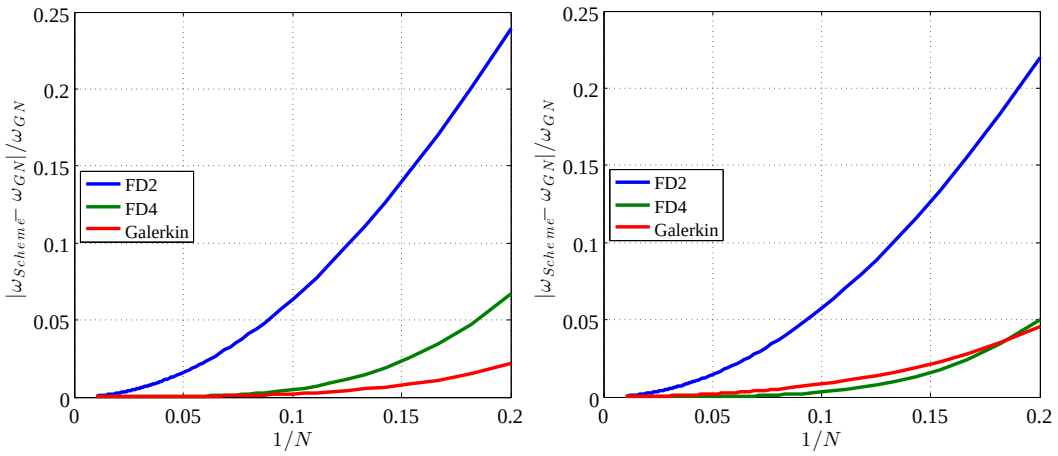

Figure 2.3: Dispersion error for the centered Galerkin FE scheme with respect to the eGN model, for $kh_0 = 0.5$ (left) and $kh_0 = 2.5$ (right): comparison with respect to the FD2 and FD4 schemes.

In section 2.2 we mentioned some implementation choices associated to the finite element solution of the elliptic problem (2.2). These boil down to the type of quadrature used to evaluate some of the integrals, or, in other words, to the use of mass lumping for the mass matrices appearing in equations (2.4), (2.10) and (2.11). The first two, in particular, influence the form of the $\tilde{\Phi}_{LIN}$ injected in the hyperbolic component. The study of the impact of this choice leads to interesting results. Four possibilities exist, for which explicit calculations are provided in the appendix B:

1. mass lumping is performed in both (2.4) and (2.10), in which case the elliptic solver is exactly the same obtained with the FD2 method ;

2. mass lumping is only performed in the computation of the auxiliary variable (2.10), and not in (2.4). In this case, the elliptic system is not identical to the FD2 one, however the third order derivative formula obtained is exactly the same as the one used in FD2 ;

3. no mass lumping is performed for the auxiliary variable (2.10), while (2.4) is lumped. In this case, the elliptic system is the same as the FD2 one, however, its right hand side contains an approximation of the third order derivatives obtained starting from an L^2 projection of the gradients of the free surface ;

4. no mass lumping is performed, leading to the first in (2.46) .

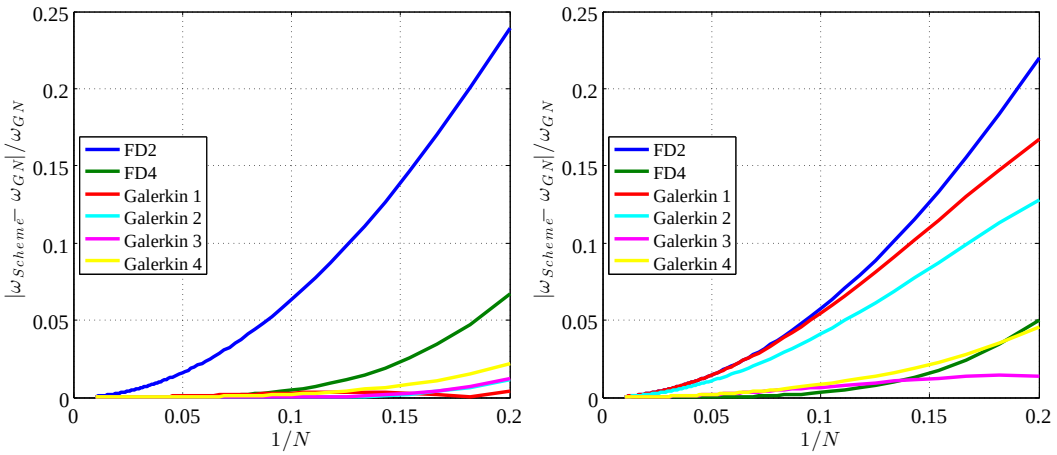

Figure 2.4: Dispersion error of the Galerkin scheme with respect to the eGN model, for $kh_0 = 0.5$ (left) and $kh_0 = 2.5$ (right): impact of lumping strategy.

The differences between these four cases are visualized in figure 2.4 for the continuous Galerkin scheme, showing that in deep waters the first and second configurations provide a considerable increase in error. This clearly means that the most relevant parameter is the approximation of the third order derivative. It appears from the results that the use of an improved approximation of the free surface gradient in the third order derivatives is the key element to reduce the dispersion error. In particular, the configurations 1 and 2 provide errors of the same magnitudes as the FD2 scheme, despite the fact that the hyperbolic phase, and part of the elliptic phase, are not the same. These are precisely the cases in which the approximation of the third order operator is the same as in FD2.

SUPG scheme: We repeat the analysis for the upwind stabilized finite element scheme (SUPG) (A.4). We refer to the appendix B for details and analytical expressions. Please, note that a system similar to (2.46)-(2.47) has to be analyzed and, in particular, that the first equation of this system is exactly the equation (2.46) itself.
We procede, as in the previous case, by first analysing the dispersion error of the scheme with respect to the NLSW model. For this, we set $\phi_i = 0$ inside (A.4), obtaining a trend of the relative phase error (*cf.* figure 2.5), which is close to the one of the Galerkin scheme and still better than that of the fourth order finite difference scheme.

For the eGN model, in figure 2.6 we visualize the impact of the mass lumping strategy on the dispersion error, as done for the non-stabilized method. Also in this case, for short waves/deep waters the largest errors are obtained

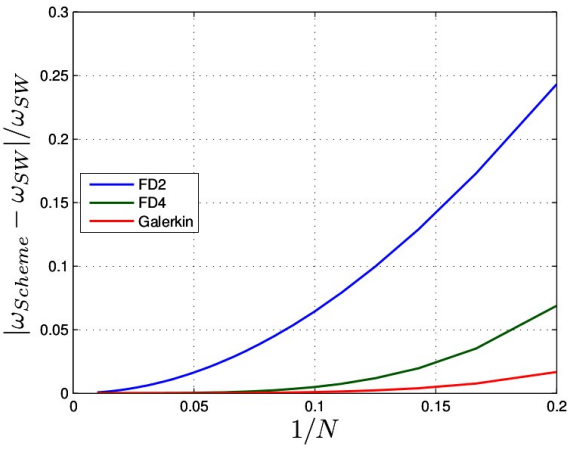

Figure 2.5: Dispersion error for the SUPG scheme with respect to the NLSW model (the error is independent from kh_0): comparison with respect to the FD2, FD4 and GAL schemes.

whenever the third order derivatives are approximated with the simple FD2 formula (cases 1 and 2). In the other two cases, involving an improved treatment of this term, we obtain errors comparable or even smaller than those of the non-stabilized method. Provided that a third order method is used in the hyperbolic phase, we see that dispersion properties equivalent to those of a fourth order method are obtained.

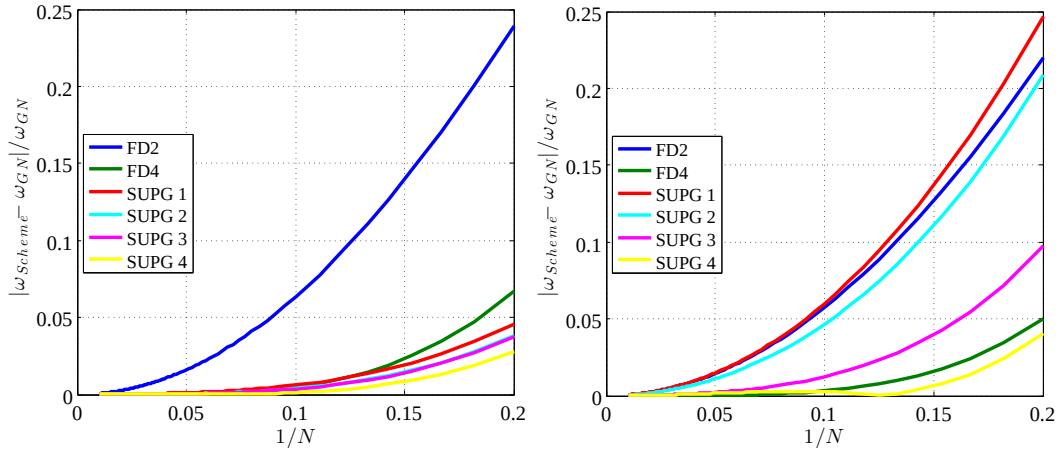

Figure 2.6: Dispersion error of the SUPG scheme for $kh_0 = 0.5$ (left) and the $kh_0 = 2.5$ (right): impact of lumping strategy.

FV scheme: We repeat the exercise for the hybrid Galerkin-FV scheme of section 2.3, whose finite difference form is given in (A.5). In the NLSW case, the error is reported in figure 2.7, compared to those of the other schemes previously analyzed, showing a trend which almost identical to the FD4 one. The main findings concerning the eGN case are, instead, reported in figure 2.8. Once more, the critical element to obtain low errors in deeper waters is the approximation of the third order derivative. The use of the FD2 approximation for this term (cases 1 and 2) provides error levels comparable to those of the FD2 scheme. The improvement in the approximation of the nodal gradient (2.10) leads to a reduction of the error of a factor three or four, providing errors close to those of the FD4 method. The best results are obtained in this case when no mass lumping is performed.

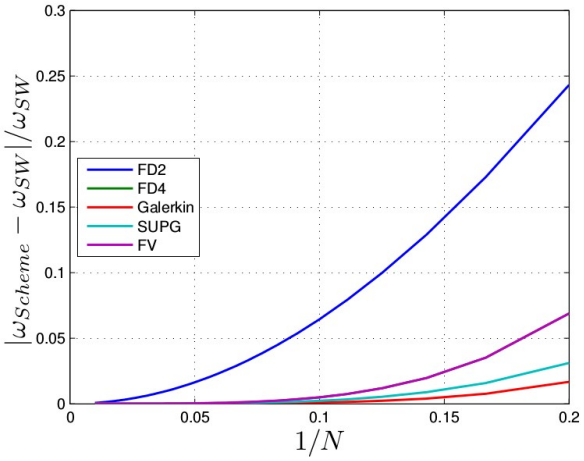

Figure 2.7: Dispersion error for the FV scheme with respect to the NLSW model (the error is independent from kh_0): comparison with respect to the FD2, FD4, GAL and SUPG schemes.

Summary: This analysis has allowed to highlight the following results. First, the behaviour of the schemes is quite similar, despite the different treatment of the hyperbolic part. It appears that the treatment of the third order derivatives is very important, and in particular that the use of exact quadrature in the L^2 projection defining the auxiliary variable (2.10), is fundamental to reduce the error for deep(er) waters/short(er) waves. When no lumping is performed, the errors are similar or smaller than those provided by the fourth order finite differences.

Finally, these similarities allow to provide a general recipe for the elliptic solver, as, for all the methods involved, the choice of the approach 4 allows to

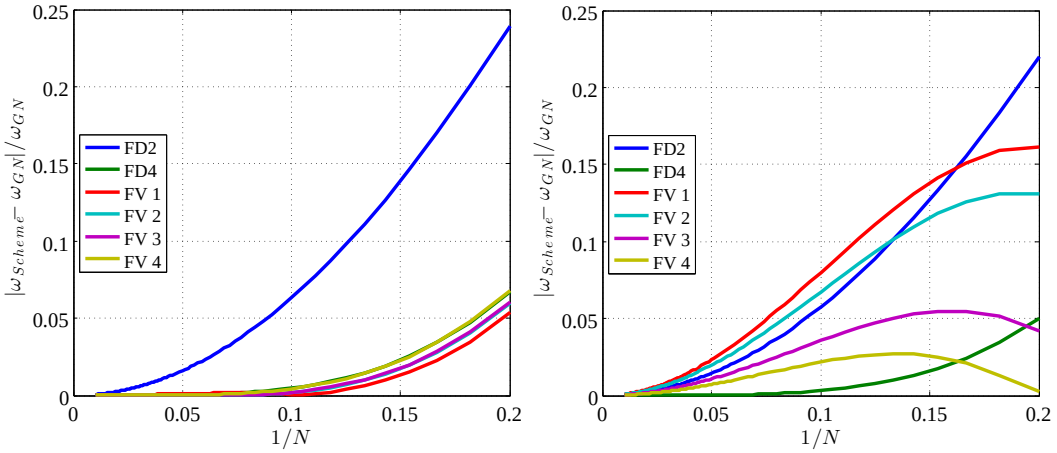

Figure 2.8: Dispersion error for the FV scheme for $kh_0 = 0.5$ (left) and the $kh_0 = 2.5$ (right): impact of lumping strategy.

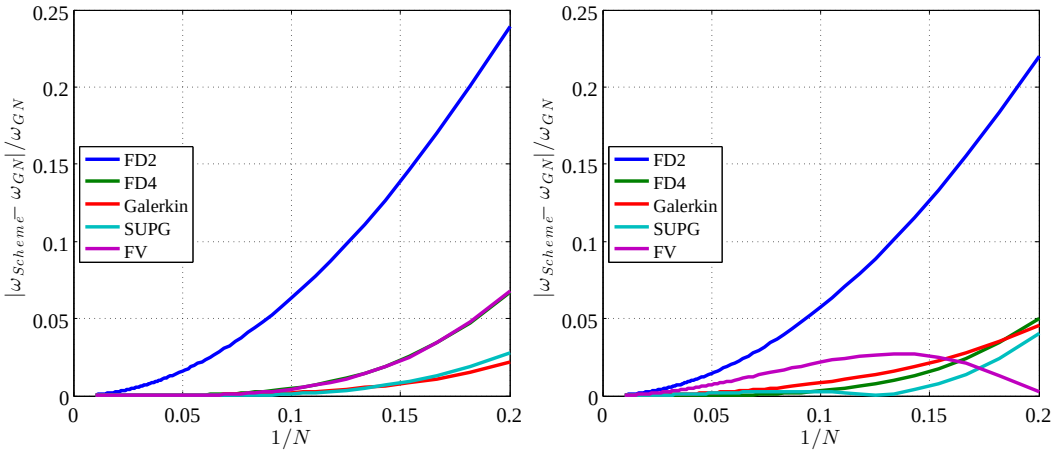

Figure 2.9: Dispersion error of FD2, FD4, Galerkin, SUPG, and FV schemes. Left: $kh_0 = 0.5$. Right: $kh_0 = 2.5$.

reduce the dispersion errors close to those of the FD4 scheme or below them. A summary of the resulting error curves is reported on figure 2.9 confirming the above observations.

2.8 Time integration and boundary conditions

2.8.1 High-order time integration methods:

Similarly to the spatial domain, the temporal domain is discretized by a set of non-overlapping slabs $[t^n, t^{n+1}]$. We will denote by $\Delta t^{n+1} = t^{n+1} - t^n$. For generality, we compare three different time discretization techniques. Only third-order time integration methods have to be considered (order greater or equal to three) in order not to spoil the dispersion characteristics of the schemes in space. One is a classical method in the context of the BT numerical models, while the other two have been chosen as representatives of boundedness or strong stability preserving methods. For all of these methods, the time step is computed by means of the CFL condition:

$$\Delta t^{n+1} = \mathrm{CFL} \frac{\Delta x}{\max_i(|u_i^n| + \sqrt{g h_i^n})} \ . \tag{2.48}$$

AB-AM predictor-corrector scheme: The first time integration scheme we consider is the Adams Bashforth - Adams Moulton (AB-AM) predictor-corrector method, well known in the community of Boussinesq modeling (see *e.g.* Wei et Kirby [1995] and Roeber *et al.* [2010]). For the general ODE:

$$\mathbf{U}' = \mathcal{L}(\mathbf{U}) \ , \tag{2.49}$$

this time integration scheme is composed by two stages:

1. Predictor stage (Adams-Basforth method)

$$\mathbf{U}^p = \mathbf{U}^n + \frac{\Delta t}{12}\left[23\mathcal{L}(\mathbf{U}^n) - 16\mathcal{L}(\mathbf{U}^{n-1}) + 5\mathcal{L}(\mathbf{U}^{n-2})\right] \ , \tag{2.50}$$

2. Corrector stage (Adams-Moulton method)

$$\mathbf{U}^{n+1} = \mathbf{U}^n + \frac{\Delta t}{24}\left[9\mathcal{L}(\mathbf{U}^p) + 19\mathcal{L}(\mathbf{U}^n) - 5\mathcal{L}(\mathbf{U}^{n-1}) + \mathcal{L}(\mathbf{U}^{n-2})\right] \ . \tag{2.51}$$

The Adams predictor corrector has stability properties close to those of the explicit Euler scheme, with respect to which we thus have an affective CFL of 1/2 (2 stages for the same time step magnitude). The method is obtained by a combination of Lagrange polynomial extrapolation, and polynomial interpolation to evaluate the integral of $\mathcal{L}$ in the interval $[t^n, t^{n+1}]$. For the autonomous ODE (2.49), fourth order of accuracy can be easily shown by standard truncation error analysis. The method used to derive the method can be generalized to include variable time step sizes, however, a simple technique to account for

variable time step sizes, while keeping constant the coefficients in the scheme, is to re-correct iteratively the solution with the Adams-Moulton step, stopping when the relative magnitude of the correction is below a given threshold (*cf.* Wei et Kirby [1995]; Roeber *et al.* [2010]). In practice, however, the improvement brought by this multi-corrector procedure are very small, and a single correction is already enough to obtain accurate results also for variable step sizes (see Wei et Kirby [1995]).

RK3 scheme: The second time integration scheme tested is the three stages third order SSP Runge-Kutta (RK3) scheme which, for the general ODE (2.49), reads (*cf.* Gottlieb *et al.* [2001]):

$$\begin{aligned}
\mathbf{U}^{p} =& \mathbf{U}^{n} + \Delta t\, \mathcal{L}(\mathbf{U}^{n}) \;, \\
\mathbf{U}^{2p} =& \frac{3}{4}\mathbf{U}^{n} + \frac{1}{4}\mathbf{U}^{p} + \frac{\Delta t}{4}\mathcal{L}(\mathbf{U}^{p}) \;, \\
\mathbf{U}^{n+1} =& \frac{1}{3}\mathbf{U}^{n} + \frac{2}{3}\mathbf{U}^{2p} + \frac{2\Delta t}{3}\mathcal{L}(\mathbf{U}^{2p}) \;.
\end{aligned} \tag{2.52}$$

The RK3 belongs to the family of strong stability preserving multi-stage methods with positive coefficients, inheriting the same stability properties of the explicit Euler scheme. In particular, compared to the latter, the RK3 has a CFL condition of 1, giving an effective CFL of 1/3.

eBDF3 scheme: Lastly, the third order extrapolated Backward Differencing Method (eBDF3) (*cf.* Hundsdorfer et Verwer [2003]; Klosa [2012]) reading:

$$\begin{aligned}
\alpha_{n+1}\mathbf{U}^{n+1} + \alpha_{n}\mathbf{U}^{n} + \alpha_{n-1}\mathbf{U}^{n-1} + \alpha_{n-2}\mathbf{U}^{n-2} =& \\
= \beta_{n}\,\mathcal{L}(\mathbf{U}^{n}) + \beta_{n-1}\,\mathcal{L}(\mathbf{U}^{n-1}) + \beta_{n-2}\,\mathcal{L}(\mathbf{U}^{n-2}) \;,&
\end{aligned} \tag{2.53}$$

with the following for of the weights:

$$\begin{aligned}
\alpha_{n+1} &= \frac{1}{\Delta t^{n+1}} + \frac{1}{\Delta t^{n+1} + \Delta t^{n}} + \frac{1}{\Delta t^{n+1} + \Delta t^{n} + \Delta t^{n-1}} \;, \\
\alpha_{n} &= -\frac{(\Delta t^{n+1} + \Delta t^{n})(\Delta t^{n+1} + \Delta t^{n} + \Delta t^{n-1})}{\Delta t^{n+1}\Delta t^{n}(\Delta t^{n} + \Delta t^{n-1})} \;, \\
\alpha_{n-1} &= \frac{\Delta t^{n+1}(\Delta t^{n+1} + \Delta t^{n} + \Delta t^{n-1})}{(\Delta t^{n+1} + \Delta t^{n})\Delta t^{n}\Delta t^{n-1}} \;, \\
\alpha_{n-2} &= -\frac{\Delta t^{n+1}(\Delta t^{n+1} + \Delta t^{n})}{(\Delta t^{n+1} + \Delta t^{n} + \Delta t^{n-1})(\Delta t^{n} + \Delta t^{n-1})\Delta t^{n-1}} \;,
\end{aligned}$$

and

$$\beta_n = \frac{(\Delta t^{n+1} + \Delta t^n)(\Delta t^{n+1} + \Delta t^n + \Delta t^{n-1})}{\Delta t^n (\Delta t^n + \Delta t^{n-1})} ,$$
$$\beta_{n-1} = -\frac{\Delta t^{n+1}(\Delta t^{n+1} + \Delta t^n + \Delta t^{n-1})}{\Delta t^n \Delta t^{n-1}} ,$$
$$\beta_{n-2} = \frac{\Delta t^{n+1}(\Delta t^{n+1} + \Delta t^n)}{(\Delta t^n + \Delta t^{n-1})\Delta t^{n-1}} .$$

The eBDF3 is part of a family of high order explicit multi step methods verifying, under a time step restriction, the same boundedness preserving property of the explicit Euler scheme for linear problems. Compared to the latter, the eBDf3 has a stability condition of CFL$= 1/3$ (*cf.* Hundsdorfer *et al.* [2003]), which gives the same effective CFL of the RK3 method.

2.8.2 Friction terms discretization

When treating the water running over shores, in proximity of dry areas and, in general, when water depth is low, the friction effect displayed by the bottom must be taken into account. Friction on the bottom is a major unknown in environmental studies an the friction laws themselves are mostly empirical and needs model calibration through parameter estimation techniques. Friction stress exerted by a horizontal plane on a flow is parallel to the flow itself and can be expressed by the formula:

$$\tau = -\frac{C_f}{2}\mathbf{u}|\mathbf{u}| , \tag{2.54}$$

where C_f can be a constant number or, more often, defined by a law which account for the local bottom steepness and water depth. This term is then added as a source term in the momentum equation. However, an explicit treatment of the friction can produce numerical oscillations (*cf.* Brufau *et al.* [2004]; Murillo *et al.* [2007, 2009]) when the roughness coefficient is high. For this reason, we use the technique proposed by Brufau *et al.* [2004]; Murillo *et al.* [2009]. More precisely, for all the three schemes proposed, at the end of each time step we upgrade the flux solution by the following relation:

$$(hu)_i^{n+1} = (hu)_i^{\star} - g(hS_f)_i^{n+1}\Delta t^n ,$$

where the values signed with $\star$ are the values computed without the friction, and $(S_f)_i$ is defined by the following relation:

$$(S_f)_i = (uR_f)_i = u_i \frac{N_m^2 ||u_i||}{h_i^{4/3}} .$$

Substituting in the above equation, we can recover:

$$(hu)_i^{n+1} = (hu)_i^\star - g(huR_f)_i^{n+1}\Delta t^n = \\ = (hu)_i^\star - g(hu)_i^{n+1}\left[(1-\theta)(R_f)_i^{n+1} + \theta(R_f)_i^n\right]\Delta t^n \ ,$$

with N_m being the Manning roughness coefficient.
Now, by separating explicit and implicit part and by assuming that $R_f^{n+1} = R_f^\star$, we can write:

$$(hu)_i^{n+1} = \frac{(hu)_i^\star - \theta g(hu)_i^n (R_f)_i^n \Delta t^n}{1 + (1-\theta) g(R_f)_i^\star \Delta t^n} \ .$$

When the implicitness parameter θ is set to zero, the friction source term is computed in a completely implicit manner, while it is computed in a totally explicit point wise manner when $\theta = 1$. We have used the value $\theta = 0$ in all the one-dimensional simulations performed. This modification, albeit very robust, but makes the scheme locally first order in time when friction is dominating. This is especially the case in wet-dry fronts. Techniques to construct high order variants for the eBFD and Runge-Kutta methods are discussed in Hundsdorfer et Verwer [2003]; Chertock *et al.* [2015]. These have been implemented in the two-dimensional scheme in order to increase the efficiency of the friction treatment and will thus be discussed in section 4.4.

2.8.3 Boundary conditions and internal wave generation

To define differential problems and the application of the model for realistic wave propagation problems, boundary conditions must be considered. It is worth emphasizing that boundary conditions affect the numerical properties of the scheme. Stability and accuracy of high-order methods can be dramatically reduced if boundary treatment is not performed carefully. However, while exact boundary conditions can be imposed in the case of hyperbolic problems, and many works are available in the literature on this topic (*cf.* LeVeque [2002]; Toro [2009] among the others), this remains argument of discussion in the case of dispersive models and an active research topic. While the fully reflective wall boundary condition can be obtained by imposing some symmetric conditions leading to the satisfaction of: $\mathbf{u} \cdot \mathbf{n} = 0$ on the wall line (being $\mathbf{n}$ the normal direction to the wall), inflow and outflow boundaries require more complex treatments. As in the aeroacustics, it has become general practice to apply heuristic techniques involving the use of artificial layers for wave dissipation of generation (*cf.* Kirby *et al.* [1998]; Wei *et al.* [1999]; Walkley [1999]; Zhang *et al.* [2014]. A nonlinear boundary condition obtained by embedding in the shallow water characteristic decomposition a dispersive correction has been proposed in Cienfuegos *et al.* [2007]. The most recent developments concerning boundary conditions for nonlinear dispersive problems, including the BBM-type equations are discussed in Besse *et al.* [2016].

In this work we use some of the existing techniques to generate and dump waves in approximately defined layers of the domain. Two types of boundary conditions are used, depending on the case: solid (fully reflective) wall or absorbing boundary conditions. For the FV scheme with third-order MUSCL reconstruction, the reconstructed values on the first and last cell of the computational domain are computed using neighbouring ghost cells (*cf.* Kazolea et Delis [2013]). For the FE schemes, ghost cells are not needed since the scheme is node centered and the degrees of freedom are located directly on the physical boundary. Dirichlet boundary conditions can be easily applied in this case.

Absorbing boundaries replace outlet conditions, trying to simulate a signal leaving the domain of study. These are applied with the goal of completely dissipating the energy of the outgoing waves possibly without introducing any spurious reflections in the domain. Several methods have been proposed in the literature (see the already cited works and references therein). Among these, we consider two. The first one consists in adding a dissipation term to all the equations of the system, premultiplied by an artificial viscosity function designed in order to be zero in the inner domain and to become predominant inside the absorbing boundary (*cf.* Walkley [1999]; Ricchiuto et Filippini [2014]). The second method, applied here, consists in damping inside the absorbing layer the computed surface elevation and/or the momentum by multiplying their values by a coefficient $m(x)$ defined as Kazolea *et al.* [2014]:

$$m(x) = \sqrt{1 - \left(\frac{x - d(x)}{L_s}\right)^2}.$$

In the previous expression, L_s is the sponge layer width and $d(x)$ is the normal distance between the cell center with coordinates x and the absorbing boundary. Typical values for the sponge layer width are related to the wavelength of the incoming wave: $\lambda \leq L_s \leq 1.5\lambda$. Thus, longer wavelengths require longer sponge layers.

A large number of tests involve the interaction of monochromatic periodic waves of small amplitude with a given bathymetry. In absence of an exact solution, the generation of such periodic waves is a bit tricky. For very small amplitude waves, some authors suggest the use of Dirichlet type conditions with imposition at the *inlet* boundary of the condition (see *e.g.* Tonelli et Petti [2009] and references therein) $(\eta_b(t),\, q_b(t))^T = (A\sin(\omega t),\, cA\sin(\omega t))^T$ with $c^2 = gh_0$. We have found numerically the use of this approach relatively inefficient: the signal obtained presented a transient phase after which it stabilized to a periodic wave of amplitude generally larger than A.
In this work we, thus, make use of the internal wave generator of Wei *et al.* [1999], which is obtained by adding a source function to the mass equation. Wei *et al.* [1999] derived the method in the context of the enhanced Boussi-

nesq equations of Nwogu [1994], but its use can be generalized for other types of Boussinesq-type equations by simply changing the dispersion relation used in the generator. In this work, as to be compatible with the equations of Green-Naghdi, we have used the dispersion relation (1.15).

2.9 Embedding wave breaking

In section 1.9, the problem of reproducing the effects of wave breaking by means of the BT models has been illustrated and a brief overview of the solutions proposed in the literature has been provided. As we have seen, a closure model is necessary to simulate the breaking process numerically. This is composed of two main elements: an energy dissipation mechanism, a trigger mechanism related to the initiation and termination of the breaking process. We have already mentioned that, in this work, an hybrid approach is applyed, consisting in reverting the dispersive eGN equations to the NLSW system, to exploit its capability to describe wave energy dissipation in breaking. More details concerning the detection and triggering of the breaking model and on the coupling between Green-Naghdi and NLSW equations are discussed hereafter.

2.9.1 Breaking front detection

The difference between the several implementations of the hybrid model strategy proposed in the literature basically boils down to choosing criterion for when turning dispersion off and when to turn it back on . The existing criteria are normally based on the computed values of the local surface velocity and free surface gradient. Tonelli et Petti [2009, 2010] based their criterion on the local ratio between surface elevation and water depth $\varepsilon = \eta/h$, thus solving the NLSW equations in regions where the nonlinearity prevails and for the BT ones elsewhere. The method does not need any calibration and its simplicity is its main advantage. Clearly the criterion acts locally, on each node of the domain and has no memory of what has happened the time-step before or in the neighbouring nodes. It may, thus, introduce instabilities in the computation and reveal inadequate, due to its static local application, in cases where a mechanism able to track propagating breaking fronts is instead needed.
Further phase resolving models have been identified in Schaffer *et al.* [1993] and Kennedy *et al.* [2000]. In Schaffer *et al.* [1993], a formula is introduced based on the tangent of the angle of the wave front slope, being a function on time, and two angles have been chosen to represent the threshold for the start and the end of wave breaking. Kennedy *et al.* [2000], instead, developed a criteria based on the value of the vertical velocity of the free surface elevation. These two criteria represent the building blocks of the trigger mechanism presented in Kazolea *et al.* [2014], and used for this work. This is composed

by the combination of two phase-resolving criteria:

- the surface variation criterion: $|\partial_t \eta| \geq \gamma\sqrt{gh}$, with $\gamma \in [0.3,\ 0.65]$;
- the local slope angle criterion: $||\nabla\eta||_2 \geq \tan(\phi_c)$, where ϕ_c is the critical front slope at breaking, and $\phi_c \in [14°,\ 33°]$;

with the value of the tuning parameters γ and ϕ_c depending on the type of breaking wave.
The first criterion assumes that wave breaking occurs when the vertical velocity component at the free surface exceeds a certain value proportional to the shallow water phase celerity $\sqrt{gh_0}$. It has been introduced in Borthwick *et al.* [2006], where a value of $\gamma = 0.3$ has been used for breaking solitary waves on sloping beach, and can be derived considering the nonlinear advection equation for the free surface (*cf.* D'Alessandro et Tomasicchio [2008]). It flags for breaking when $\partial_t \eta$ is positive, as breaking starts on the front face of the wave, and has the advantage that can be easily calculated during the running of the code. This criterion works well for moving fronts, but it is inefficient in presence of steady hydraulic jumps for which $\partial_t \eta \approx 0$. In order to be able to detect possible breaking fronts also for these cases, the second criterion is introduced, which is complementary to the first one and based on the critical front slope approach (*cf.* Schaffer *et al.* [1993]; Sørensen *et al.* [1998]). This criterion depends strongly on the wave breaking type (*e.g.* spilling or plunging). For some BT models, this criterion has been considered as the least sensitive breaking threshold, with correct breaking locations predicted using $\phi_c \approx 30°$. However, the discussion on nonlinear shoaling in chapter 1 shows clearly that this value cannot be used for all BT models. In practice, in the numerical tests of chapters 3 and 5 the values of ϕ and γ used for the computations are $\gamma = 0.6$ and $\phi = 30$ everywhere, unless otherwise specified.

2.9.2 Practical implementation

The practical implementation of the criteria discussed above consists in mainly three steps:

1) *Initial flagging :* The surface variation criterion turns into:

$$\frac{|\eta_i^{n+1} - \eta_i^n|}{\Delta t} \geq \gamma\sqrt{g|h_i|}\ ,$$

while the local slope angle criteria becomes:

$$\max\left(\frac{\eta_{i-1}-\eta_{i+1}}{2\Delta x}, \frac{\eta_i-\eta_{i+1}}{\Delta x}, \frac{\eta_{i-1}-\eta_i}{\Delta x}\right) \geq \tan\phi \ .$$

At any time step, for any node of the mesh, we check if any of the two criteria above is satisfied and we activate the breaking mechanism in the interested node. The computational domain may contain several breaking waves at the same time. Different breaking waves are distinguished as discussed in Kazolea *et al.* [2014] and Tissier *et al.* [2012], and each one is processed individually. In one-dimensional problems any consecutive group of flagged nodes defines a breaking wave, it is thus relatively easy to distinguish between different breaking waves of the domain.

2) *Flagged region enhancement :* Once identified, each breaking wave is treated individually. For each flagged wave front we compute peak and trough depths: h_{peak} and h_{trough} respectively (*cf.* figure 2.10). The length of the wave roller has be found experimentally to be $l_r \approx 2.9(h_{peak} - h_{trough})$. The computational region flagged for breaking defines a length l_{NLSW}, which is roughly centered around the wave front. Non-physical oscillations may originate at the interface between the regions where the BT equations are solved and those in the NLSW regime. In Tissier *et al.* [2012], l_{NLSW} was extended to be larger than the order of magnitude of the physical length of the wave roller. The value of l_{NLSW} adopted in the present work is $l_{NLSW} = 2.5l_r$, as the one proposed by Kazolea *et al.* [2014].

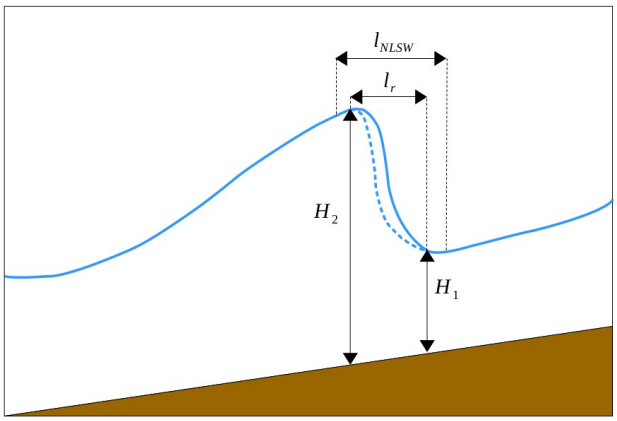

Figure 2.10: Sketch of a roller wave and definition of the breaking zone where the NLSW equations are solved.

3) *Froude number computation:* In order to decide when a wave front has ended to break, we use an analogy between breaking waves and bores. Tidal bores undergo a transition from breaking to undular character,

when the Froude number drops below a certain critical value. Tissier *et al.* [2012] identified this value as $Fr_c = 1.3$. The Froude number of the wave can be computed through:

$$\mathrm{Fr} = \sqrt{\frac{(1 + 2h_{\mathrm{peak}}/h_{\mathrm{trough}})^2 - 1}{8}} \,. \tag{2.55}$$

If the computed Froude number is $Fr \leq Fr_c$, then the breaking mechanism is switched off.

2.9.3 Embedding breaking regions in the GN solver

In the region flagged as breaking the flow quantities are evolved using the Shallow Water equations, thus switching off the dispersive terms. The particular solution strategy proposed allows to do it in a very simple way, since all the dispersive terms are lumped in the variable ϕ, computed through the elliptic equation (2.2). In the numerical results of section 3.9, we will compare two different approaches:

- Simply neglect the terms related to ϕ in the spatial discretization. For a breaking node i, this means setting $\overline{\mathbf{\Phi}}_i = 0$ in (2.13), or (2.30). In this case, the two phases of the discretization (elliptic and hyperbolic) are completely independent on one another. In particular, only the hyperbolic phase is aware of the breaking process;

- For each breaking wave, the computational region where the NLSW equations are solved is roughly centered around the wave front. However, non-physical effects may appear at the interface between two regions governed by the two different models. In Tissier *et al.* [2012], the breaking region is extended, assuming a length larger than the physical scale of the wave roller, trying to minimize this effect. To have a tighter coupling between the two phases, and hopefully a smoother transition, the breaking condition is embedded in the elliptic phase as a sort of Dirichlet boundary condition. In particular, for a breaking node i the line of the matrix issuing form the finite element discretization, discussed in section 2.2, is replaced by $\delta_{ij}\Delta x$, δ_{ij} denoting Kroenecker's δ, while the right hand side is set to zero. The elliptic problem being second order, the discrete solution for ϕ is now expected to go to zero in breaking nodes trying to keep also the continuity of its first derivative. As the source term $\overline{\mathbf{\Phi}}$ is kept into the discretization, and as it involves an average of

neighbouring values of ϕ, a smoother transition may be expected.

In both cases, the nonlinear limiters involved in the discretizations are turned on only if the nodes are in the shallow water regime. In other words, in non breaking regions we set $\psi = 1$ in both (2.16) and (2.28).

Chapter 3

Numerical Tests and Results in One-Dimension

Contents

In this chapter, the solution strategy for the eGN model (1.117) and the three spatial discretizations, presented in chapter 2, are tested against standard test cases. To start, we first asses the theoretical order of accuracy of the schemes in discretizing only the hyperbolic part of system (2.2)-(2.3), *i.e.* the NLSW system, without accounting for dispersion: $\phi = 0$. The same hyperbolic context will be also used to verify the behaviour of the schemes on discontinuous solutions and dry areas.
Then, other benchmarks will be used to ascertain the schemes accuracy on the eGN equations, to validate the numerical treatment of the dispersive terms of the equations and of the wave breaking treatment, through the comparison with respect to laboratory data ans analytical solutions. The tests involving shocks, together with the Shallow Water benchmarks, only the upwind schemes are used. The most part of these results are included in the published work Filippini *et al.* [2016].

3.1 Shallow Water grid convergence

In order to verify the accuracy of the implemented schemes in the Shallow Water limit, we perform a grid convergence using the Method of Manufactured Solutions (*cf.* Salari et Patrick [2000]; Roy *et al.* [2004]). The strength of this method, compare to the Method of Exact Solutions, is that allows to check the order of accuracy of a numerical method using an infinite multiplicity of solutions which are not exact solutions of the system of equations concerned. In the simple differential equation:

$$\boldsymbol{D}\boldsymbol{u}(\mathbf{x},t) = \mathbf{g} \ , \tag{3.1}$$

where $\mathbf{D}$ is the differential operator, $\mathbf{u}$ is the variables vector and $\mathbf{g}$ is a source term, one manufactures a solution $\tilde{\mathbf{u}}(\mathbf{x},t)$ and then applies $\mathbf{D}$ to $\tilde{\mathbf{u}}$ to find a new $\tilde{\mathbf{g}} \neq \mathbf{g}$. The new source term will be then added to the original equations and discretized with them. The manufactured solution $\tilde{\mathbf{u}}(\mathbf{x},t)$ will be thus exact solution of:

$$\boldsymbol{D}\boldsymbol{u}(\mathbf{x},t) = \tilde{\mathbf{g}} \ , \tag{3.2}$$

and can be used to check the scheme accuracy in approaching $\tilde{\mathbf{u}}(\mathbf{x},t)$, solving 3.2. In our case we exploit this method using the exact solitary wave solution of the GN equation. It is known that for horizontal bottoms, the GN model (1.115) has an exact solitary wave solution, which is given by:

$$\tilde{h}(x,t) = h_0 + a\mathrm{sech}^2(k(x-ct)) \ , \tag{3.3}$$

$$\tilde{u}(x,t) = c\left(1 - \frac{h_0}{h(x,t)}\right) \ , \tag{3.4}$$

with $k = \frac{\sqrt{3a}}{2h_0\sqrt{h_0+a}}$ and $c = \sqrt{g(h_0+a)}$. (3.4) are used in (1.58) to compute the analytic expression of the source term $\tilde{\mathbf{g}}$ to add to the system. Since (3.4) is exact solution of the continuity equation, we have that $\tilde{\mathbf{g}} = (0,\ g_q)^T$, with g_q equal to the exact evaluation of the non-hydrostatic term of the GN equation $\tilde{\phi} = \tilde{q}_t + (\frac{\tilde{q}^2}{\tilde{h}})_x + g\tilde{h}\tilde{\eta}_x$ (*cf.* equation (2.3)), with $\tilde{q} = \tilde{h}\tilde{u}$.
We consider the case of a solitary wave propagating over a flat bathymetry, with depth $h_0 = 10$ [m], and with $\varepsilon = 0.2$. The computational domain has been set between [0, 2000] [m] and the initial wave have been placed in $x_0 = 1000$ [m]. In order to quantify the numerical accuracy and assess the convergence of the numerical scheme, the numerical solution is computed for several cell sizes Δx, over a duration $t = 1$ [s]. Starting with $\Delta x = 5$ [m], the test case is performed on a set of six meshes successively dividing the space step by two up to $\Delta x = 0.15625$ [m] while keeping the time step small enough to ensure that the leading error order is provided by the spatial discretization. For this, the corresponding time step size of the simulation has been refined according to (2.48), with CFL ≈ 0.2. The relative error on the total water depth $E_{L_2}(h) = ||h_{num} - h_{ex}||_2/||h_{ex}||_2$, with h_{num} is the numerical solution and h_{ex} is the analytical one, is computed at $t = 1$ [s].
The convergence of the L^2 error is plotted in Figure 3.5, where the slopes 2.5 and 3 are also plotted for reference. Similar behaviours are observed with other norms. The slopes obtained from the error reveal convergence rates in between close to 3 for all the combinations, showing that the dominant component of the error is the one related to the spatial discretization and confirming the results of the truncation error analysis of the linear scheme, performed in section 2.7.1.

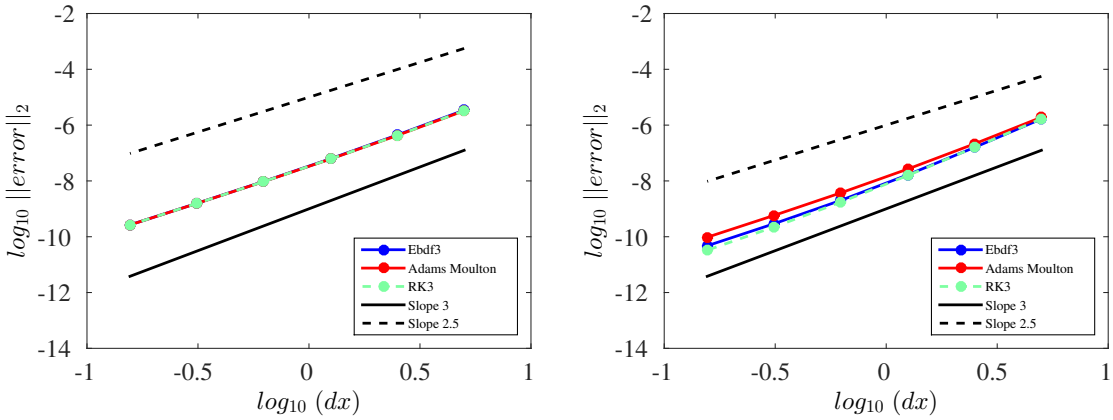

Figure 3.1: Shallow Water grid convergence: convergence rates for the FV scheme (left) and the SUPG scheme (right) computed on a manufactured solution using the exact GN solitary wave shape (3.4).

3.2 Riemann problem

Shock capturing methods, such as the FV and SUPG schemes discussed in sections 2.3 and 2.4.2, must verify a discrete analogous of the Rankine-Hugoniot jump conditions, so that the proper shock speed and strength are obtained. We thus present a preliminary verification of the behaviour of the FV and SUPG schemes, presented in the previous sections, in the case of a Riemann problem with initial solution characterized by left state $h_L = 1$ [m] and right state $h_R = 0.5$ [m]. The discontinuity is placed at the center of a computational domain $x \in [0, 100]$ and the final time of the simulation is $t = 10$ [s]. The computed results are shown in figure 3.2, where they are also compared with respect to the exact analytical solution (*cf.* Ambrosi [1995]; Stoker [1992]; Toro [2001]; Delestre *et al.* [2013]), implemented as reported in Delestre *et al.* [2013]:

$$h(x,t) = \begin{cases} h_L & \text{if } x \leq x_A(t) \ , \\ \dfrac{4}{9g}\left(\sqrt{gh_L - \dfrac{x_i - x_0}{2t}}\right)^2 & \text{if } x_A(t) \leq x_B(t) \ , \\ \dfrac{c_m^2}{g} & \text{if } x_B(t) \leq x_C(t) \ , \\ h_R & \text{if } x_C(t) \leq x \ , \end{cases}$$

$$u(x,t) = \begin{cases} 0 & \text{if } x \leq x_A(t) \ , \\ \dfrac{2}{3}\left(\dfrac{x_i - x_0}{t} + \sqrt{g}h_L\right) & \text{if } x_A(t) \leq x_B(t) \ , \\ 2\left(\sqrt{gh_L} - c_m\right) & \text{if } x_B(t) \leq x_C(t) \ , \\ 0 & \text{if } x_C(t) \leq x \ , \end{cases}$$

with $x_A(t) = x_0 - t\sqrt{gh_L}$, $x_B(t) = x_0 + t(2\sqrt{gh_L} - 3c_m)$, $x_C(t) = x_0 + 2t(\sqrt{gh_L} - c_m)c_m^2/(c_m^2 - gh_R)$, and being c_m the solution of:

$$-8gh_R(\sqrt{gh_L} - c_m)^2 c_m^4 + (c_m^2 - gh_R)^2(c_m^2 + gh_R)c_m^2 = 0 \ ,$$

as follows from Stoker [1992].
The numerical results shown in figure 3.2 display a smooth trend for all the schemes discussed. The Van Albada limiter function, in the case of the FV scheme, and the smoothness sensor limiter, in the case of the SUPG scheme, act properly, killing the numerical oscillations which normally originate in proximity of the shock when high-order schemes are used.

The test is repeated considering an initial dry right state: $h_R = 0$ [m]. This test allows to assess the numerical treatment of the wet/dry front, discussed in section 2.5. The red lines in figure 3.3 represents the numerical solution given by the SUPG (top left and right) and the FV (bottom) schemes, when

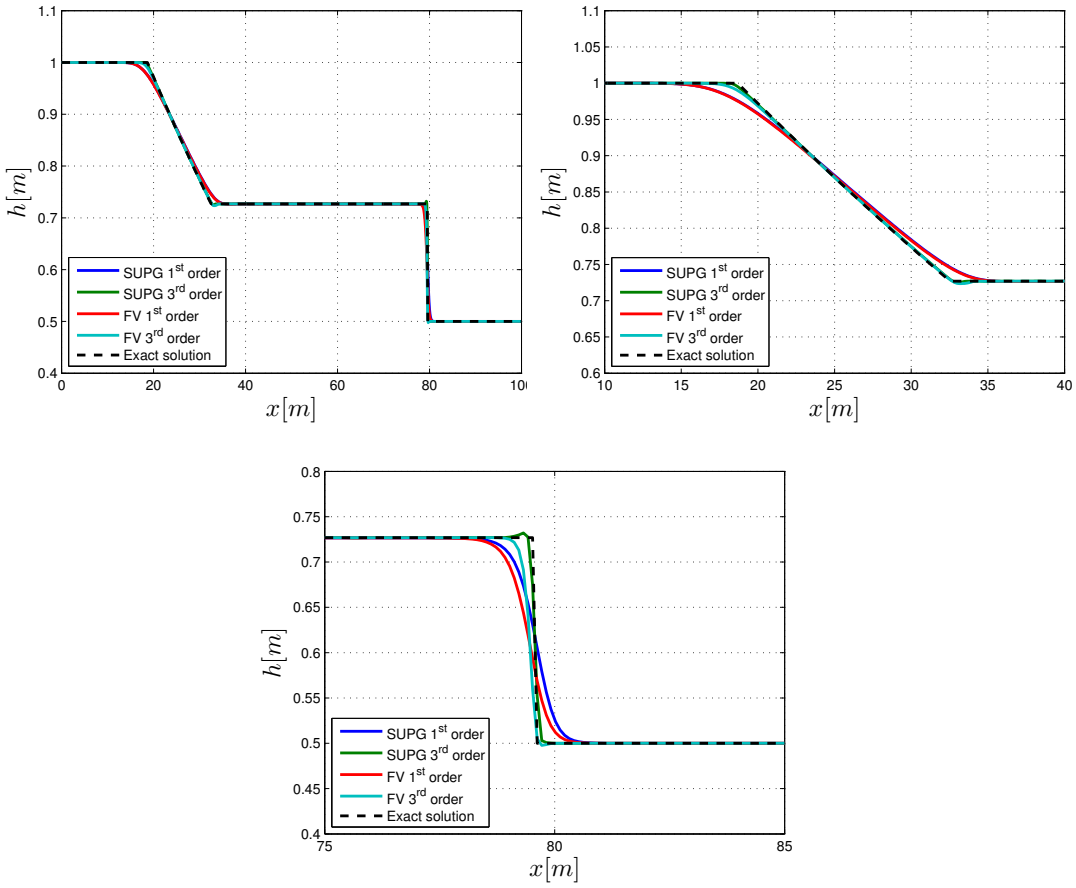

Figure 3.2: Solution of a Riemann problem: Case (a). Comparison of the computed water depth h with respect to the analytical solution (top-left). Zoom on the flow expansion (top-right). Zoom on the shock region (bottom).

no entropy correction is made, after $t = 5$ [s] from the beginning of the computation. It is clearly visible that an unphysical shock is numerically obtained with the two schemes in the middle of the rarefaction region. This is not an admissible solution, since the characteristic lines of the hyperbolic model are coming out from the shock and not converging on it. The size of the shock appears to be much bigger for the FV than for the SUPG one. This may be due to the averaging effect played by the mass matrix of the finite element scheme.
When the two schemes are corrected by means of the entropy fix technique, described in section 2.6, the results obtained do not present any unphysical expansion shock. Completely smooth solutions are obtained even in the sonic region.

One of the most critical aspects in the simulation of the Riemann problem

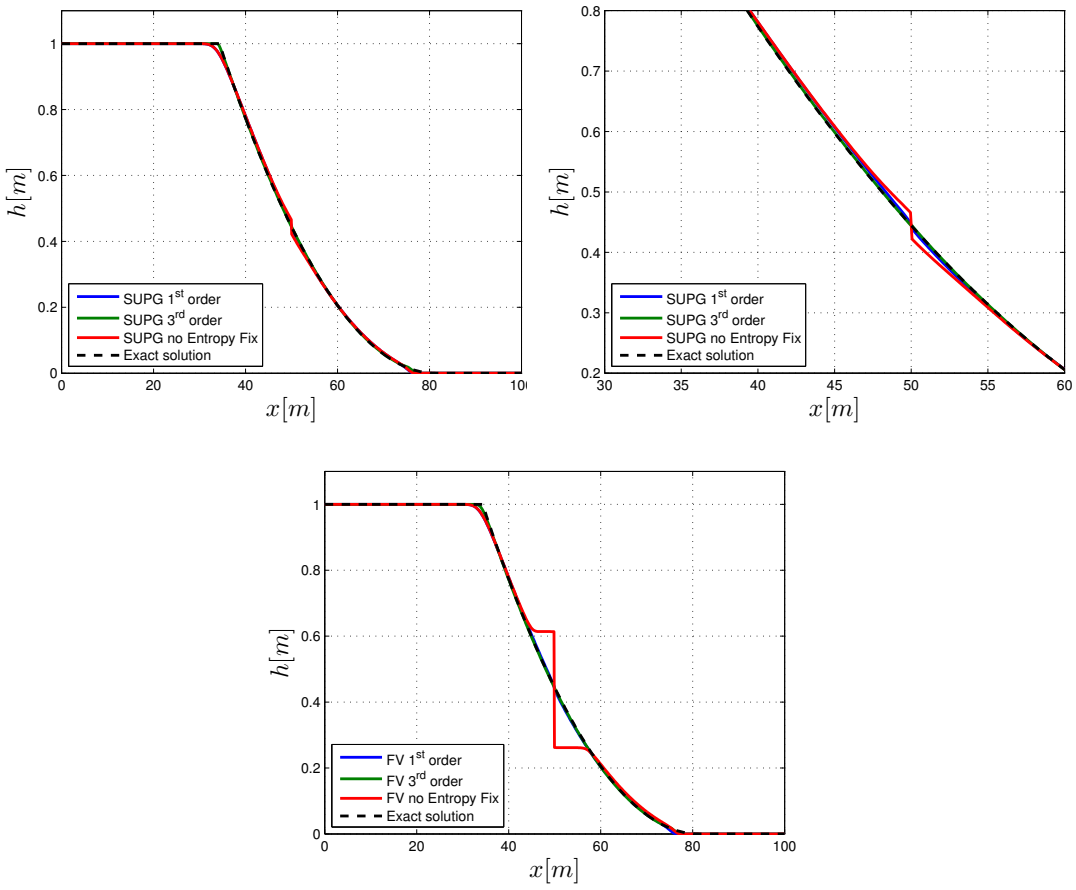

Figure 3.3: Solution of a Riemann problem: Case (b). Comparison of the computed water depth h, with and without the entropy fix correction, respect to the analytical solution. SUPG scheme (top-left) and a zoom and the sonic region (top-right). FV scheme (bottom).

with a dry right state is the computation of the velocity close to the interface with the dry region. In fact, the system is solved for the conservative variables h and $q = hu$ and the velocity is constructed only *a posteriori* by the expression: $u = q/h$. The wet/dry treatment technique of section 2.5 allows to define a value for ϵ_u^{wd} for which the singularity, which may originate from dividing the flux value by zero, is avoided. However, the velocity may not be correctly calculated close to the wet/dry front line, generating oscillation or unphysical values. The values of q and u in the computational domain, at the final time of the simulation, are reported in figure 3.4, showing that the schemes implemented are able to compute all the unknowns of the problem without spurious variations. The impact of the cutoff can however be seen in the velocity plots, which go to zero before the theoretical shock position.

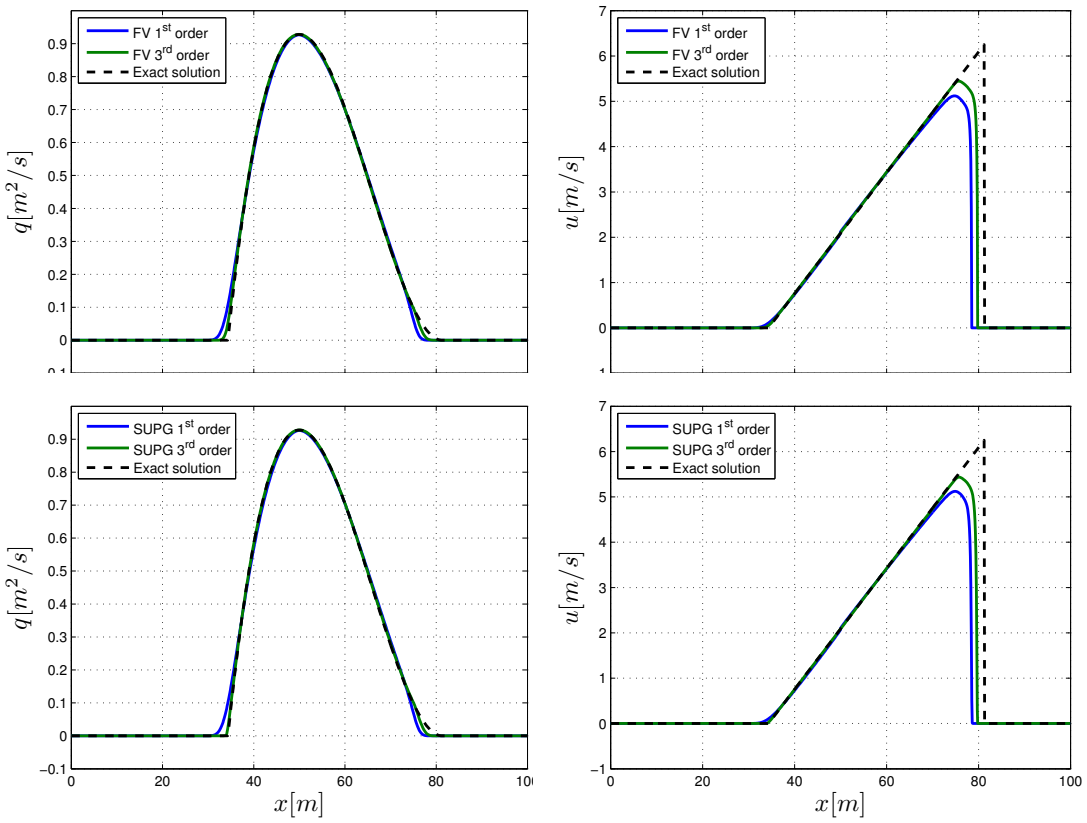

Figure 3.4: Solution of a Riemann problem: Case (b). Comparison of the computed volume flux q and velocity u respect to the analytical solutions: SUPG scheme (on top left-right) and FV scheme (on bottom left-right).

3.3 Grid convergence for a GN solution

We, now, verify the accuracy of the numerical schemes proposed for the GN equations, performing a convergence analysis with respect to space and time step size. Once again, we consider the propagation of a solitary wave over a flat bathymetry, with depth $h_0 = 10$ [m], and with $\varepsilon = 0.2$. The wave solution 3.4 is now exact solution of the equations and we compute the rate of convergence of the numerical solution to the exact one computing the relative error on the total water depth $E_{L_2}(h) = ||h_{num} - h_{ex}||_2/||h_{ex}||_2$, with h_{num} is the numerical solution and h_{ex} is the analytical one. The convergence test have been performing using the same set-up considered in section 3.1, using a set of six uniform meshes with the first characterized by Δx and halving every time the mesh size. The computation run for $t = 1$ [s] and the results obtained are the one illustrated in figure 3.5 together with slopes 2.5 and 3 as references. The slopes obtained reveal convergence rates of the norm of the error considered always in between 2.5 and 3 for all the combinations, confirming the

results of the truncation error analysis of the linear scheme, performed in section 2.7.1. Similar behaviours are also observed with other norms.

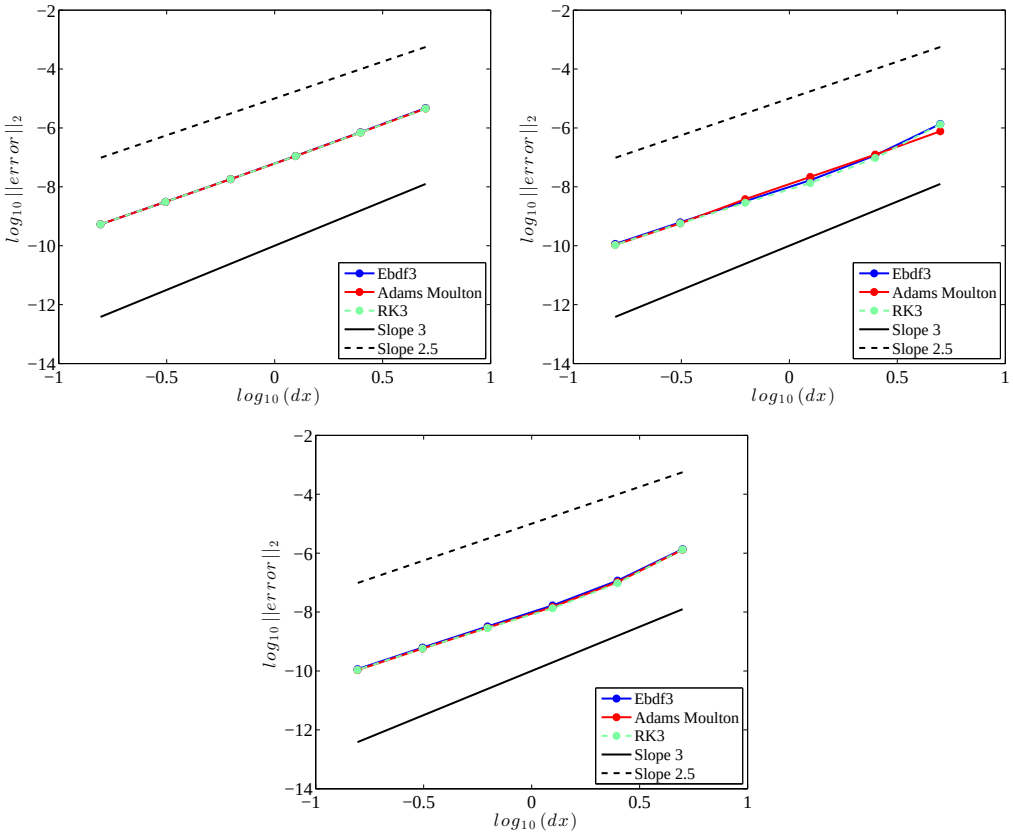

Figure 3.5: Grid convergence for a GN solution: convergence rates for the FV scheme (top-left), the SUPG scheme (top-right) and the Galerkin scheme (bottom).

3.4 Wave propagation over a submerged bar

The next test case considers monochromatic waves propagating over a submerged bar. For this test extensive experimental data exist (*cf.* Beji et Battjes [1994]). This benchmark allows to investigate the frequency dispersion characteristics of the schemes in presence of nonlinear interactions of complex waves. The geometry of the test is sketched on figure 3.4. Monochromatic waves are generated and propagate on a depth of $h_0 = 0.4$ [m] before reaching the submerged bar. The periodic waves shoal over the $1:20$ front slope, developing higher harmonics which are then released, from the carrier frequency, on the $1:10$ slope of the lee side of the obstacle. The submerged trapezoidal bar was

0.3 [m] high with front slope of 1 : 20 and lee slope of 1 : 10, separated by a level plateau 2 [m] in length. The periodic wave is generated by means of an internal source function (cf section 2.8.3) located at $x = 10$ [m] in the domain $[0, 35]$ [m]. Two sponge layers with 3 [m] of thickness are used at the left and rightmost boundaries in order to absorb any reaching wave. The grid used for the computation has a uniform size of $\Delta x = 0.04$ [m] and the CFL number has been set equal to 0.2.
We consider two test configurations and the numerical results are compared with the data of Beji et Battjes [1994]. In particular, the first gauge is always used to calibrate the phase of the signal with the experiments, while the others are used to compare and validate the computations. For further details on the experiment and for the exact location of the gauges the interested reader can consult Beji et Battjes [1994]; Dingemans [1997]; Kazolea *et al.* [2014].

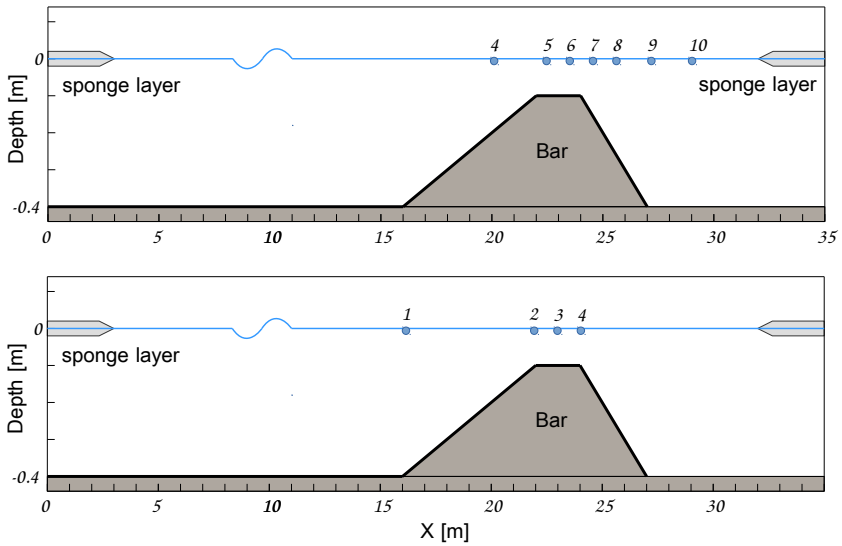

Figure 3.6: Wave propagation over a submerged bar: sketch of the computational configuration and of the gauges position; case (a) on top, case (b) on bottom.

Case (a): In this case, the amplitude of the incident wave is $a = 0.01$ [m] and $T = 2.02$ [s] is its period. This case is often used to validate dispersive wave propagation models. The water depth parameter is $kh_0 \approx 0.67$ with depth to wavelength ratio $h_0/\lambda = 0.11$ [m]. The propagating waves shoal along the front slope of the bar causing the growth of the wave amplitude and the surface profile to become asymmetric. In the back slope the waves separate into independent signals which travel at their own speed. Figure 3.7 presents the comparison between experimental data and the numerical results provided by the FV scheme, combined with all the three time schemes considered in this work. Figures 3.8 and 3.9 present the same gauge signals for the Galerkin

and the SUPG schemes respectively. For brevity, we only show the results registered in gauge 4, 7, 8 and 10, placed respectively at the toe of the bar, before the plateau, on the top and after the bar.

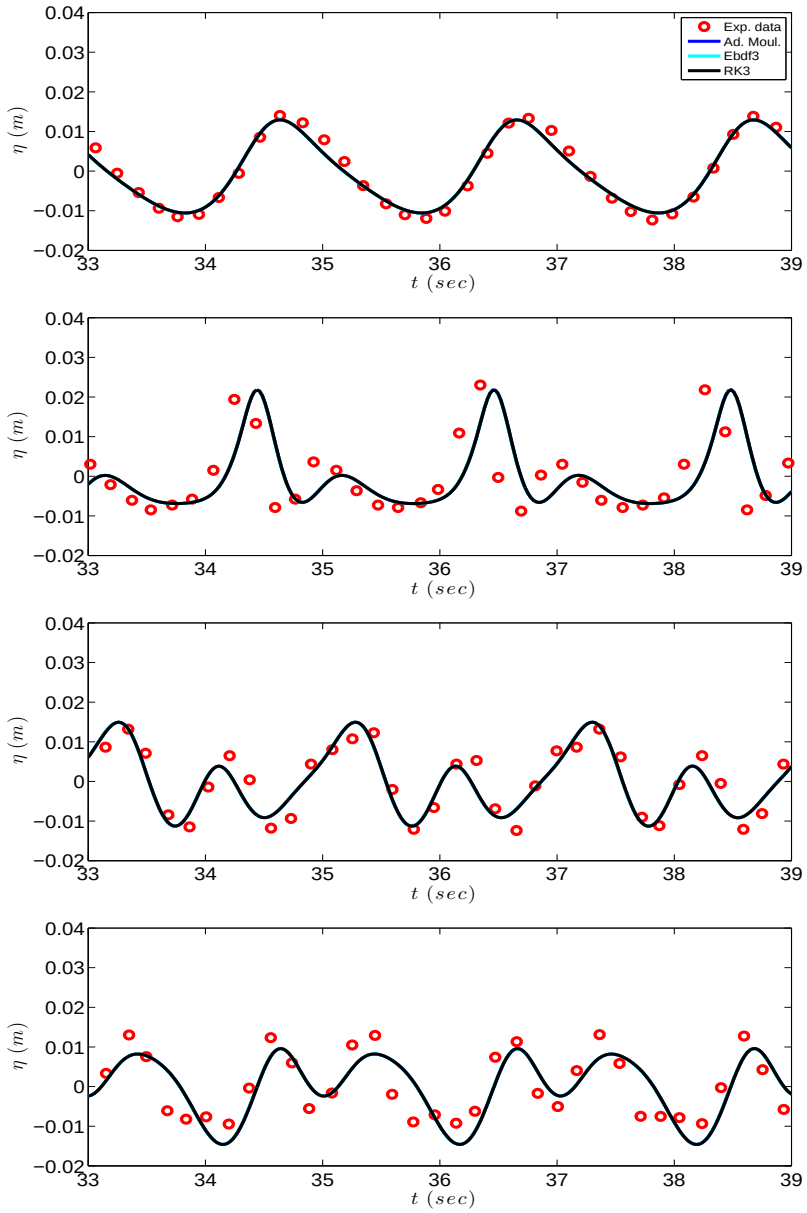

Figure 3.7: Wave propagation over a submerged bar, Case (a): time series of water surface elevation in gauges 4,7,8,10 (from top to bottom). Numerical results computed using the FV scheme discussed in section 2.3.

In the first figure we can see that the results obtained are independent from the time scheme used. Moreover, we remark that the FV scheme pro-

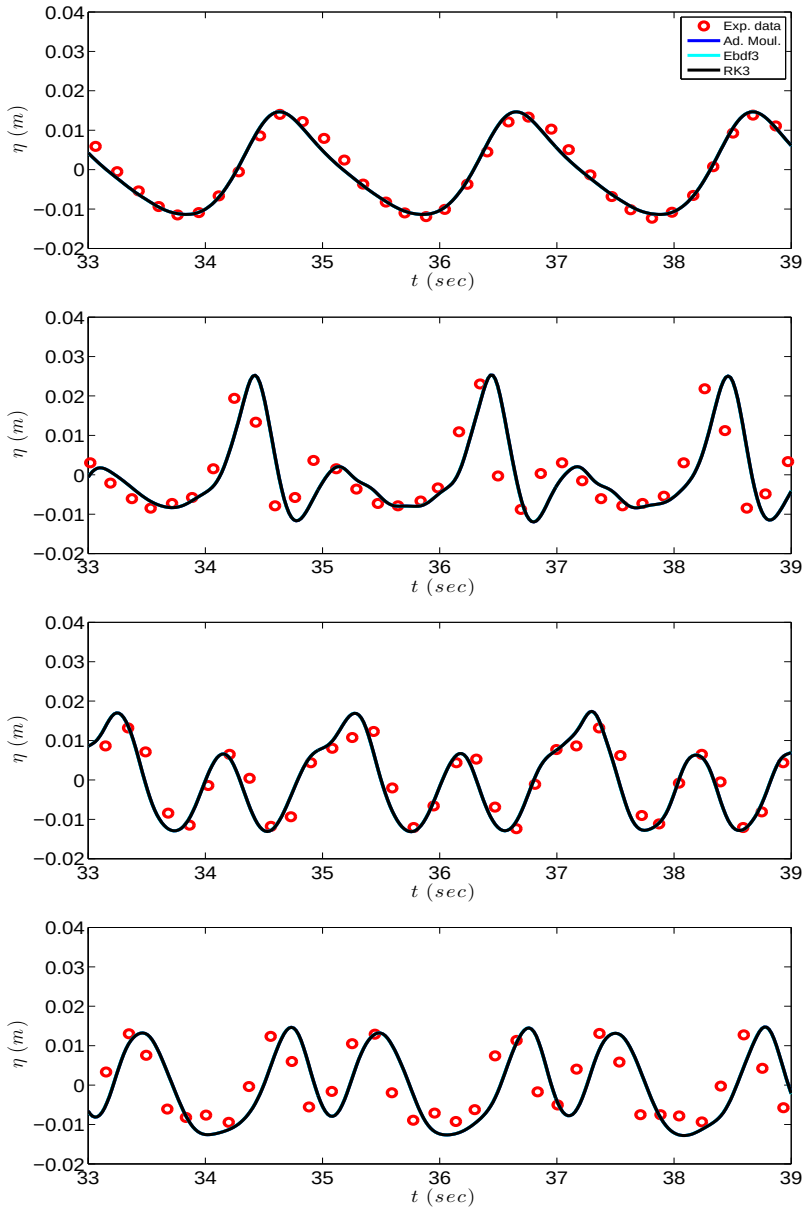

Figure 3.8: Wave propagation over a submerged bar, Case (a): time series of water surface elevation in gauges 4,7,8,10 (from top to bottom). Numerical results computed using the Galerkin scheme discussed in section 2.4.1.

duces slightly less accurate results in the lee side of the bar compared to the two FE schemes, as can be seen from gauge 10 signals in figures 3.7, 3.8 and 3.9. In this region the water depth parameter kh increases rapidly so a worst description may be expected from the linear dispersion analysis results of figure 2.9. Nevertheless, the agreement is still acceptable as the wave shape and

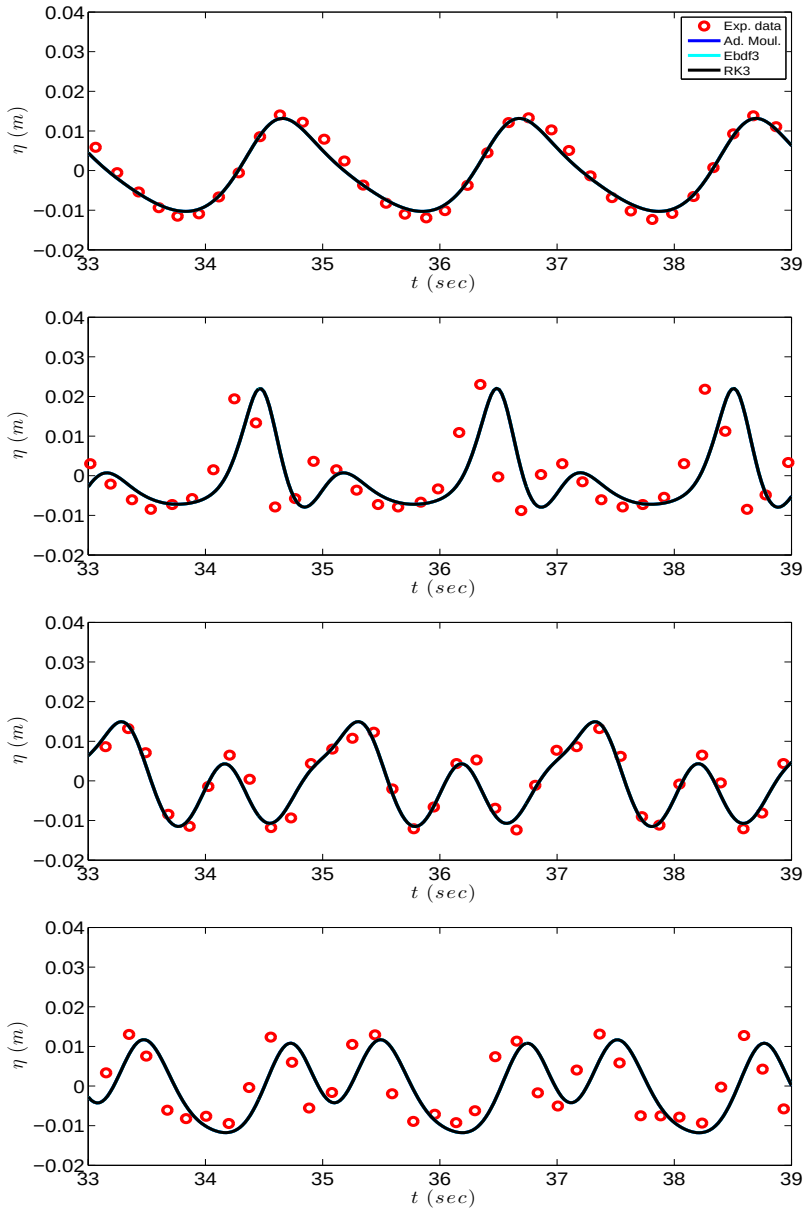

Figure 3.9: Wave propagation over a submerged bar, Case (a): time series of water surface elevation in gauges 4,7,8,10 (from top to bottom). Numerical results computed using the SUPG scheme discussed in section 2.4.2.

amplitudes are quite well reproduced overall the schemes proposed represent quite accurately the nonlinear and dispersive properties of the original continuous model and the phase resolution properties of the schemes are confirmed.

Case(b): In this case, the monochromatic wave height is 0.054 [m] and

the period is $T = 2.5$ [s], that corresponds to the water depth parameter $kh_0 \approx 0.52$, with depth to wavelength ratio of $h/\lambda = 0.0835$. Considerably nonlinear conditions are obtained toward the end of the first slope, where wave breaking is expected to occur after the shoaling of the waves. The value of the surface breaking criterion γ is set to 0.3 for the simulation, while $\phi = 30°$ was used for the local slope angle criterion. We must note that, for the numerical treatment of the wave breaking (in all the test cases), we use the second approach described in section 2.9.3. A discussion on the topic will follow in section 3.9. The numerical results along with the experimental data are recorded in four wave gauges (1 to 4). They are all presented in figures 3.10 and 3.11 for the FV and the SUPG schemes respectively.

The wave shape is well-reproduced for all wave gauges. As expected, the waves shoal along the front slope, since nonlinear effects cause the waves propagating along this slope to steepen and broke at the beginning of the bar crest. For this experiment, breaking is classified as plunging. Bound higher harmonics are developed along the front slope, which are then released from the carrier frequency on the lee side of the bar, as the water depth parameter kh increases rapidly.
Figures 3.12 and 3.13 illustrate the phase-resolving breaking criteria working in the wave-by-wave treatment. The bounded region between the two red dashed vertical lines represents l_{NLSW}, the area where the NLSW systems is solved to reproduce the wave dissipation mechanism. It is plotted at different time instants (covering roughly one wave period) and for the two discretization techniques adopted for this test (FV and SUPG). Results were performed using the AB-AM method in time for both FV and SUPG, but similar results can be obtained using the RK3 and eBDF3. The onset of breaking is correctly predicted for both schemes, close to the beginning of the bar crest and continues along the flat of the bar leading to a wave height decay. We can observe that, during the breaking process, the SUPG scheme is more diffusive, leading to a slightly earlier termination of breaking and, after that, a small amplification of the wave height compared to the FV scheme. Different calibrations of the breaking model may be needed for different numerical schemes but this study is beyond the purpose of this work.

3.5 Solitary wave run-up on a planar beach

To further verify and validate our wave breaking implementation, we use one of the most intensively studied problems in long-wave modeling: the solitary wave-run-up on a plane beach. Synolakis [1987] carried out laboratory experiments for incident solitary waves of multiple relative amplitudes over a planar beach with a slope 1 : 19.85. Performing this test, we want to asses the ability of our model to describe propagation, shoreline motions, breaking and run-up.

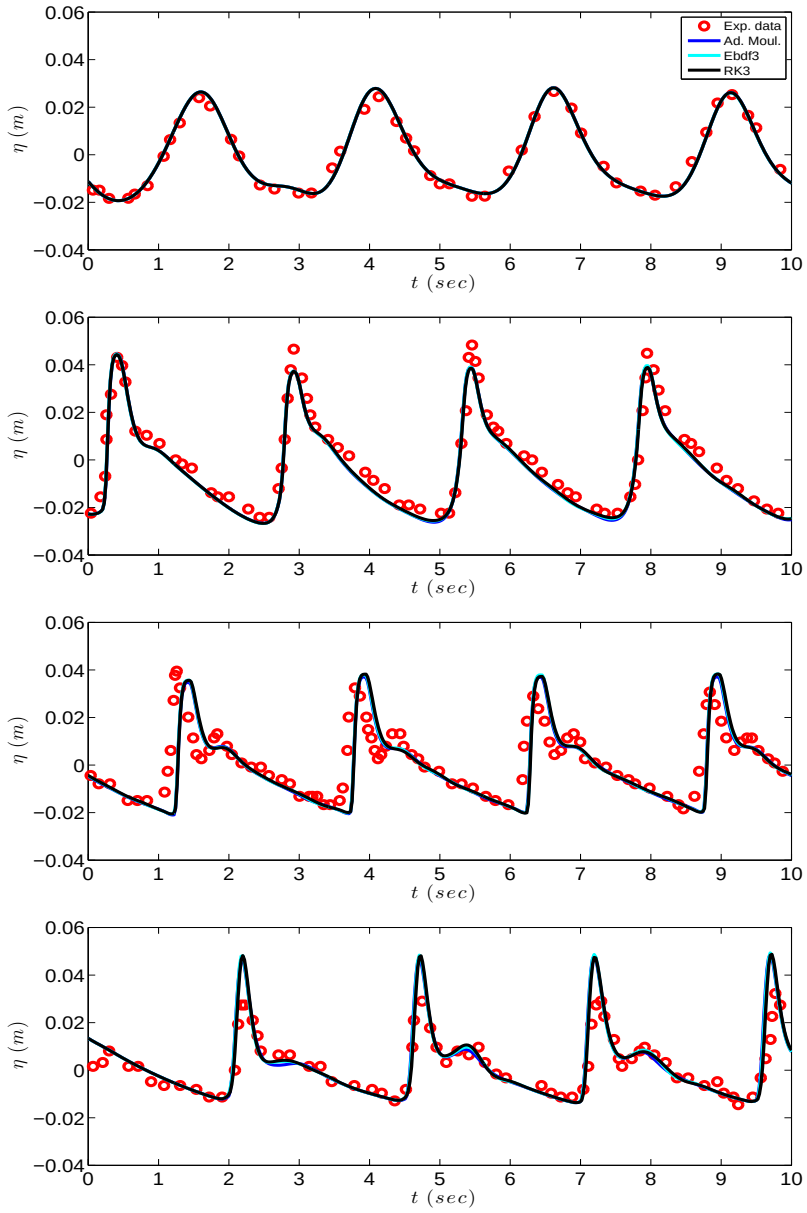

Figure 3.10: Wave propagation over a submerged bar, Case (b): time series of water surface elevation in gauges 1,2,3,4 (from top to bottom). Numerical results computed using the FV scheme discussed in section 2.3.

Detailed description of the test case, along with the initial conditions, can be found *e.g.* in Synolakis [1987]; Bonneton *et al.* [2011a]; Tonelli et Petti [2010]; Roeber et Cheung [2012]; Cienfuegos *et al.* [2010] among many others. The incident wave height used in this work is $a/h_0 = 0.28$ with $h_0 = 1$ [m]. This wave breaks strongly both in the run-up and run-down phases of the motion.

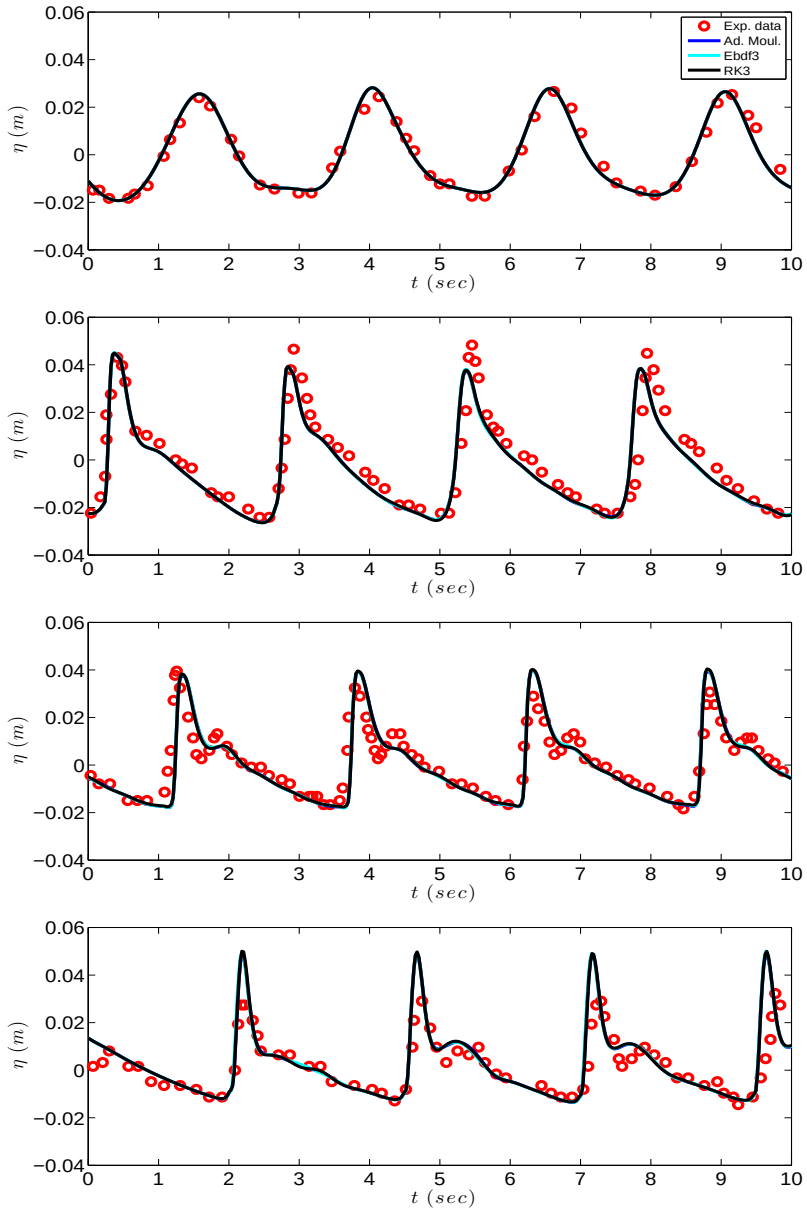

Figure 3.11: Wave propagation over a submerged bar, Case (b): time series of water surface elevation in gauges 1,2,3,4 (from top to bottom). Numerical results computed using the SUPG scheme discussed in section 2.4.2.

The computational domain used is $x \in [-20,\ 100]$ [m] with a uniform grid of $\Delta x = 0.05$ [m]. The CFL number is set equal to 0.2, a sponge layer is applied offshore with length $L_s = 5$ [m] and γ, in the breaking tracking criteria, is set equal to 0.6. Finally, a Manning coefficient of $n_m = 0.01$ is used to define the glass surface roughness used in the experiments.

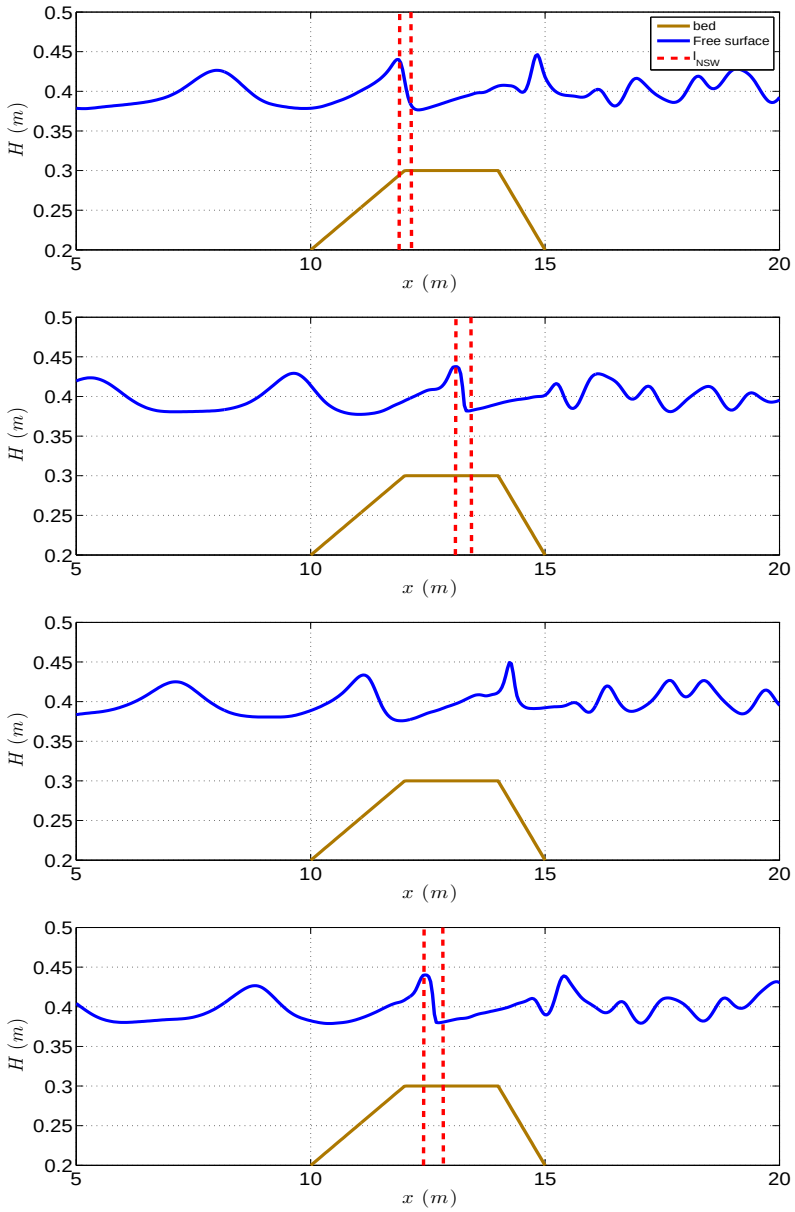

Figure 3.12: Wave propagation over a submerged bar, Case (b): snapshots of the free surface elevation at different increasing times of the simulation (from top to bottom) for FV scheme. Vertical lines define the region of of the domain solved by the NLSW equations.

Figure 3.14 provides a comparison of the measured free surface profiles and the numerical models results at different non-dimensional times. The blue line denotes the numerical results produced by the FV scheme, green dotted

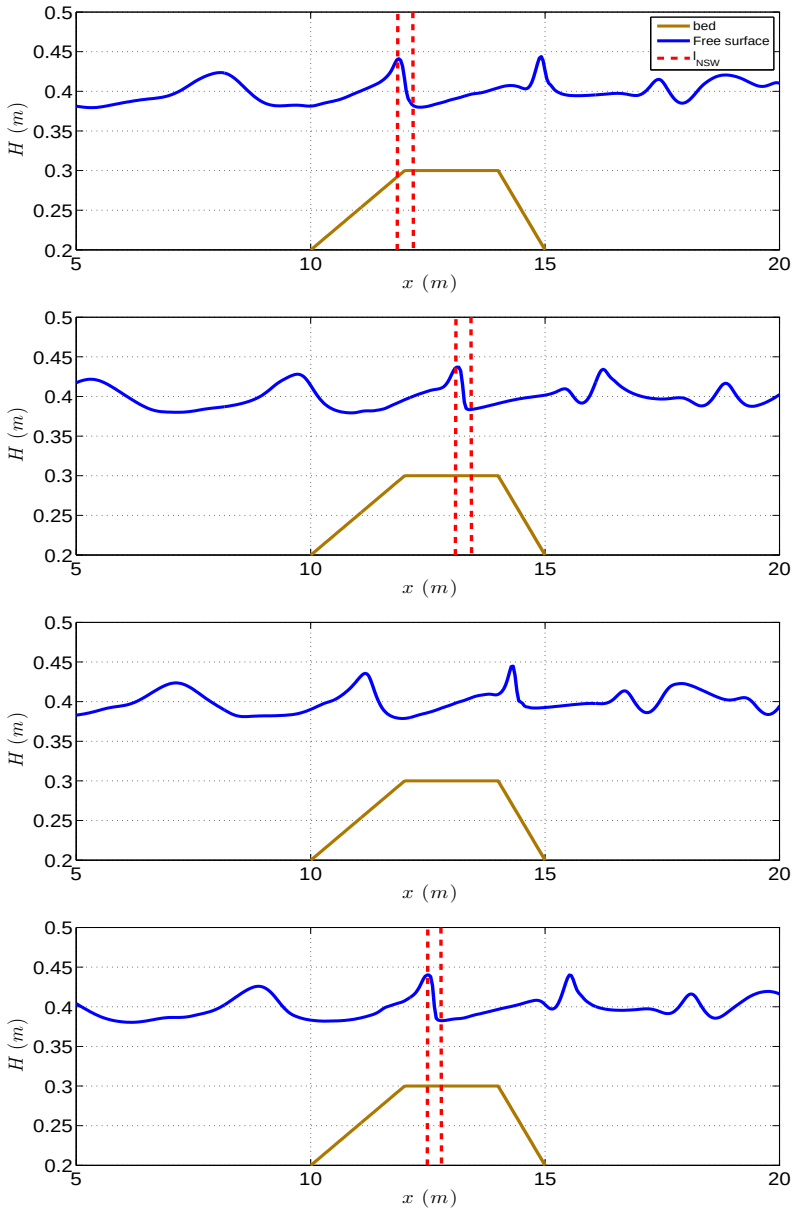

Figure 3.13: Wave propagation over a submerged bar, Case (b): snapshots of the free surface elevation at different increasing times of the simulation (from top to bottom) for SUPG scheme. Vertical lines define the region of of the domain solved by the NLSW equations.

line those given by the SUPG scheme and red circles denote the experimental data.
Until time $t\sqrt{g/h} = 10$, the solitary propagates to the shore and the two models produce identical results, since wave breaking has not started yet. We

can already observe that, due to the well-balanced wet/dry treatment (*cf.* 2.5) applied on the shoreline, no unphysical overtopping or water movement appears in the solution, starting from the wet/dry front. The experimental wave breaks around $t\sqrt{g/h} = 20$. The numerical solution is represented like a bore, storing the water spilled from the breaking wave behind the front. A slight difference can be seen in the two solutions at time $t\sqrt{g/h} = 20$, which may be due to the use of two different limiters (SUPG scheme uses the smooth sensor limiter, while FV scheme uses the MIN-MOD one). At time $t\sqrt{g/h} = 25$, the bore collapses at the shore and the results show a really good agreement with respect to the data. After that, the wave starts to run-up. The time of maximum run-up occurs for $t\sqrt{g/h} = 45$. During the backwash, a breaking wave is created at $t\sqrt{g/h} = 55$ right below the initial still water level. The numerical solution is approximated as a hydraulic jump for both models which can be fully resolved since the breaking criterion recognizes it and the NLSW equations are used in this region.
Globally, the experimental data are very well fit by the numerical results. The breaking criteria used detect the right instant and position of both the initial breaking of the incoming wave and of the hydraulic jump formed during the backwash. Small numerical oscillations originate from the interface with breaking regions. The effort made in order to minimize this effect motivates the study about a different breaking formulation, discussed in section 3.9.

We perform this test case using all the time schemes described up to now. Like in the previous propagation of a periodic wave over a bar, we obtain numerical results independent from this choice. We thus present only two snapshots concerning their comparison in figure 3.15. Since the three time schemes used up to now provide the same results for all the tests, from now on we will just present those obtained using AB-AM. Of course, the choice is not restricted to the methods described in the manuscript. Any time scheme of order greater than (or equal to) three can be used.

3.6 Influence of mesh regularity

In order to assess the influence of mesh regularity on the results, we present some examples of computations on perturbed point distributions. These are obtained from uniform grids, by displacing all the points by a factor of $\rho_i \Delta x$, with ρ_i a random number such that $|\rho_i| \leq 0.2$, and with Δx the initial mesh size. For completeness we consider both a smooth case, and a case involving wave breaking.
For the elliptic part, the continuous Galerkin scheme have been introduced in section 2.4 in a completely general way, valid for both uniform and non-uniform grids. In this case, due to the compact stencil of the P^1 basis functions chosen for the discretization, each one of the integrals of section 2.4 can be evaluated

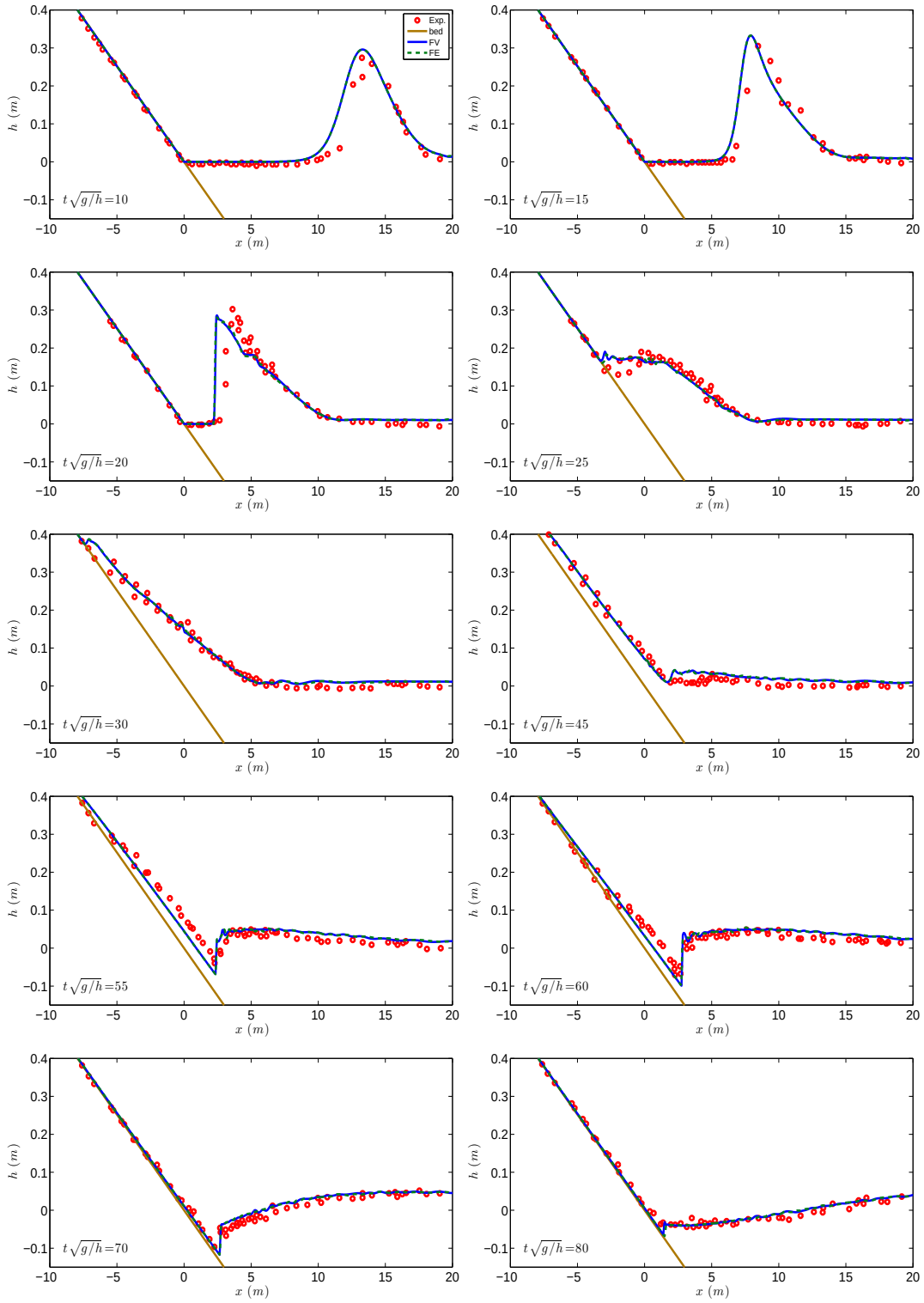

Figure 3.14: Solitary wave run-up on a planar beach: computed free surface elevation at different increasing times of the simulation (from top-left to bottom-right) for the FV and SUPG (named FE in the figures legend) schemes.

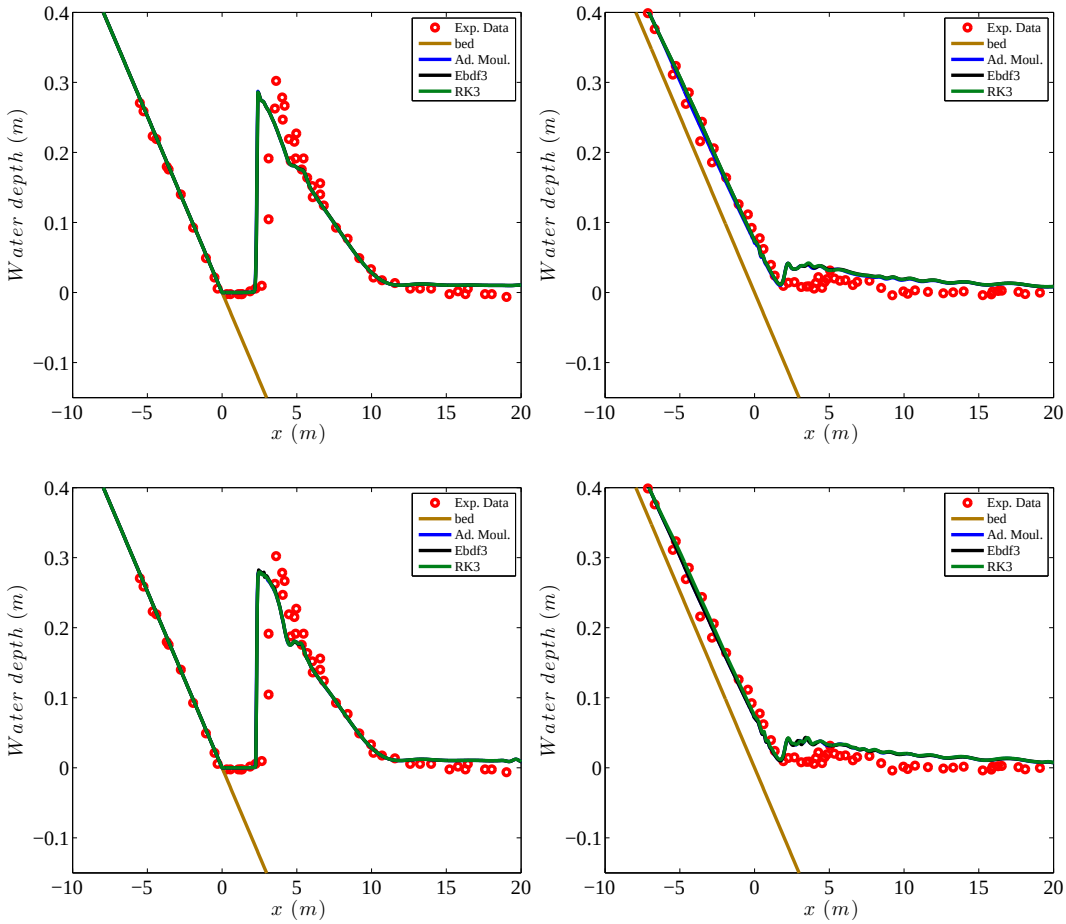

Figure 3.15: Solitary wave run-up on a planar beach: comparison of different time schemes on a solitary wave run-up on a plane beach, for the FV scheme (up) and the SUPG scheme (down).

as the sum of the two contributions on the left and right elements containing the node i:

$$\int_{\Omega_h} \varphi_i \, u = \int_{i}^{i+1} \varphi_i \, u + \int_{i-1}^{i} \varphi_i \, u \ .$$

When, now, solving the integrals with a quadrature formula, $\Delta x = x_{i+1} - x_i = x_i - x_{i-1}$ will appear in the discrete terms when the mesh is uniform, rather than $\Delta x_i = x_{i+1} - x_i$ and $\Delta x_{i-1} = x_i - x_{i-1}$ if a non-uniform mesh is instead used. The same consideration is also valid for the Galerkin and SUPG schemes discussed in section 2.4.2 to discretize the hyperbolic part of the system.
Concerning the FV scheme of section 2.3, one has to deal with a variable size

of the finite volume dual cells $(x_{i+\frac{1}{2}} - x_{i-\frac{1}{2}})$, which can be now defined as: $|C_i| = \frac{\Delta x_{i-1}}{2} - \frac{\Delta x_i}{2}$. The cell volume $|C_i|$ will thus substitute Δx in equations (2.12) and (2.13), while $\overline{\mathbf{\Phi}}$ is evaluated using the formula:

$$\overline{\mathbf{\Phi}} = \frac{1}{|C_i|}\int_{C_i}\phi_h = \frac{\Delta x_{i-1}}{2}\left(\frac{3}{4}u_i + \frac{1}{4}u_{i-1}\right) + \frac{\Delta x_i}{2}\left(\frac{1}{4}u_{i+1} + \frac{3}{4}u_i\right) \tag{3.5}$$

Smooth case: The first test involves the interaction of two symmetric solitary waves, propagating in opposite directions in a flat frictionless channel. This head-on collision is a common test for Boussinesq-type and non-hydrostatic models. After the interaction, one should ideally recover the initial profiles of the two waves with exchanged positions. However, this simple test presents additional challenges to the model by a sudden change of the nonlinear and frequency dispersion characteristics. The numerical model must handle the equilibrium between amplitude and frequency dispersion to propagate the wave profile at a constant shape and speed. We consider a channel 200 [m] long, depth $h_0 = 1$ [m] and two solitary waves with an equal initial hight of $a/h_0 = 0.3$, initially centered respectively at $x = 60$ [m] and $x = 140$ [m]. The computational parameters used are CFL value 0.2, number of nodes 4000 and domain $x \in [0,\ 200][m]$.
Figure 3.16 shows the free surface profiles of the solitary waves in time $t = 5,\ 11$ and 17 [s] for the FV model. Virtually identical results are obtained using the Galerkin and SUPG methods and have not been reported. Each subfigure compares the numerical solutions obtained from the uniform (continuous lines) and the non-uniform meshes (dashed lines). The waves initially propagate undisturbed until they collide. After the collision, as expected, the waves are transformed and a dispersive tail appears. Any influence of mesh irregularity on the results can be observed at this scale.

Breaking case: As an example including wave breaking, we repeat on a perturbed mesh the computation of a solitary wave run-up on a plane beach. The results obtained are shown on figure 3.17 for both the hybrid FV and SUPG methods, using the AB-AM time integrator. Comparing to the results of the previous section, we can again see that the influence of mesh regularity is very small, and perhaps the main impact of the irregularity is on the efficiency of the limiters implemented in detecting the shocks, especially for the SUPG scheme. This is clearly a topic for future improvement.

3.7 Solitary wave on a composite beach

One of the benchmark methods for tsunami model validation and verification, according to the NOOA center for tsunami research, is the propagation

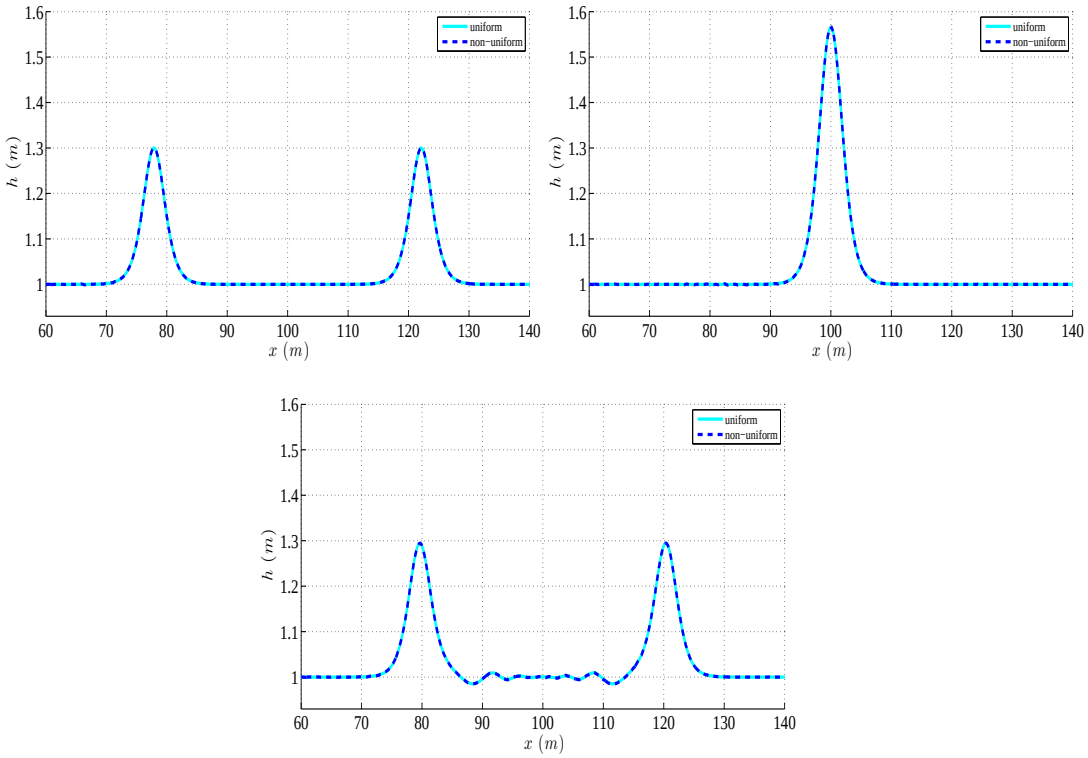

Figure 3.16: Head-on collision of two solitary waves: surface profiles of the solution computed at times $t = 5,\ 11,\ 17$ [sec] for the FV scheme.

of a solitary wave over a composite beach, simulating the Revere beach in Massachusetts. A physical model was constructed at the Coastal Engineering Research Center in Vicksburg, Mississippi by the U.S. Army Corps of Engineers. The configuration of the problem can be found in Marche et Lannes [2015]; Synolakis *et al.* [2007]. The setup of the problem is shown in figure 3.18. The time series of the surface elevation is registered in six gauges, placed at $x = 15.04,\ 17.22,\ 19.04,\ 20.86,\ 22.33,\ 22.80$ [m]. We consider two different configurations. The first one is the propagation and breaking of a solitary wave of $\varepsilon = 0.3$, while the second one involves a solitary wave of higher nonlinearity: $\varepsilon = 0.7$. The computational domain used is $x \in [-5,\ 23.23]$ [m], with the initial wave placed at $x = 0$ [m] and $h_0 = 0.218$ [m]. The CFL number is set to 0.2 and a uniform grid is considered with $\Delta x = 0.046$ [m]. A sponge layer of 2 [m] is placed at the left boundary of the domain, while a vertical wall is placed on the right. In the wave breaking tracking criterion a value of $\gamma = 0.6$ is used for the time variation of the surface elevation.

Case (a): Figure 3.19 shows, for the less nonlinear case, the comparison between the experimental data (red circles) and the numerical results:

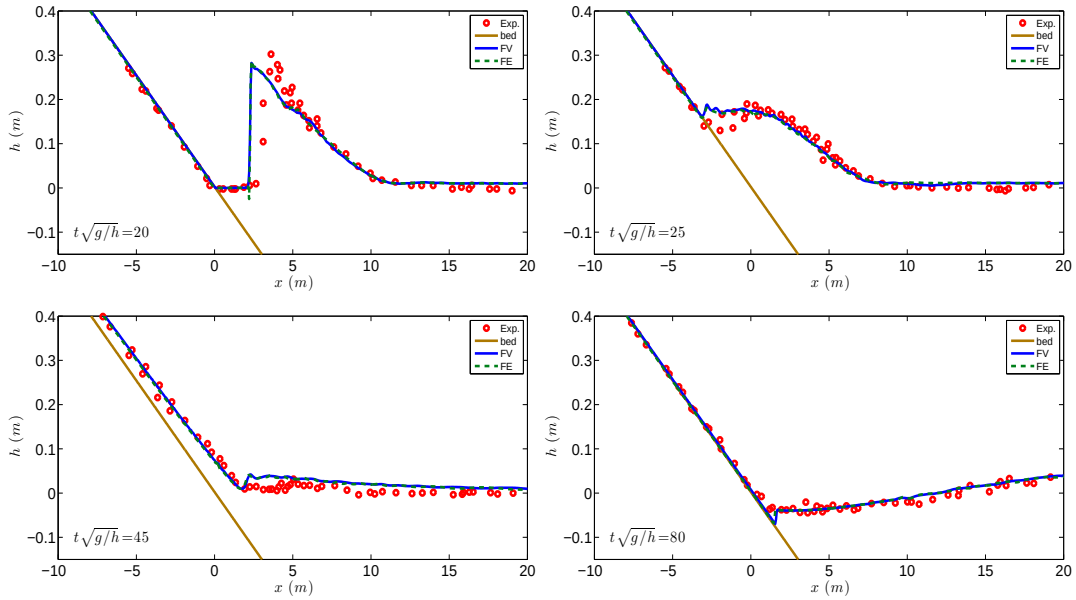

Figure 3.17: Solitary wave run-up on a planar beach: free surface elevation at different increasing times of the simulation (from top-left to bottom-right) performed by the FV and the SUPG (named FE in the figures legend) schemes using a non-uniform mesh.

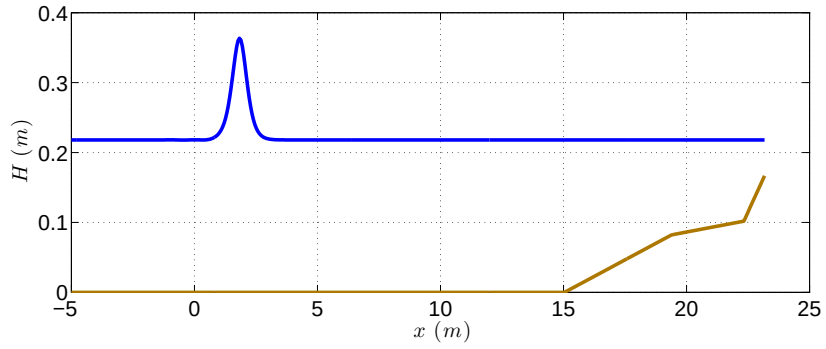

Figure 3.18: Solitary wave on a composite beach: initial setup.

blue lines denote the FV scheme, while green dashed line stay for the SUPG scheme. The solitary travels down the domain, shoals and breaks between the second and the third gauge. After breaking, it continues to travel onshore until it hits the wall, reflects and starts to propagate offshore. A very good match between the experimental data and the numerical results is observed for both the schemes tested in all the wave gauges. Only in gauge 10, the closest to the left boundary of the domain, an equal overestimation of the two amplitude

peaks can be noted for both the methods.

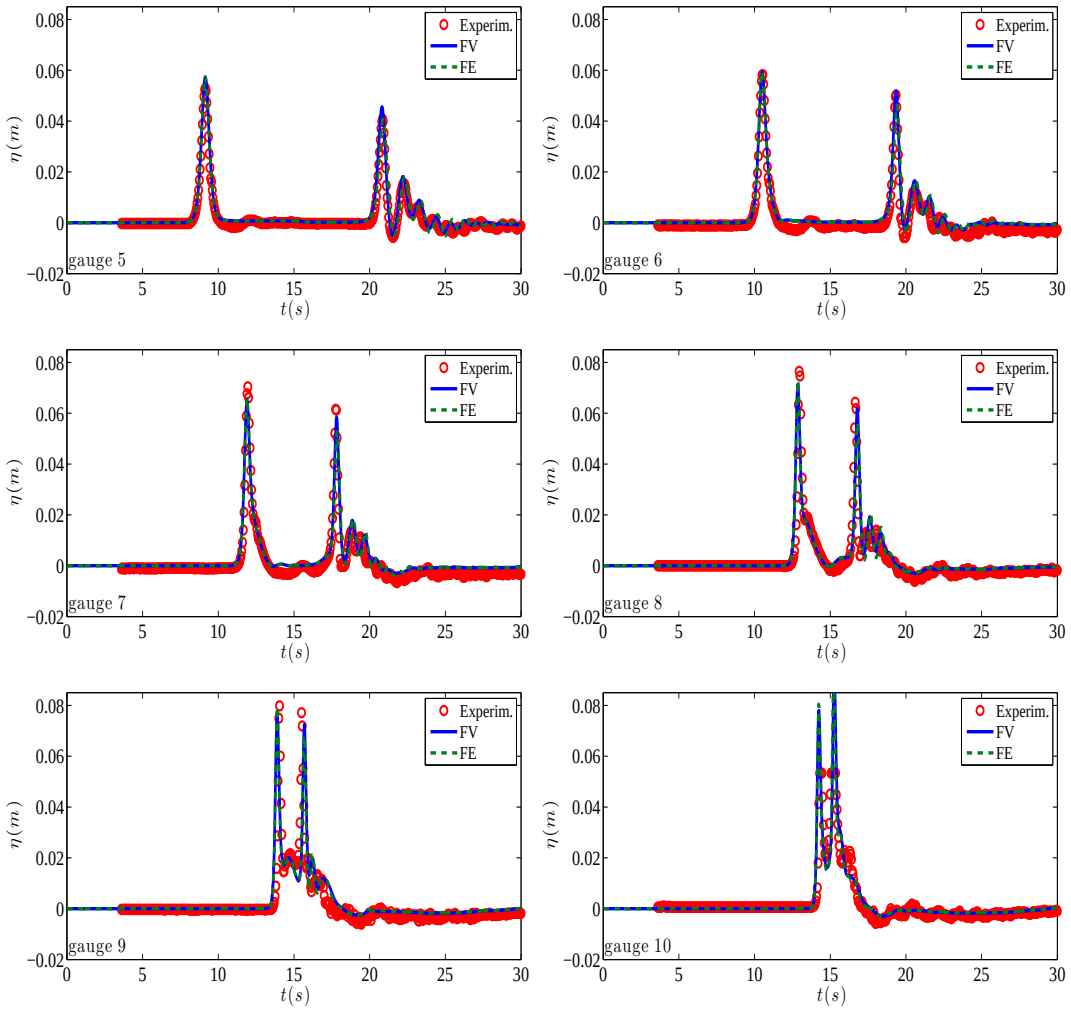

Figure 3.19: Solitary wave on a composite beach, Case (a): Time series of the free surface elevation at gauges locations.

Case (b): In figure 3.20 the numerical results along with the experimental data for the more nonlinear case ($\varepsilon = 0.7$) are presented. The solitary wave is highly non-linear and presents the same behavior described above. It breaks between the second and the third wave gauges, reflects on the wall and travels offshore. Also in this case, the numerical results are in very good agreement with the experimental data.

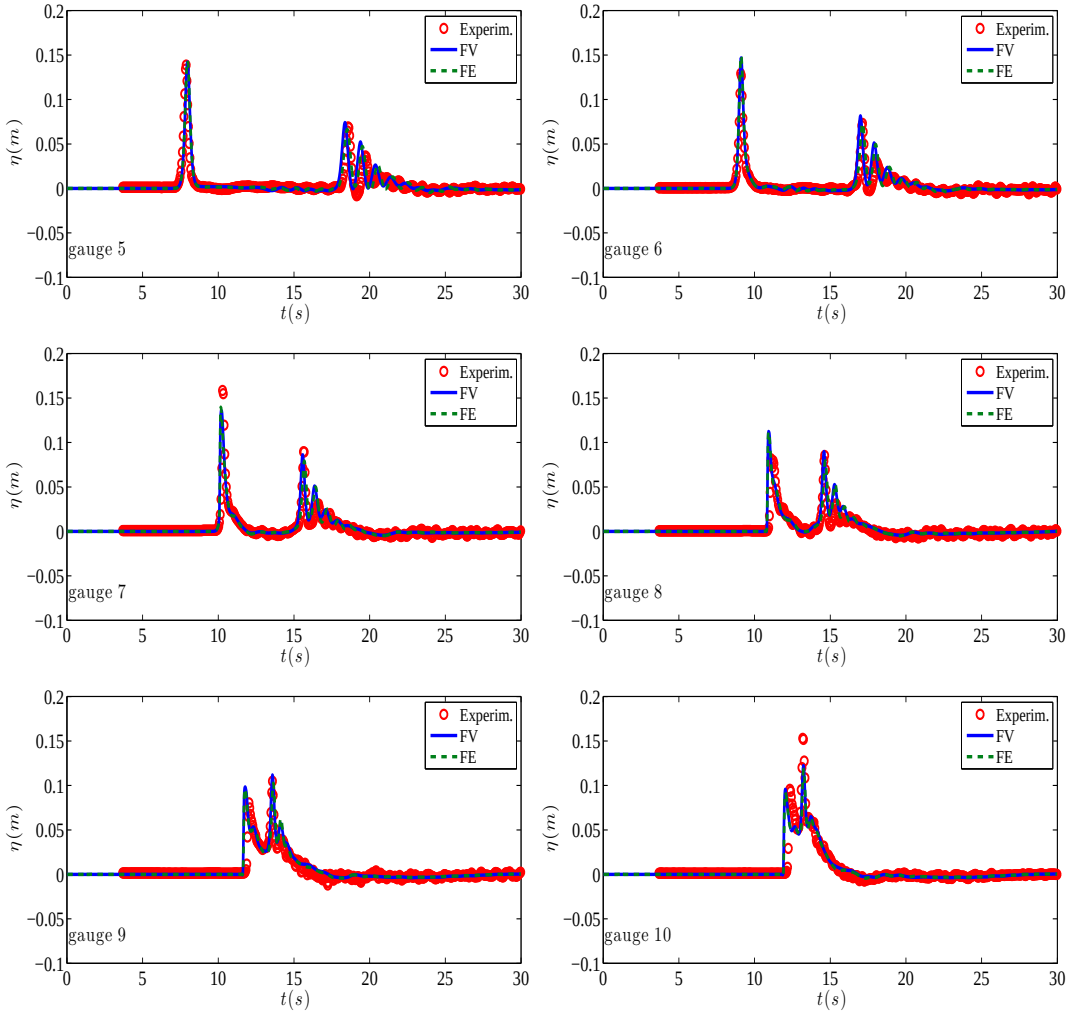

Figure 3.20: Solitary wave on a composite beach, Case (b): Time series of the free surface elevation at the gauges locations.

3.8 Solitary wave propagation over a two dimensional reef

The last experimental test case we consider in one dimension is the solitary wave transformation over an idealized fringing reef. The problem is very challenging and tests the model capability in handling non-linear dispersive waves along with wave breaking, bore propagation, hydraulic jump detection and wall reflection. It has been initially presented in Roeber *et al.* [2010] and the laboratory experiments have been carried out at the O.H. Hinsdale Wave Research Laboratory of Oregon state University from 2007-2009. The test includes a steep slope, along with a reef crest in order to represent fringing reefs. The to-

pography includes a fore reef slope of 1/12, a 0.2 [m] reef crest and an offshore water depth $h_0 = 2.5$ [m]. The reef crest is then exposed by 0.06 [m] and submerges the flat with $h = 0.14$ [m]. The computational domain is $x \in [0, 83.7]$ [m], discretized with a constant grid of size $\Delta x = 0.1$ [m]. A solitary wave of 0.75 [m] amplitude is set at $x = 17.64$ [m]. A CFL number of 0.2 is used, and $\gamma = 0.6$ in wave breaking detection criteria. Wall boundary conditions are placed at each boundary of the computational domain and, as suggested in Roeber et Cheung [2012], a Manning coefficient $n_m = 0.012$ [s/m$^{1/3}$] is used to define the roughness of the concrete surface of the reef. Experimental results for the free surface elevation were recorded at 14 wave gauges along the centerline of the computational domain. Please refer to Roeber *et al.* [2010] for the complete setup of the experiment and the precise position of the gauges.

Figures 3.21 and 3.22 show the measured and computed wave profiles, for both FV and SUPG schemes, as the numerical solitary wave propagates. For additional comparison purposes, we also account for the results obtained by Kazolea et Delis [2013], solving Nwogu's equations (*cf.* Nwogu [1994]) with a FV scheme. As the initially symmetric solitary wave propagates along the inclined bottom, it starts to shoal across the toe of the slope, at $x = 25.9$ [m], and it begins to skew to the wave front. As expected (*cf.* Filippini *et al.* [2015]), during the shoaling (at $t\sqrt{g/h} = 65$), Nwogu's equations slightly over predict the wave height, which is instead better described by the eGN model. The wave begins to break as it approaches the reef, developing a plunging breaker on the top of the reef crest that collapses around $t = 34.5$ [s]. Both the Nwogu and enhanced Green-Naghdi models (and all schemes) are mimicking the breaker as a collapsing bore that slightly underestimates the wave height, but conserved the total mass. The two models give identical results as the wave overtops the reef, deforming both a hydraulic jump and a downstream propagating bore. A difference can be observed in the approximation of the undular bore that forms after the reflection on the wall, overtop the reef and travels offshore. Here, higher amplitudes are observed in the computation using the weakly nonlinear model of Nwogu, clearly visible in the gauge signals on figures 3.23 and 3.24. The figures compare the computed and recorded surface elevation time series at specific wave gauges, respectively before and after the reef. The higher amplitude oscillations may indicate that a different treatment of the breaking mechanism is needed for different PDE models, but this study is beyond the scope of this work.
This experiment is particularly challenging for the breaking criteria used (*cf.* 2.9), which has to deal with stationary and nearly stationary jumps and reflected bores on the flow profile. Stationary hydraulic jumps are correctly recognized by the local slope angle criterion in all instances. The development of an undular bore in the flow justifies the use of the critical Froude termination criterion, which correctly recognizes the non-breaking undular bore which

is resolved by the Green-Naghdi model as it travels in deeper waters.

The recorded data from the wave gauges at $x \leq 50.4$ [m] shows the effect of the dispersive waves on the free surface. The produced train of waves over the increasing water depth and the resulting undulations were intensified as higher harmonics were released. As a matter of fact, wave gauges near the toe of the slope recorded highly dispersive waves of $kh_0 > 30$ Roeber *et al.* [2010]. The hybrid BT model manage to reproduce these highly dispersive waves with the correct phase and height strengths. The time series at $x = 58.1$ [m] present the initial and subsequently overtoppings at the reef crest and confirm the efficiency of the applied wet/dry front treatment. The numerical model reproduced these overtoppings at the correct phase, but slightly overestimated the height of the arrival waves. At the gauges located at $x = 65.38$ [m], 72.7 [m] and 80 [m], the arrival of the initial wave, the first reflected bore from the end wall, its subsequent reflection from the back reef, as well as any subsequent reflections are almost correctly reproduced by the numerical models.
Both the models reproduce the long and intermediate-period oscillations after a long simulation involving a series of wave breaking and reflection in the flume. The conservative structure of the model allows a good description of the transition between super and subcritical flows and the present wave breaking model reproduces surging and plunging waves over the reef. The local deactivation of the dispersive terms in the breaking regions is efficient, it does not originate any source of instability into the simulation and does not alter the dispersion properties of the wave transformation process.

3.9 Discussion on two different breaking formulations

As mentioned in section 2.9.3, in this work we consider two different approaches for the implementation of wave breaking technique in the hybrid schemes. The first approach takes advantage from the fact that the elliptic and the hyperbolic part of the system are completely independent of one another and only the hyperbolic phase is aware of the breaking process. This makes it particular easy to implement in any Shallow Water code, by simply using $\bar{\mathbf{\Phi}}$. In the second approach, we expect to achieve a smoother transition between the two phases, but the breaking condition must be embedded in the elliptic part. In this section we use the two different wave breaking formulations for both the FV and SUPG schemes, with the goal of revealing the differences, if any, the limitations and advantages of each approach by performing test cases involving different wave characteristics and breaking conditions.

First: The first test case performed is the solitary wave propagation over

a plane beach, described in section 3.5. Figure 3.25 shows the numerical results obtained by applying the two different approaches to both schemes and depicts the breaking procedure before the run-up of the wave. The left column corresponds to the FV scheme and the right column to the SUPG scheme. Each snapshot presents the values in space of the free surface elevation and the computed quantity $\bar{\mathbf{\Phi}}$. We must mention that, while for the FV scheme $\bar{\mathbf{\Phi}}_i$ contributes only to the momentum equation, this is not the case for the SUPG scheme in which $\bar{\mathbf{\Phi}}_i$ is coupled by the stabilization term (see eq. 2.30). In all the results, we present only the term contributing to the momentum equation. The numerical results obtained for both schemes are quite similar. We can observe that the first approach of wave breaking tends to be slightly more oscillatory, while the second provides smoother wave profiles.

Second: Next figure describes the same problem but with a refined mesh of 4800 nodes. Here the oscillatory behavior of the first approach is revealed in both schemes, but is more pronounced in the FV scheme. Oscillations are produced during breaking and due to the abrupt switching between the two formulations. They travel offshore and they affect the back of the wave. We must mention that the SUPG scheme is more diffusive during breaking due to the different nature of the limiters used, compared to the FV scheme. Further research on the effects of the limiters during breaking is necessary. We observe that the more we refine the mesh the more oscillations on $\bar{\mathbf{\Phi}}$ are observed. These are introduced to the free surface elevation and eventually lead to solution blow up on refined meshes (*cf.* figure 3.27). A similar behaviour has been observed with other implementations of the hybrid approach (*cf.* Bacigaluppi *et al.* [2014b]; Duran et Marche [2014]; Kazolea *et al.* [2014]).

Third: Figure 3.27 presents the numerical results for a solitary wave of $\varepsilon = 0.5$ propagating in the same inclined topography as before. As expected the wave breaks at an earlier time and once again the figures depict the strong breaking close to the shore. Once more, it can be noticed that the second approach is able to reduce the spurious oscillations originating at the interface between breaking and non-breaking region, producing a smoother transition. Still, the SUPG scheme provides neater free surface profiles with respect to the FV one, thank to a more efficient dissipation of the spurious perturbation which may be due to the different nature of the limiter implemented for the two methods.

Fourth: A different trend can be observed for the wave propagation over a bar test case (*cf.* figure 3.28). The test have been firstly performed using the same uniform mesh with $\Delta x = 0.04$, used to compute the results of section 3.4, without remarking any big difference between the two approaches. The results in this case are not reported inside this manuscript. The simulation has been,

thus, repeated using a finer mesh containing 4000 nodes; the results displayed in figure 3.28 refers to this case. The two formulations provide different descriptions of the water field after the submerged bar, with a phase lag which is perhaps related to the perturbation disturbing the upstream signal. Moreover, we found that the second approach reduces the spurious noise derived from wave breaking on the top of the bar.

Summary: From this brief investigation we can conclude that smoother results can be generally performed using the second breaking formulation. This, also, allows all the coupling to be embedded in the computation of $\overline{\mathbf{\Phi}}$ without the need to modify the hyperbolic part of the code, opening to the possibility to easily introduce both the computation of the dispersive terms and the hybrid wave breaking treatment into an existing Shallow Water solver. Still, the open problem of blowing up solutions for $\Delta x \to 0$ has not been solved, so a fundamental problem of the hybrid schemes remains. Further research on the topic is thus needed.

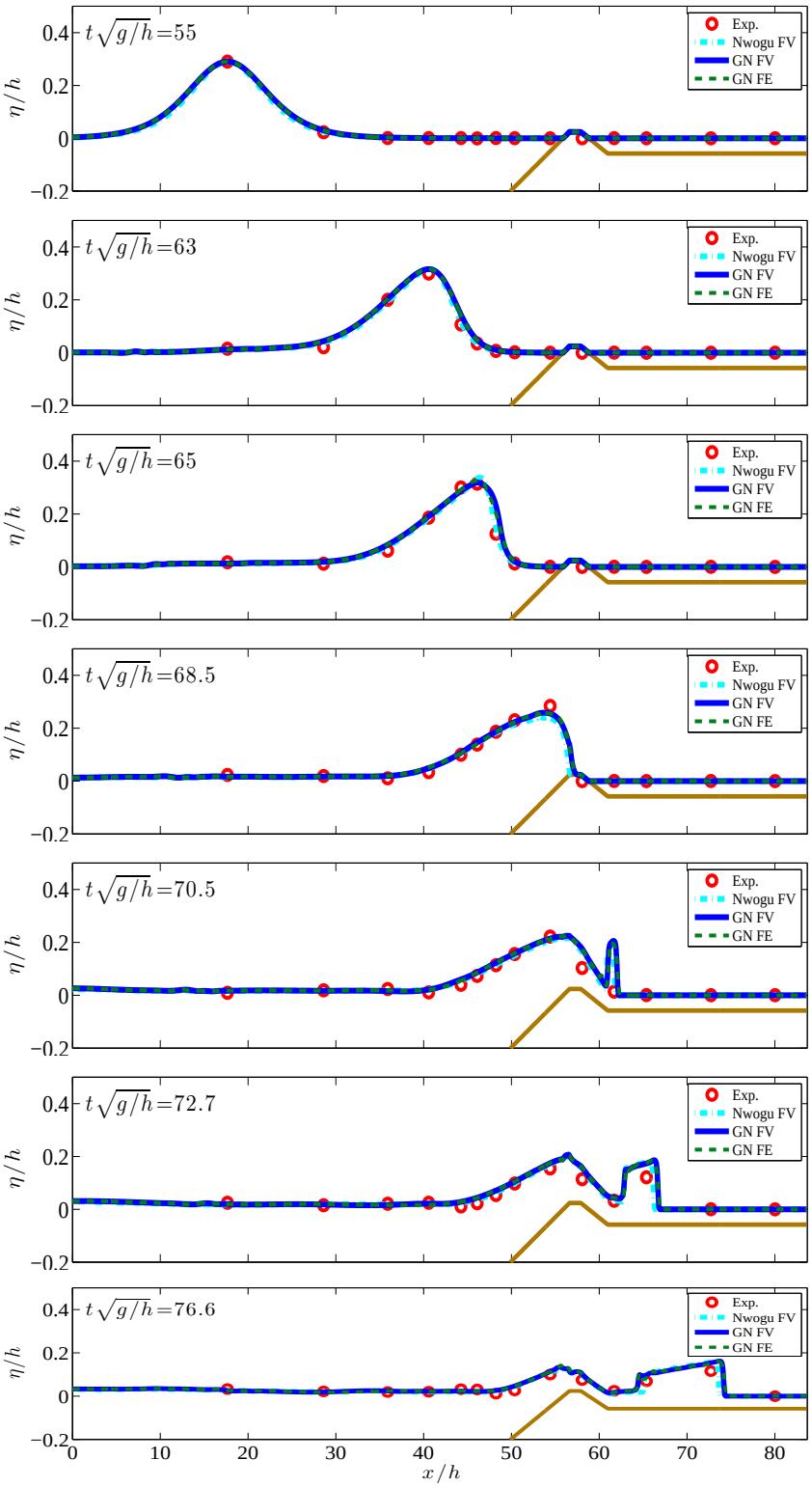

Figure 3.21: Solitary wave propagation over a two dimensional reef (Part I): evolution of the free surface profiles computed by the two GN schemes of this work (FV and SUPG) and by the FV solver of Kazolea *et al.* [2014] for the weakly nonlinear BT equations of Nwogu.

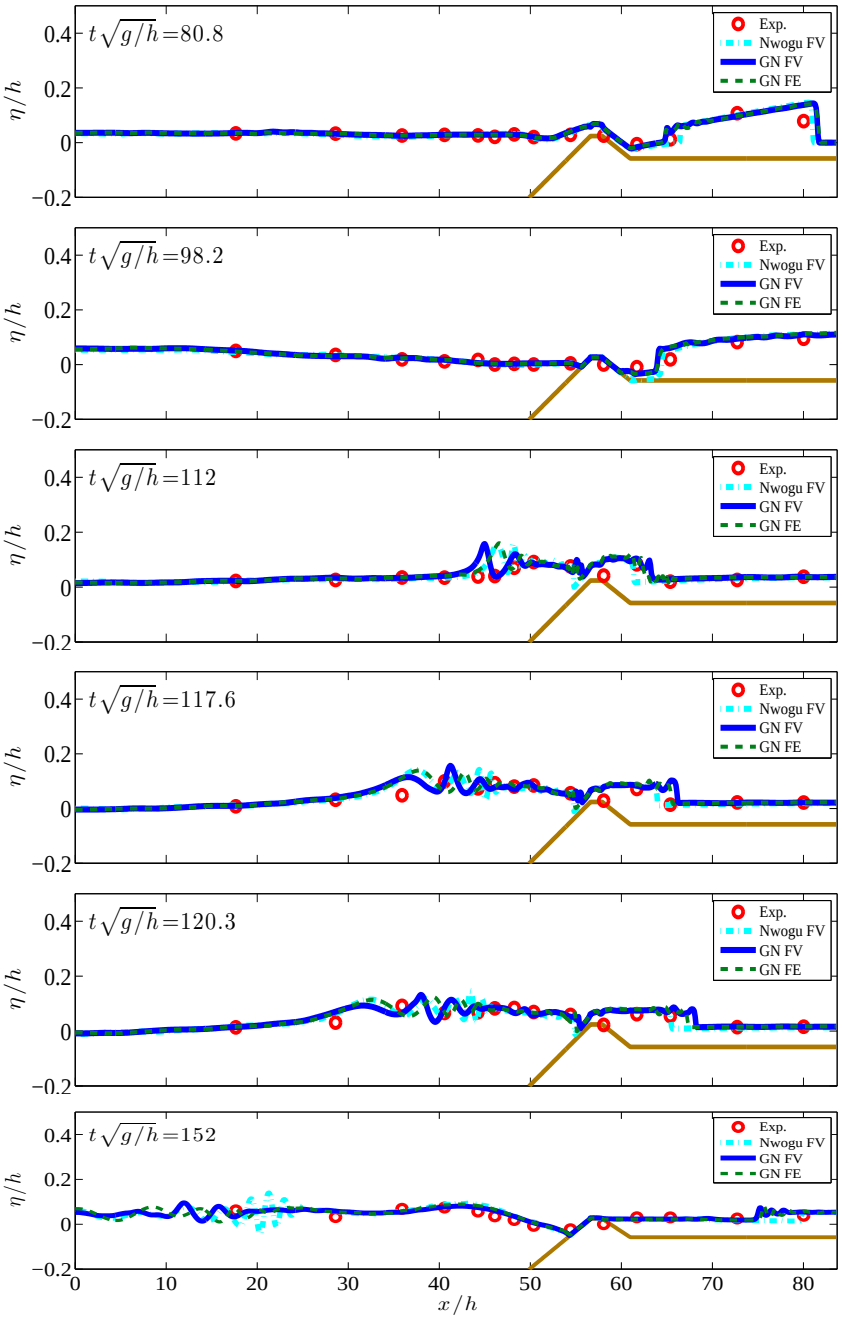

Figure 3.22: Solitary wave propagation over a two dimensional reef (Part II): evolution of the free surface profiles computed by the two GN schemes of this work (FV and SUPG) and by the FV solver of Kazolea *et al.* [2014] for the weakly nonlinear BT equations of Nwogu.

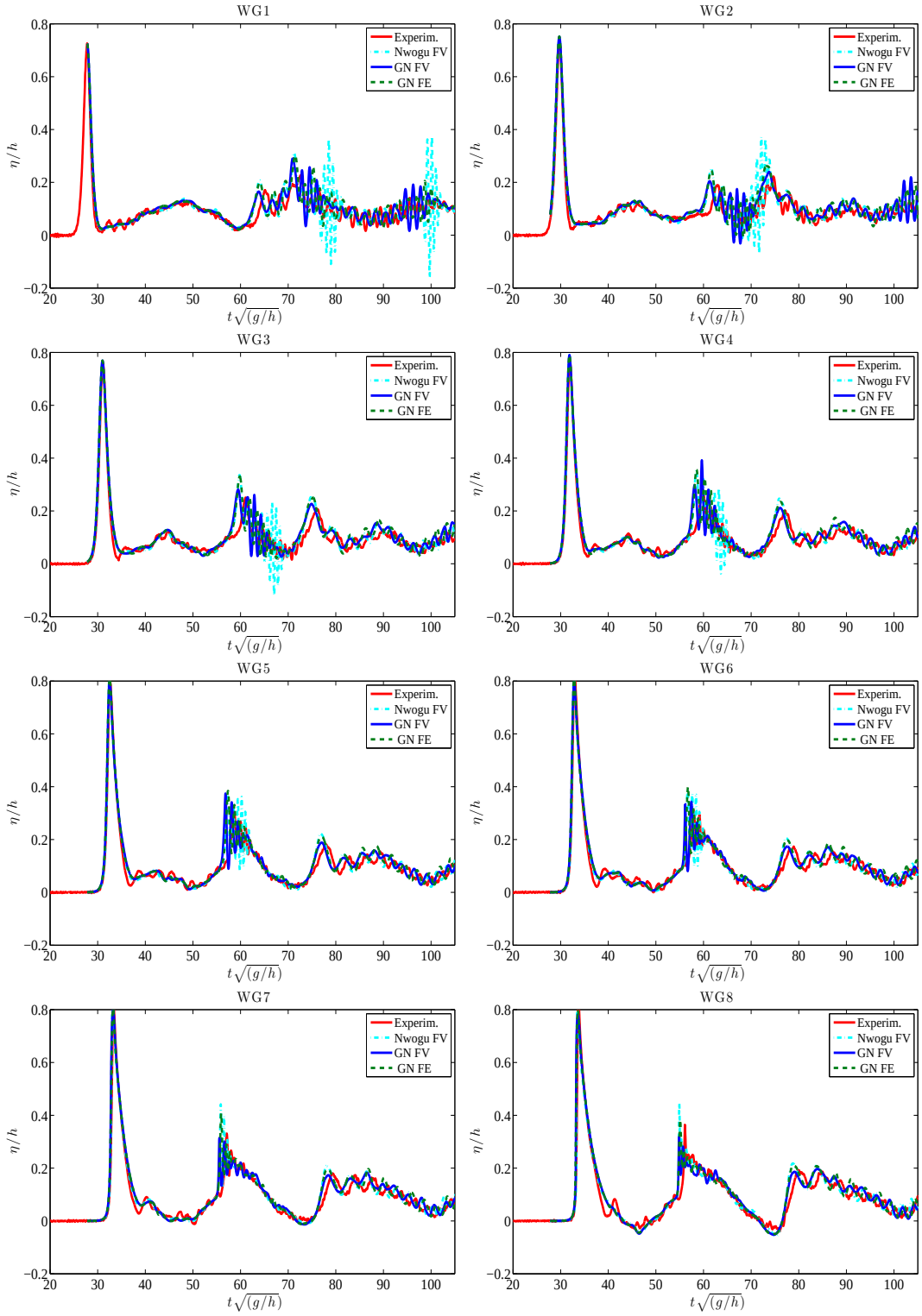

Figure 3.23: Solitary wave propagation over a two dimensional reef: time series of the normalized free surface elevation at the wave gauges locations, before the reef (gauges from 1 to 8).

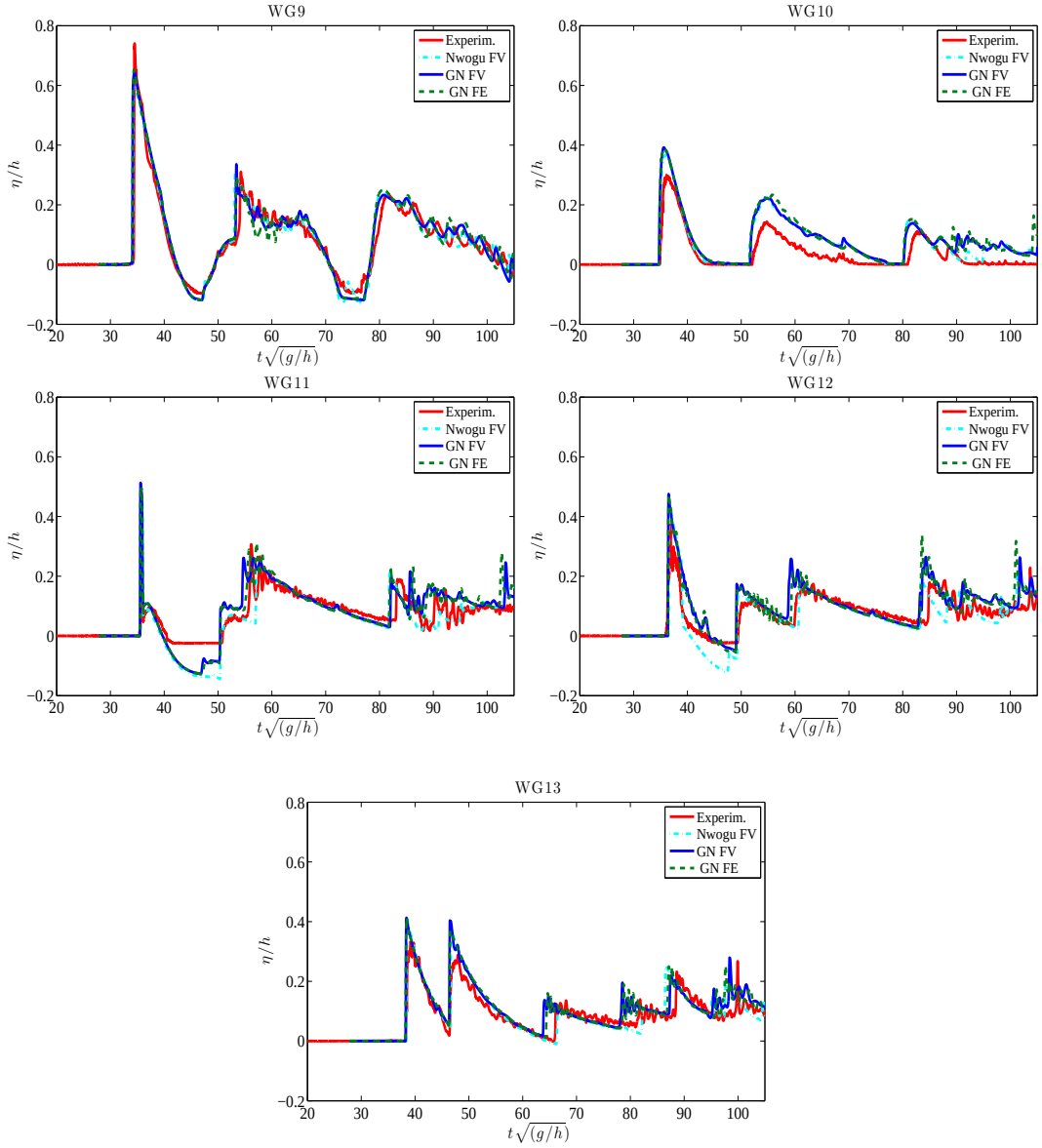

Figure 3.24: Solitary wave propagation over a two dimensional reef: time series of the normalized free surface elevation at the wave gauges locations on top and after the reef (gauges fro 9 to 13).

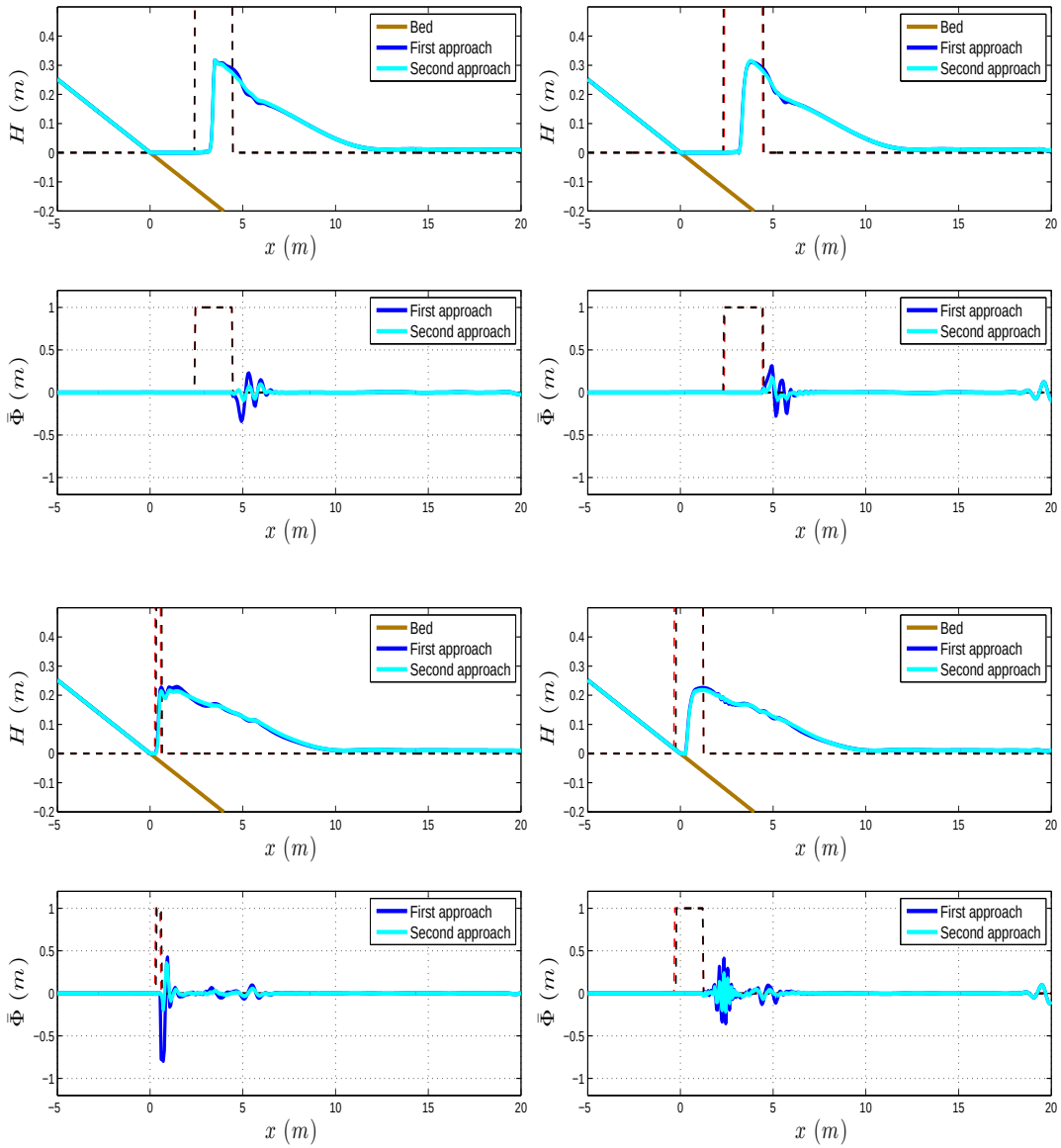

Figure 3.25: Different breaking treatments: values of the free surface elevation and of the non-hydrostatic correction $\bar{\mathbf{\Phi}}$ at two significant time instant (top and bottom), computed by the FV (left) and SUPG (right) schemes, using the two different approaches for wave breaking treatment in the case of a solitary wave of amplitude of $\varepsilon = 0.28$ propagating towards a planar beach. Vertical dashed lines define the breaking region l_{NLSW} where the NLSW equations are solved.

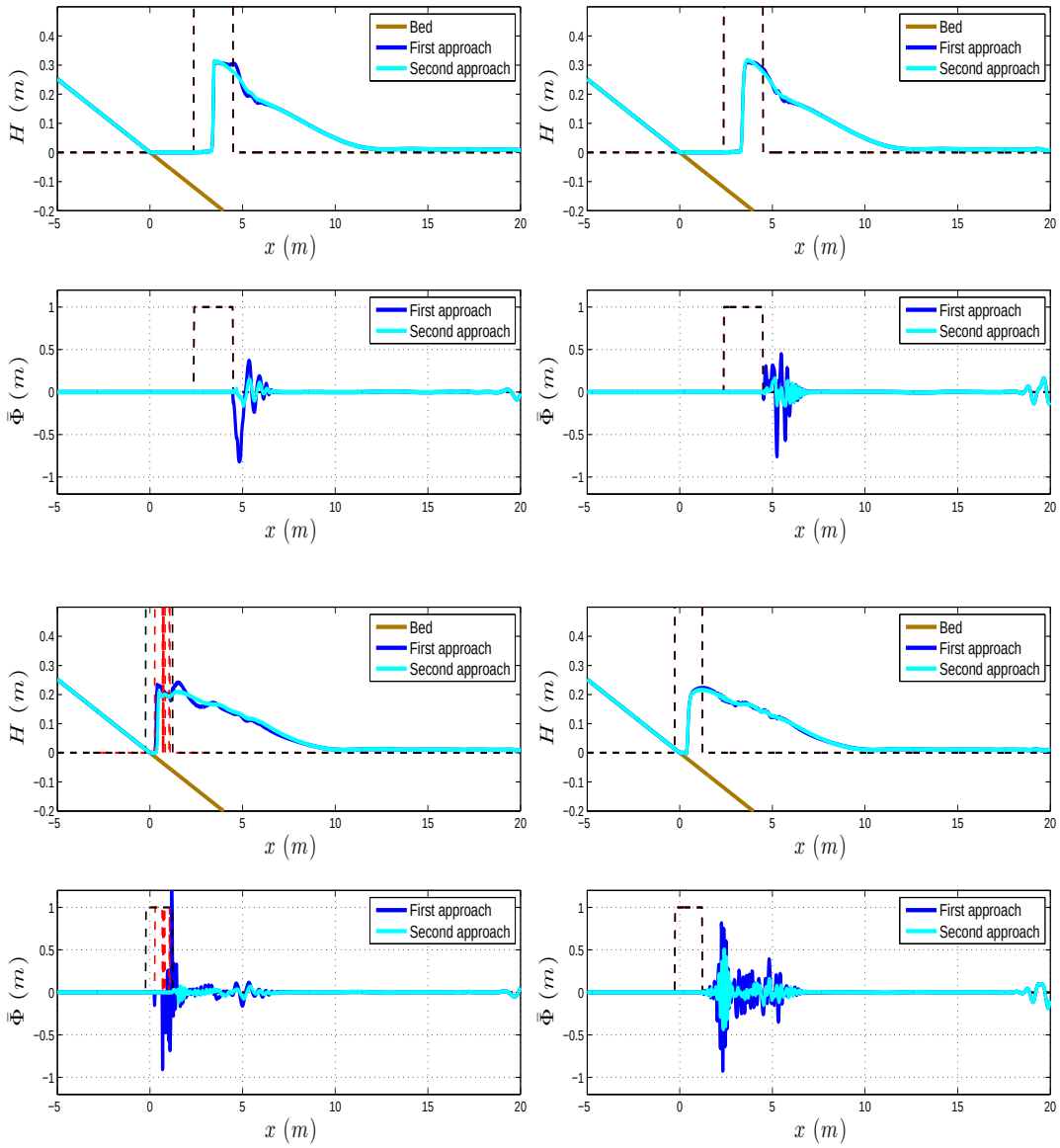

Figure 3.26: Different breaking treatments: values of the free surface elevation and of the non-hydrostatic correction $\bar{\mathbf{\Phi}}$ at two significant time instant (top and bottom), computed by the FV (left) and SUPG (right) schemes, using the two different approaches for wave breaking treatment in the case of a solitary wave of amplitude of $\varepsilon = 0.28$ propagating towards a planar beach. Computation on a refined mesh of 4800 nodes. Vertical dashed lines define the breaking region l_{NLSW} where the NLSW equations are solved.

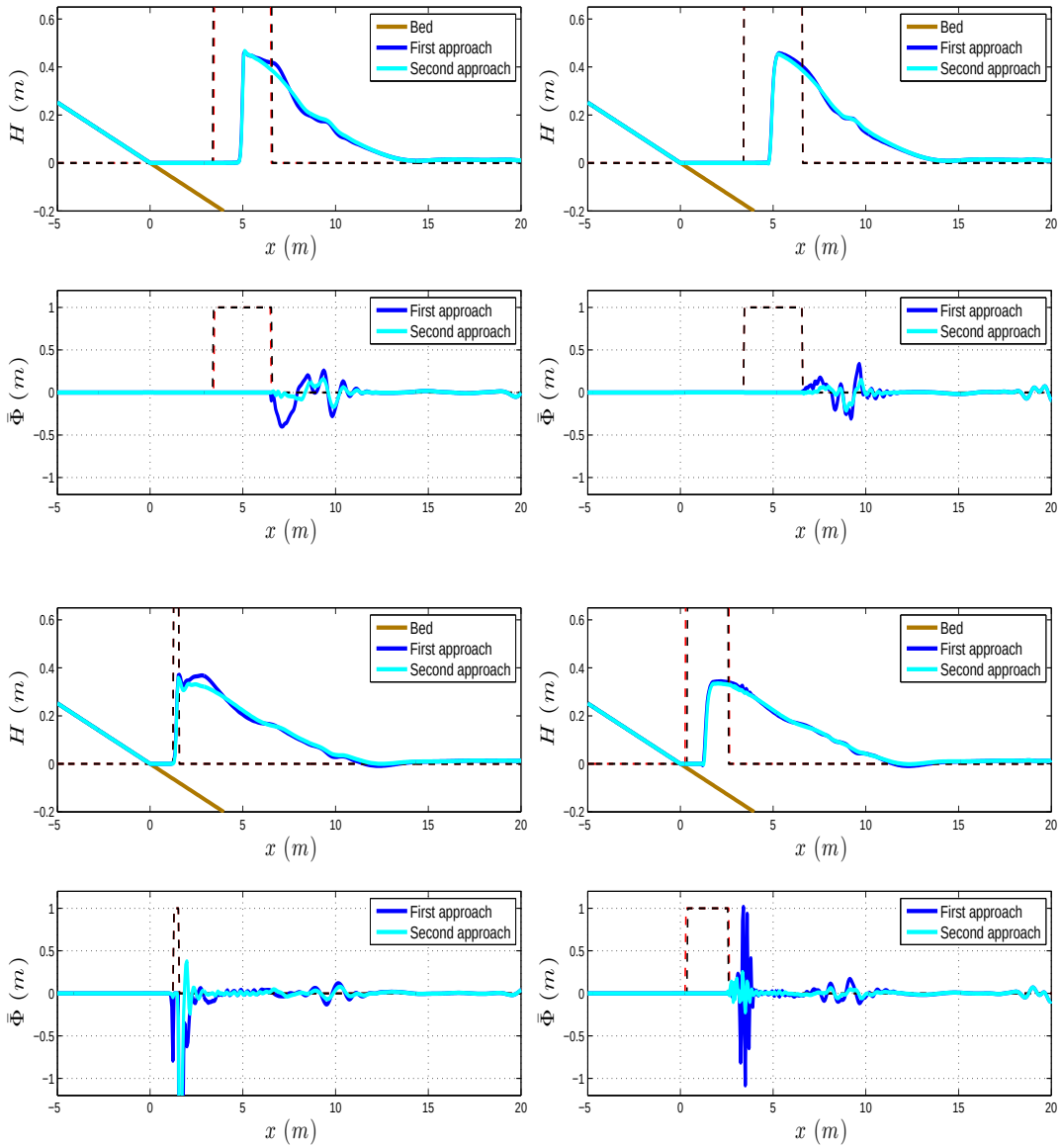

Figure 3.27: Different breaking treatments: values of the free surface elevation and of the non-hydrostatic correction $\bar{\mathbf{\Phi}}$ at two significant time instant (top and bottom), computed by the FV (left) and SUPG (right) schemes, using the two different approaches for wave breaking treatment in the case of a solitary wave of amplitude of $\varepsilon = 0.5$ propagating towards a planar beach. Vertical dashed lines define the breaking region l_{NLSW} where the NLSW equations are solved.

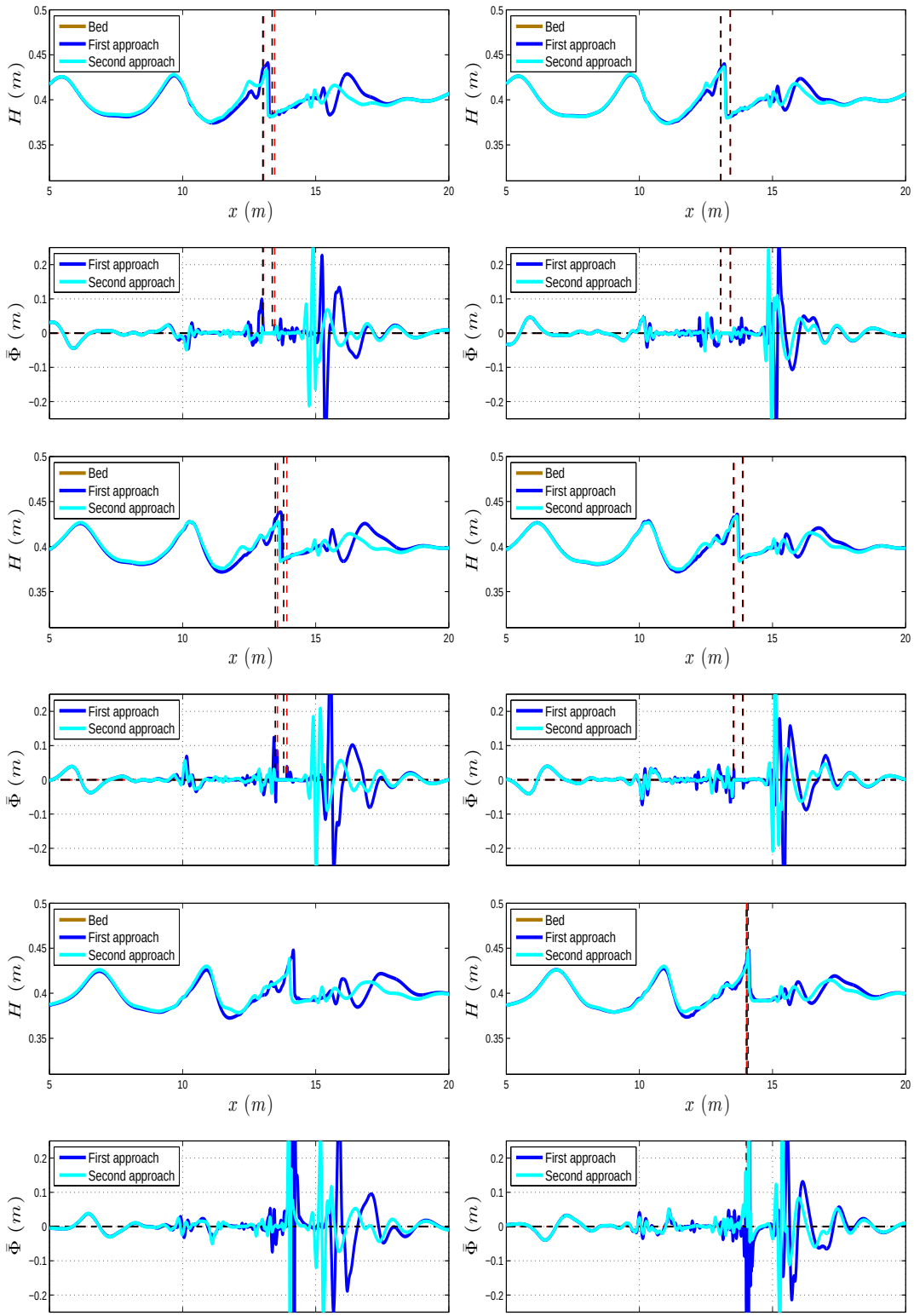

Figure 3.28: Different breaking treatments: free surface elevation and non-hydrostatic term $\bar{\mathbf{\Phi}}$ at three consecutive times (from top to bottom), computed using the FV (left) and SUPG (right) schemes, for periodic waves propagating over a bar. Results performed on a refined mesh containing 4000 nodes.

Chapter 4

Numerical Discretization in Two-Dimensions

Contents

In this chapter we extend the solution strategy, discussed and validated in the previous chapters 2 and 3, to the two-dimensional problem. The system of two-dimensional enhanced Green-Naghdi equations (1.118) is rewritten as in section 2.1:

$$
\begin{aligned}
(I + \alpha T)\,\boldsymbol{\phi} &= \mathcal{W} - \mathcal{R}\,, && (4.1)\\
h_t + \nabla \cdot \mathbf{q} &= 0\,, && (4.2)\\
\mathbf{q}_t + \nabla \cdot \left(\frac{\mathbf{q} \otimes \mathbf{q}}{h} \right) + gh\nabla\eta &= \boldsymbol{\phi}\,,
\end{aligned}
$$

by splitting the original system in its elliptic (4.2) and hyperbolic (4.1) parts, through the definition of the new variable $\boldsymbol{\phi} = [\phi^x \quad \phi^y]^T$, accounting for the dispersive effects and having the role of a non-hydrostatic pressure gradient in the Shallow Water equations. Similarly to what has been done in the one-dimensional case, we use the following definitions: $\mathcal{W} = T(gh\nabla\eta)$ and $\mathcal{R} = h\mathcal{Q}_1(\mathbf{u})$, where the operators $T(\cdot)$ and $\mathcal{Q}_1(\cdot)$ have been defined respectively in (1.119) and (1.120).
We propose an hybrid FE-FV scheme, where the elliptic part of the system is discretize by means of the continuous Galerkin finite element method. In order to increase the efficiency of the scheme in 2D, we have looked to a different implementation of the elliptic solver, which ensures the invertibility of the matrix derived by the discretization of the operator $(I + \alpha T)$. The hyperolic part of the system is discretize, instead, by the two dimensional formulation of the finite volume scheme described in section 2.3 and inspired by the works of Kazolea *et al.* [2012]; Delis *et al.* [2011]; Nikolos et Delis [2009]. In particular we refer to the node centered finite volume approach of Kazolea *et al.* [2012] which has proven to be robust and capable of simulating wave transformations providing accurate results in complex scenarios and over two-dimensional unstructured meshes.

4.1 Elliptic phase: Continuous Finite Element formulation

4.1.1 Exploiting the self-adjoint character of T

In section 1.8, we have already stressed the fact that the coercivity of the operator $(I + \alpha T)$ can be proved, via the variational form of T (*cf.* equation (1.123)). This property descends on the self-adjoint nature of the operator T, and is of primary importance to ensure the invertibility of the matrix derived from the discretization of $(I+\alpha T)$, which is necessary condition for the discrete

equation to be solved. Knowing that, as discussed in section 2.5, the result of the elliptic equation will not be used inside the hyperbolic part in nodes where $h_i \leq \epsilon_h^{wd}$, and simply $\boldsymbol{\phi}_i = (0\,,0)^T$ is set, we define a specific (per unit depth) dispersive correction $\boldsymbol{\psi}$ such that:

$$\boldsymbol{\phi} = h\boldsymbol{\psi}\ . \tag{4.3}$$

We can, thus, formulate the elliptic step using the unknown ψ. The definitions of the operator T (1.121) and of $S_1(\cdot)$ and $S_2(\cdot)$, given in (1.122), lead to the following variational form of the elliptic equation:

$$\int_\Omega h\,\boldsymbol{\nu}\cdot\boldsymbol{\psi} + \alpha\int_\Omega S_1(\boldsymbol{\nu})\,h\,S_1(\boldsymbol{\psi}) + \alpha\int_\Omega S_2(\boldsymbol{\nu})\,h\,S_2(\boldsymbol{\psi}) = \mathrm{RHS}\ , \tag{4.4}$$

being RHS a compact form to write the variational formulation of the right hand side of the equation, and being $\boldsymbol{\nu}$ the vector of components respectively $(\varphi_i\,,0)^T$ or $(0\,,\varphi_i)^T$ (with φ_i the standard linear Lagrange basis functions), if the equation in the x or y direction is taken into account. $\boldsymbol{\psi}_i = (0\,,0)^T$ is imposed when $h_i \leq \epsilon_h^{wd}$.
The use of $\boldsymbol{\psi}$ as an unknown in the FE phase leads to a symmetric positive definite bilinear form on the left hand side of the variational equation (4.4), namely for the matrix of the differential operator $(h + \alpha T)$. The elliptic part of the system is, thus, solved for $\boldsymbol{\psi}$. The value of $\boldsymbol{\phi}$, to use in the conservative hyperbolic equations (4.2), are then recovered nodally *a posteriori* by reverting the definition (4.3).

4.1.2 Discrete Formulation:

Let Ω_h denote, in this chapter, an unstructured triangulation of the spatial domain Ω, with h the reference element size and with K denoting the generic element of area $|K|$. For a node $i \in \Omega_\mathrm{h}$, let K_i denote the set of elements containing the node i. As done in the one space dimension, we consider piecewise linear continuous approximations η_h and $\mathbf{q}_\mathrm{h}$ of the variables of type (2.4), with standard piecewise linear continuous Lagrange bases (*cf.* figure 4.1).

Denoting with $(\cdot)^x$ the component of the vectorial quantity $(\cdot)$ along the x-axis and with $(\cdot)^y$ the one along the y-axis, we define $\boldsymbol{\Psi} = [\Psi^x,\,\Psi^y]^T$, with $\Psi^x = [\psi_1^x(t), \psi_2^x(t), ..., \psi_N^x(t)]^T$ and $\Psi^y = [\psi_1^y(t), \psi_2^y(t), ..., \psi_N^y(t)]^T$, and $\boldsymbol{U} = [U,\,V]^T$, being $U = [u_1(t), u_2(t), ..., u_N(t)]^T$ and $V = [v_1(t), v_2(t), ..., v_N(t)]^T$. The discrete form of the elliptic equation (4.1) will thus read:

$$(\mathbb{M}_\mathrm{H}^\mathrm{G} + \alpha\mathbb{T})\boldsymbol{\Psi} = \mathbb{W} - \mathbb{R}\ , \tag{4.5}$$

$$\mathbb{W} = \mathbb{T}\,\boldsymbol{\delta}\ , \tag{4.6}$$

$$\mathbb{R} = \mathbb{Q}\,(h, \mathbf{U})\ , \tag{4.7}$$

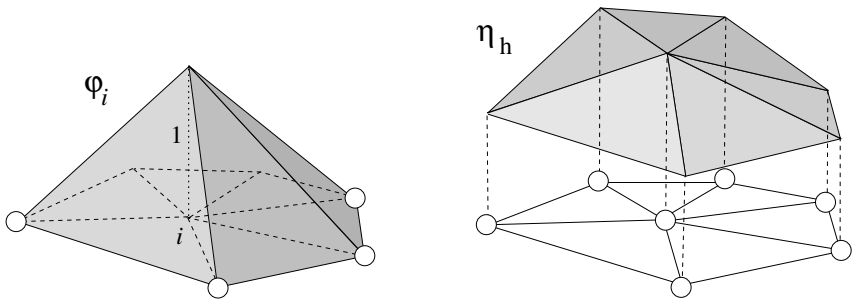

Figure 4.1: P^1 finite element interpolation

with $\boldsymbol{\delta}$ an approximation of $g\nabla\eta$.
The matrix $\mathbb{M}_{\mathrm{H}}^{\mathrm{G}}$ is the four block matrix with zero off-diagonal terms:

$$\mathbb{M}_{\mathrm{H}}^{\mathrm{G}} = \begin{bmatrix} \mathrm{M}_{\mathrm{H}}^{\mathrm{G}} & 0 \\ 0 & \mathrm{M}_{\mathrm{H}}^{\mathrm{G}} \end{bmatrix} ,$$

where $\mathrm{M}_{\mathrm{H}}^{\mathrm{G}}$ is the symmetric positive definite matrix whose entries are represented by:

$$\left(\mathrm{M}_{\mathrm{H}}^{\mathrm{G}}\right)_{i,j} = \int_{\Omega_{\mathrm{h}}} h\,\varphi_i\,\varphi_j \ . \tag{4.8}$$

The matrix is no more time invariant, as instead was M^{G}, and needs to be recomputed at any time iteration.
The operator $\mathbb{T}(h_{\mathrm{h}}, b_{\mathrm{h}})$ is a matrix differential operator of order two, acting on two dimensional vectors, which can be written as:

$$\mathbb{T} = \begin{bmatrix} \mathrm{T}^{11} & \mathrm{T}^{12} \\ \mathrm{T}^{21} & \mathrm{T}^{22} \end{bmatrix} .$$

We call $\mathbb{T}_{i,j}^{m,n}$ the element (i,j) belonging to the block (m,n) of the matrix $\mathbb{T}$. Its fully discrete expression is obtained evaluating, with approximate numerical quadrature over each mesh element and the hypothesis of piecewise linear variations of all the quantities involved, the following series of integrals (obtained by the assumption of periodic boundary conditions):

$$\mathbb{T}_{i,j}^{m,n}(h_{\mathrm{h}}, b_{\mathrm{h}}) = \frac{1}{3}\int_{\Omega_{\mathrm{h}}} \partial_{X_m}(\varphi_i)\, h_{\mathrm{h}}^3\, \partial_{X_n}(\varphi_j) - \frac{1}{2}\int_{\Omega_{\mathrm{h}}} \varphi_i\, h_{\mathrm{h}}\, \partial_{X_n}(\varphi_j)\, \partial_{X_m}(b_{\mathrm{h}}) +$$
$$- \frac{1}{2}\int_{\Omega_{\mathrm{h}}} \partial_{X_m}(\varphi_i)\, h_{\mathrm{h}}^2\, \partial_{X_n}(b_{\mathrm{h}})\, \varphi_j + \int_{\Omega_{\mathrm{h}}} \varphi_i\, h_{\mathrm{h}}\, \partial_{X_n}(b_{\mathrm{h}})\, \varphi_j\, \partial_{X_m}(b_{\mathrm{h}}) \ ,$$

where $\{X\} = \{x,\, y\}$ and $m = 1, 2$ and $n = 1, 2$.
As already remarked in section 1.8, T does not define a scalar elliptic equation,

but a coupled system for the vector $\boldsymbol{\Psi}$. This makes the computation of this phase costly compared to the diagonal model proposed by Lannes et Marche [2015].

Proceeding similarly, the full discrete form for the operator $\mathbb{Q}[h_\mathrm{h}, \mathbf{u}_\mathrm{h}, b_\mathrm{h}, \boldsymbol{\delta}_{b\mathrm{h}}]$ is found by evaluating, with a quadrature approximation over each triangle of the mesh and with the hypothesis of piecewise linear variation of the quantities involved, the following series of integrals:

$$\begin{aligned}\mathbb{Q}[h_\mathrm{h}, \mathbf{u}_\mathrm{h}, b_\mathrm{h}, \boldsymbol{\delta}_{b\mathrm{h}}] = &-\frac{2}{3}\int_{\Omega_\mathrm{h}} \nabla\varphi_i \left(h_\mathrm{h}^3\big(\nabla u_\mathrm{h}\cdot\nabla^\perp v_\mathrm{h}\big) + \big(\nabla\cdot\mathbf{u}_\mathrm{h}\big)^2\right) + \\ &+\int_{\Omega_\mathrm{h}} \varphi_i\, h_\mathrm{h}^2 \left(\big(\nabla u_\mathrm{h}\cdot\nabla^\perp v_\mathrm{h}\big) + \big(\nabla\cdot\mathbf{u}_\mathrm{h}\big)^2\right)\nabla b_\mathrm{h} + \\ &-\frac{1}{2}\int_{\Omega_\mathrm{h}} \nabla\varphi_i\, h_\mathrm{h}^2 \left(u_\mathrm{h}^2\,\partial_x\boldsymbol{\delta}^x_{b\mathrm{h}} + v_\mathrm{h}^2\,\partial_y\boldsymbol{\delta}^y_{b_\mathrm{h}} + 2\,u_\mathrm{h}\,v_\mathrm{h}\,\partial_x\boldsymbol{\delta}^y_{b\mathrm{h}}\right) + \\ &+\int_{\Omega_\mathrm{h}} \varphi_i\, h \left(u_\mathrm{h}^2\,\partial_x\boldsymbol{\delta}^x_{b\mathrm{h}} + v_\mathrm{h}^2\,\partial_y\boldsymbol{\delta}^y_{b_\mathrm{h}} + 2\,u_\mathrm{h}\,v_\mathrm{h}\,\partial_x\boldsymbol{\delta}^y_{b\mathrm{h}}\right)\nabla b_\mathrm{h}\ .\end{aligned} \tag{4.9}$$

As direct consequence of the linear dispersion analysis performed on the one-dimensional scheme in section 2.7.2 and of the resulting optimum configuration that have been found to minimize the dispersion error with respect to the continuous expression (1.15), also in the two-dimensional scheme we use non-lumped mass matrix in equation (4.5) and for the reconstruction of the auxiliary variables $\boldsymbol{\delta}_\mathrm{h}$ and $\boldsymbol{\delta}_{b\mathrm{h}}$:

$$\begin{aligned}\big(\mathbb{M}^\mathrm{G}\boldsymbol{\delta}_\mathrm{h}\big)_i &= \int_{\Omega_\mathrm{h}} \varphi_i\, g\, h_\mathrm{h}\,\nabla\eta_\mathrm{h}\ , \\ \big(\mathbb{M}^\mathrm{G}\boldsymbol{\delta}_{b\mathrm{h}}\big)_i &= \int_{\Omega_\mathrm{h}} \varphi_i\,\nabla b_\mathrm{h}\ .\end{aligned} \tag{4.10}$$

Note that the cost of solving the additional linear system (4.10) is payed just once at the beginning of the simulation since the bed is invariant in time. Finally, the complete discrete linear system is solved by making use of the standard functionalities of the MUMPS algebraic library (*cf.* Amestoy *et al.* [2001, 2006]) to factorize the $(\mathbb{M}^\mathrm{G}_\mathrm{H} + \alpha\mathbb{T})$ matrix in any time step of the simulation. Please refer to the cited references and to the official documentation of the library for more informations about MUMPS and the techniques there implemented. Here we limit to say that MUMPS is a direct solver, the use of iterative methods (or matrix free as GMRES) or simple methods exploiting the symmetric nature of the system (*cf.* conjugate gradient) must be exploited in the future.

4.2 Hyperbolic phase: Finite Volume Scheme

For the two-dimensional spatial discretization of the hyperbolic part of the eGN system (4.1)-(4.2), we use the node centered finite volume scheme developed and validate in Kazolea [2013]; Kazolea *et al.* [2012]; Delis *et al.* [2011]; Nikolos et Delis [2009], based on a third order MUSCL reconstruction of the fluxes.
In this finite volume framework, the triangulation of Ω used for the finite element discretization of the elliptic phase provides what we refer to as *mesh*. In the node-centered discretization, a *median-dual* partition is used to generate non-overlapping control volumes, covering the entire computational domain (*cf.* figure 4.2). We denote by C_i the median dual cell obtained by joining the gravity centers of the triangles in K_i with the midpoints of the edges meeting in the node i, being K_i the set of triangles of the mesh containing i (as in the FE notation). We can thus write:

$$|C_i| = \sum_{\mathrm{K}\in\mathrm{K}_i} \frac{|\mathrm{K}|}{3} \ .$$

The interface belonging to adjacent nodes i, j is named ∂C_{ij} and is composed by the union of two segments connecting the barycenters of the two triangles satisfying $K \ni i, j$ with the midpoint of the edge ij (*cf.* figure 4.2). The boundary of the median dual cell of i can thus be defined as:

$$\partial C_i = \sum_{j\in\mathrm{K}_i} \partial C_{ij} \ .$$

Moreover, we define $\mathbf{r}_{ij}$ the vector connecting nodes i and j, while the normal and the area associated to the interface ij are:

$$\mathbf{n}_{ij} = \frac{1}{2} \sum_{\mathrm{K}\ni i,j} \mathbf{n}_{ij}^{\mathrm{K}} \ , \qquad |C_{ij}| = \sum_{\mathrm{K}\ni i,j} |C_{ij}^{\mathrm{K}}| \ ,$$

with $|C_{ij}^{\mathrm{K}}| = \frac{|\mathrm{K}|}{6}$.

The scheme will evolve approximations of the solution averages over the standard median dual cells that will be denoted, as in the one-dimensional case, as:

$$\mathbf{U}_i(t) = \frac{1}{|C_i|} \int_{C_i} \mathbf{U}(\mathbf{x}, t) \ , \tag{4.11}$$

being $\mathbf{U}$ the vector of the conservative variables $\mathbf{U} = [h,\, hu,\, hv]^T$.
To be consistent with the notation used in section 2.3, we rewrite the system of conservation laws (4.2) as:

$$\mathbf{U}_t + \nabla \cdot \mathbf{H}(\mathbf{U}) = \mathbf{S}_b + \mathbf{\Phi} \ , \tag{4.12}$$

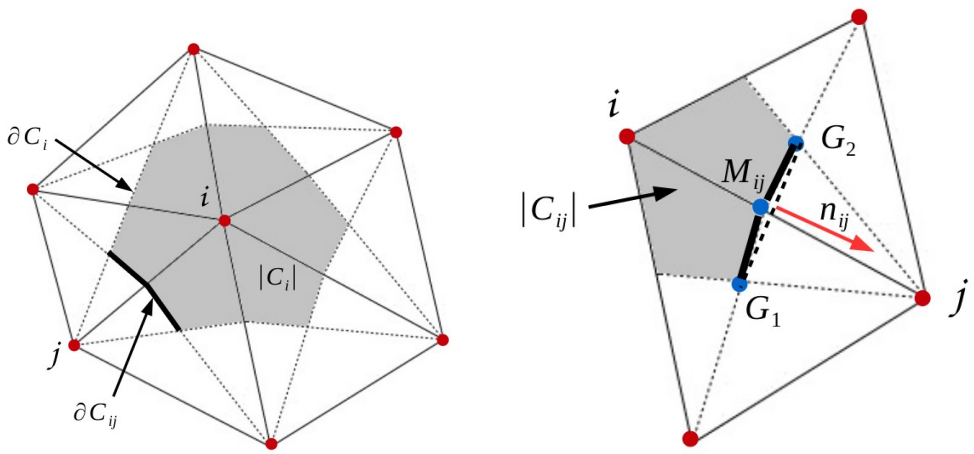

Figure 4.2: Finite volume: median dual control cell definition for an internal node i of the mesh (left), basic notation for the ij interface.

where $\mathbf{H}(\mathbf{U})$ denote the flux vector of components $\mathbf{F}(\mathbf{U})$ and $\mathbf{G}(\mathbf{U})$ in respectively the x and y directions, and $\mathbf{\Phi} = [0, \phi^x, \phi^y]^T$ represents the dispersive terms of the eGN equations, computed in the elliptic part via the continuous finite element discretization and treated here just like a simple source term, thank to the decoupled approach proposed.
The integral form of (4.12) reads:

$$\frac{\partial}{\partial t}\int_\Omega \mathbf{U} + \int_\Omega \nabla \cdot \mathbf{H}(\mathbf{U}) = \int_\Omega (\mathbf{S}_b + \mathbf{\Phi}) \ . \tag{4.13}$$

After the application of the Gauss divergence theorem to the flux integrals, the integral conservation law (4.13) becomes:

$$\frac{\partial}{\partial t}\int_\Omega \mathbf{U} + \int_{\partial\Omega} \left(\mathbf{H}(\mathbf{U}) \cdot \hat{\mathbf{n}}\right) = \int_\Omega \left(\mathbf{S}_b + \mathbf{\Phi}\right) \ ,$$

being $\hat{\mathbf{n}} = [\hat{n}^x, \hat{n}^y]^T$ the unitary outward vector normal to the boundary of the computational domain $\partial\Omega$.
Using (4.11) in the expression above, we find the evolution equation for the averaged quantities $\mathbf{U}_i$:

$$\frac{\partial \mathbf{U}_i}{\partial t} + \frac{1}{|C_i|}\int_{\partial\Omega} \left(\mathbf{F}\hat{n}^x + \mathbf{G}\hat{n}^y\right) = \frac{1}{|C_i|}\int_\Omega \left(\mathbf{S}_b + \mathbf{\Phi}\right) \ .$$

The flux integral is then split over the interfaces ∂C_{ij} between connected nodes, while the integral of the source term is partitioned in the subcells of the dual mesh contributions C_{ij}, giving:

$$\frac{\partial \mathbf{U}_i}{\partial t} + \frac{1}{|C_i|}\sum_{j\in \mathrm{K}_i}\int_{\partial C_{ij}}\Big(\mathbf{F}\hat{n}^x + \mathbf{G}\hat{n}^y\Big) = \frac{1}{|C_i|}\sum_{j\in \mathrm{K}_i}\int_{C_{ij}} \mathbf{S}_b + \overline{\mathbf{\Phi}}\ , \tag{4.14}$$

where $\overline{\mathbf{\Phi}} = \int_{C_{ij}} \mathbf{\Phi}$, that, as in the one-dimensional approach, is computed by exactly integrating over C_i the piecewise linear polynomial $\boldsymbol{\phi}_{\mathrm{h}}$, obtained from the elliptic phase discussed in the previous section.

For all the edges of the unstructured mesh, the flux vector:

$$\mathbf{H}^*_{ij} = \int_{\partial C_{ij}}\Big(\mathbf{F}\hat{n}^x + \mathbf{G}\hat{n}^y\Big)\ ,$$

has to be computed and added, with the proper sign, to the flux summations for the two adjacent nodes considered i and j. The flux vector is approximated assuming a uniform distribution over ∂C_{ij} and equal to the value that can be computed at the midpoint of the ij edge, namely M_{ij}:

$$\mathbf{H}^*_{ij} = \int_{\partial C_{ij}}\Big(\mathbf{F}\hat{n}^x + \mathbf{G}\hat{n}^y\Big) \approx \Big(\mathbf{F}\hat{n}^x + \mathbf{G}\hat{n}^y\Big)\Big|_{\mathrm{M}_{ij}} ||\mathbf{n}_{ij}|| = \Big(\mathbf{F}n^x_{ij} + \mathbf{G}n^y_{ij}\Big)\Big|_{\mathrm{M}_{ij}}\ . \tag{4.15}$$

A fundamental aspect of the finite volume methods, as already pointed out in one dimension, is the idea of substituting the exact flux at the interface by an approximated Riemann flux depending on the left (L) and right (R) states existing on the two sides of the point M_{ij}. We define these two states as respectively $\mathbf{U}^L_{ij}$ and $\mathbf{U}^R_{ij}$. As in 2.3, in this work we solve the Riemann problem at each interface using the well known and widely used approximate Riemann solver of Roe Roe [1981], based on the assumption that the Jacobian matrix of the system is constant and computed using consistency and conservation conditions. Thus, being $\mathbf{Z}(\mathbf{U}^L_{ij},\, \mathbf{n}_{ij})$ a short notation to represent the scalar product $\mathbf{H}(\mathbf{U}^L_{ij}) \cdot \mathbf{n}_{ij} = \mathbf{F}(\mathbf{U}^L_{ij})\, n^x_{ij} + \mathbf{G}(\mathbf{U}^L_{ij})\, n^y_{ij}$, the Roe-type numerical flux reads:

$$\mathbf{H}^*_{ij} = \frac{1}{2}\Big(\mathbf{Z}(\mathbf{U}^L_{ij},\, \mathbf{n}_{ij}) + \mathbf{Z}(\mathbf{U}^R_{ij},\, \mathbf{n}_{ij})\Big) - \frac{1}{2}|A_{ij}|\Big(\mathbf{U}^R_{ij} - \mathbf{U}^L_{ij}\Big)\ ,$$

with $|A_{ij}|$ the Roe-averaged Jacobian matrix, computed using the Roe-averaged values of the primitive variables $(h,\, u,\, v)$ as:

$$\tilde{h} = \sqrt{h^L h^R}\ ,\ \tilde{c} = \sqrt{g\frac{h^L + h^R}{2}}\ ,$$

$$\tilde{u} = \frac{u^L\sqrt{h^L} + u^R\sqrt{h^R}}{\sqrt{h^L} + \sqrt{h^R}}\ ,\ \tilde{v} = \frac{v^L\sqrt{h^L} + v^R\sqrt{h^R}}{\sqrt{h^L} + \sqrt{h^R}}\ ,$$

and equal to to $[\mathbf{X}|\mathbf{\Lambda}|\mathbf{X^{-1}}]_{ij}$, where $\mathbf{X}_{ij}$ and $\mathbf{X}_{ij}^{-1}$ are respectively the left and right eigenvector matrices and $\mathbf{\Lambda}_{ij}$ is the diagonal matrix having the eigenvalues on the main diagonal.

Higher-Order Reconstruction: In the first part of this work, we have often emphasize the importance to use at least at third order scheme in space and time for the discretization of the BT equation in order to limit the influence of the scheme on the dispersive error of the model. As also in the one-dimensional case, the upwind scheme presented above is only first-order accurate when a constant distribution is assumed on the computational dual cells C_i, namely when the left and right states are approximated with their corresponding values at the dual cells i and j: *i.e.* $\mathbf{U}_{ij}^L = U_i$ and $\mathbf{U}_{ij}^R = U_j$. In order to improve the spatial order of accuracy of the scheme concerned, some finite volume schemes adopt an evaluation of the values of the fluxes at the interface by linear extrapolation of the primitive variables values. This MUSCL reconstruction, proposed by Van Leer [1979], reads for each w component of $\mathbf{W} = [\mathrm{h},\ \mathrm{u},\ \mathrm{v}]^T$:

$$\begin{aligned} w_{ij}^L &= w_i + (\nabla w)_{ij}^L \cdot \hat{\mathbf{r}}_{ij} \ , \\ w_{ij}^R &= w_j - (\nabla w)_{ij}^R \cdot \hat{\mathbf{r}}_{ji} \ , \end{aligned} \tag{4.16}$$

with :

$$\begin{aligned} \hat{\mathbf{r}}_{ij} &= \overline{\mathbf{r}}_i + \frac{\mathbf{r}_{ij}}{2} \ , \\ \hat{\mathbf{r}}_{ji} &= \overline{\mathbf{r}}_j + \frac{\mathbf{r}_{ij}}{2} \ , \end{aligned} \tag{4.17}$$

being $\mathbf{r}_{ij}$ the distance vector between nodes i and j. $\overline{\mathbf{r}}_i$ and j and $\overline{\mathbf{r}}_j$ are respectively the distance between the node i of the mesh and the center of gravity of the dual cell C_i, and the distance between the node j of the mesh and the center of gravity of the dual cell C_j. Note that, when symmetric meshes are used, $\overline{\mathbf{r}}_i = 0$. This term becomes relevant only if very stretched cells are considered but is fundamental for the conservation of the mean property.

The extrapolating gradients $(\nabla w)_{ij}^L$ and $(\nabla w)_{ij}^R$ are computed using a combination of centered and upwind gradients (*cf.* Barth [1992]; Delis et Kazolea [2011]) in order to increase the accuracy of the basic MUSCL reconstruction:

$$
\begin{aligned}
(\nabla w)^L_{ij} \cdot \hat{\mathbf{r}}_{ij} &= \frac{1}{2}\Big((1-\beta)(\nabla w)^u_i \cdot \hat{\mathbf{r}}_{ij} + (1+\beta)(\nabla w)^c_{ij} \cdot \hat{\mathbf{r}}_{ij}\Big) \ , \\
(\nabla w)^R_{ij} \cdot \hat{\mathbf{r}}_{ji} &= \frac{1}{2}\Big((1-\beta)(\nabla w)^u_j \cdot \hat{\mathbf{r}}_{ji} + (1+\beta)(\nabla w)^c_{ij} \cdot \hat{\mathbf{r}}_{ji}\Big) \ ,
\end{aligned}
\tag{4.18}
$$

where $(\nabla w)^c_{ij}$ is the centered gradient and $(\nabla w)^u_i$ and $(\nabla w)^u_j$ are the upwind gradients at nodes i and j respectively, defined by the following formulae:

$$
\begin{aligned}
(\nabla w)^c_{ij} \cdot \hat{\mathbf{r}}_{ij} = (\nabla w)^c_{ij} \cdot \hat{\mathbf{r}}_{ji} &= w_j - w_i \ , \\
(\nabla w)^u_i &= 2(\nabla w)_i - (\nabla w)^c \ , \\
(\nabla w)^u_j &= 2(\nabla w)_j - (\nabla w)^c \ .
\end{aligned}
$$

Following Barth et C. [1989]; Barth [2003]; Barth et M. [2004], the gradient $(\nabla w)_i$ is computed as integral averaged by taking into account that the discrete solution w varies linearly into the dual cell C_i, meaning that the gradient will be constant on C_i (Green-Gauss linear reconstruction). This can be proven to result:

$$
(\nabla w)_i = \frac{1}{|C_i|} \sum_{j \in \mathrm{K}_i} \frac{1}{2}(w_i + w_j)\mathbf{n}_{ij} \ .
$$

The parameter β in (4.18) can be chosen in order to control a family of schemes, as the central differencing (using $\beta = 1$), or the fully upwind scheme (when $\beta = -1$). The value of β which is used in this work is $\beta = 1/3$. This particular value, in fact, leads to a third order accurate upwind scheme, although the strictly third order accuracy is only reached in linear problems and for sufficiently regular meshes (*cf.* Barth [1992]; Koobus *et al.* [2008]).
Alternative higher-order reconstructions have been considered and tested: *e.g.* the reconstruction of the states at the cells interfaces by means of the solution of a least-square minimization problem up to the second order derivatives, or the use of two Gauss quadrature points to solve integral 4.15 (*cf.* Gooch et Van Altena [2002]; Gooch *et al.* [2009] and references therein). However, the approach just presented was preferred due to its simplicity and to the fact that no sensible improvement of the results was observed with the other methods considered.
In order to prevent numerical oscillations in the solution in proximity of discontinuous regions, a strict monotonicity is enforced in the reconstruction by the use of a limiter function ψ. This results in reconstructed values:

$$w_{ij}^L = w_i + \frac{1}{2}\psi\Big((\nabla w)_i^u \cdot \hat{\mathbf{r}}_{ij}, (\nabla w)_{ij}^c \cdot \hat{\mathbf{r}}_{ij}\Big)(\nabla w)_{ij}^L \cdot \hat{\mathbf{r}}_{ij} \ ,$$
$$w_{ij}^R = w_j - \frac{1}{2}\psi\Big((\nabla w)_j^u \cdot \hat{\mathbf{r}}_{ji}, (\nabla w)_{ij}^c \cdot \hat{\mathbf{r}}_{ji}\Big)(\nabla w)_{ij}^R \cdot \hat{\mathbf{r}}_{ji} \ ,$$

where, for our implementation, we have chosen to use the Van Albada-Van Leer edge-based nonlinear slope limiter defined by:

$$\psi(a,b) = \frac{ab + |ab| + \epsilon}{a^2 + b^2 + \epsilon} \ ,$$

with $\epsilon \ll 1$, used to prevent divisions by zero and the limiters activations in smooth regions (usually $\epsilon \approx 10^{-14}$) (*cf.* Venkatakrishan [1993]). As also in the 1D scheme, the limiter is activated only in regions where the NLSW equations are solved.

Interface with FE: As previously mentioned, the FV scheme just discussed will evolve the average solutions over the dual cells C_i. However, the FE elliptic phase needs to know the values of the variables in the nodes of the mesh. When the mesh is symmetric the two values of course coincides, since the mesh node is also the barycenter of C_i. This is not the case anymore when unstructured meshes are used. In very stretched meshes, in particular the error becomes significant. The nodal values are thus reconstructed at every time step using the following approximation:

$$w_i^{\mathrm{h}} = w_i - (\nabla w)_i \cdot \bar{\mathbf{r}}_i \ . \tag{4.19}$$

Topography source term: In order to derive a scheme which respects the C-property, the source term due to the bathymetry gradient must be treated as shown in section 2.3 for the one-dimensional case. This means that it has to be linearized and evaluated at the same Roe-averaged state as the flux flux term. Thus, we introduce the following flux vector $\mathbf{R}_{ij}$ due to the topography source:

$$\int_{C_i} \mathbf{S}_b(\mathbf{U}) = \sum_{j \in K_i} \mathbf{R}_{ij} \ .$$

The upwind discretization of this flux provides, in the case of a first order scheme (*cf.* Hubbard et García-Navarro [2000]; Nikolos et Delis [2009]; Kazolea *et al.* [2012]):

$$\mathbf{R}_{ij} = \frac{1}{2}\Big(\mathbf{X}\big(\mathbf{I} - |\mathbf{\Lambda}|\mathbf{\Lambda}^{-1}\big)\mathbf{X}^{-1}\tilde{\mathbf{S}}_b\Big)_{ij} \ ,$$

which has to be added to the computational cells in order to balance the corresponding flux terms in the hydrostatic conditions, with $(\mathbf{S}_b^*)_{ij}$ approximated in the following way :

$$(\tilde{\mathbf{S}}_b)_{ij} = \begin{bmatrix} 0 \\ -g\dfrac{h^L + h^R}{2}(b^R - b^L)n_{ij}^x \\ -g\dfrac{h^L + h^R}{2}(b^R - b^L)n_{ij}^y \end{bmatrix} .$$

When, instead a MUSCL reconstruction of the state at the interface is used to improve the order of the scheme, as in this case, an additional term $(\mathbf{S}_b^*)_{ij}$ has to added to the previous one in order to keep the balance. This term reads:

$$(\mathbf{S}_b^*)_{ij} = \begin{bmatrix} 0 \\ -g\dfrac{h^L + h_i}{2}(b^L - b_i)n_{ij}^x \\ -g\dfrac{h^L + h_i}{2}(b^L - b_i)n_{ij}^y \end{bmatrix} .$$

Note that the above term vanishes in the case of a first order scheme since $b^L = b_i$.

4.3 Wet/dry fronts treatment

Also in the two-dimensional discretization, some modifications of the scheme are needed in order to treat wet/dry fronts. The same techniques discussed in section 2.5, are adapted for 2D applications. In particular, two thresholds are defined: ϵ_h^{wd} indicates the value below which a cell is considered as dry, while ϵ_u^{wd} indicates the value below which the velocity on a cell is considered as zero. Generally $\epsilon_h^{wd} \ll \epsilon_u^{wd}$, with ϵ_u^{wd} defined by:

$$\epsilon_u^{wd} = \frac{\mathrm{h}^2}{L^2} ,$$

with h the characteristic mesh length and L the characteristic length of the spatial domain. The water mass cut in this way is linearly redistributing among the wet cells of the domain.
In the presence of wet/dry fronts it is fundamental to keep a consistent computation between ∇h and ∇b. In cells without any wet/dry interface, for hydrostatic conditions, it holds $\nabla h = -\nabla b$. However, this is not the case anymore in cells having wet/dry interfaces. In this cases, a first order approximation of the states at the cell interfaces is thus performed.
Moreover, in order to preserve the conservation of the lake at rest condition

when the computational domain contains emerging topographies, the bed elevation is redefined at the wet/dry interface . The exact balance between the bed slope and the hydrostatic terms is obtained by applying (see section 2.5):

$$\Delta b = \begin{cases} h^L & \text{if } h^L > \epsilon_h^{wd} \text{ and } h^R \leq \epsilon_h^{wd} \text{ and } b^R < (b^R - b^L) \ , \\ (b^L - b^R) & \text{otherwise .} \end{cases}$$

In addition to the above bed redefinition, to avoid the flow in motion over adverse slope, we impose at the two faces having a wet/dry front the following conditions for the computation of the corresponding numerical fluxes and source terms:

$$\begin{aligned} &\text{if: } \ h^L > \epsilon_h^{wd} \ \text{ and } \ h^R \leq \epsilon_h^{wd} \ \text{ and } \ h^L < (b^R - b^L) \ , \\ &\text{then: } \ u^L = u^R = 0 \text{ and } v^L = v^R = 0 \ . \end{aligned}$$

This treatment will be, of course, symmetric in the case when the right state is wet and the left one dry.

4.4 Time integration and boundary conditions

In the previous sections we have discussed the spatial discretization of the the two-dimensional eGN system of equations (1.118). In order to obtain a fully discrete scheme, the time evolution operator must be also discretized. In section 2.8, three numerical scheme have been used in the one-dimensional case. In 2D the third order strong stability preserving (SSP) Runge-Kutta (RK) scheme is applied, whose structure has already been described in section 2.8 for the general ODE $\mathbf{U}' = \mathcal{L}(\mathbf{U})$ and will be here just reported for completeness:

$$\begin{aligned} \mathbf{U}^p &= \mathbf{U}^n + \Delta t \, \mathcal{L}(\mathbf{U}^n) \ , \\ \mathbf{U}^{2p} &= \frac{3}{4}\mathbf{U}^n + \frac{1}{4}\mathbf{U}^p + \frac{\Delta t}{4}\mathcal{L}(\mathbf{U}^p) \ , \\ \mathbf{U}^{n+1} &= \frac{1}{3}\mathbf{U}^n + \frac{2}{3}\mathbf{U}^{2p} + \frac{2\Delta t}{3}\mathcal{L}(\mathbf{U}^{2p}) \ . \end{aligned} \tag{4.20}$$

Also in 2D, most of the numerical applications, that will be presented need the addition of a friction term. This term has the form (2.54), it is added to the momentum equation where it plays the role of a stiff dumping term. The explicit treatment of this term may impose a severe time step restriction in presence of dry areas. The semi-implicit approach discussed and applied in section 2.8 is only first order accurate when friction becomes dominating. In

order to tackle this problem, Chertock *et al.* [2015] developed SSP-RK based semi-implicit methods, on both a scalar ODE and system of ODEs, arising from the semi-discretization of the shallow water equations with stiff friction term, which are able to conserve the high-order accuracy of the initial scheme. Denoting a general ODE:

$$\mathbf{U}' = \mathcal{L}(\mathbf{U}) + G(\mathbf{U})\mathbf{U} \ ,$$

with $G(\mathbf{U})$ a general friction term, the approach of Chertock *et al.* [2015] modify the previous RK3 (4.20) steps in the following way:

$$\begin{aligned}
\mathbf{U}^{p} =& \frac{\mathbf{U}^{n} + \Delta t\, \mathcal{L}(\mathbf{U}^{n})}{1 - \Delta t\, G(\mathbf{U}^{n})} \ , \\
\mathbf{U}^{2p} =& \frac{3}{4}\mathbf{U}^{n} + \frac{1}{4} \cdot \frac{\mathbf{U}^{p} + \Delta t\, \mathcal{L}(\mathbf{U}^{p})}{1 - \Delta t\, G(\mathbf{U}^{p})} \ , \\
\mathbf{U}^{3p} =& \frac{1}{3}\mathbf{U}^{n} + \frac{2}{3} \cdot \frac{\mathbf{U}^{2p} + \Delta t\, \mathcal{L}(\mathbf{U}^{2p})}{1 - \Delta t\, G(\mathbf{U}^{2p})} \ , \\
\mathbf{U}^{n+1} =& \frac{\mathbf{U}^{3p} - (\Delta t)^2\, \mathcal{L}(\mathbf{U}^{3p}) G(\mathbf{U}^{3p})}{1 + \left(\Delta t\, G(\mathbf{U}^{3p})\right)^2} \ .
\end{aligned} \tag{4.21}$$

where the fourth additional step is using to perform a correction which allows to recover the third order of the scheme even for friction dominating problems. This scheme is the one used in the applications shown in the next chapter.

Boundary Treatment: As also in 1D, only wall reflective and absorbing boundary conditions have been used in this work. Considering first the wall boundary conditions, a strong imposition is made on the elliptic system considering the following conditions:

$$\boldsymbol{\phi} \cdot \mathbf{n} = 0 \ , \qquad \partial_n \phi^t = 0 \ ,$$

While the first condition simply seems reasonable and can be derived from the momentum equation, considering that $\mathbf{u} \cdot \mathbf{n} = 0$, the second one, which forces the tangent component of $\boldsymbol{\phi}$ to be constant in the normal direction with respect to the wall, seems artificial. Note that this condition can be obtained by requiring that $\nabla \wedge \Phi$ on the wall boundaries (with $\nabla\wedge$ indicating the curl operator), and using the fact that $\partial_t(\phi \cdot \mathbf{n}) = 0$ along these boundaries. The imposition is made by directly modifying the right hand side of (4.5) and the related entries of the matrix operator $(\mathbb{M}^{\mathrm{G}}_{\mathrm{H}} + \alpha\mathbb{T})$.
A strong imposition of the reflective wall boundary is also applied in the hyperbolic phase through the condition: $\mathbf{u} \cdot \mathbf{n} = 0$.

Concerning absorbing boundary conditions and internal wave generation, the techniques used are the same already reported in section 2.8 for the one-dimensional case and they are applied with no changes in the 2D case. We thus refer the interested reader to the cited section and references therein for details.

4.5 Embedding wave breaking

Like in 1D, the hybrid strategy for wave breaking treatment is implemented in the scheme. We first estimate the location of breaking waves using explicit criteria, applying the NLSW equations to solve the flow in the flagged cells and the eGN ones elsewhere. Hybrid wave breaking treatment has been applied by many authors in the last years using different BT models (*cf.* in particular Tonelli et Petti [2009]; Roeber et Cheung [2012]; Shi *et al.* [2012]; Kazolea [2013]; Kazolea *et al.* [2014]) but very rarely on unstructured meshes (*cf.* Kazolea *et al.* [2014]). In Tonelli et Petti [2009, 2010], the authors apply on structured meshes the nonlinearity criterion $\varepsilon = \frac{\eta}{d} > 0.8$ to decide if a wave is breaking, switching off the wave energy dissipation when the value drops below $0.35 - 0.55$. The limitation of this treatment remains, as in 1D, its static and local application, despite its great simplicity. In here, following Kazolea *et al.* [2014], we apply in the two-dimensional framework the combination of two phase-resolving criteria discussed in section 2.9:

- the surface variation criterion: $|\eta_t| \geq \gamma\sqrt{gh}$ with $\gamma \in [0.35, 0.65]$;
- the local slope angle criterion: $||\nabla\eta|| \geq \tan\phi_c$ with ϕ_c the critical angle value .

As in 1D the first criterion flags for breaking when η_t is positive, since breaking starts on the front face of the wave, while the second criterion, acting complementary to the first, is useful for the detection of hydraulic jumps. In this work the value of $\phi_c = 30°$ is used. Moreover, the estimation of the Froude number of the wave is used to established when to switch of the breaking and to detect non-breaking bores.

4.5.1 Practical implementation

It should be stressed that the application of any hybrid approach to the unstructured FV scheme presented here, is not straightforward and a special treatment is in need to perform a stable switch between the eGN and the NLSW equations which minimizes mesh dependence and stability issues on finer meshes. At every time step, the hybrid scheme is applied with the following steps:

1) Check, for any node of the mesh, if any of the two criteria for wave breaking triggering is satisfied.

2) Identify each breaking wave of the domain, creating a list of the nodes belonging to the breaking front. The list is created by starting from a random flagged node and adding the neighboring nodes which are also flagged. The procedure will be iterate considering the neighbors of each new node add into the list and ends when no more breaking nodes are found from the algorithm, or if the ones found are already inside the list.

3) An extension of each wave breaking region is performed, according to the corresponding wave height, following Tissier *et al.* [2012]. We select the nodes of each list having the maximum and minimum values of the coordinates x (x_{max} and y_{max}) and those having the maximum and minimum values of the coordinate y. Further, concerning the x-direction, if $l_{NLSW} = x_{max} - x_{min} < 2.5 l_r$ (see section 2.9) we extend the breaking region including in the nodes list of the breaking wave front those laying in the interval $[x_{min} - 0.5(l_{NLSW} - 2.5 l_r),\ x_{max} + 0.5(l_{NLSW} - 2.5 l_r)] \times [y_{min},\ y_{max}]$. Of course the procedure can be easily adapted for a breaking wave front traveling in the y-direction, but it is not general. In this work, we limit to consider numerical benchmarks with main wave fronts aligned with axis of the computational domain. Of course, a more general procedure to extend the breaking region, considering the direction of propagation of the wave front in the xy plane, remains an important theme for future developments.

4) For each breaking front, we measure the water depth at the wave crest and at the wave trough to compute the Froude number of the wave through (2.55). If $Fr \leq Fr_c$ all the breaking points of the interested wave are un-flagged ans the wave is considered as non-breaking. Following Tissier *et al.* [2012], we have set $Fr_c = 1.3$.

After the characterization of the breaking regions, the NLSW model has to be solved in the flagged part of the domain. For simplicity, in the initial development of the scheme the first approach studied in sections 2.9.3 and 3.9 has been used. The suppression of the dispersive terms of the eGN equations is accomplished in breaking nodes by nodally imposing $\bar{\mathbf{\Phi}}_i = 0$ into 4.14. The elliptic phase of the system is thus not aware of the breaking process.

Chapter 5

Numerical Tests and Results in Two-Dimensions

Contents

In this chapter the two dimensional scheme discussed in chapter 4 is tested against several standard two-dimensional benchmarks, designed in order to assess its accuracy with respect to both experimental data and analytical solutions. We first want to verify our implementation of the schemes to assess that the expected order of accuracy is obtained and test their ability to handle discontinuous solutions and wet/dry fronts in the Shallow Water case. Some of the one-dimensional tests of chapter 3 will be then reproposed and solved using the two-dimensional scheme implemented. This will allow a direct comparison with the results obtained with the 1D hybrid FE-FV scheme of sections 2.2 and 2.3. Finally, genuinely multidimensional benchmarks will be presented, including complex interactions between wave shoaling, breaking, reflections, diffractions.

5.1 Travelling vortex

To verify the numerical order of accuracy for the 2D finite volume scheme in the Shallow water context, we consider the vortex problem proposed in Ricchiuto et Bollermann [2009]. This problem allows to test the ability of the scheme to transport, along the $x-$direction, a vortex described by an analytical perturbation of the total water depth h and of the velocity $\mathbf{u}$, with respect to a rest state characterized by constant $h = 10$ [m] and $u = 6$ [m/s]. For the analytical expressions of the initial conditions of the test, please refer to Ricchiuto et Bollermann [2009]. The vortex is initially placed in the center of a square domain $[0, 1] \times [0, 1]$; periodic boundary conditions are applied to left and right boundaries of the domain, such that after $T = 1/6$ [s] the vortex comes back to its initial position. The computations have been performed on four unstructured grids with topology shown on figure 5.1 (left). The elements of the coarsest mesh had a reference size of $h_K \approx 0.0125$; the other three have been constructed halving the mesh size at each step.

For comparison purposes, the test has been not only performed with the third order finite volume scheme (FV3), discussed in section 4.2, but also using its second order variant. This second order finite volume scheme (FV2) can be obtained by simply setting $\beta = -1$ (*cf.* Barth [1992]) inside the reconstruction of the values of the variables gradients on the left and right states of each edge discontinuity (*cf.* equation (4.18)). The scheme obtained in this way will be also exploited in chapter 6 to investigate the large scale estuarine dynamics of coastal alluvial estuaries.
The grid convergence history of the L^2 norm of the error is plotted in figure 5.1 (right), confirming for both the schemes the theoretical second and third order of accuracy.

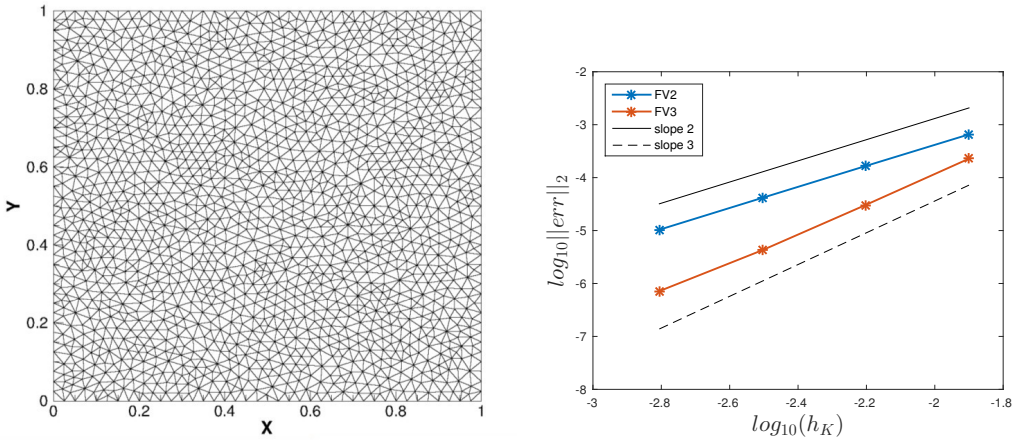

Figure 5.1: Vortex transport: representation of the coarser unstructured mesh used for the computation (left); grid convergence for the 2D FV scheme of section 4.2 (right).

5.2 Asymmetric break of a dam

The next test will assess the capability of the two dimensional scheme to deal with a discontinuous initial solution. The test performed, taken from Ricchiuto *et al.* [2007]; Seaid [2004], consists of the asymmetric break of a dam separating two basins with water depths of 5 and 10 [m]. The computational domain is represented in figure 5.2 (top-left), formed by a square basin of $[0,\ 200]\times[o,\ 200]$ [m], with the discontinuity initially placed in $x = 95$ [m]. For the precise sizes of the geometry please address to the cited works of Ricchiuto *et al.* [2007]; Seaid [2004]. Reflective boundary conditions are used on all boundaries of the computational domain, discretized with a regular unstructured mesh of reference size $h_K = 2.5$ [m], represented in figure 5.2 (top-right) and corresponding to 7480 nodes.

The computation have been run up to time $T = 7.2$ [s]. Figure 5.2 (top-right) shows a 3D visualization of the free surface level computed by the third order finite volume scheme (FV3), while data extracted from along the line $y = 132$ [m] are shown in the bottom picture. Here reference solutions are computed using a finer mesh and a first order finite volume scheme (without the use of the MUSCL reconstruction 4.16). The third order FV scheme appears to well behave in presence of discontinuous solutions, describing sharper shocks and stronger rarefactions and performing a solution which is close to the one performed on a finer mesh of 39130 nodes and in good agreement with what perform by others in the literature (*cf.* Ricchiuto *et al.* [2007]; Ricchiuto [2015]; Seaid [2004]; Nikolos et Delis [2009]). The results show also the good implementation of the Van Albada-Van Leer limiter: in fact, no spurious oscillations appears from the discontinuity.

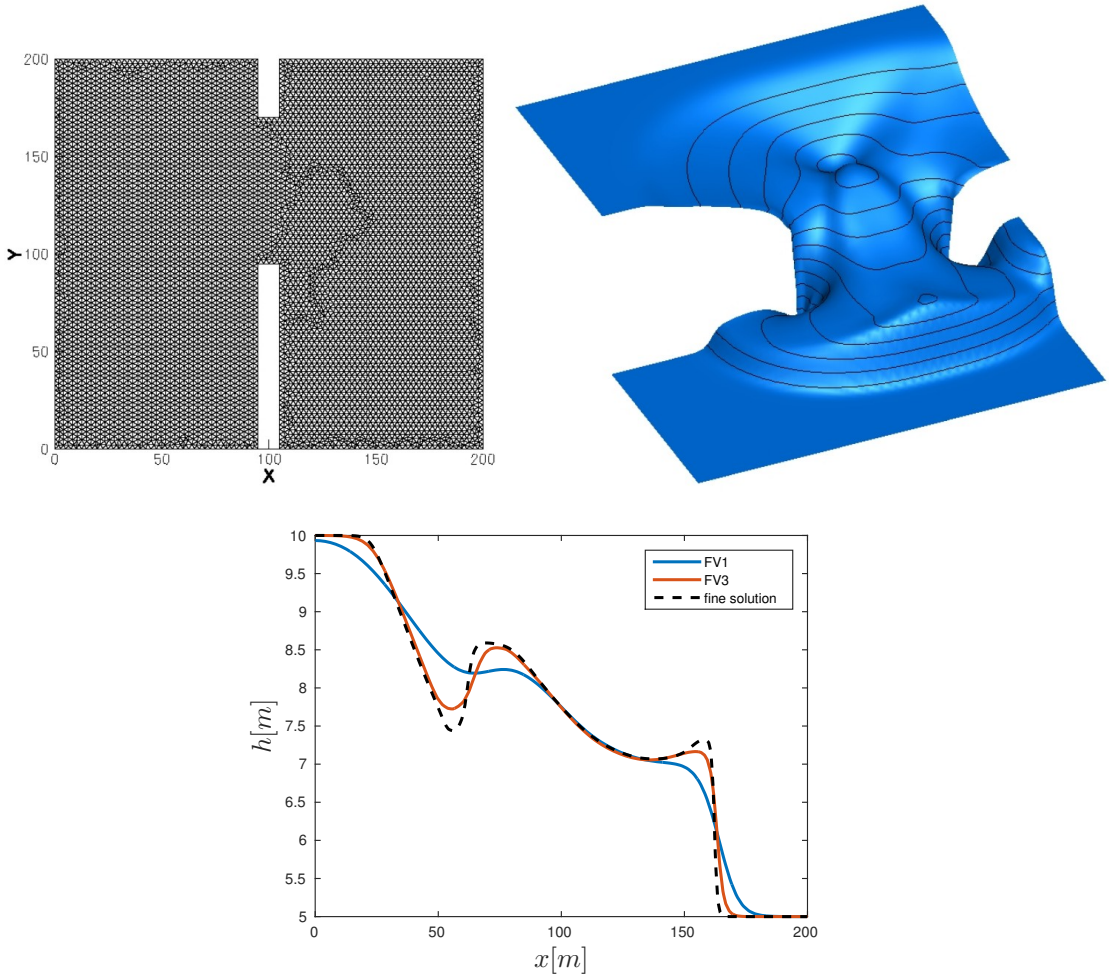

Figure 5.2: Asymmetric break of a dam: sketch of the domain and of the mesh used for the computation (top-left), 3D visualization of the computed solution after $T = 7.2$ [s] (top-right), data extracted along the line $y = 132$ [m] (bottom).

5.3 Thacker's oscillations in a parabolic bowl

To verify the capability of the scheme to provide an accurate and stable approximation of moving shorelines, we consider the periodic oscillations of a curved free surface in a paraboloid (*cf.* Thacker [1981]). Thacker's solutions have been used by a number of researchers in order to evaluate their numerical models (*cf.* Hubbard et Dodd [2002]; Brocchini et Dodd [2008]; Lynett *et al.* [2002]; Marche *et al.* [2007]; Nikolos et Delis [2009]; Ricchiuto et Bollermann [2009]), and the details concerning the setup and exact solutions of the test can be found in Thacker [1981]. Here, a square spatial domain of $[-1.5, 1.5] \times [-1.5, 1.5]$ is considered, which is discretized using an unstructured triangulation with the topology shown in figure 5.3 (right), characterized by reference size of $h_K = 0.025$ and containing 11180 nodes.

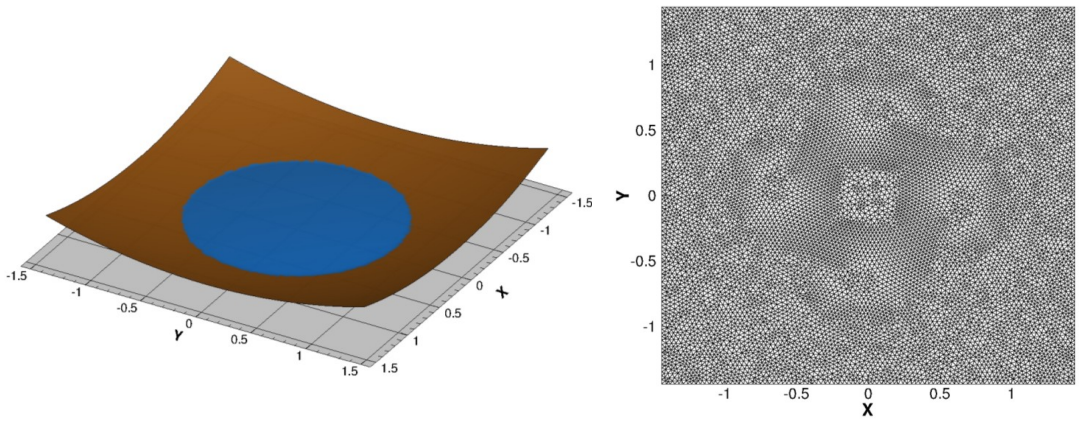

Figure 5.3: Thacker's oscillations in a parabolic bowl: (left) 3D view of the initial solution, (right) topology of the unstructured mesh used for the computation.

The test case chosen has considered as being perhaps the most difficult for a numerical model to accurately represent. One major difficulty is the correct determination of the wet region with acceptable precision. The initial free surface is set at $t = 0$ [s] and let oscillating in absence of friction for three full periods. The results are sketched in figure 5.4 (top left) and 5.4 (bottom left), considering the extracted free surface solution along $y = 0$ at times $t = 3T + \delta t$ with $\delta t = T/6$, $T/3$, $T/2$, $2T/3$, $5T/6$ and T. The computed solutions are nicely close to the analytical ones. Moreover, the close up of the wetting/drying region reported on the right column of figure 5.4 show a very accurate and oscillation free capturing of the moving shoreline.

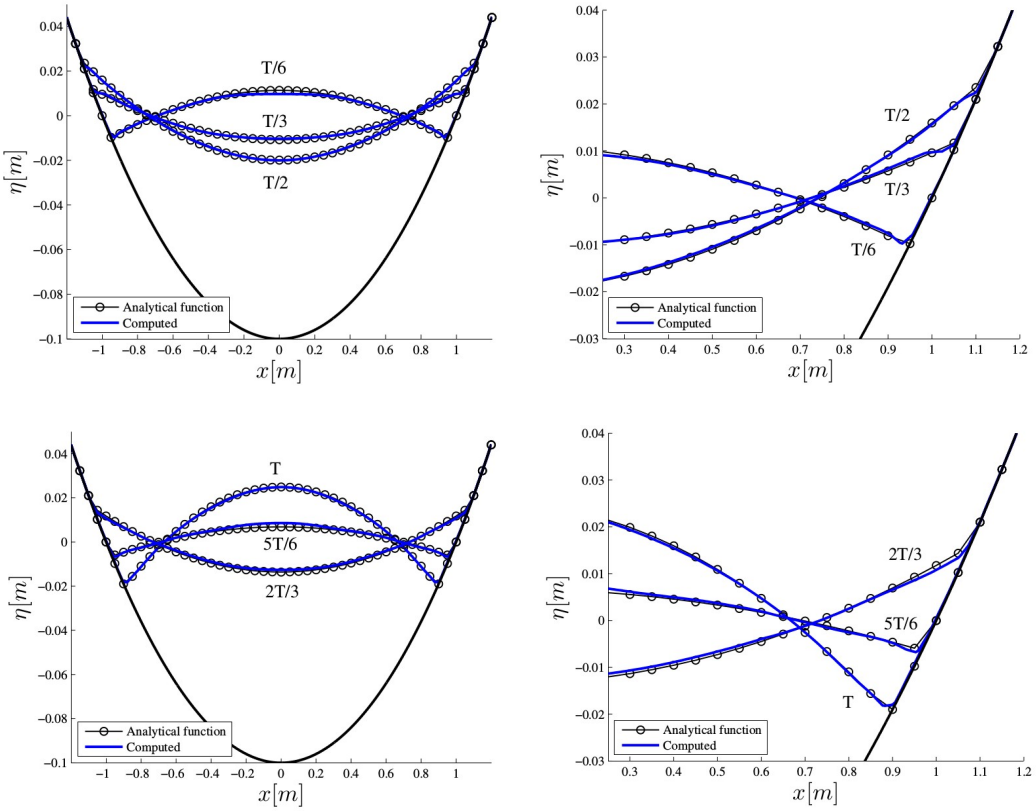

Figure 5.4: Thacker's oscillations in a parabolic bowl: section of the analytical and computed free surface levels at $t = 3T + \delta t$ with $\delta t = T/6,\ T/3,\ T/2$ (top left) and $\delta t = 2T/3,\ 5T/6,\ T$ (bottom left); on the right: close up views on the wet/dry interface.

5.4 2D Solitary wave propagation

The accuracy of the two-dimensional scheme proposed for the GN equations is verified by performing a convergence analysis on a solitary wave propagation problem. A solitary wave of amplitude 0.2 [m] and with the shape described by (3.4) is left propagating for $t = 1$ [s] inside a computational domain of $[0, 70] \times [0, 0.8$ [m], characterized by a value of still water depth of $h_0 = 1$ [m]. Once again, to measure the rate of convergence of the numerical solution to the exact one, we compute the relative error on the total water depth $E_{L_2}(h) = ||h_{num} - h_{ex}||_2 / ||h_{ex}||_2$, with h_{num} is the numerical solution and h_{ex} is the analytical one. The convergence test have been performed considering hexagonal meshes as the one shown in figure 5.5 (left) and characterized by element size of $h_K = [0.2,\ 0.1,\ 0.05,\ 0.025]$. The results obtained are illustrated in the right picture of figure 5.5, together with slopes 2.5 and 3 as references, confirming the expected order of accuracy for the scheme implemented.

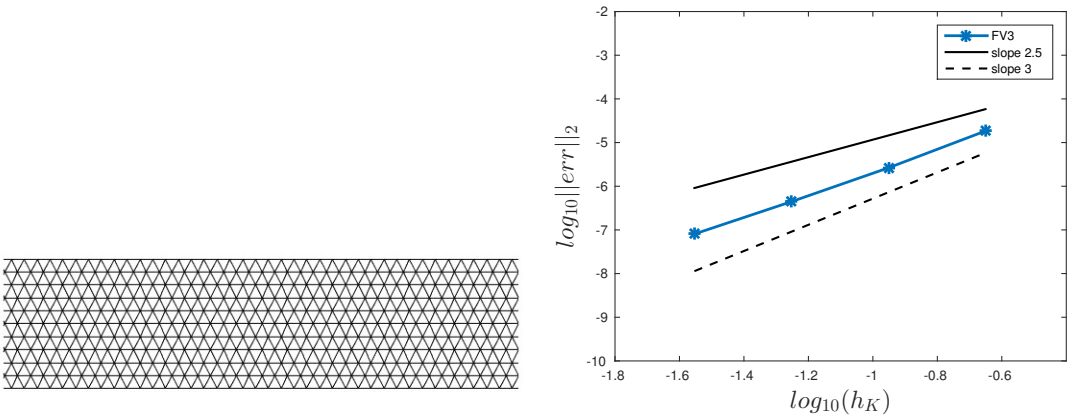

Figure 5.5: 2D Solitary wave propagation: close up view of the hexagonal mesh used for the computation (left), grid convergence for the 2D FV scheme of section 4.2 (right).

5.5 Solitary wave run-up on a plane beach

We consider again the case described in section 3.5, performed on the 2D computational domain $[0\ , 70] \times [0\ , 0.08]$ with wall reflecting boundaries on the top and on the bottom. The numerical model uses an unstructured triangular grid consisting of elements with characteristic length $h_K \approx 0.1$ [m] (*cf.* figure 5.6), leading to a mesh with $N = 6931$ nodes. The CFL number is set to 0.5.

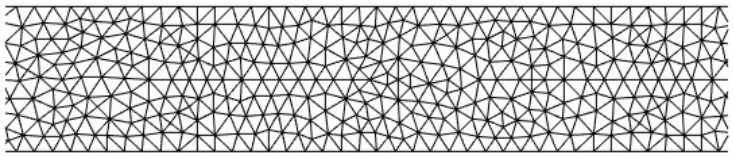

Figure 5.6: Solitary wave run-up on a plane beach: close up view of the unstructured mesh used for the computation.

Figure 5.7 compares the measured surface profiles with respect to experimental data for different non-dimensional times. The hybrid wave breaking model (*cf.* section 2.9) is used with $\gamma = 0.6$ and $\tan(\phi_c) = 0.37$. We can appreciate that the numerical result not only fit well the experimental data, accurately reproducing all the physics of the test, composed by wave shoaling, breaking, run-up and down, hydraulic jump etc., but also correspond to the ones obtained in the one dimensional case (*cf.* figure 3.14), validating the 2D scheme implementation.

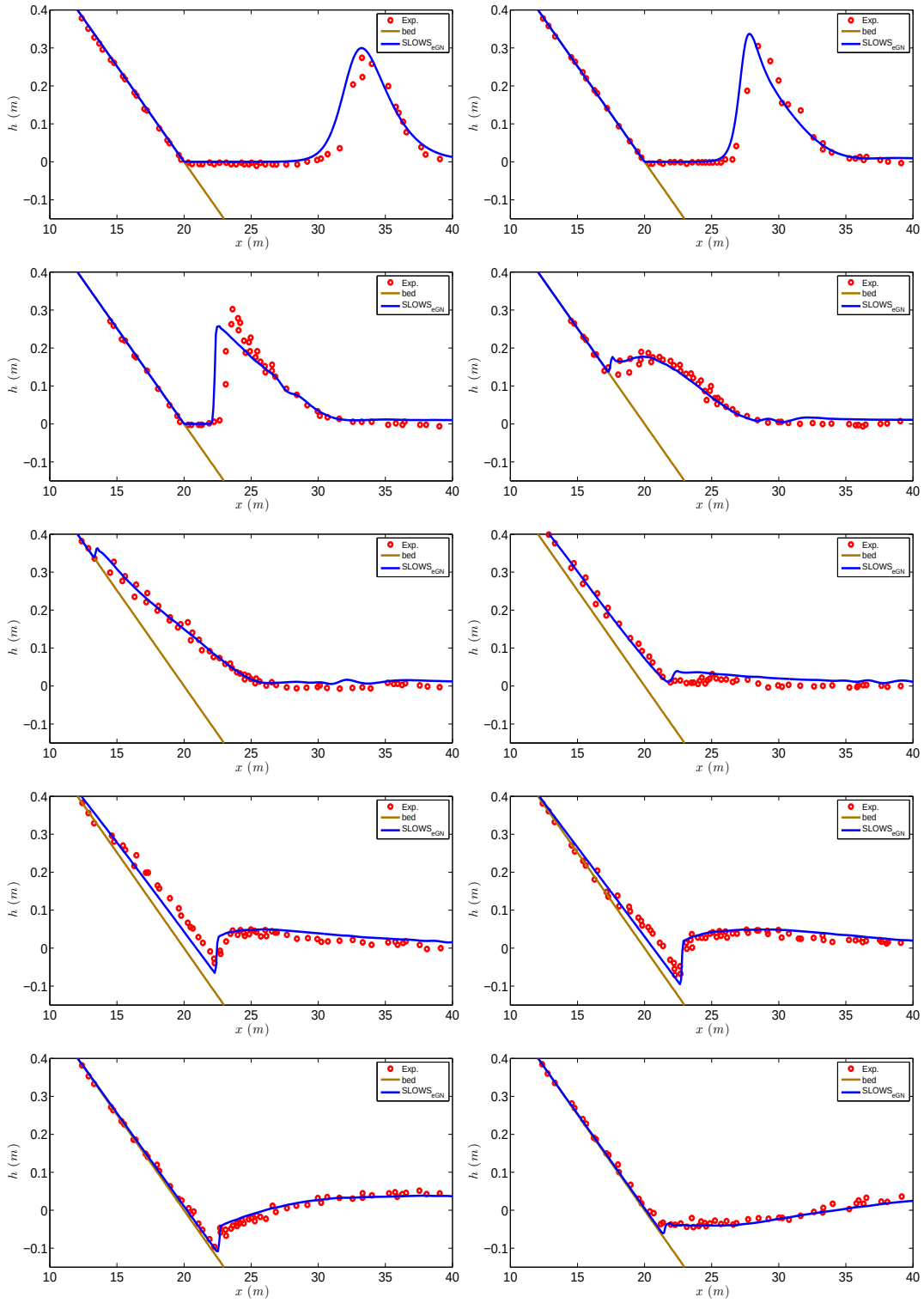

Figure 5.7: Solitary wave run-up on a plane beach: snapshots of the free surface elevation for increasing time of the simulation (from top-left, to bottom-right).

5.6 Solitary wave propagation over a two dimensional reef

In the next test case we have performed in two dimensions the solitary wave propagation over a two dimensional reef, already described in section 3.8. The computational domain has been extended in the y direction for 1 [m] and it has been discretized using a uniform hexagonal mesh (*cf.* left picture of figure 5.5) with triangles of characteristic length $h_K = 0.1$ [m], resulting in 9223 nodes. The CFL condition used for the simulation was set to 0.5 and the parameters for breaking tracking was $\gamma = 0.6$. Wall boundary conditions have been set to each boundary of the domain. The Manning coefficient has been set to $N_m = 0.0014$ [s/m$^{\frac{1}{3}}$] to represent the roughness of the bathymetry.

Figures 5.8 and 5.9 represent the measured and computed free surface level in the whole domain at several time instants along the simulation, allowing also a direct comparison with respect to the one-dimensional results of section 3.8. These results, together with the computed time series at gauges positions of figures 5.10 and 5.11, are very satisfying. The implemented two-dimensional scheme reproduces the same results obtained with the one-dimensional one, accurately describing the physics of this very challenging test. The use of the proposed breaking criteria is critical, including nonlinear shoaling and run-up, multiple wave breaking front, undular bores and hydraulic jumps.

5.7 Solitary wave propagation over a three dimensional reef

Swigler et Lynett [2011] performed laboratory experiments at the O.H. Hinsdale Wave Research Laboratory of Oregon State University to study the specific phenomena which occurs when a tsunami like wave approaches the coast, including shoaling, refraction, breaking and run-up. They performed their test in a 45×26.4 [m] basin. A complex three-dimensional bathymetry was set down consisting of a $1 : 30$ slope connected with a triangular reef flat, submerged between 0.075 [m] and 0.09 [m] below the still water level. The offshore shelf edge has an elevation of 0.71 [m], with the apex located at $x = 12.6$ [m]. The steepest slope of the shelf is at the apex and becomes milder moving along the shelf edge, toward the basin side walls. The planar beach continues to $x = 31$ [m], becoming then horizontal until the end of the basin. In addition, a concrete cone of 6 [m] diameter and 0.45 [m] height is placed to the apex of the reef, between $x = 14$ [m] and $x = 20$ [m]. Nine wave gauges were placed into the basin in order to measure the variation of the free surface elevation (*cf.* figure 5.12 (left)): gauges 1, 2, 3, 7 were located at $y = 0$ [m]

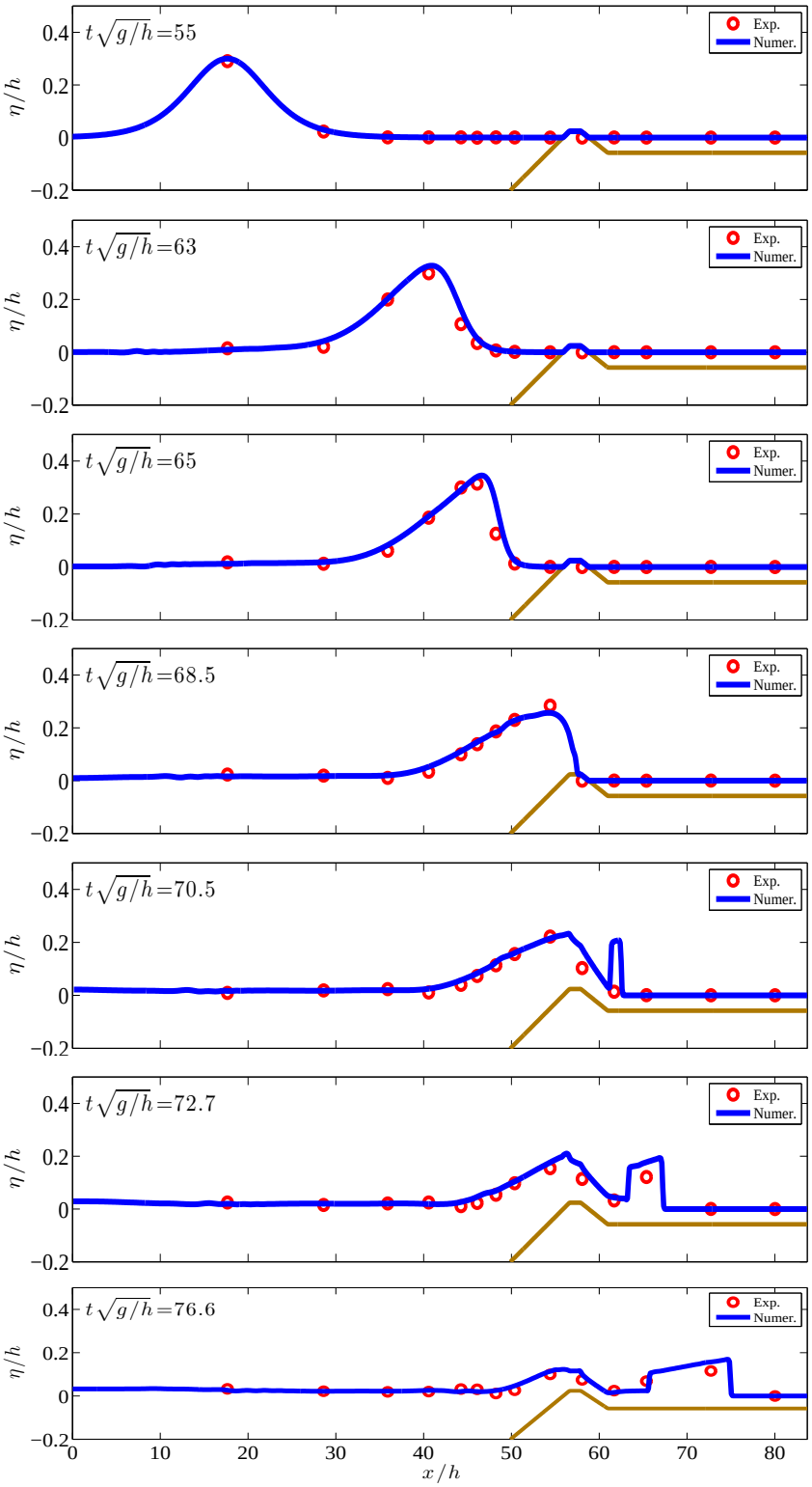

Figure 5.8: Solitary wave propagation over a two dimensional reef, Part I: Evolution of free surface profiles and wave transformations over an exposed reef for a solitary wave of $a/h = 0.3$ and $1:12$ slope.

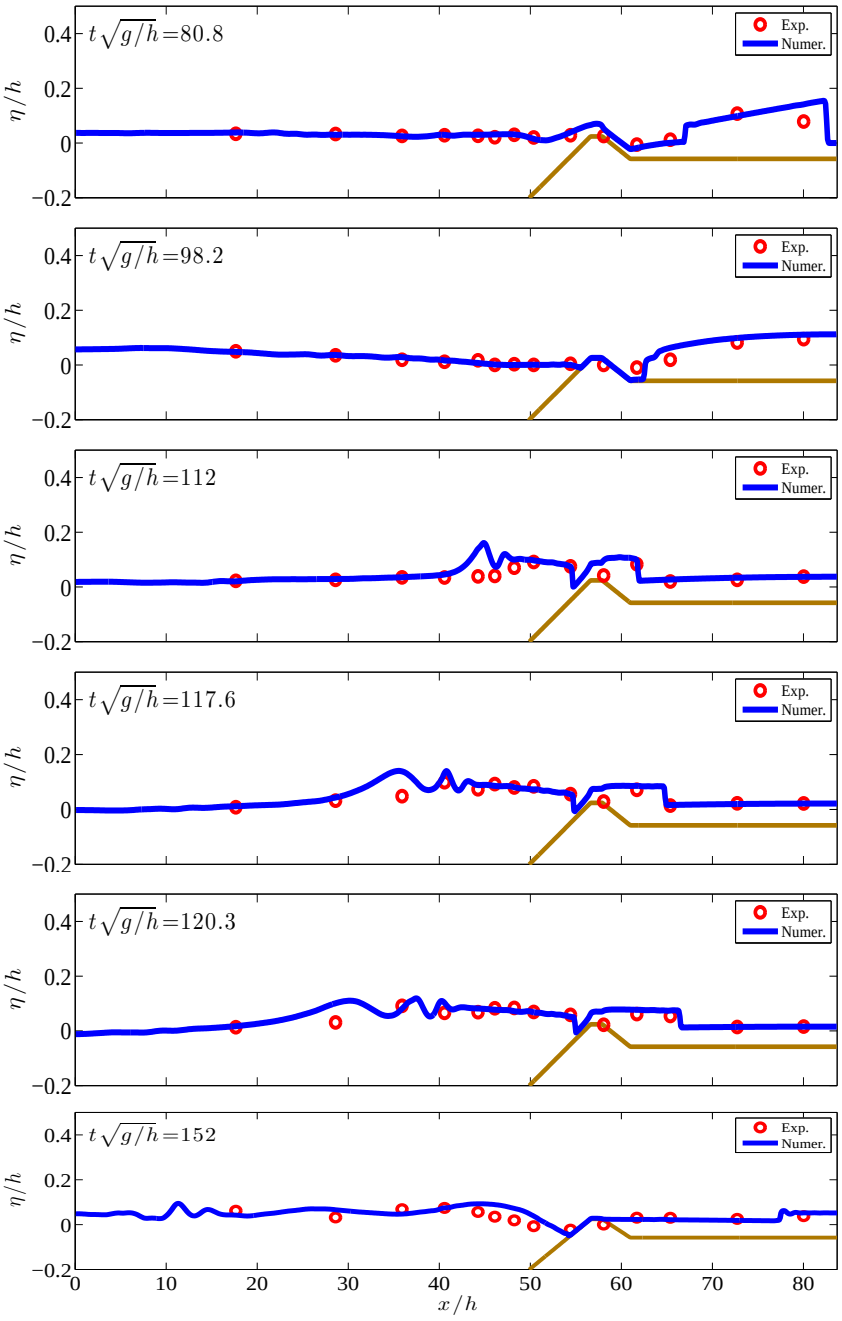

Figure 5.9: Solitary wave propagation over a two dimensional reef, Part II: Evolution of free surface profiles and wave transformations over an exposed reef for a solitary wave of $a/h = 0.3$ and $1 : 12$ slope.

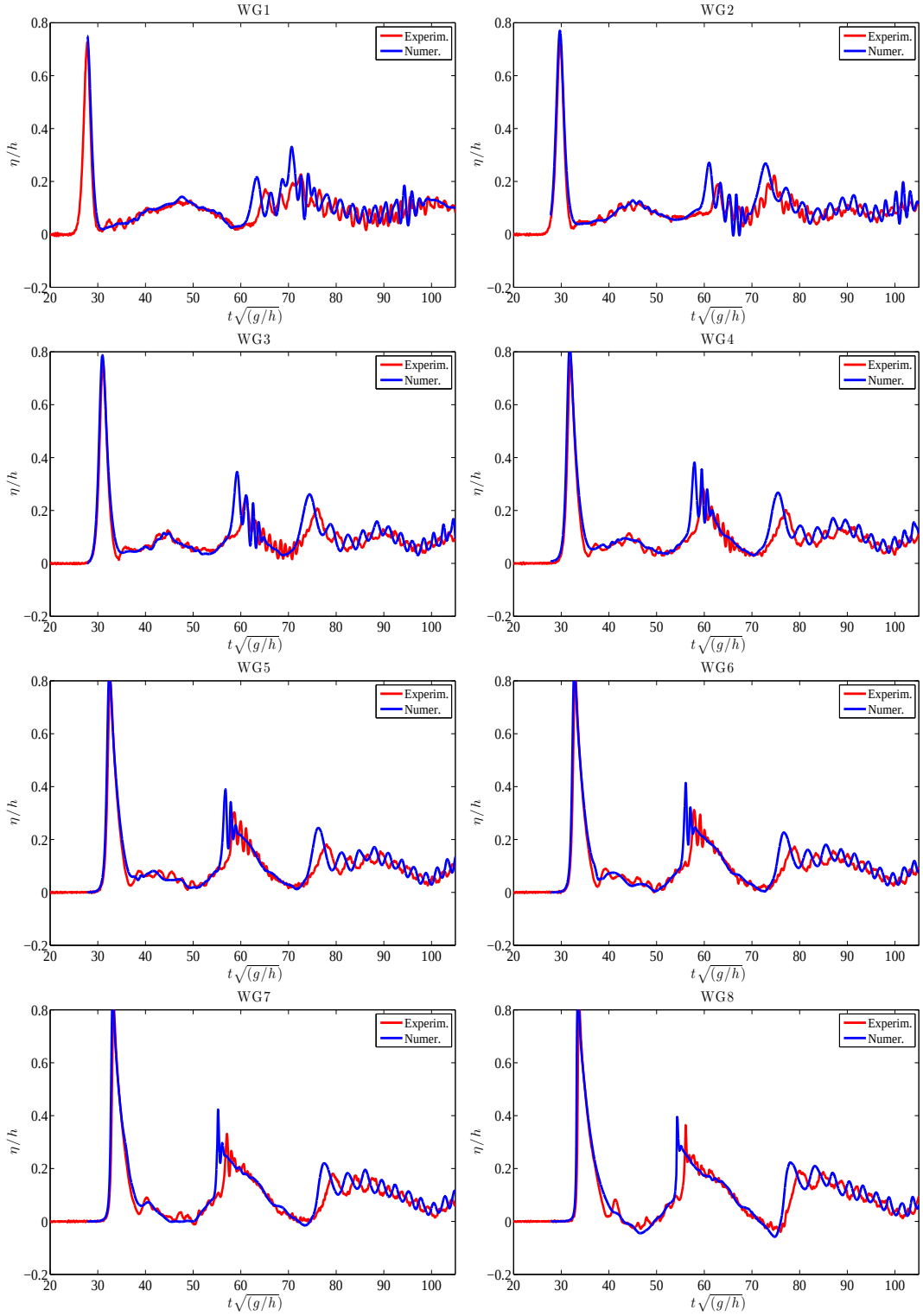

Figure 5.10: Solitary wave propagation over a two dimensional reef: time series of the normalized free surface at the wave gauges location, before the reef.

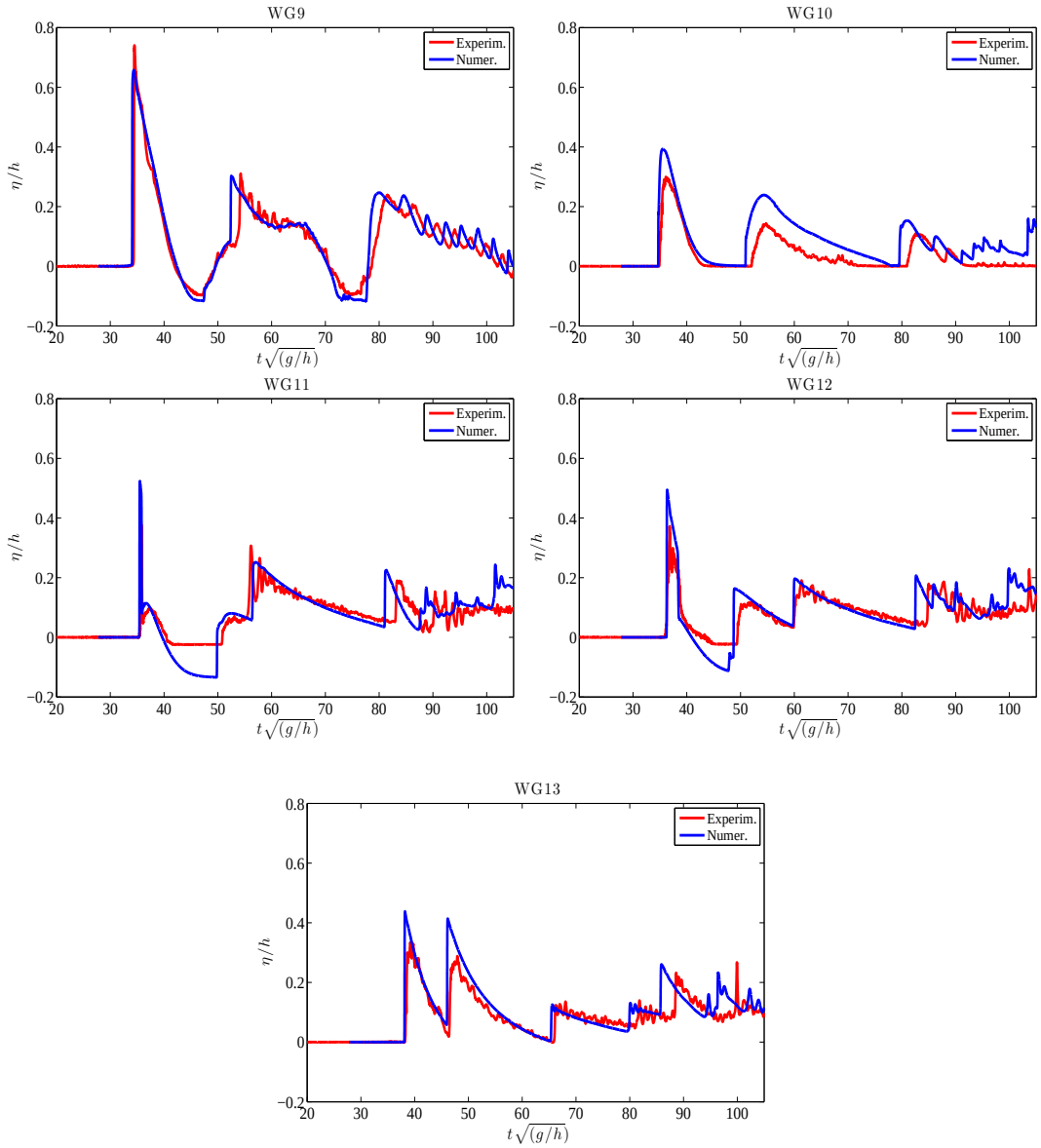

Figure 5.11: Solitary wave propagation over a two dimensional reef: time series of the normalized free surface at the wave gauges location, on top and after the reef

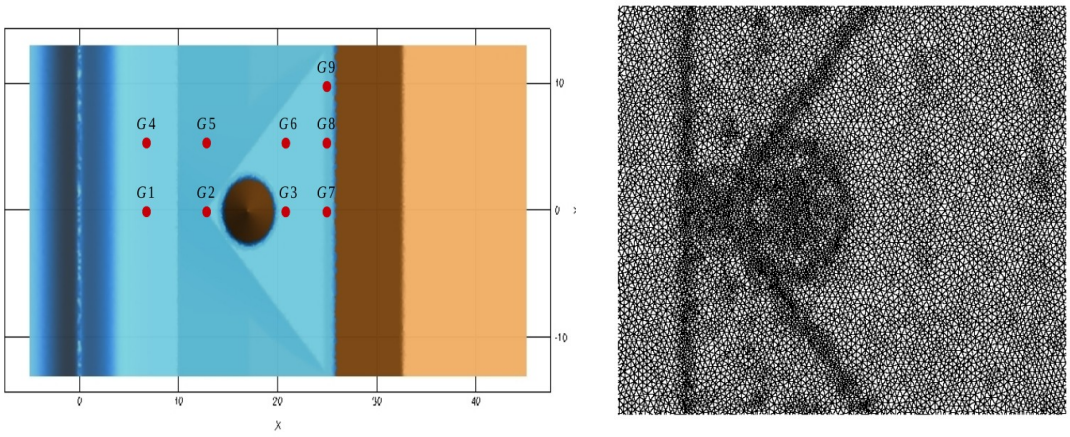

Figure 5.12: Solitary wave propagation over a three dimensional reef: (left) geometry along with wave gauge's position; (right) close up view of the adapted mesh used for the computation.

and $x = 7.5$, 13, 21, 25 [m]; gauges 4, 5, 6, 8 were located at $y = 5$ [m] and $x = 7.5$, 13, 21, 25 [m], while gauge 10 have been set at $y = 10$ [m] and $x = 25$ [m].
Compared to the experiment, the computational domain has been extended from $x = 0$ [m] to $x = -5$ [m] in order to be able to completely contain the initial solitary wave. It has been discretized by means of a non-uniform unstructured grid, adapted to the bed curvature, as shown in 5.12 (right), and characterized by reference maximum and minimum size respectively: $\max(\mathrm{h}_K) = 0.3$ [m] and $\min(\mathrm{h}_K) = 0.125$ [m]). A solitary wave of amplitude $a = 0.39$ [m], corresponding to $\varepsilon = 0.5$, is initially placed in $x = 0$ [m] and wall reflecting boundary conditions are imposed in each boundary of the domain. We perform two computations, one is frictionless, while the other uses a Manning coefficient $N_m = 0.0014$ for representing bed roughness. For the two simulations, a CFL number of 0.5 was used, together with $\gamma = 0.6$ for the breaking detection criterion.

Figure 5.13 shows the computed free water surface at difference time instant during the simulation. Moreover, we show in figure 5.14 the time evolution of the breaking reagions detected by the criteria described in section 4.5. As the solitary wave propagates towards the beach it shoal, increases its steepness and nonlinearity, up to reaching a breaking point at $t = 5$ [s] on the center line of the domain, when it reaches the apex of the triangular shelf. At $t = 6.5$ [s], the central part of the wave has completely overtopped the concrete cone, while on the two sides, the surge continues to shoal, diffracting around the base of the cone. By $t = 8.5$ [s], the refracted and diffracted waves collide on the lee

side of the shelf. After $t = 9$ [s], the water starts to withdraw from the cone top and a bore-front forms, from the combined waves after the diffraction, and propagates on the shelf behind the cone and then onshore. After $t = 15$ [s], a new bore is creates from the the drawn-down of the water and collides with the refracted waves.
The computed free surface time series at the nine gauge positions are illustrated in figure 5.15 and compared with respect to experimental ones. The arrival of the first incoming wave is correctly captured in gauges 1 and 2, as it is for the refracted and diffracted waves at the lee side of the cone, as can be seen from gauge 3, except for the minimum of water height registered at $t \approx 8.5$ [s], which is partially caught only in the frictionless case. A slight deviation from the measurements is displayed after $t \approx 35$ [s], maybe due to late arrival of the reflected waves from the extended left wall boundary. The signal at gauges 4, 5, 6, 7 and 8, located on the north side of the cone, indicates that wave shoaling, breaking and propagation on the shelf is accurately predicted, together with the complex nonlinear interaction between diffracted and refracted waves. The onshore propagation of the surge and the subsequent water recession are registered in gauges 7, 8 and 9, placed along the initial shore line. The experimental data are well represented also in this case. As expected, the results computed with the frictionless simulation are characterized by bigger waves and are more oscillatory. However, in gauges 3, 7 and 9 they are closer to the experimental data and able to better reproduce the drying phenomenon behind the obstacle due to the strong reflections taking place in the interactions.

5.8 Wave diffraction over a semi-circular shoal

We consider here the reproduction of the tests carried out in Whalin [1971] involving the study of the focusing effect induced by a semicircular shoal on wave trains of different periods. The experiments were carried out in a wave tank 6.096 [m] wide and 25.6 [m] long, its middle portion consisted in a semicircular shoal leading the water depth to decrease from $h_0 = 0.4572$ [m] (at the wave maker) to 0.1524 [m] at the end of the tank. The bottom topography is described by the equation:

$$z = \begin{cases} 0 & \text{if} \quad 0 \leq x < 10.67 - G(y) \ , \\ (10.67 - G(y) - x)/25 & \text{if} \quad 10.67 - G(y) \leq x < 18.29 - G(y) \ , \\ 0.30480 & \text{if} \quad 10.29 - G(y) \leq x \ , \end{cases}$$

with $G(y) = \sqrt{y(6.096 - y)}$. The depth h is obtained as $h = h_0 - z$. A contour plot of the bathymetry is reported on the left on figure 5.8. This test is

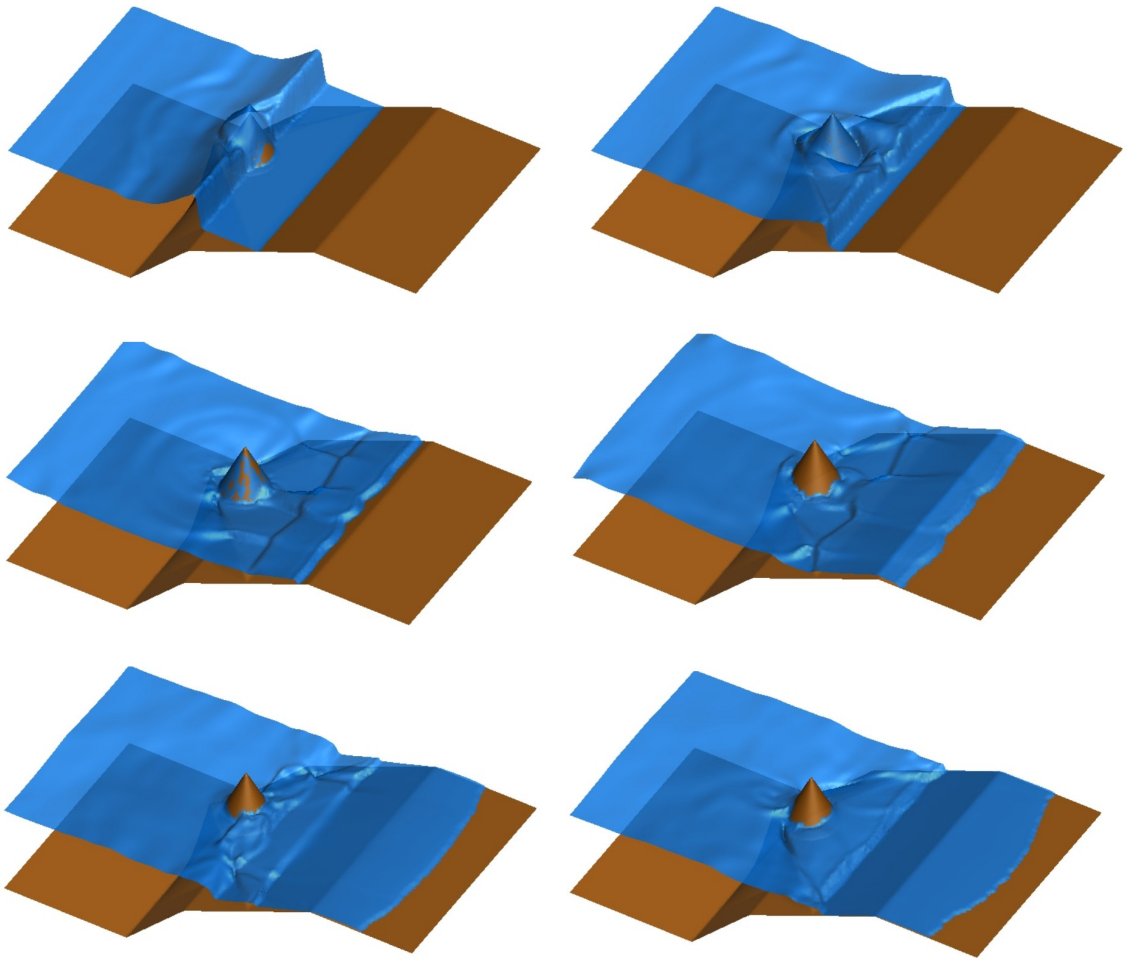

Figure 5.13: Solitary wave propagation over a three dimensional reef: computed free surface solution with friction at times $t = 6.5, 8.5, 11.5, 14.5, 20.5, 27.5$ [s] from the top-left picture to the bottom-right one.

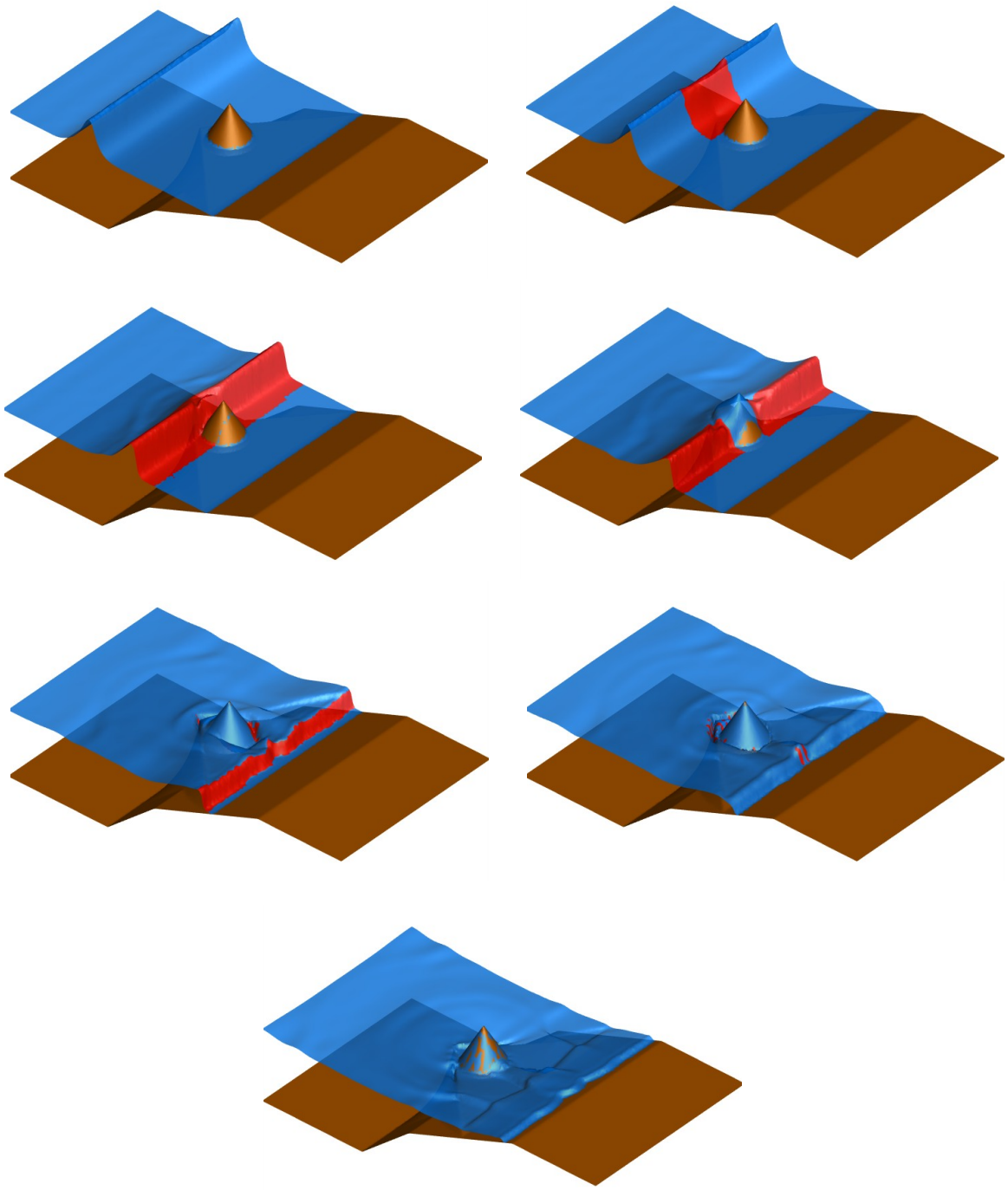

Figure 5.14: Solitary wave propagation over a three dimensional reef: computed free surface solution with friction at times $t = 3.5, 4.5, 5.5, 6.5, 8.5, 9.5, 11.5$ [s] (from the top-left picture to the bottom one). The red area represents the region where wave breaking is detected and the NLSW equations are solved.

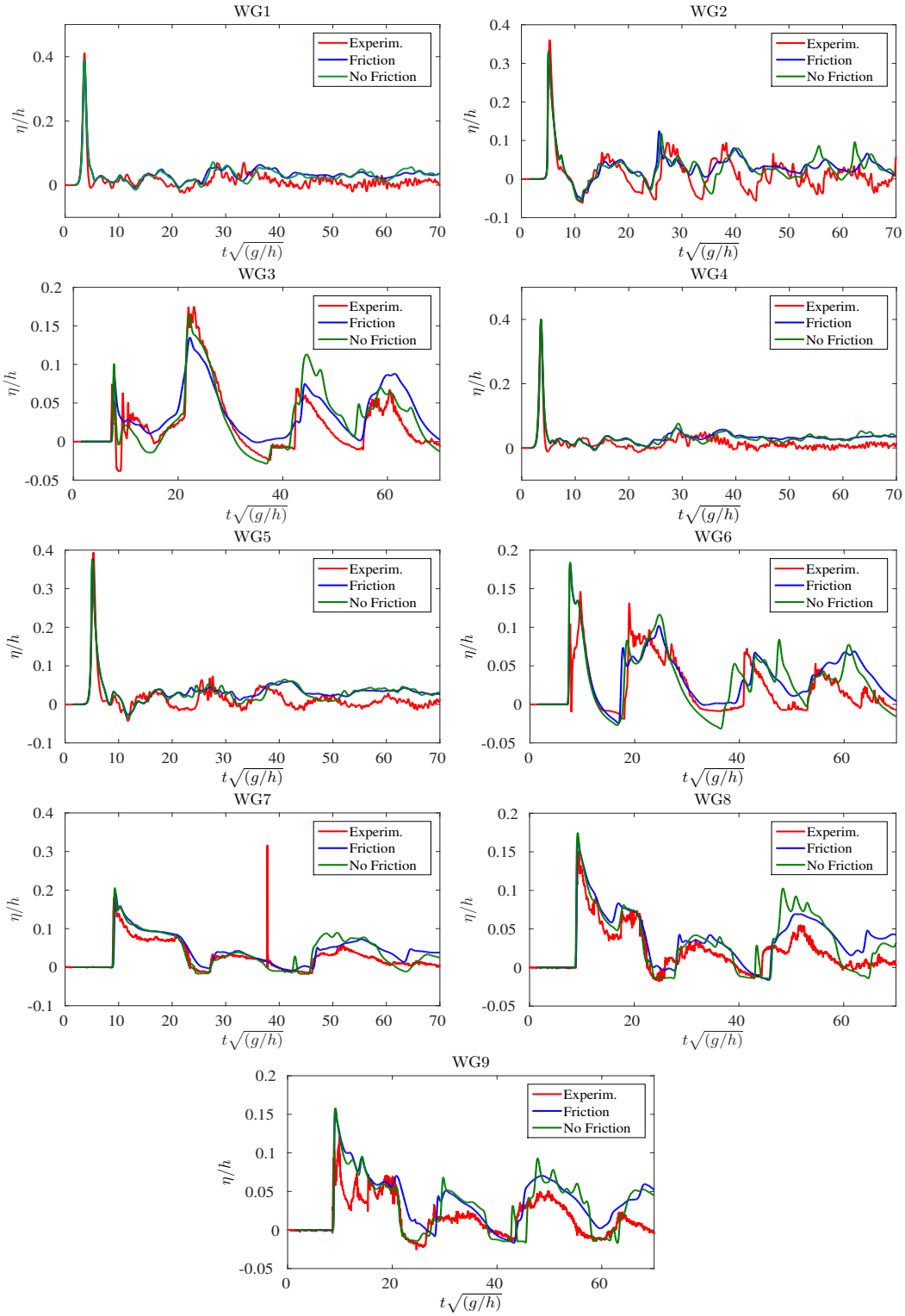

Figure 5.15: Solitary wave propagation over a three dimensional reef: computed time series of the free surface elevation on gauges positions .

a standard benchmark for 2D dispersive model, being used by several authors (*cf.* Madsen et Sørensen [1992]; Beji et Nadaoka [1996]; Walkley et Berzins [2002]; Sorensen *et al.* [2004]; Eskilsson *et al.* [2006]; Tonelli et Petti [2009]; Kazolea *et al.* [2012]; Ricchiuto et Filippini [2014] and references therein).

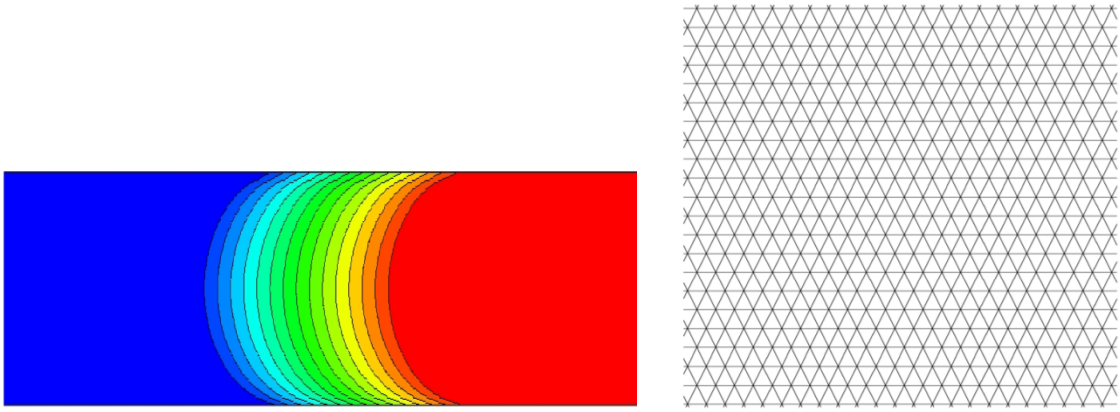

Figure 5.16: Wave diffraction over a semi-circular shoal. Left: bathymetry contours. Right: close up view of the structured grid

Three cases are considered here, with wave trains characterized by Whalin [1971]:

(a) T=1 s, A = 0.0195 m, $h_0/\lambda = 0.306$;

(b) T=2 s, A = 0.0075 m, $h_0/\lambda = 0.117$;

(c) T=3 s, A = 0.0068 m, $h_0/\lambda = 0.074$;

having denoted by T the period and by λ the wavelength.
For all the cases, the harmonic analysis of free surface elevation measurements taken along the tank centerline are available, and are used to verify the capabilities of a model to reproduce nonlinear refraction and diffraction. The computational domain is the rectangle $[-10, 36] \times [0, 6.096]$ [m]. Periodic waves are generated by means of the internal generator described in section 2.8.3, centered at $x = -4$ [m]. Sponge layers (*cf.* section 2.8.3) of a length of 6 [m] are set at the left and right ends of the domain, while reflective boundary conditions are imposed along the top and bottom boundaries. Following Walkley et Berzins [2002]; Kazolea *et al.* [2012], the tests have been run on regular triangulations (*cf.* right picture on figure 5.8) of size approximately $h \approx 0.05$ in the x direction, for case (a), and $h \approx 0.1$ for case (b) and (c). The mesh size in the y direction is instead 0.1 [m] for all the cases. The two meshes used

was thus containing 28151 and 56211 nodes respectively. The CFL condition used for the simulations was 0.5.

For all the cases, we compare the solution obtained with the experimental data. In particular, we report in figures 5.17, 5.18, and 5.19 a three dimensional visualization of the wave patterns obtained from the computation (top pictures), the centerline signal at the final time of the simulation (bottom-left pictures), and comparisons of the harmonic components of the $\eta(t)$ signal along the channel centerline with respect to the experiments ones.
In order to make sure that a steady periodic state is obtained, we start sampling the solution after at least 15 periods of oscillations. The then perform a DFT of the centerline data collected over one period of the main incoming wave.

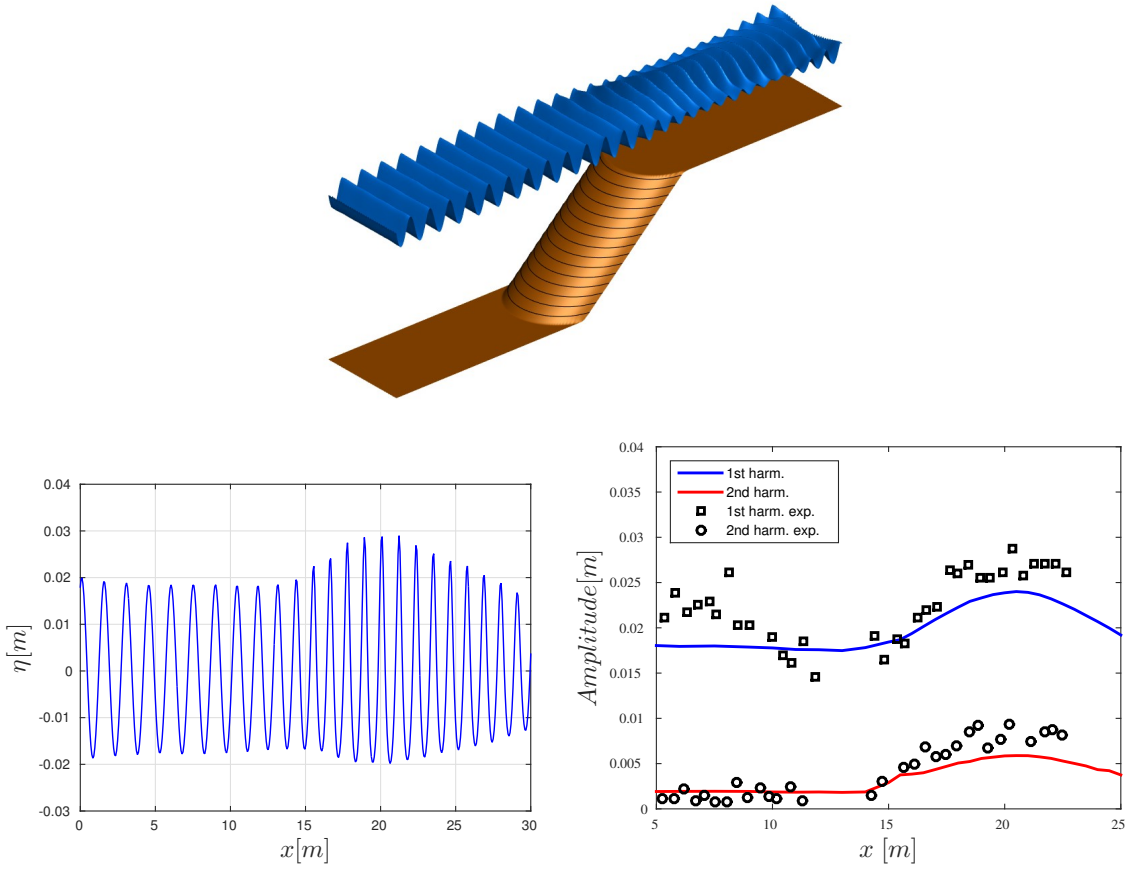

Figure 5.17: Wave diffraction over a semi-circular choal, case (b). Top: rescaled 3D view of the free surface. Bottom-left: computed free surface elevation, data extract from the centerline of the domain, Bottom-right: comparison of DFT of the computed centerline data with experiments.

The results reported are comparable to those presented by others (*cf.* Mad-

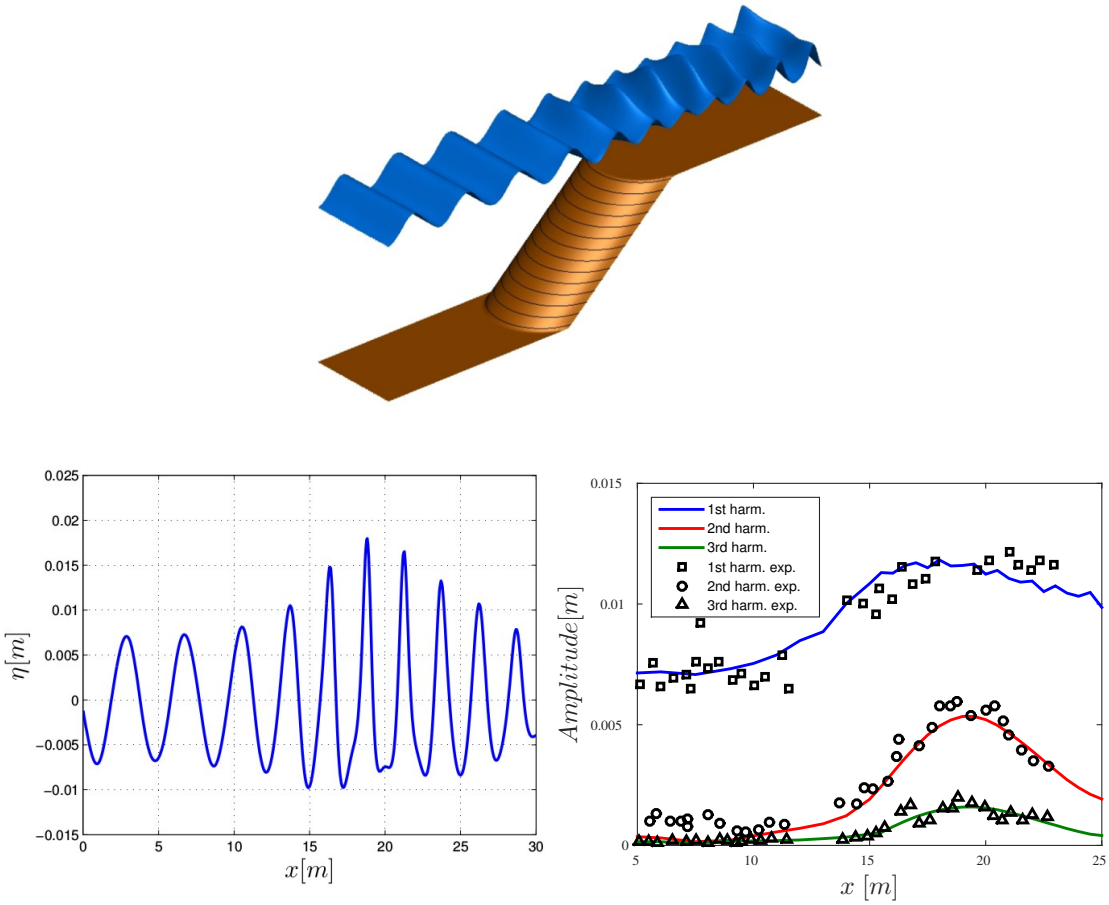

Figure 5.18: Wave diffraction over a semi-circular choal, case (b). Top: rescaled 3D view of the free surface. Bottom-left: computed free surface elevation, data extract from the centerline of the domain, Bottom-right: comparison of DFT of the computed centerline data with experiments.

sen et Sørensen [1992]; Beji et Nadaoka [1996]; Walkley et Berzins [2002]; Sorensen *et al.* [2004]; Eskilsson *et al.* [2006]; Tonelli et Petti [2009]; Kazolea *et al.* [2012]; Ricchiuto et Filippini [2014]). The incoming waves are linear in the deeper portion of the tank but, as they propagate onto the topography, they become steeper due to shoaling. Wave energy gradually spreads out to higher harmonics, which increase in amplitude in the shoaling region.
In particular, case (c), which we consider as being resolved concerning both the spatial and temporal scales, a slight overestimation of the first harmonic can be noted, which is common to many computational results presented in literature, while both the second and third harmonics are underestimated, as also quite common in literature.
In case (b), which we also consider well resolved, a very good match between the harmonic content of the computed signal and the experiments is found.

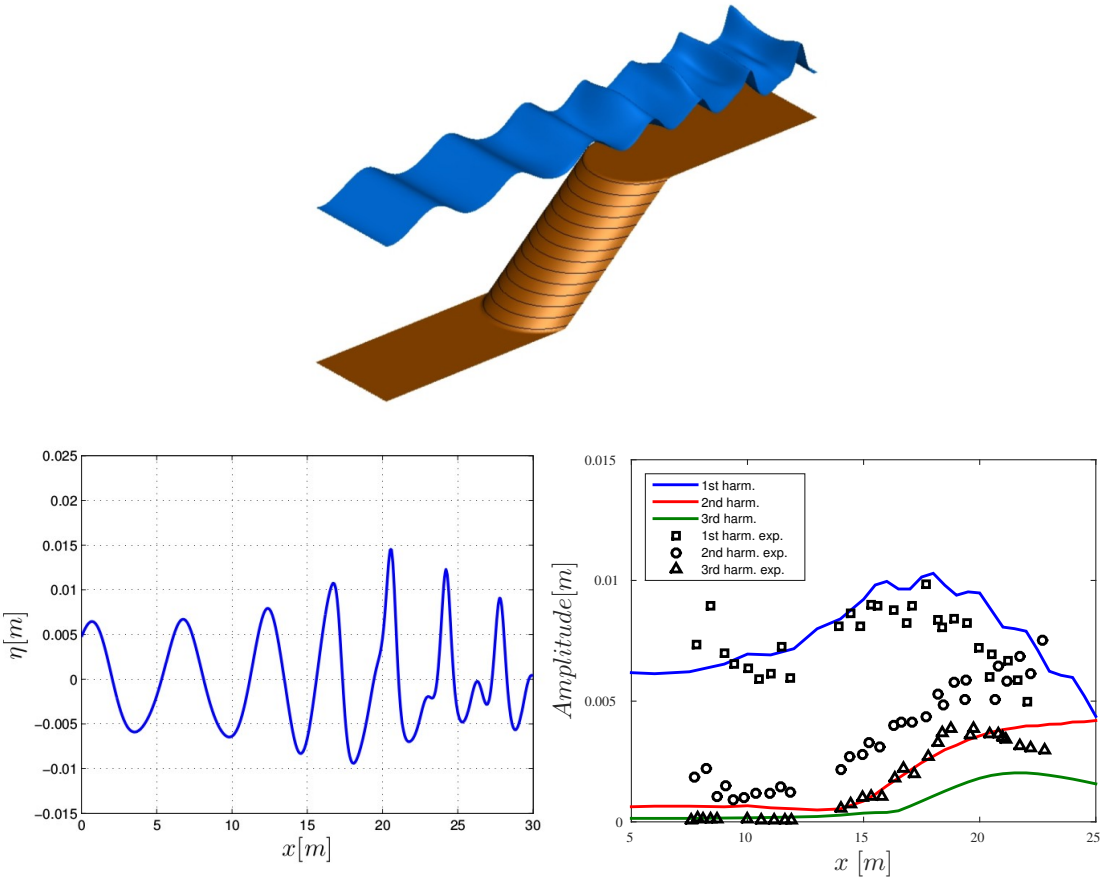

Figure 5.19: Wave diffraction over a semi-circular shoal, case (c). Top: rescaled 3D view of the free surface. Bottom-left: computed free surface elevation, data extract from the centerline of the domain, Bottom-right: comparison of DFT of the computed centerline data with experiments.

Finally, in case (a), a slight dissipation of the incoming wave amplitude can be observed in both the bottom-left and bottom-right pictures of figure 5.17. This induces a slight underestimation of the amplitude of the first and second harmonic in all the computational domain, compared to other published results. Refined meshes on the x-direction should be applied in this case.
Overall we judge these results very encouraging. In particular we believe that they confirm our observations in one space dimension.

5.9 Wave diffraction over an elliptic shoal

This test reproduces the experiment of Berkhoff *et al.* [1982] studying the refraction and diffraction of monochromatic waves over a complex bathymetry. This is a standard test to verify models based on the mild-slope equations but

it is often also used as a test for extended Boussinesq models (see *e.g.* Tonelli et Petti [2009]; Walkley et Berzins [2002]; Walkley [1999]; Wei et Kirby [1995]; Ricchiuto et Filippini [2014]; Kazolea [2013] and references therein). A sketch of the experiment is reported on the left picture on figure 5.20. The actual wave tank is 20 [m] wide and 22 [m] long. The bathymetry consists of an elliptic shoal mounted on a ramp of constant slope, forming a 20° angle with the x axis. The maximum water depth is $h_0 = 0.45$ [m] at the wave maker, while the bathymetry is given by the formula $z = z_0 + z_s$, where:

$$z_0 = \begin{cases} (5.82 + y_r)/50 & \text{if} \quad y_r \leq -5.82 \ , \\ 0 & \text{otherwise} \ , \end{cases}$$

$$z_s = \begin{cases} -0.3 + \dfrac{1}{2}\sqrt{1 - \left(\dfrac{x_r}{5}\right)^2 - \left(\dfrac{4y_r}{15}\right)^2} & \text{if} \quad \left(\dfrac{x_r}{4}\right)^2 + \left(\dfrac{y_r}{3}\right)^2 \leq 1 \ , \\ 0 & \text{otherwise} \ , \end{cases}$$

with the transformed coordinates $(x_r,\, y_r)$ defined as: $x_r = x\cos(20°) - y\sin(20°)$, $y_r = x\sin(20°) + y\cos(20°)$. The incoming periodic wave has period $T = 1$ [s], and amplitude $a = 0.0232$ [m], corrispondent to $\varepsilon = 0.3$. In Berkhoff *et al.* [1982], the wave elevation was measured in 8 different sections along which the normalized time average wave height distribution has been computed. A sketch of the problem with the indicative position of the measurement sections is reported in the left picture on figure 5.20 (*cf.* Berkhoff *et al.* [1982] for details).
The computational domain is the square $[-10,\, 10] \times [-17,\, 15][m]$. The incoming periodic wave is obtained by means of the internal wave generator described in section 2.8.3, centered at $y = -13$ [m], while sponge layers of 4 [m] thickness are placed at the bottom and top ends of the domain. As in Tonelli et Petti [2009] and Ricchiuto et Filippini [2014], reflective boundary conditions are imposed on the left and right boundaries. Concerning the mesh size, we have run this case on an unstructured grid, refined in the region of the shoal. In particular, the grid size in the y direction varies from $\mathrm{h}_y \approx 0.1$ [m] on the bottom and top boundaries to $\mathrm{h}_y \approx 0.05$ [m] in the region around the shoal. In the x direction, the grid size is $\mathrm{h}_x = 2\mathrm{h}_y$. A close up view of the mesh refinement in the bottom left region of the computational domain is reported in the right picture on figure 5.20. Computations have been run until time $t = 50$ [s] with CFL= 0.5.

Three dimensional visualizations of the water elevation computed at time $t = 50$ [s] are reported on figure 5.21. The left picture shows the region of the interaction with the mesh superimposed. Both pictures provide a visualization of the complex pattern obtained from the diffraction of the incoming periodic wave on the elliptic shoal. To compare our results with the experiments of Berkhoff *et al.* [1982] time dependent data have been extracted from

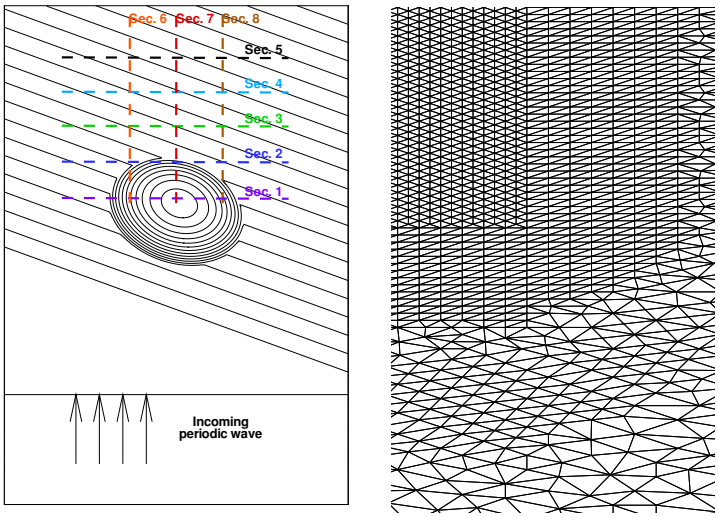

Figure 5.20: Wave diffraction over an elliptic shoal. Left: sketch of the problem with bathymetry contours and position of the experimental sections; Right: close up view of the mesh used for the computation.

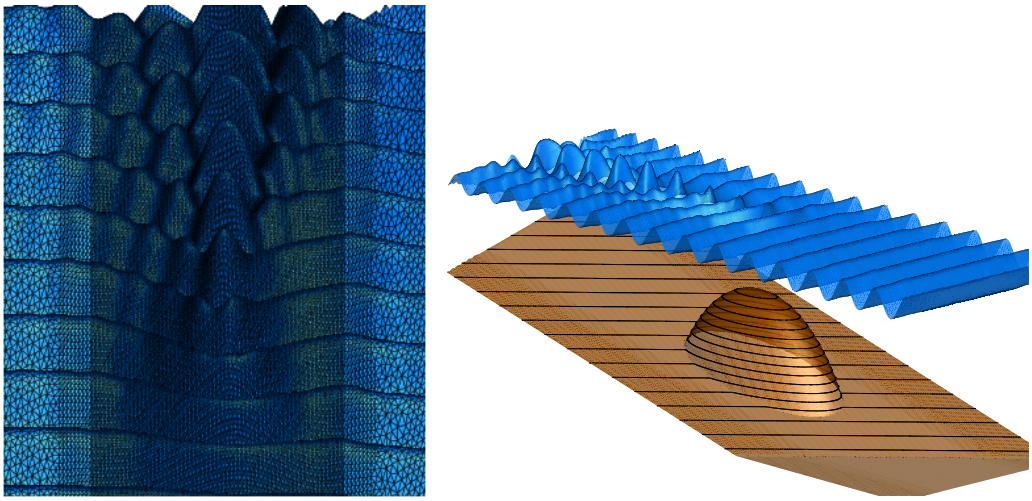

Figure 5.21: Wave diffraction over an elliptic shoal, results at $t = 50$ [s]. Left: top view of the free surface with mesh; Right: exaggerated 3D view of the free surface with bathymetry.

$t = 25$ [s] to $t = 50$ [s] from the sections (*cf.* left picture on figure 5.20 and Berkhoff *et al.* [1982]): section $1 \equiv \{y = 1m | -5m \leq x \leq 5m\}$; section $2 \equiv \{y = 3m | -5m \leq x \leq 5m\}$; section $3 \equiv \{y = 5m | -5m \leq x \leq 5m\}$; section $4 \equiv \{y = 7m | -5m \leq x \leq 5m\}$; section $5 \equiv \{y = 9m | -5m \leq x \leq 5m\}$; section $6 \equiv \{x = -2m | 0m \leq y \leq 10m\}$; section $7 \equiv \{x = 0m | 0m \leq y \leq 10m\}$ and section $8 \equiv \{x = 2m | 0m \leq y \leq 10m\}$. The data obtained have been ana-

lyzed using the *zero up-crossing* principle to isolate single waves and compute the average wave height distributions, the wave height of a single wave being defined as $\eta_{\max} - \eta_{\min}$.

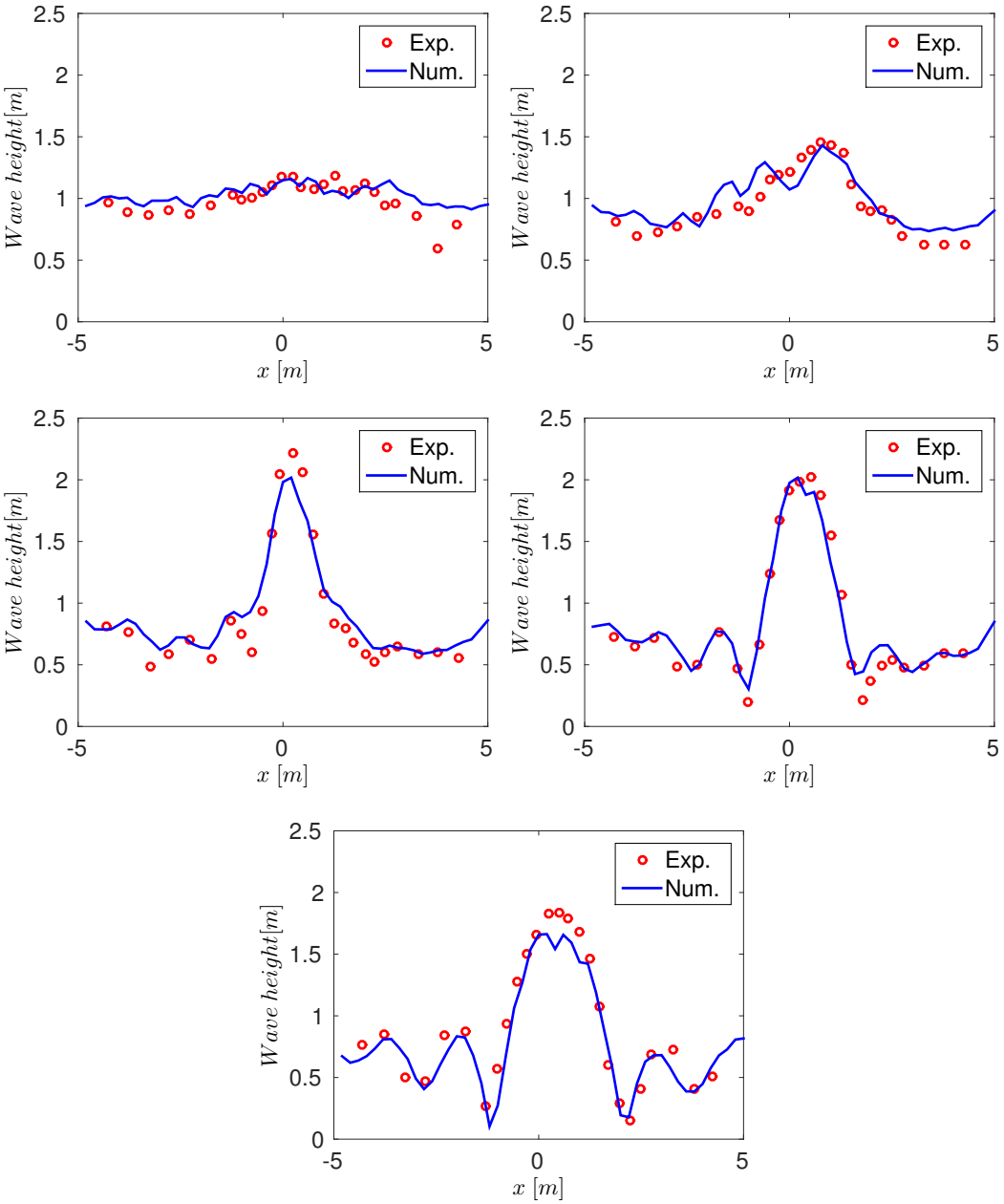

Figure 5.22: Wave diffraction over an elliptic shoal: comparison of the computed average wave height with the experimental data of Berkhoff *et al.* [1982] (sections 1 to 5).

The results, normalized by the incoming wave height $2a = 0.0464$ [m], are reported on figures 5.22 and 5.23. Our computational results compares well with the experiments and with what can be found in published literature (see *e.g.* Tonelli et Petti [2009]; Walkley et Berzins [2002]; Ricchiuto et Filippini [2014]; Kazolea [2013] and references therein).

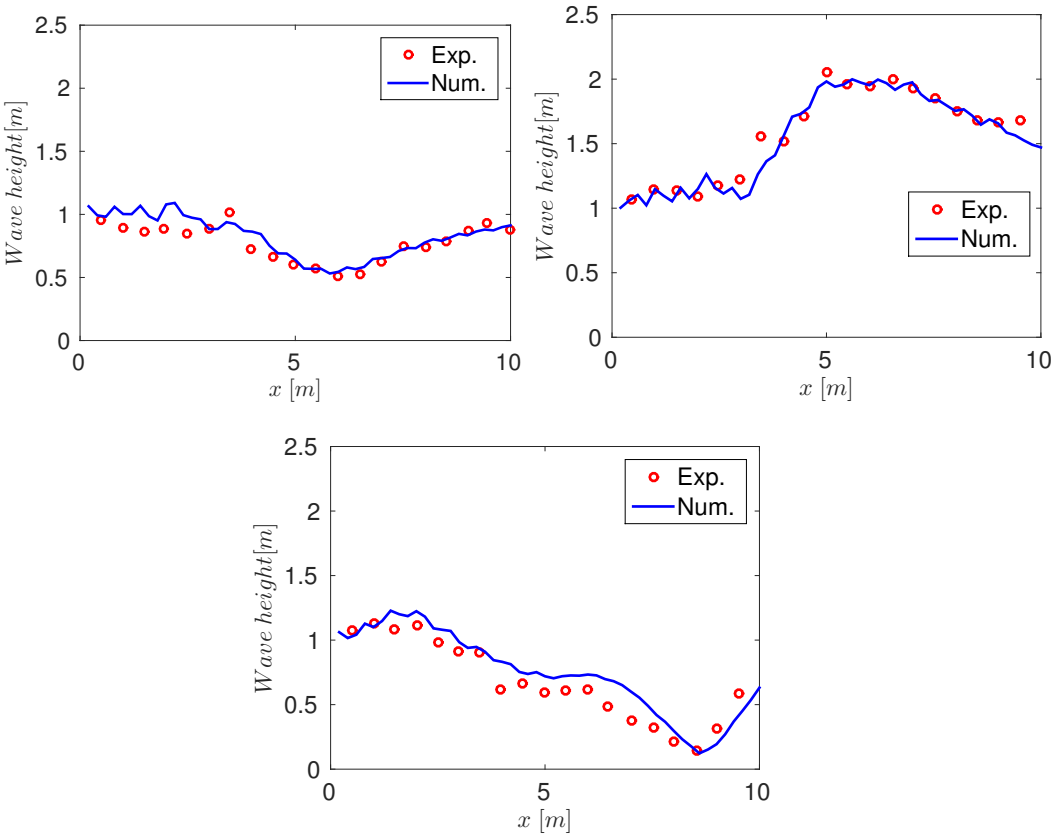

Figure 5.23: Wave diffraction over an elliptic shoal: comparison of the computed average wave height with the experimental data of Berkhoff *et al.* [1982] (sections 6 to 8).

Chapter 6

Modeling tidal bore formation in convergent estuaries

Contents

The analysis of tidal wave transformation in convergent alluvial estuaries have been the subject of intensive scientific research. It has already received considerable attention to tackle a sustainable management of water resources and to adequately understand the human impact on estuarine ecosystem. Parametric studies conducted in Lanzoni et Seminara [1998]; Toffolon *et al.* [2006]; Bonneton *et al.* [2015]; Munchow et Garvin [1991]; Cai *et al.* [2014], have shown that, when neglecting river discharge effects, the estuarine hydrodynamics is controlled by only three dimensionless parameters. These parameters represent a combination of the properties of the tidal forcing at the estuary mouth (wave amplitude and period), the large-scale geometrical characteristics of the channel and the friction coefficient. For particular conditions of the above dimensional variables, of freshwater flow and of river channel bathymetry, the tidal wave may result strongly distorted when the flow turn to rise, and a bore can be observed at the beginning of the flood tide. This chapter is precisely devoted to the numerical study of the physical conditions that lead to the formation of tidal bores in estuaries.

Tide propagation in funnel shaped estuaries is both a nonlinear and a dispersive wave phenomenon. Two types of tidal bores have been observed, undular bores and breaking bores. In order to provide a physically relevant description of the wave transformation, one should typically use a nonlinear and dispersive model, such as the Green-Naghdi system, that has demonstrated to accurately simulate these complex scenarios (*cf.* Tissier *et al.* [2011]). However, at large spatial and temporal scales, where the non-hydrostatic effects associated with tidal bores can be neglected, the physical processes of tidal amplification/damping and distortion can be accurately described by the use of the simple nonlinear and non-dispersive Saint-Venant system of equations, as it will be also shown later on in this chapter. Some numerical studies already used the Saint-Venant system to simulate the propagation of tidal waves in rivers up to bore formation, but they are limited to a single (*cf.* Madsen *et al.* [2005]; Pan et Lu [2010]) or to a small number (*cf.* Munchow et Garvin [1991]) of estuaries. A similar limitation concerns also field data: since every estuary in nature represents a unique combination of the three dimensionless variables, we dispose only of a limited number of points in the parameter space coming from *in situ* measurements. Based on the set of data available, it is very difficult to understand how such parameters influence the bore development process. Our interest is, firstly, in bypassing this major constraint through a numerical investigation, by means of the NLSW system and on idealized convergent channels, of the whole space of the dimensionless variables, leading to a better understanding of the physics dominating the estuarine dynamics.

The small database available has generated, over time, a fragmentary and incomplete comprehension of the bore formation mechanism. Although the

basic conditions are well known (*cf.* Bartsch-Winkler et Lynch [1988]) (large tidal range, shallow and convergent channel, low freshwater discharge), a parametric estuarine classification in terms of bore occurrence does not exist in the literature. Based on measurements on the Garonne river and using available data from existing estuaries, Bonneton *et al.* [2015] showed that the dominant dimensionless parameter for bore formation appears to be the dissipation one, which multiplies the frictional term of the Saint-Venant equations. They concluded that bore generation is associated with large values of the dissipation parameter. On the other hand, it is also generally accepted that tidal bores form in estuaries which amplify the incoming tidal wave (*cf.* Chanson [2012]). In the next section we show that these empirical criteria based on one dimensionless flow parameter cannot be relevant, being the underlying physics of bore formation more complex with many processes involved. We propose a new scaling for the equations that ensures a clear separation of the different effects. As a consequence, we end up with a set of dimensionless parameters defining a space in which real alluvial estuaries developing bores are clearly divided from those where bores are not observed. The main findings of this chapter refers to the published work of Bonneton *et al.* [2016] and to the submitted work of Arpaia *et al.* [2016].

6.1 Physical background

The study of large scale tidal wave propagation in funnel shaped estuaries is often performed under several simplifying assumptions. The geometry of real alluvial estuaries in coastal plains can be well-approximated by an exponentially decreasing width variation and flat bathymetry (*cf.* Davies et Woodroffe [2010]; Friedrichs et Aubrey [1994]; Savenije [2012]). This morphology is the natural result of a morphodynamic equilibrium of the erosion/sedimentation process. An alluvial estuary geometry can, thus, generally be characterized by two characteristic length scales: the mean water depth h_0 and the convergence length L_B, defined as $L_B = |B/\frac{dB}{dx}|$, where $B(x)$ is the channel width and x is the along channel coordinate directed landward. Our study will, thus, be performed on the simplified case (figure 6.1) of a tide propagating in an idealized convergent channel of constant depth h_0 and width $B(x)$, assumed to decrease exponentially in the x-direction with the law:

$$B(x) = B_0 e^{-x/L_B} \ .$$

We assume a rectangular cross-section suitable, as a first approximation, to describe the behaviour of a real section with the same area.

The shallow water equations for flows in open channel with exponentially decreasing cross section area are defined by:

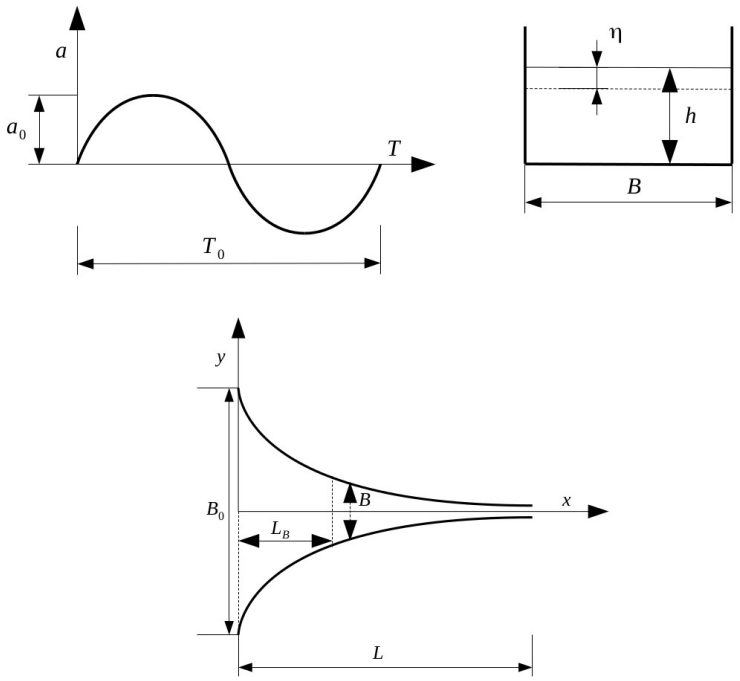

Figure 6.1: Sketch of the idealized geometry of the channel and basic notations.

$$\begin{aligned} \frac{\partial \eta}{\partial t} + u\frac{\partial \eta}{\partial x} + h\frac{\partial u}{\partial x} - \frac{uh}{L_B} &= 0 \,, \\ \frac{\partial u}{\partial t} + u\frac{\partial u}{\partial x} + g\frac{\partial \eta}{\partial x} + C_{f0}\frac{u|u|}{h} &= 0 \,, \end{aligned} \tag{6.1}$$

The friction term has been modelled by a quadratic law, with C_{f0} the friction coefficient.
Several non-dimensional forms of system (6.1) have been proposed in literature, here we refer the reader in particular to Munchow et Garvin [1991]; Lanzoni et Seminara [1998]; Toffolon *et al.* [2006]; Cai *et al.* [2014]; Bonneton *et al.* [2015]. These studies are based on the following scaling of the variables:

$$x = L_0 x' \,, \qquad t = \frac{t'}{\omega_0} \,, \qquad h = h_0 h' \,, \qquad \eta = a_0 \eta' \,, \qquad u = U_0 u' \,, \tag{6.2}$$

where h_0, a_0 and $\omega_0 = \frac{2\pi}{T_0}$ form a set of reference external parameters, respectively the water depth, the amplitude and the angular frequency of the tidal wave, while L_0 and U_0 are respectively the *a priori* unknown scales of length and velocity related to the channel response. As a result, they can be formulated as functions of the previous external variables. With the above scaling,

the dimensionless governing equations become (dropping the primes for the sake of clarity):

$$\begin{aligned} \frac{\partial \eta}{\partial t} + \frac{K}{\mathcal{L}}\left(\epsilon_0 u \frac{\partial \eta}{\partial x} + h\frac{\partial u}{\partial x}\right) - Kuh &= 0 \ , \\ \frac{\partial u}{\partial t} + \frac{K}{\mathcal{L}}\epsilon_0 u\frac{\partial u}{\partial x} + \frac{1}{K\mathcal{L}}\delta_0^2\frac{\partial \eta}{\partial x} + K\frac{\epsilon_0\phi_0}{\delta_0}\frac{u|u|}{h} &= 0 \ . \end{aligned} \tag{6.3}$$

These equations appear to be fully controlled by the three external dimensionless parameters ϵ_0, δ_0 and ϕ_0 defined by:

$$\epsilon_0 = \frac{a_0}{h_0} \ ; \qquad \delta_0 = \frac{L_{w0}}{L_B} \ ; \qquad \phi_0 = \frac{C_{f0}(gh_0)^{1/2}}{\omega_0 h_0} \ . \tag{6.4}$$

in here, ϵ_0 represents the standard nonlinearity parameter, δ_0 is the convergence ratio and ϕ_0 is a friction parameter and $L_{w0} = (gh_0)^{1/2}\omega_0^{-1}$ is the frictionless tidal-wave length scale. Moreover, for later use, we define the dissipation parameter as the ratio between friction terms and local inertia:

$$D_i = K\frac{\epsilon_0\phi_0}{\delta_0} \ . \tag{6.5}$$

K and $\mathcal{L}$ are functions of the length and velocity scales of the phenomenon:

$$\mathcal{L} = \frac{L_0}{L_b} \ ; \qquad K = \frac{U_0 D_0}{A_0\omega_0 L_b} \ . \tag{6.6}$$

Note that K represents the ratio between the temporal variation of water depth and the kinematic effects of channel convergence, as described in Lanzoni et Seminara [1998].

According to Lanzoni et Seminara [1998], the dimensionless parameters K and D_i allow the classification of the natural estuaries into four main categories: as strongly/weakly dissipative, respectively for values of the dissipation parameters $D_i \gg 1$ and $D_i \ll 1$; as strongly/weakly convergent, respectively for values of $K \sim \mathcal{O}(1)$ and $K \ll 1$. Field observations, reported in Bonneton *et al.* [2015], showed that tidal bore estuaries displays $K \simeq 1$. In this case, the comparison between the two nonlinear terms of the momentum equations (advection and friction) shows that $D_i^* = \epsilon_0\phi_0/\delta_0$ fully characterizes the tidal wave nonlinearity, being in nature always one order of magnitude greater than ϵ_0. This comparison is reported in figure 6.2 for 21 natural alluvial estuaries, characterized (red) or not (blue) by a tidal bore, the interested reader is referred to table C.1 for an overview on the used database. The data have been collected from several published works in the literature, selecting alluvial and regular funnal-shaped estuaries. Eight tidal-bore (TB) and thirteen non tidal-bore (NTB) estuaries have been collected. We have not considered

TB estuaries with complex morphologies such as the Sée/Mont Saint Michel estuary (*cf.* Furgerot [2014]) or the Petitcodiac river (*cf.* Bartsch-Winkler et Lynch [1988]). It is worth mentioning that the morphology of most estuaries presented in table C.1 is now constrained by manmade structures and their morphology cannot evolve naturally anymore.
Both theoretical studies (*cf.* Lanzoni et Seminara [1998]) and experimental observations Bonneton *et al.* [2015] agree that large values of the dissipation parameter D_i^* produce great distortion and peaking of the free surface and velocity profiles of the tidal wave, leading to flood dominance; characteristics which correspond to necessary conditions for tidal bore formation ($D_i^* \geq 1.7$ in Bonneton *et al.* [2015]). However, large values of D_i^* correspond also to high energy dissipation, leading to tidal damping; unfavourable to tidal bore formation. For this reason, $D_i^* \geq 1.7$ could not represent a sufficient condition for tidal bore formation and many natural estuaries, despite having high values of D_i^*, don't display a bore (see figure 6.2). To this purpose, we point out the mixed distribution of red and blue points in figure 6.2.

In order to evaluate the relative importance of friction in the momentum balance, several definitions of the friction parameter have been introduced in the literature. Since they rely on the same scaling of the equations, it is worth clarifying the relation with our set of parameters. Lanzoni et Seminara [1998] introduced $R/S = K\epsilon_0\phi_0\delta_0^{-1}$, whereas Toffolon *et al.* [2006] and Savenije *et al.* [2008] defined $\chi = \epsilon_0\phi_0$, and finally Munchow et Garvin [1991] used $\phi = (\epsilon_0\phi_0)^{-1/3}$. Although the definitions are analogous from a physical point of view, the one introduced in this work allows to investigate separately the opposite effects of peaking and dissipation which take place for high values of D_i^*. We will thus explore numerically the space of the external parameters ϵ_0, δ_0 and ϕ_0 to understand the complex equilibrium between these two effects.

6.2 First observations

In order to start analyzing tidal bore occurrence as a function of the three external dimensionless parameters (ϵ_0, δ_0 and ϕ_0), we start by presented the respective positions of the 21 estuaries of table C.1 in the two planes (ϵ_0, δ_0) and (ϕ_0, ϵ_0).
Figure 6.3 (left) shows the data projection on the space of parameters (ϵ_0, δ_0). We can see that no clear separation between TB and NTB estuaries emerges in this plane: the TB estuaries are characterized by large δ_0 values with a relative low dispersion around the mean value of 2.4 . It can also be noted that large dimensionless tidal amplitudes correspond to large estuary convergences. This observation, which points to a coupling between the tidal forcing and the estuary morphology, is in agreement with previously results

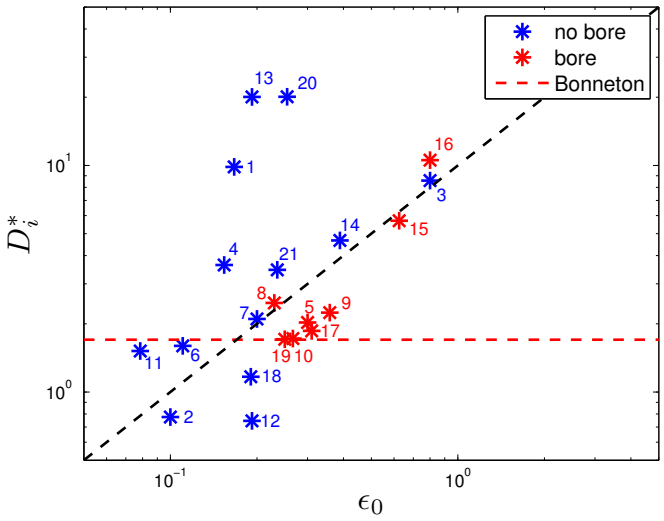

Figure 6.2: The relationship between the two nonlinear parameters ϵ_0 and D_i^* displayed by the 21 alluvial estuaries listed in table C.1. The log-log plot highlights the different order of magnitude assumed by the two terms. The black dashed line (- -) delineates points where $D_i^*/\epsilon_0 = 10$, displaying the dominance of D_i^* in influencing the nonlinear behaviour of tidal propagation in natural estuaries. Red line (- -) represents the limit of Bonneton's necessary condition for tidal bore formation ($D_i^* \geq 1.7$). For brevity and completeness, we list here the name and number of the estuaries included in the picture: 1. Chao Phya; 2. Columbia; 3. Conwy; 4. Corantijin; 5. Daly; 6. Delaware; 7. Elbe; 8. Gironde; 9. Hooghly; 10. Humber; 11. Limpopo; 12. Loire; 13. Mae Klong; 14. Maputo; 15. Ord; 16. Pungue; 17. Qiantang; 18. Scheldt; 19. Severn; 20. Tha Chin; 21. Thames. Sources: Savenije [2012] for estuaries 1, 4, 11, 13, 14, 18, 20; Lanzoni et Seminara [1998] for 2, 3, 6, 7, 15, 19, 21; Bonneton *et al.* [2015] for 8, 9, 10, 16, 17; Wolanski *et al.* [2006] for 5; Winterwerp *et al.* [2013] for 12.

from Prandle [2003] and Davies et Woodroffe [2010]. Moreover, it is worth mentioning that these convergence ratios are close to the critical convergence δ_c introduced by Jay [1991]; Savenije *et al.* [2008]. δ_c is a threshold condition for the transition from the mixed tidal wave to the *apparent standing* tidal wave. Savenije *et al.* [2008] derived the following equation, relating the critical convergence and the dimensionless parameter $\chi = \epsilon_0\phi_0$:

$$\chi(\delta_c) = \frac{1}{2}\delta_c(\delta_c^2 - 4) + \frac{(\delta_c^2 - 2)}{2}\sqrt{\delta_c^2 - 4}\ .$$

The position of the 21 estuaries in the plane (δ_0, χ) are plotted in figure 6.3 (right). It can be seen that tidal bores occur near critical convergence. At

this stage, we have no physical explanation for this observation and further theoretical and numerical investigations would be desirable.

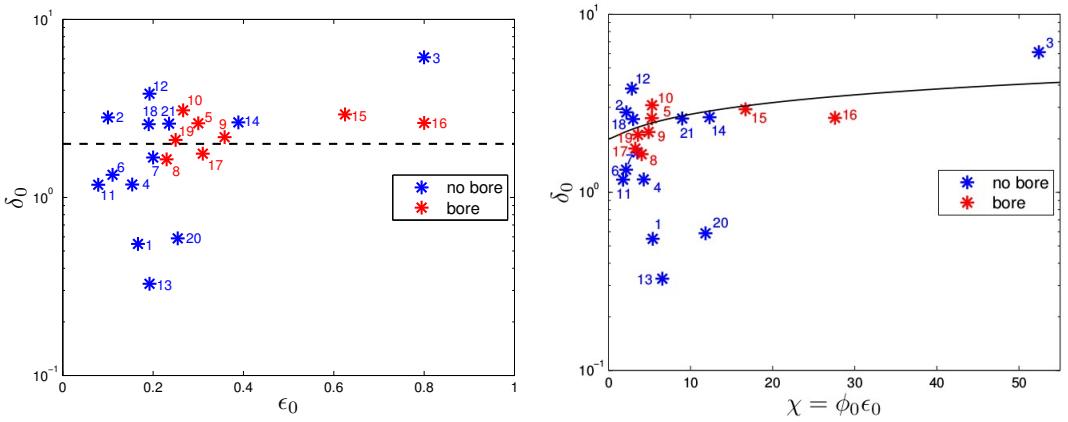

Figure 6.3: Projection of the real estuaries of table C.1 on the plane (ϵ_0, δ_0) (on the left) and on the plane (χ, δ_0) (on the right). The dashed black line (- -) represents points with $\delta_0 = 2$, while the black continuous line (–) stays for the critical curve $\chi(\delta_c)$, defined in Savenije *et al.* [2008]. The database used to generate the picture can be found in table C.1, for brevity and completeness we list here the name and number of the estuaries included in the picture: 1. Chao Phya; 2. Columbia; 3. Conwy; 4. Corantijin; 5. Daly; 6. Delaware; 7. Elbe; 8. Gironde; 9. Hooghly; 10. Humber; 11. Limpopo; 12. Loire; 13. Mae Klong; 14. Maputo; 15. Ord; 16. Pungue; 17. Qiantang; 18. Scheldt; 19. Severn; 20. Tha Chin; 21. Thames. Sources: Savenije [2012] for estuaries 1, 4, 11, 13, 14, 18, 20; Lanzoni et Seminara [1998] for 2, 3, 6, 7, 15, 19, 21; Bonneton *et al.* [2015] for 8, 9, 10, 16, 17; Wolanski *et al.* [2006] for 5; Winterwerp *et al.* [2013] for 12.

The projection of the available data on the plane (ϕ_0, ϵ_0) is instead plotted in figure 6.2. In this parameter plane, we can observe a clear separation between TB and NTB estuaries. Tidal bores occur when the nonlinearity parameter ϵ_0 is greater than a critical value, ϵ_c, which is an increasing function of ϕ_0. For small ϕ_0 values ($\phi_0 \sim 15$), corresponding to estuaries such as that of the Severn river, tidal bores can form for $\epsilon_0 > 0.2$. In contrast, for large ϕ_0 values, the tidal bore formation requires much larger nonlinearities. For instance, in the Conwy estuary, the tidal wave dynamics is strongly nonlinear ($\epsilon_0 = 0.8$), but its very large friction parameter value ($\phi_0 = 65$) prevents tidal bore formation. Due to the limited number of estuaries documented in the literature, it is difficult to accurately characterize the function $\epsilon_c(\phi_0)$. A numerical investigation can be overcome this limitation.

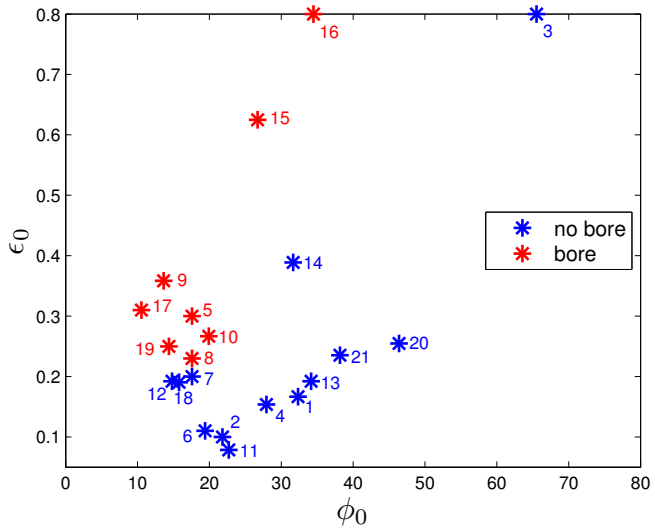

Figure 6.4: Projection of the real estuaries of table C.1 on the plane (ϕ_0, ϵ_0), for brevity and completeness we list here the name and number of the estuaries included in the picture: 1. Chao Phya; 2. Columbia; 3. Conwy; 4. Corantijin; 5. Daly; 6. Delaware; 7. Elbe; 8. Gironde; 9. Hooghly; 10. Humber; 11. Limpopo; 12. Loire; 13. Mae Klong; 14. Maputo; 15. Ord; 16. Pungue; 17. Qiantang; 18. Scheldt; 19. Severn; 20. Tha Chin; 21. Thames. Sources: Savenije [2012] for estuaries 1, 4, 11, 13, 14, 18, 20; Lanzoni et Seminara [1998] for 2, 3, 6, 7, 15, 19, 21; Bonneton *et al.* [2015] for 8, 9, 10, 16, 17; Wolanski *et al.* [2006] for 5; Winterwerp *et al.* [2013] for 12.

6.3 Case study

Considering that, for most alluvial estuaries, the convergence ratio δ_0 is close to 2 (as showed in figure 6.3), we have chosen to perform our analysis using a constant value $\delta_0 = 2$. Due to such a simplification, the expression of the dissipation parameter (6.5) reduces to: $D_i^* = \alpha\epsilon_0\phi_0$ (with α constant). Thus, it is possible to investigate the separate effects of peaking and dissipation, both contained in D_i^*, by numerically exploring the plane of the dimensionless parameters (ϕ_0, ϵ_0).

We will, at first, neglect the effects of both bathymetric variations, and river discharge. The latter will be investigated in section 6.6, confirming that, if limited to small values, the river discharge has no significant influence on the phenomenon. Nevertheless, in nature, tide propagation up to an estuary is partly limited by an increasing bottom slope and by discharge. In our idealized channel, instead, even the weakest and linear tidal wave would be able to propagate landward and, being dissipated by only friction, it would reaches

non-physical distances with unnatural generation of shock solutions. For this reason, a characteristic physical length L_c has been introduced to limit the region in which the tidal signal is assumed to be physically relevant. In particular, examining real estuaries data, we observed that tidal bores occur, before reaching a distance of $3L_B$ from the estuary mouth, see table 6.1. We, thus, have chosen to limit the region of interest for our simulations to $L_c = 3L_B$.

Estuaries	L_b [km]	x_c [km]	x_c/L_b
Gironde/Garonne	43	90	2.09
Hooghly	25	60	2.4
Humber	25	75	3.0
Pungue	17	50	2.94
Qiantang	40	90	2.25
Severn	41	55	1.34

Table 6.1: Ratio between the location of tidal bore inception x_c and convergence length L_b for some alluvial estuaries. Data taken from Bonneton *et al.* [2015].

In nature, tidal bore inception is a continuous process which takes place as a gradual increase of the free surface slope at the beginning of the flood phase. The same continuous increase of steepness is observed in our simulations. A criterion is thus needed to detect the bore onset, within the domain $[0, L_c]$ just defined. During the two measurement campaigns on the Garonne river, Bonneton *et al.* [2015] observed that bore passage was associated to an increase in the value of the free surface spatial gradient, at the start of the flood, with at least one order of magnitude (from $\mathcal{O}(10^{-4})$ in the smooth case without tidal bore). For each numerical simulation we compute, in a post-processing phase, the spatial slope of the free surface all along the domain, up to L_c, retaining for each position x the maximum value in the tidal period. The quantity A_{max} has been defined as:

$$A_{max} = \max_{x \in L_c} \left[\max_{t \in T_0} \left(\frac{\partial \zeta(x,t)}{\partial x} \right) \right] ,$$

and the following criterion for determining tidal bore occurrence is used: $A_{max} \geq 10^{-3}$. We observe that the function $A(x) = \max_{t \in T_0} \left(\frac{\partial \zeta(x,t)}{\partial x} \right)$ is monotone for all the simulations performed. In practice, A_{max} has been thus evaluated by only considering the last section of the channel at $x = L_c$:

$$A_{max} = \max_{t \in T_0} \left(\frac{\partial \zeta}{\partial x}\Big|_{L_c} \right) .$$

6.4 Numerical model

For robustness, we performed our simulations with both second order finite volume (FV2) and residual distribution schemes (RD2), solving the conservative form of the two-dimensional NLSW equations (1.59), with now a friction term written in the form: $\tau = C_f \mathbf{u}|\mathbf{u}|$. The former one consists in the scheme obtained by imposing $\beta = -1$ in the MUSCL formula of the left and right gradients computation (4.18), whose accuracy on the Shallow Water system have been tested on the traveling vortex case (*cf.* 5.1). The second order residual based scheme is the one discussed and validated in Ricchiuto [2015]. It consists of a shock capturing residual distribution scheme with an explicit predictor-corrector time integrator. The numerical method is based on a flux limited non-linear residual distribution approach, allowing a fully second order approximation of smooth waves, and a monotone approximation of bores. This method has been used in Bonneton *et al.* [2016] to perform the results that will be discussed in the following. At the mesh used for the computations, the two schemes perform almost identical results on the large scale of the phenomenon, as illustrated by figure 6.5. They can be thus considered as mesh converged results, leading to a numerical analysis completely independent from the method used.

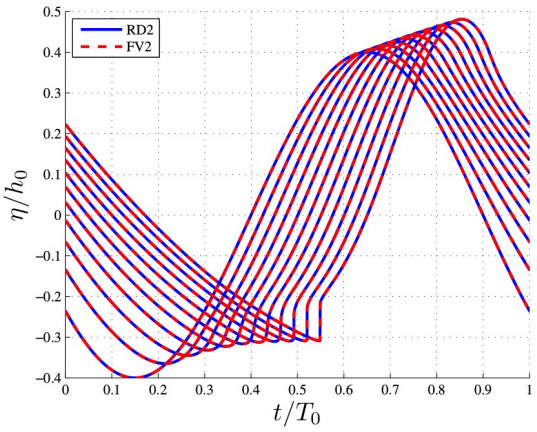

Figure 6.5: Illustrative result of tidal propagation into an idealized channel with the shape described in section 6.1, $\epsilon_0 = 0.4$, $\phi_0 = 20$. Computed free surface profile, measured at 11 stations along the channel corresponding to $x = \alpha L_B$ with $\alpha = 0 : 1/3 : 3$. The simulation have been realized using both the FV2 and RD2 schemes.

In section 6.1, some dominant dimensionless parameters have been derived under the hypothesis of quasi-one-dimensional flow. At the beginning of our investigation, this assumption has been verified, founding that the largest

transversal deviations from the average values were below 1.5%. Thank to this, the flow field inside the channel can be fully described by the values of the variables measured on the longitudinal axis. Moreover, due to the symmetry of the geometry, only half of the domain will be used in the simulation, imposing wall reflecting boundary conditions on the symmetry axis. Wall boundary conditions are also imposed in the exponential varying edge of the domain.

Seaward boundary condition: The choice of the boundary conditions on the two shorter edges of the domain, namely the inflow and outflow boundaries, affects the flow field significantly Toffolon [2002]. The seaward boundary condition is given, in terms of the free surface, by the sea level, which is assumed to be determined by the tidal oscillation without any influence of the internal response of the estuary. The following temporal law:

$$\zeta(t) = A_0 \sin\left(\frac{2\pi t}{T_0}\right) ,$$

is thus applied at the estuary mouth by imposing the incoming Riemann invariant. We consider here the case of semi-diurnal tides with period $T_0 = 12.41$ $[h]$.

Numerical Validation: Lanzoni et Seminara [1998] performed several one-dimensional computations using the Saint-Venant system (6.1). For the case of strongly convergent and medium/strongly dissipative channels, they have presented many solutions corresponding to a progressive increase of the value of the friction parameter ϕ_0. Our numerical scheme and inlet boundary condition have thus been validated by reproducing the numerical test case contained in Lanzoni et Seminara [1998] characterized by values of the external parameters: $\epsilon_0 = 0.15$, $\delta_0 = 1.98$ and $\phi_0 = 26.41$ (*cf.* figure 9 of Lanzoni et Seminara [1998]). Figure 6.6 shows the comparison between our results and the ones presented in Lanzoni et Seminara [1998] in terms of the time evolution of the dimensionless flow surface elevation η/h_0 and tidal velocity u/U_0 at distances $x/L_B = m/4$ ($m \in [0, 4]$). These are recovered by imposing a wall boundary condition at the end of the channel $x/L_B = 1$. The results show globally a very good match on this smooth case.

Landward boundary condition: On the landward boundary, the information of still water (we recall that the river discharge is neglected at this level) coming from far on the right should be generally imposed by means of the Riemann invariants. However, such condition is not known *a priori* due

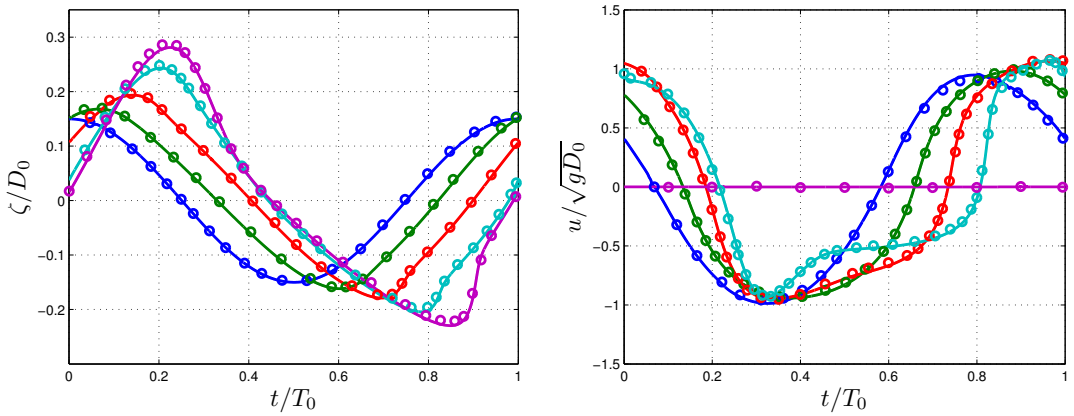

Figure 6.6: Time evolution of the dimensionless flow surface elevation (left) and tidal velocity (right) at locations: $x/L_B = 0$ blue, $x/L_B = 1/4$ green, $x/L_B = 1/2$ red, $x/L_B = 3/4$ cyan, $x/L_B = 1$ magenta. Continuous lines (−) represent the results computed by our 2D numerical scheme, while circles (o) represent the results of Lanzoni et Seminara [1998].

to the presence of the friction, which is not easy to take into account in the computation of the Riemann invariants. Because of this, imposing correctly the landward boundary condition is not a trivial operation. Up to the authors knowledge, there is not an efficient and systematic method to impose absorbing boundary conditions in the presence of friction and convergence. Toffolon Toffolon [2002] revealed the difficulties of imposing such conditions. He considered two limit cases: the reflecting barrier and the transparent condition. On the former, a wall boundary condition was imposed at the end of the channel, which determined a complete reflection of the wave. The latter condition, instead, referred to a situation where the tidal wave exited from the computational domain without being deformed or reflected. This condition was implemented by replacing, on the last cells of the domain, mass and momentum conservation laws with a scalar advection equation for each conservative variable, characterized by an advection speed equal to the outgoing eigenvalue. Even though, the need of considering a longer estuary in order to vanish the influence of the boundary on the solution, remained.
Here we set an absorbing boundary by means of the homogeneous NLSW invariants. A sensitivity analysis has been performed in order to quantify the influence of the inexact boundary condition that has been implemented. Two tests have been conducted: one for a low and the other for a high value of the nonlinear parameter ϵ_0, respectively $\epsilon_0 = 0.1$ and $\epsilon_0 = 0.7$. We compare two solutions: the former computed by setting the absorbing boundary condition at the location $x = 5L_B$, and the latter, considered as a reference, derived by imposing a reflective wall at the further distance $x = 8L_B$, where the tidal wave

is assumed to be completely dissipated. Figure 6.7 shows the time evolution profiles of the non-dimensional free surface and velocity at different positions along the channel. In order to measure the deviation from the reference solution we use the L_2-norm $\frac{||\eta-\eta_{ref}||_{L_2}}{||\eta_{ref}||_{L_2}}$. At the station $x = 3L_B$, the percentage values of the deviation are 3.3% for η and 3.98% for u in the case with $\epsilon_0 = 0.1$, while being respectively 5.27% and 7.67% in the case with $\epsilon_0 = 0.7$.

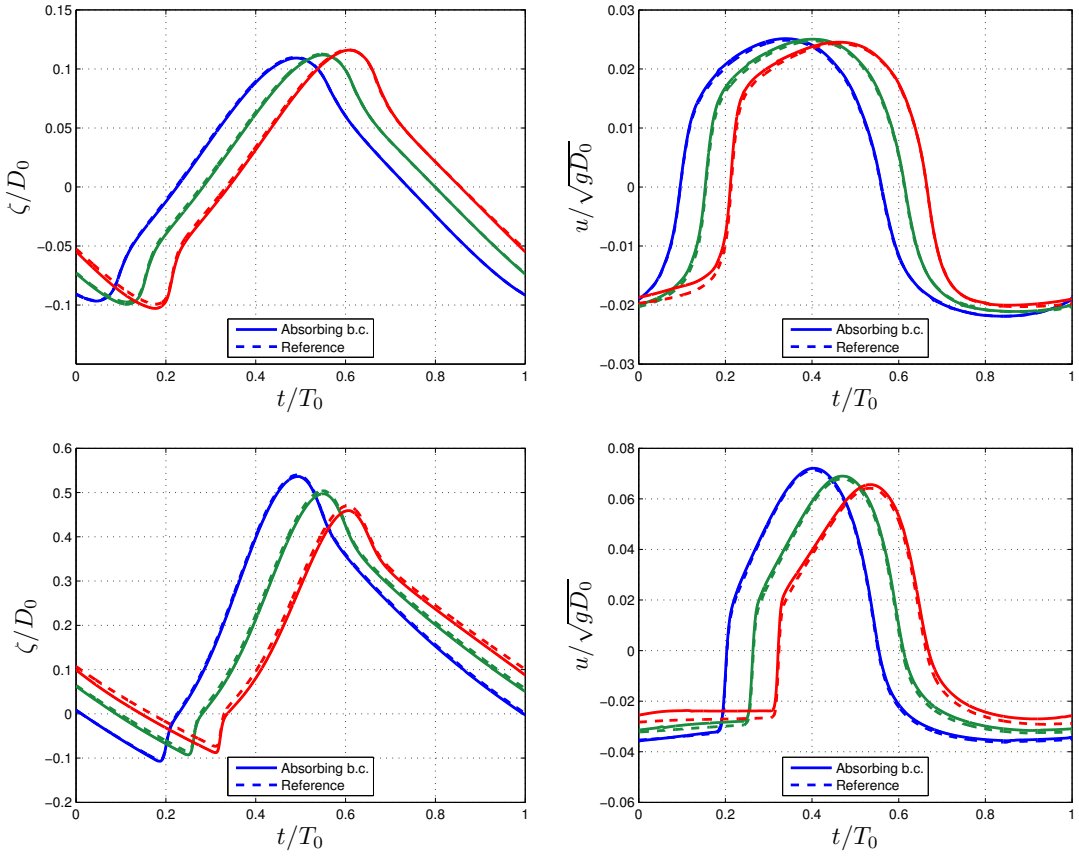

Figure 6.7: Time evolution profiles of the non-dimensional free surface (left) and velocity (right) measured at $x = 2L_B$ (–), $x = 2.5L_B$ (–) and $x = 3L_B$ (–) for the two test cases performed with $\epsilon_0 = 0.1$ (top) and $\epsilon_0 = 0.7$ (bottom). In the two computations ϕ_0 has been set constant and equals to $\phi_0 = 35$. Continuous lines represent the results obtained by using absorbing landward boundary conditions by means of the homogeneous NLSW invariants at $x = 5L_B$; while dashed lines were obtained by imposing wall boundary conditions at $x = 8L_B$.

	$\epsilon_0 = 0.1$		$\epsilon_0 = 0.7$	
Location	$\frac{\|\|\eta - \eta_{ref}\|\|_{L_2}}{\|\|\eta_{ref}\|\|_{L_2}}$	$\frac{\|\|u - u_{ref}\|\|_{L_2}}{\|\|u_{ref}\|\|_{L_2}}$	$\frac{\|\|\eta - \eta_{ref}\|\|_{L_2}}{\|\|\eta_{ref}\|\|_{L_2}}$	$\frac{\|\|u - u_{ref}\|\|_{L_2}}{\|\|u_{ref}\|\|_{L_2}}$
$x = 2L_b$	0.0113	0.0132	0.0133	0.0188
$x = 2.5L_b$	0.0197	0.0232	0.0274	0.0384
$x = 3L_b$	0.0330	0.0398	0.0527	0.0767

Table 6.2: L2 norm of the error of the computation performed using an absorbing boundary condition at the landward boundary of the domain at $x = 5L_B$, with respect to a reference solution is computed using a wall boundary condition at $x = 8L_B$.

In addition, figure 6.8 shows the comparison with the solution performed by implementing the transparent boundary condition used in Toffolon [2002]. The percentage deviations from the reference are of the same order of magnitude as those recovered using our approach and, most importantly, the two approaches provide identical topologies for both the water depth and the velocity. We can conclude that the results of our study are independent from the choice of the method used.

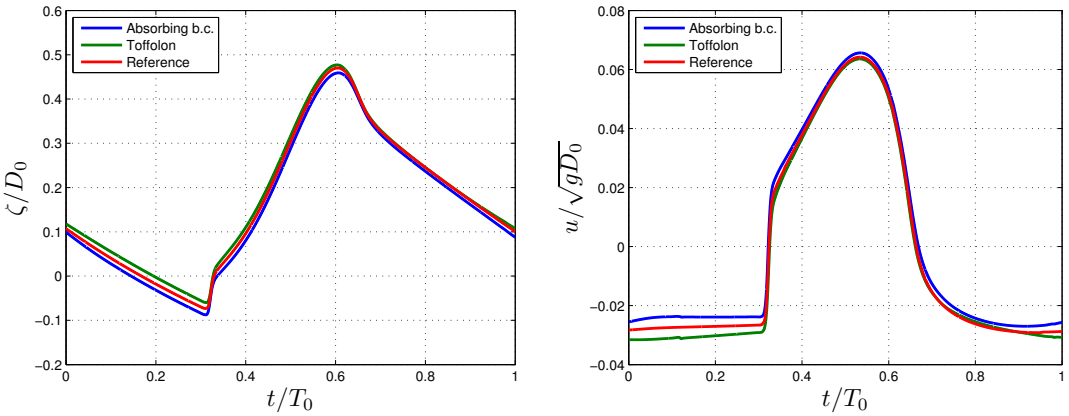

Figure 6.8: Time evolution profiles of the non-dimensional free surface (left) and velocity (right) measured at $x = 3L_B$, obtained by setting the absorbing homogeneous b.c. (–) and the transparent b.c. of Toffolon [2002] (–). The red curve (–) represents the reference solution computed by imposing wall b.c. on a longer domain of $L = 8L_B$ ($\epsilon_0 = 0.7$ and $\phi_0 = 35$).

As pointed out by Cai et al. Cai *et al.* [2014], the frictional effect increases the mean (tidally averaged) water level landward. The imposition of the homogeneous invariants cannot take into account this effect, introducing a non-physical behaviour of the solution in the outlet proximity. For this reason, the absorbing boundary conditions should be coupled with an extension of the

computational domain, to reduce these spurious influences on the solution in the region of study. In practice it has been enlarged up to $x = 6L_B$, to further limit non-physical effects due to the boundary conditions.

Dispersive effects: In the introduction of the chapter, we state that we perform an investigation looking to the long spatial scale of the phenomenon, where the effects of dispersion do not play a significant role and the free surface profile can be well described by the NLSW equations. In order to give a direct proof of this, we have performed the computation of a very nonlinear and less dissipative channel ($\epsilon = 0.7$ and $\phi_0 = 10$) with both the NLSW and the eGN system of equation, discussed in the previous chapters of this work. The eGN system is discretized using the third order hybrid FE/FV approach described in chapter 4. Also to be noted: while for SW one could use pseudo-1D models, there are no fully nonlinear weakly dispersive pseudo-1D models. Their derivation is still a subject of research (for a weakly nonlinear model see *e.g.* Winckler et Liu [2015]). The results obtained are compared in figure 6.9. They are performed in a section of the channel with $x \in [0.9L_B, 1.8L_B]$, where the bore is expected to originate, on a very refined mesh in order to catch the right wavelength of the dispersive effects.
It can be seen that the two models perform identical results in the whole domain except when the shock is formed (*cf.* top of figure 6.9). On the discontinuity the GN model describes the formation of an undular bore with a very local effect on the free surface profile. The characteristic wavelength and wave period of the secondary waves are shown in the two pictures on the bottom of figure 6.9. In particular it can be computed $\lambda \approx 50$ [m] and $T \approx 6$ [s] which is in good agreement with observations *insitu* from Bonneton *et al.* [2015].

6.5 Numerical investigation results

The (ϵ_0, ϕ_0) space: We have performed 225 simulations of the idealized case of study defined in section 6.3, corresponding to an equivalent number of estuaries. We recall that the value of convergence ratio is constant, $\delta_0 = 2$, and thus each simulation represents a unique combination of the parameters ϵ_0, ϕ_0, corresponding to precise conditions of the tidal forcing at the mouth and to specific geometrical and physical properties of the channel. In such a way we have systematically investigated the plane (ϕ_0, ϵ_0), applying the criterion described in section 6.3 in order to detect bore formation. Figure 6.10 shows the contour lines of the quantity A_{max} in the plane of the parameters (ϕ_0, ϵ_0), performed by collecting and linearly interpolating the simulations results. The red color denotes the region where the bore detection criterion is satisfied,

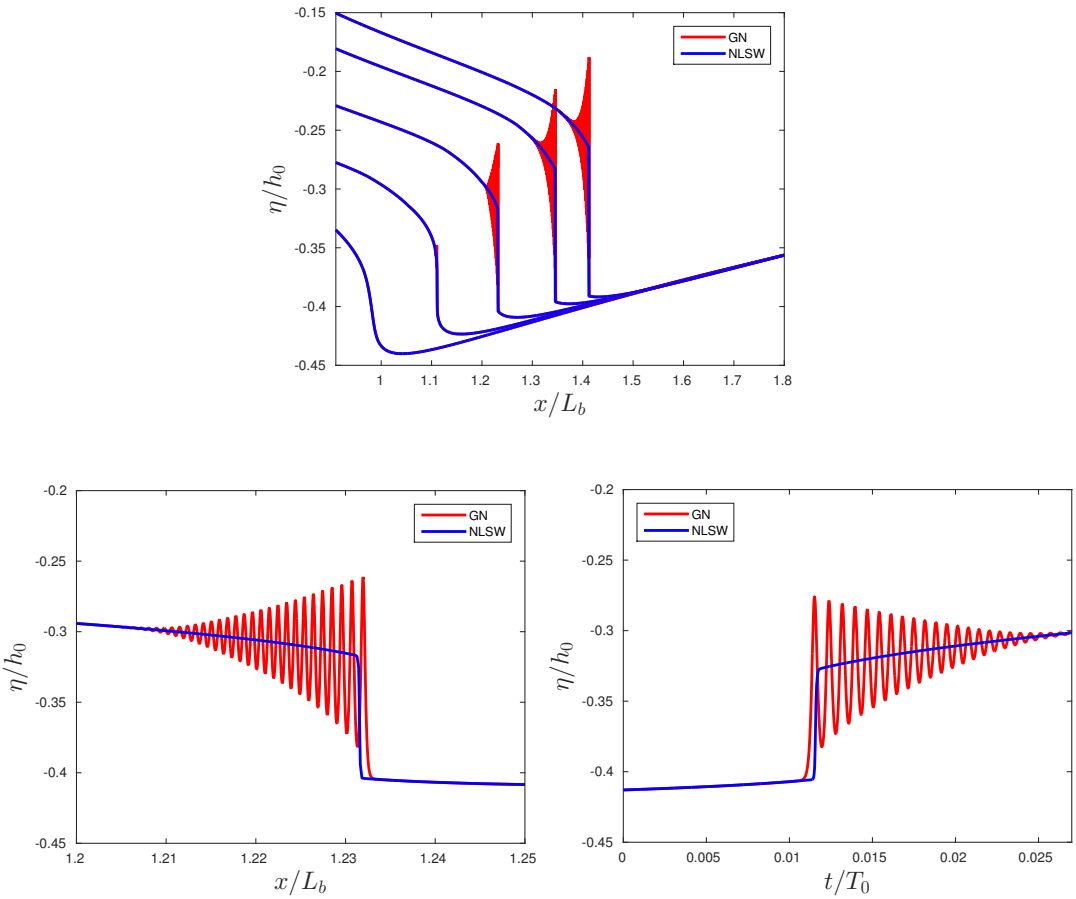

Figure 6.9: Illustrative result of tidal propagation into an idealized channel with the shape described in section 6.1, $\epsilon_0 = 0.7$, $\phi_0 = 10$. Top: computed free surface profile at different increasing times of the simulation. Bottom-left: free surface signal in space. Bottom-right: free surface signal in time.

while the blue one represents cases characterized by a smooth solution. The results show that there exists a critical curve $\epsilon_c(\phi_0)$ that can be traced in this plane, dividing tidal-bore and no-tidal-bore estuaries. This curve is the white dashed line traced in figure 6.10. Observing the shape of the isolines in figure 6.10, two different behaviours can be distinguished, depending on the values assumed by the friction parameter ϕ_0.

The first region is characterized by values of the friction parameter in the range $1 < \phi_0 \leq \sim 20$. Here the mechanism of bore inception appears to be fully controlled by the nonlinear parameter ϵ_0. Figure 6.11 shows a comparison between two numerical results computed using two different values of ϵ_0, one just above the critical curve and one just below it ($\epsilon_0 = 0.3$ and $\epsilon_0 = 0.225$ respectively), at a constant value of ϕ_0 equal to 13.33. The comparison is made in terms of the free surface and velocity time series, respectively in fig-

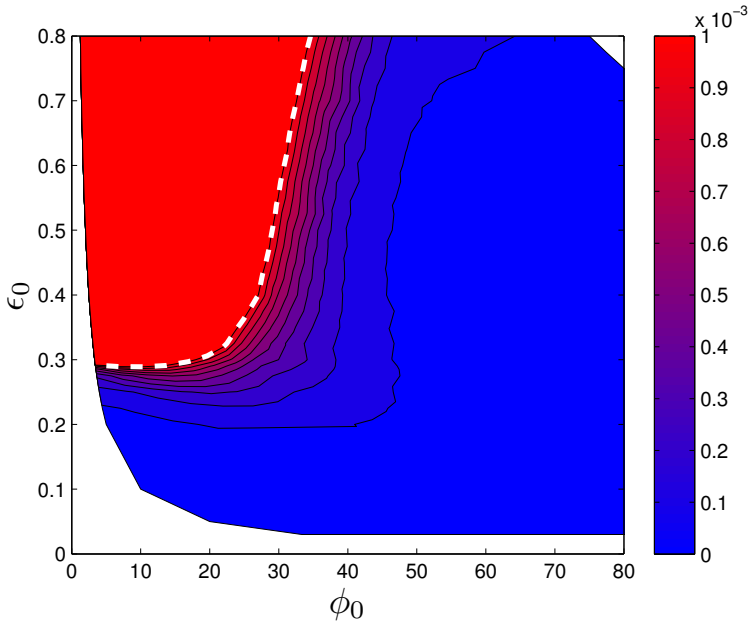

Figure 6.10: Isocurves of the quantity A_{max} in the plane of the parameters (ϕ_0, ϵ_0), the white dashed line represents the $\epsilon_c(\phi_0)$ curve, namely the limit for tidal bore appearance following the criterion $A_{max} \geq 10^{-3}$.

ure 6.11(top-left) and 6.11(top-right), measured at the location $x = L_c$. In both figures, the signals associated to the case at higher ϵ_0 are characterized by a greater distortion at the beginning of the flood phase, leading to bore formation according to our threshold. The two zooms, displayed in figures 6.11(bottom-left) and (bottom-right), allow to better appreciate the different time gradients exhibited by the water wave on the time scale of the tidal bore (around 20 minutes). It is also interesting to note that the free surface profile of figure 6.11(top-left) does not display a Burger's like shock, but rather a *knee* shape is observed. This is mainly due to the fact that the nonlinear effect of friction prevails on the advective one, remaining the dominant nonlinearity for the major part of the wave transformation. Figures 6.12 and 6.13 display the relative importance of the various terms in the governing equations (6.1) during a tidal cycle in the previous case of bore development ($\epsilon_0 = 0.3$ and $\phi_0 = 13.33$). In the figures, the time evolution of these quantities is represented at three equispaced locations along the channel, in particular at $x = \frac{1}{3}L_c$, $x = \frac{2}{3}L_c$ and $x = L_c$. It emerges that the advective term remains negligible in the momentum equation and the bore formation results from a balance between acceleration, friction and hydrostatic terms. Only in the presence of incipient bore, the relative importance of the advective term rises up overcoming the frictional nonlinearity.

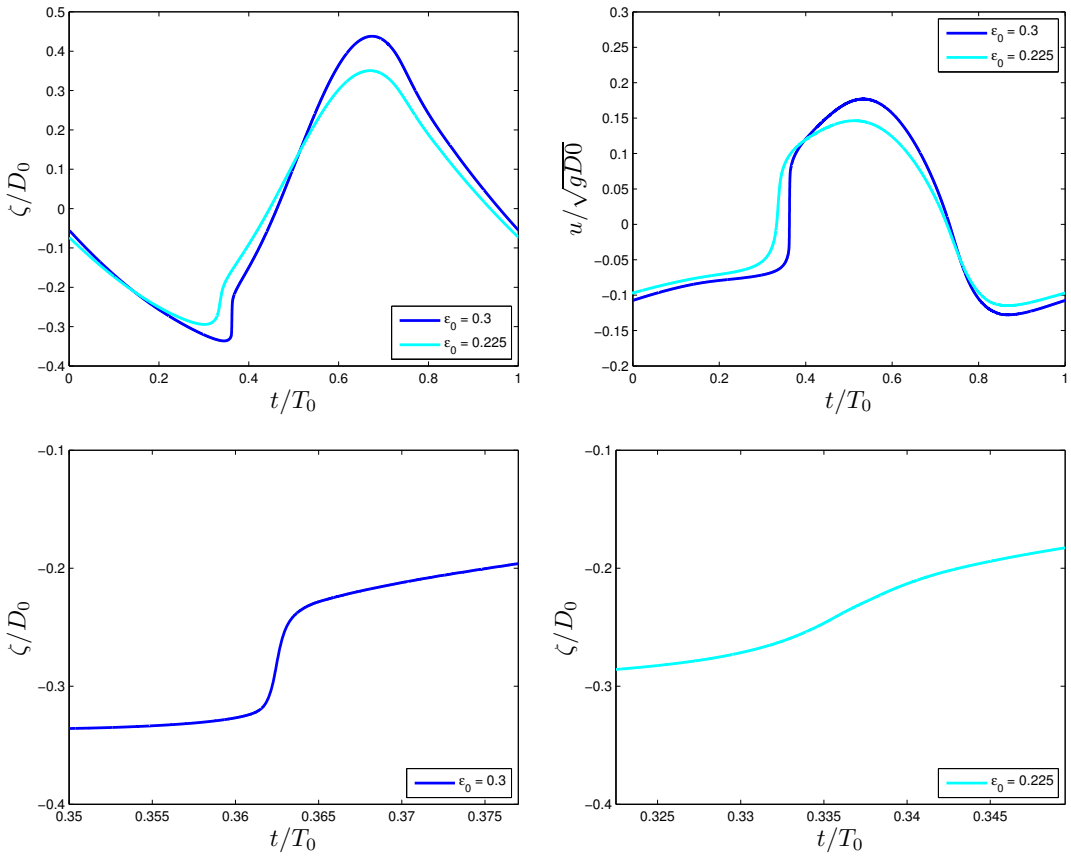

Figure 6.11: Time variation of the free surface elevation (top-left) and the velocity (top-right) signals measured at $x = L_c$ for a fixed value of $\phi_0 = 13.33$ and the two different values of $\epsilon_0 = 0.225$ (–) and $\epsilon_0 = 0.3$ (–). (bottom-left) and (bottom-right) are two zooms on the water wave profile at the beginning of the flood phase, on the time scale of the tidal bore (around 20 minutes).

For higher values of ϕ_0 ($\phi_0 \geq \sim 20$), the isolines of A_{max} spread out forming a wider transition region but, more important, display an almost vertical slope. This implies an increasing role of the friction parameter in the physical mechanism of bore formation. In figure 6.14, we show the solutions computed for two cases across the transition zone ($\phi_0 = 20$ and $\phi_0 = 40$ respectively), keeping constant $\epsilon_0 = 0.4$. Once again, we look to the free surface and velocity time signals to compare the two results, figures 6.14(top-left) and 6.14(top-right) respectively. It clearly appears that an increase of the value of the friction parameter ϕ_0 is directly associated to both potential and kinetic energy dissipation, leading to more damped profiles. This process decreases the local nonlinearity of the wave which, in turn, is smeared out, as one can see from the free surface zooms on the time scale of the bore (figures 6.14(bottom-left) and 6.14(bottom-right)). Moreover, figures 6.14(top-right) displays the par-

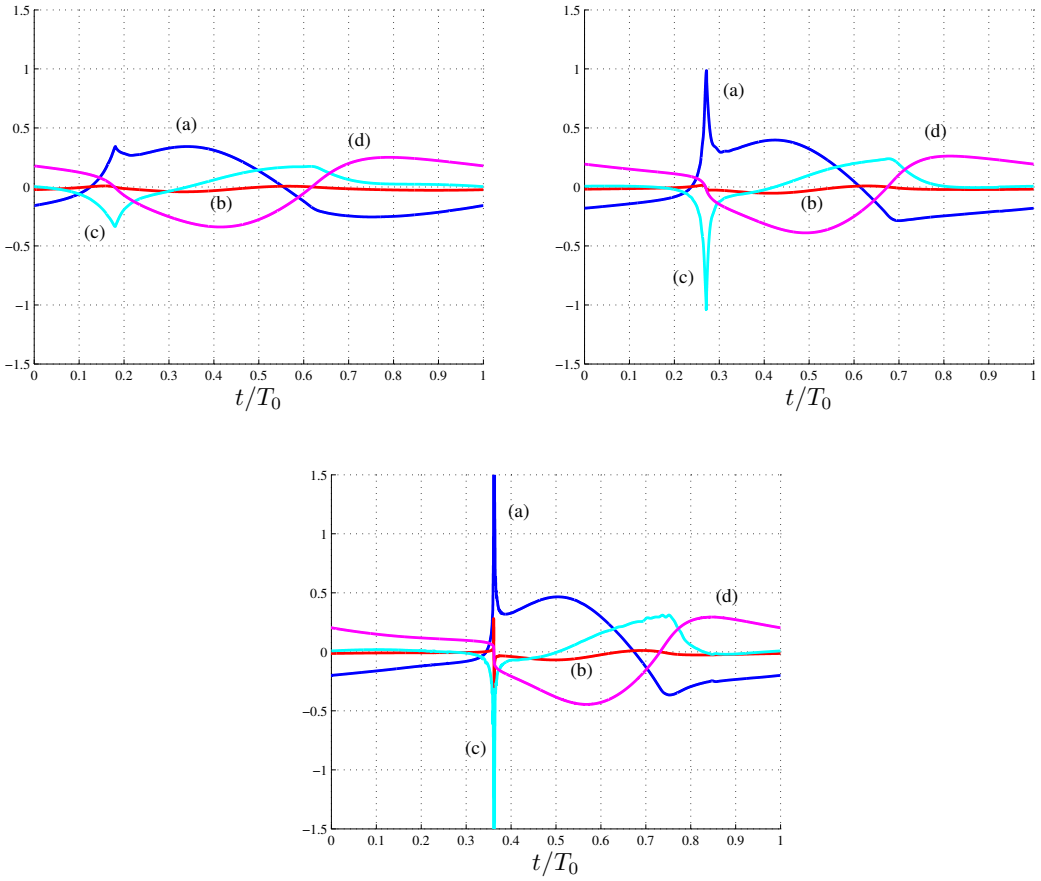

Figure 6.12: The order of magnitude of the several dimensionless terms in the continuity equation of system (6.3); three test sections are presented: at $x = \frac{1}{3}L_c$ (top-left), $x = \frac{2}{3}L_c$ (top-right) and $x = L_c$ (bottom): (a) $\frac{\partial \eta}{\partial t}$, (b) $\frac{K}{\mathcal{L}}\epsilon_0 u\frac{\partial \eta}{\partial x}$, (c) $\frac{K}{\mathcal{L}}D\frac{\partial u}{\partial x}$ and (d) $-KuD$. Upper and lower peaks on the figure (right) reach values respectively of 13.38 and -12.

ticular tendency of the flow river to become constant during the ebb tide for large values of the friction parameter (strongly dissipative estuaries), recovering what already observed in Lanzoni et Seminara [1998] and Bonneton *et al.* [2015].

The separation between estuaries displaying or not a tidal bore, which emerges from our numerical results, is also in qualitative agreement with figure 6.2, realized using the estuary database of table C.1. A critical curve can be traced by hand on figure 6.2, inspired by the trend emerged from the numerical results of figure 6.10. In this case, we could notice that the two curves only slightly differ. This is due to the several simplifying modeling assumptions. In

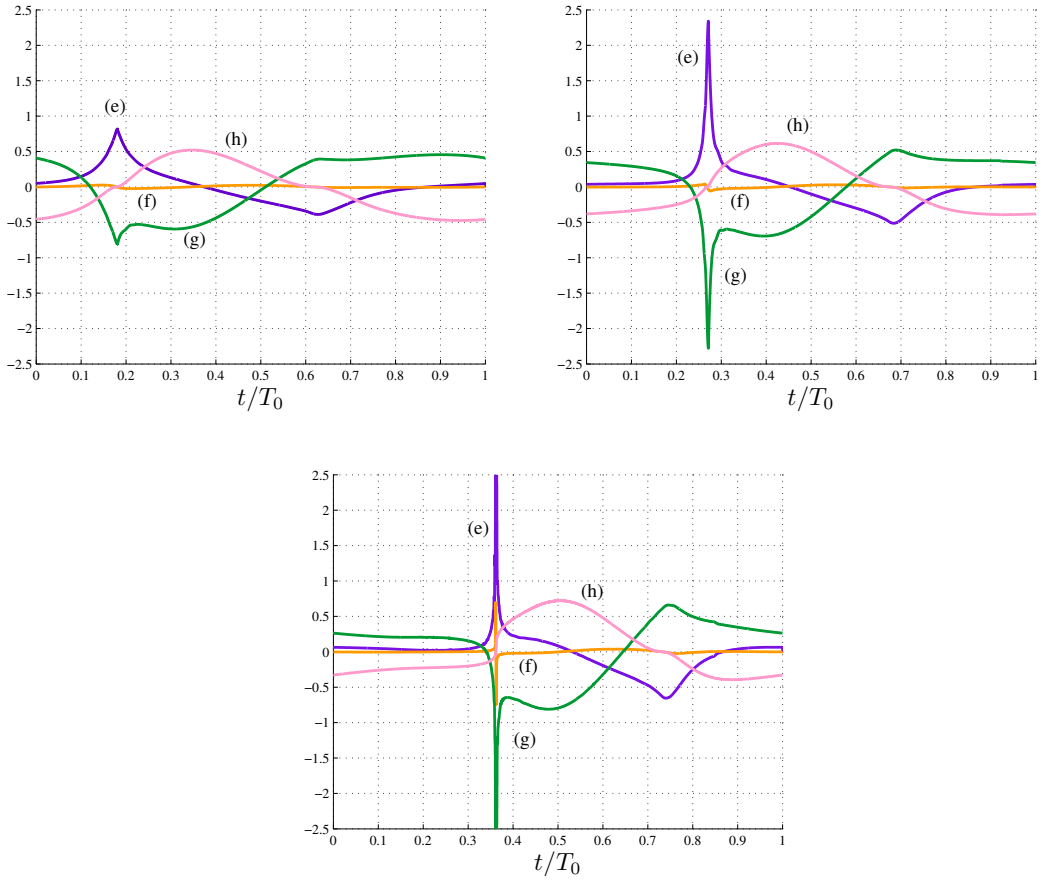

Figure 6.13: The order of magnitude of the several dimensionless terms in the momentum equation of system (6.3); three test sections are presented: at $x = \frac{1}{3}L_c$ (top-left), $x = \frac{2}{3}L_c$ (top-right) and $x = L_c$ (bottom): (e) $\frac{\partial u}{\partial t}$, (f) $\frac{K}{\mathcal{L}}\epsilon_0 u\frac{\partial u}{\partial x}$, (g) $\frac{1}{K\mathcal{L}}\delta_0^2\frac{\partial \eta}{\partial x}$ and (h) $K\frac{\epsilon_0\phi_0}{\delta_0}\frac{u|u|}{D}$. Upper and lower peaks on the figure (right) reach values respectively of 30.65 and -28.61.

particular, in real alluvial estuaries the general decrease of depth landward is favourable to bore inception and this can cause the transition curve in figure 6.2 to be located slightly below with respect to the one on figure 6.10. Moreover, the fact that a constant value $\delta_0 = 2$ has been used for the simulations contributes to the deviation, since each estuary on figure 6.2 is characterized by its own value of δ_0 and they are, here, just projected on the same plane for sake of clarity.

Summary: We can schematically summarize that the nonlinear parameter ϵ_0 mainly relates to the distortion mechanism which leads to bore formation,

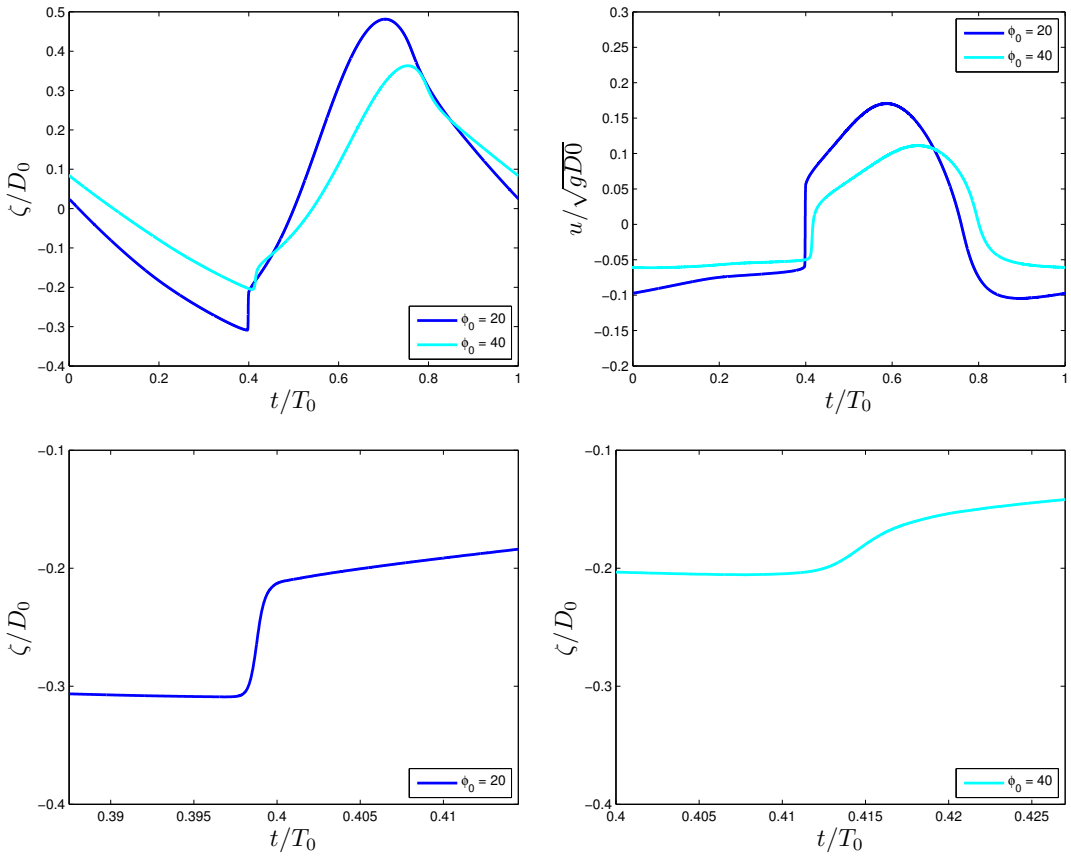

Figure 6.14: Time variation of the free surface elevation (top-left) and the velocity (top-right) signals measured at $x = L_c$ for a fixed value of $\epsilon_0 = 0.4$ and the two different values of $\phi_0 = 20$ (–) and $\phi_0 = 40$ (–). (bottom-left) and (bottom-right) are two zooms on the water wave profile at the beginning of the flood phase, on the time scale of the tidal bore (around 20 minutes).

while the friction parameter ϕ_0 mainly relates the dissipation of the tidal wave, unfavourable to bore generation. It is worth noting that only the particular definition of ϕ_0 as the friction parameter allows to clearly separate this two effects on the parameter space. Other choices, which includes the dependence from ϵ_0 (as the case of χ), although allowing to define a critical curve for bore formation would not have provide us the right comprehension of the bore formation mechanism. To support this, it is note that any competition between different effects can be recognized from figure 6.15, where an almost linear relationship between the two parameters ϵ_0 and χ_0 is displayed. The use of ϕ_0 seems a better choice because it highlights the existence of two different regimes for the critical curve (*cf.* figure 6.10): in this way the nonlinear distortion and the tidal wave dissipation effect can be schematically separated.

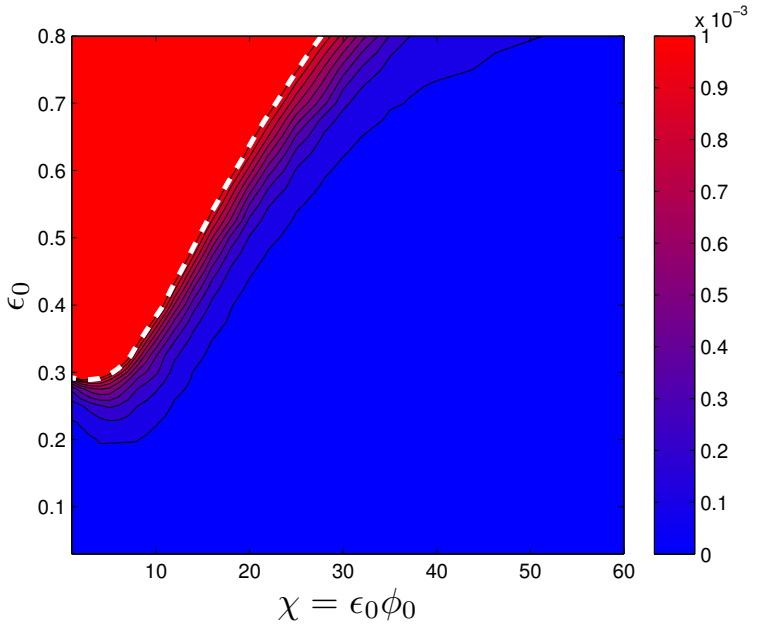

Figure 6.15: Isocurves of the quantity A_{max} in the plane of the parameters (χ_0, ϵ_0). The white dashed line represents the critical curve for bore formation ($\epsilon_c(\chi_0)$) following the criterion $A_{max} \geq 10^{-3}$.

Tidal wave amplification/damping: From the observations made in the previous paragraph, a close relation between bore formation and tidal damping emerges. A standard parameter used in the literature (*cf.* Savenije et Veling [2005]; Savenije [2001]) to measure the amplification/damping of the tidal wave during its propagation along the estuary is the rate of change of the tidal range Tr, defined in accordance to Savenije [2001] as:

$$\delta_{\mathrm{Tr}} = \frac{1}{\mathrm{Tr}} \frac{d\mathrm{Tr}}{dx} \ . \tag{6.7}$$

In the present work we integrate equation (6.7), from the estuary mouth to $x = L_c$ (end of our region of study), and we compute, for each simulation performed, the quantity:

$$\Delta_{\mathrm{Tr}} = \frac{\mathrm{Tr}(L_c) - \mathrm{Tr}(0)}{\mathrm{Tr}(0)} \ ,$$

using the tidal range at the estuary mouth Tr(0) as a scaling factor.
Figure 6.16 (left) shows, on the same plane (ϕ_0, ϵ_0) of figure 6.10, the contour lines of the computed quantity Δ_{Tr}, obtained by linearly interpolating the values of each simulation. The black dashed line is the contour line for $\Delta_{\mathrm{Tr}} = 0$, namely the marginal curve for tidal range amplification, where all the estuaries with unamplified and undamped wave lie. It represents an ideal situation for

which the amplification effect associated to funnelling is exactly balanced by friction. The marginal curve divides the plane into two regions; estuaries located below are characterized by a tidal range amplification while estuaries located above are affected by damping. A simple analytical model, derived by Savenije et Veling [2005] in the linearized framework, allows to explicitly compute the damping factor of an estuary as a function of the three external independent parameters of the estuarine dynamics. According to this model, Toffolon *et al.* [2006] found that synchronous estuaries ($\delta_{\mathrm{Tr}} = 0$) lie on a curve, which can be recast in terms of our parameters as:

$$\epsilon_0 = \frac{\delta_0(\delta_0^2 + 1)}{\phi_0} \ . \tag{6.8}$$

Using the value of $\delta_0 = 2$ in (6.8), we get the red curve plotted in figure 6.16 (left). A good agreement is observed between the marginal curve obtained through numerical simulations (black dashed line) and the one of the analytical model of Savenije (red line), especially for low values of ϵ_0, namely the linear regime.

From figure 6.16 (left) it is interesting to note that ϵ_0 plays a fundamental role also in the damping/amplification process. If we fix the physical and geometrical properties L_B, C_{f0}, D_0, this corresponds to a specific estuary configuration with ϕ_0 constant in addition to $\delta_0 = 2$. In this context, the variations of ϵ_0 can be considered as associated with neap-spring tide cycles. We can, thus, conclude that strong tides lead to weaker tidal wave amplification values and, for particularly strong tides, the wave most likely will be damped. This result is in qualitative agreement with respect to the physical observation made by Bonneton *et al.* [2015] on the Garonne river. Their measurements showed that, for such estuary always characterized by tidal wave amplification, minor amplifications were related to higher values of ϵ_0, observed during spring tides (figure 10(a) of the cited paper).

The superimposition of the computed marginal curve on the contour lines of the quantity A_{max}, in figure 6.16 (right), shows that a large part of the red region in the figure lies in the part of the plane (ϕ_0, ϵ_0) characterized by damping of the tidal range. This means that, despite a reduction of the local nonlinearity of the wave, this remains high enough to develop distorted profiles and to produce bores. We can conclude that, contrary to what is generally accepted, tidal range amplification along the estuary is not a necessary condition for tidal bore formation.

The critical curve intersects the computed marginal curve of amplification, dividing the plane into four main areas. Estuaries will thus experience tidal range amplification or damping, tidal bore formation or not, depending on

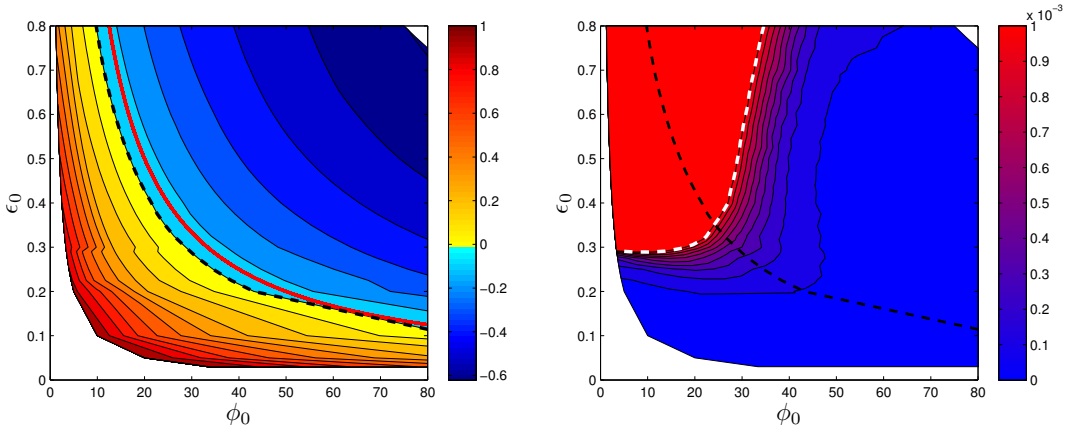

Figure 6.16: (Left): contour lines of the quantity Δ_{Tr} on the plane (ϕ_0, ϵ_0); the black dashed line (- -) represents the marginal curve resulting from the computations, while the continuous red one (–) is the analytical marginal curve of the Savenije model Savenije [2001]. Hot colours cover the region of amplification of the tidal wave during propagation; cold colours represent damping. (Right): the computed marginal curve (- -) is superimposed on the A_{max} contour lines.

which region in the plane they belong to. This separation is sketched in figure 6.17. The existence of a sector characterized by tidal bore generation and tidal range damping shows that tidal range amplification along the estuary is not a necessary condition for tidal bore occurence, as it is instead commonly assumed in the literature Chanson [2012]. The tidal dynamics which take place in the Ord and Punge rivers (data taken respectively from Wright *et al.* [1973] and Chanson [2012]; Savenije [2001]), which are in this region of the plane (numbers 15 and 16 respectively in figure 6.2), provide clear evidence of this.

6.6 River Discharge

In the previous sections, we have analyzed tidal wave transformation and tidal bore occurrence in a simplified context in which freshwater river discharge was neglected. However, it is well known that tide in estuaries may be significantly affected by the rate of discharge (*cf.* Horrevoets *et al.* [2004]; Cai *et al.* [2014]). The effects of river discharge become much more important moving landward from the mouth of the estuary and can influence for bore formation. The present section will provide a qualitative estimation on the effects of discharge, leaving a full quantitative study for future works.

In the experimental campaigns on the Garonne river, Bonneton *et al.* [2015] observed that small river discharges Q were favourable to tidal range ampli-

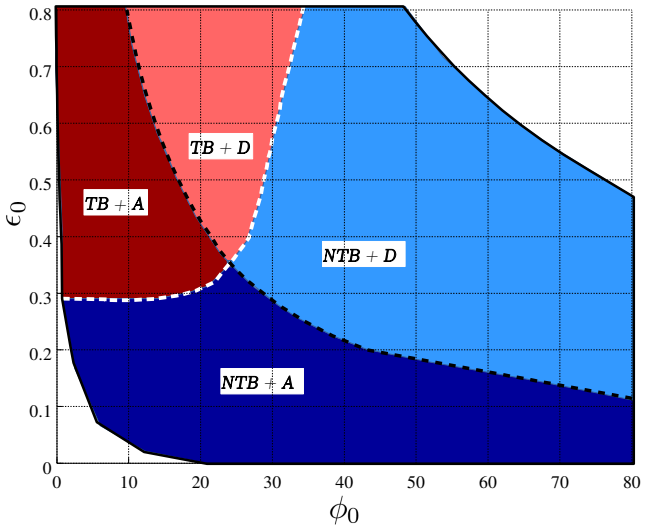

Figure 6.17: The computed critical line for bore formation (white dashed line) and the computed marginal curve of amplification (black dashed line) divide the (ϕ_0, ϵ_0) plane into four main areas. In the picture, TB stands for tidal-bore estuaries, while NTB stands for no tidal-bore estuaries; A indicates amplification of the tidal wave along the estuary, D damping.

fication and bore occurrence, while significant freshwater discharges offsets the amplification mechanism related to estuary convergence. Horrevoets *et al.* [2004] described, with an analytical model, that the influence of river discharge on tidal damping takes place mainly through friction. Generally speaking, the tidally averaged free surface elevation along the estuary does not coincide with the mean sea level, due to the nonlinear frictional effect on the averaged water level $\bar{h}(x)$. An analytical expression for the mean free surface elevation, valid also for the case of a non negligible river discharge, has been derived by Vignoli et al. Vignoli *et al.* [2003]. The validity of such expression have been tested and confirmed also by Cai et al. Cai *et al.* [2014] by means of a numerical investigation through a fully nonlinear one-dimensional numerical model accounting for river discharge. These works show that the mean water depth $\bar{h}(x) = \frac{1}{T}\int_T h(x,t)dt$ is a monotonically increasing function of x and that higher values of Q_0 correspond to bigger deviations. This increase of local mean water depth $\bar{D}(x)$, together with the damping of the local tidal range $Tr(x)$ pointed out by Bonneton et al. Bonneton *et al.* [2015], results in a local nonlinear parameter $\epsilon(x) = Tr(x)/(2\bar{h}(x))$, which is decreasing function of Q_0. Due to this damping effect, tidal bores are rarely observed for strong freshwater river discharges.

For a fixed estuary (fixed δ_0 and ϕ_0), the dimensionless parameters gov-

erning the flow dynamics are the amplitude of tidal forcing ϵ_0 and the dimensionless intensity of river discharge Q_0. The goal of the present section is to explore the space of parameters (ϵ_0, Q_0) in order to find, for an estuary characterized by $\delta_0 = 2$ and $\phi_0 = 18$ (values closed to the ones of the Garonne river), a critical curve $\epsilon_c(Q_0)$ for tidal bore development, following the criterion $A_{max} \geq 10^{-3}$.
In order to perform our investigation, we have to express Q_0 as a function of the external variables of the problem. A characteristic velocity scale can be derived from the fact that in convergent alluvial estuaries $K \sim 1$. In fact, definition (6.6) implies that $U_0 = \epsilon_0 \omega_0 L_b$. Using this velocity scale and the width at the estuary mouth B_0 (figure 6.1), we thus define:

$$Q_0 = \frac{Q}{A_0 B_0 L_b \omega_0} \ . \tag{6.9}$$

The river discharge is introduced by the boundary condition already described in section 6.4, through the incoming Riemann invariant from far on the right. Figures 6.18 shows, for the particular estuary considered, the effect of an increasing river flow in terms of normalized free surface elevation and velocity signals at the position $x = L_c$ along the channel. The simulations were performed using $\epsilon_0 = 0.32$ and a range of values $Q_0 \in [0, 4.16 \times 10^{-3}]$, obtained by scaling the typical values of the Garonne river through relation (6.9). In particular, the values $Q_0 = 4.16 \times 10^{-4}$ and $Q_0 = 4.16 \times 10^{-3}$ correspond to the low and high characteristic fresh water discharges measured in the Garonne (respectively $Q = 150\ [m^3/s]$ and $Q = 1500\ [m^3/s]$).
In figure 6.18 (top-left), we observe that the dimensionless mean water depth $\bar{h}(L_c)/h_0$ increases with Q_0, from 1.033 with $Q_0 = 0$ to 1.219 with $Q_0 = 4.16 \times 10^{-3}$. We can also measure the damping effect of freshwater river discharge on the tidal range; the dimensionless value $\Delta_{Tr}(L_c)$ (as defined in (6.7)) goes from 0.156 with $Q_0 = 0$ (amplified case) to -0.041 with $Q_0 = 4.16 \times 10^{-3}$ (damped case).
An important vertical shift of the velocity curve, in agreement with experimental observations *in situ* (*cf.* Horrevoets *et al.* [2004]), can be observed in figure 6.18 (top-right), moving towards the condition of unidirectional flow. Moreover, it can be noticed that this result confirms the theoretical predictions set by Horrevoets *et al.* [2004] concerning the evolution of the phase lag between high water and high water slack (and at the same time between low water and low water slack). Note that all the effects described are small below the value of $Q_0 = 4.16 \times 10^{-4}$ and the discharge does not affect the topology of the tidal wave for the river flow values typically observed in the Garonne river at the end of the summer season. Thus, the parametric analysis performed in section 6.1, by neglecting Q_0, can be considered valid in this range of small Q_0.

In figure 6.18 (bottom), the zoom on the time scale of the bore displays

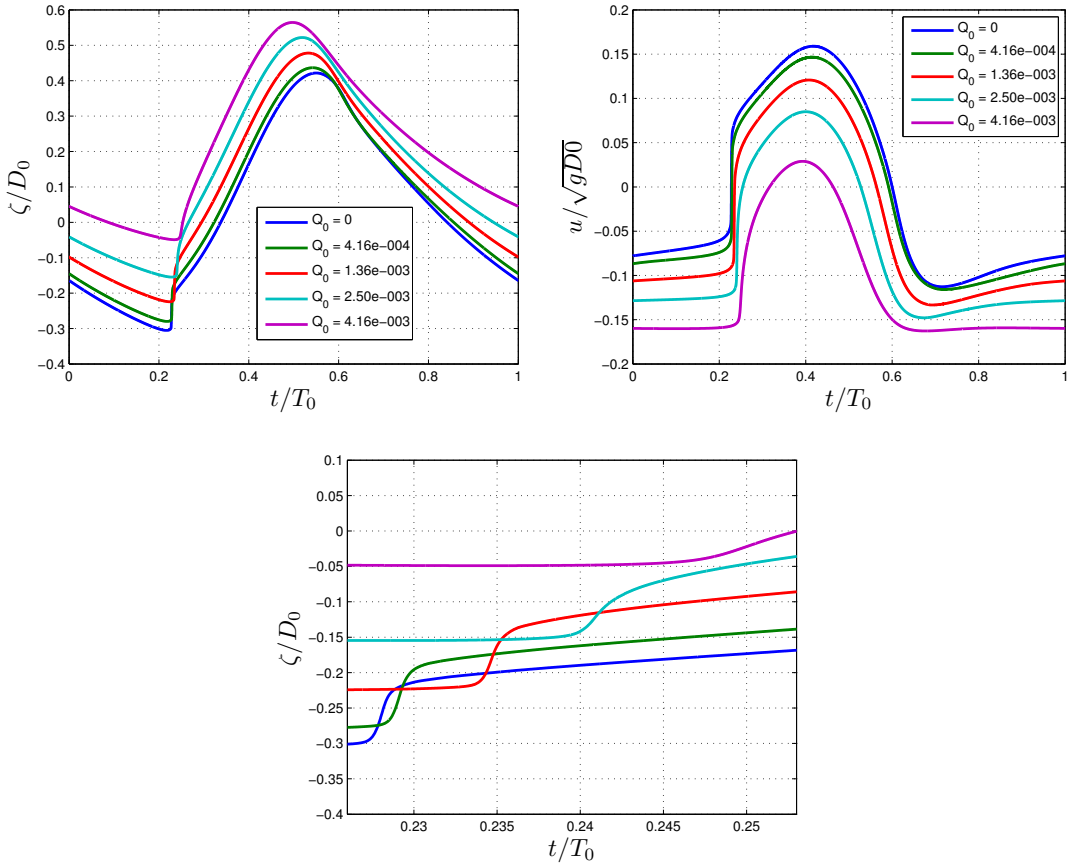

Figure 6.18: Time variation of the free surface elevation (top-left) and the velocity (top-right) signals measured at $x = 3L_B$ for an ideal estuary characterized by $\epsilon_0 = 0.32$, $\phi_0 = 18$ and increasing values of freshwater discharge from $Q_0 = 0$ to $Q_0 = 4.16 \times 10^{-3}$ (in particular the values have been chosen considering the typical range of values displayed by the Garonne river and measured by Bonneton *et al.* [2015]). Figure (bottom) represents a zoom on free surface signal in the time scale of the bore (around 20 min).

the tendency of the free surface profile to become much smoother as the value of river discharge increases. In order to explore better this point, we have performed 47 simulations for different combinations of tidal amplitude and river discharge (ϵ_0, Q_0). The values of A_{max}, obtained for all the simulations, have been plotted in figure 6.19. Note that we chose to represent in the y-axis of the figure the product $Q_0\epsilon_0$, rather than simply Q_0, in order to remove the dependence of Q_0 from A_0 (*cf.* (6.9)). The figure shows that, in the presence of weak river discharges, estuarine dynamics is not influenced by Q_0 and, consequently, the effects of discharge can be considered negligible in the bore formation process.

A qualitative critical curve $\epsilon_c(Q_0)$ has been traced by hand (grey dashed line in figure 6.19) according to the few computations performed. This trend is in qualitative agreement with experimental data for the Garonne river, presented in figure 6 of Bonneton *et al.* [2016].

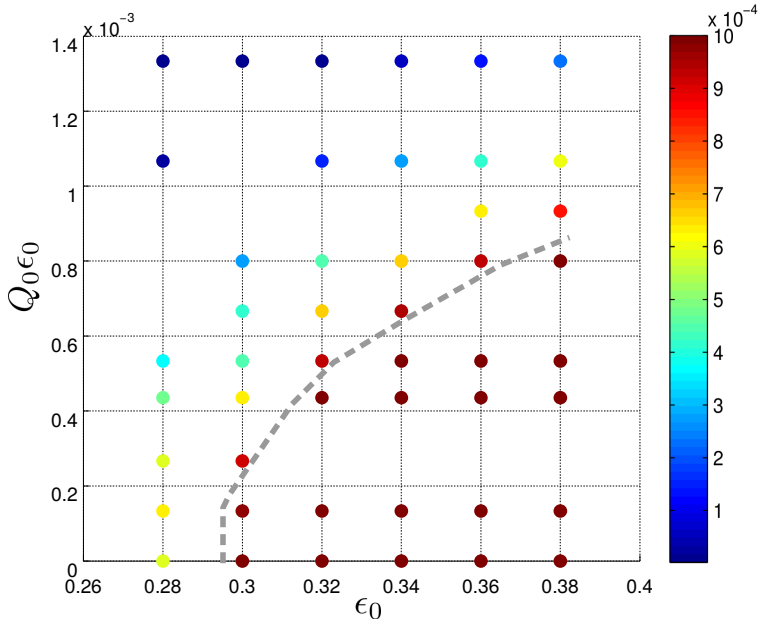

Figure 6.19: Circles represent computations performed for a fixed estuary ($\delta_0 = 2$ and $\phi_0 = 18$) varying the values of the tidal forcing amplitude A_0 and river discharge Q_0; colors represent the intensity of A_{max} for each computation; with a gray dashed line we have represented by hand the $\epsilon_c(Q_0)$ curve, namely the limit for tidal bore appearance following the criterion $A_{max} \geq 10^{-3}$.

Conclusions

This work proposes several developments related to the study and numerical simulation of free surface flows in near shore environments. In this chapter we recall the main contributions and propose some possible avenues for future works.

Analysis of BT models:

The first chapter of the thesis has considered the form of the equations used to describe dispersive wave propagation. We have, thus, presented the main steps for the derivation of the class of depth-averaged Boussinesq-type models, from the initial Euler system of equation. Since these asymptotic models are designed in order to optimize their linear dispersion representation with respect to the one given by the Airy theory, we have analyzed their linear and nonlinear dispersion and shoaling properties, which also define the range of practical applicability of these models in real applications. In particular, we have stressed the impact of the formulation of weakly nonlinear BT models on their behavior in situations in which nonlinearity is not negligible. We have recalled how, within the same asymptotic truncation, a given linearized form, hence a given dispersion relation and shoaling coefficient, allows to derive two sets of PDEs : one, referred to as amplitude-velocity form, in which dispersive terms contain differential operators applied to the velocity; the other, referred to as amplitude-flux form, in which these operators are applied to the flux. We have given two examples of these couples, including the widely known models of Peregrine, Abbott and Madsen and Sørensen (more BT models are considered in Filippini *et al.* [2015]). The analytical and numerical study of these models has shown that: as soon as nonlinear effects start being relevant, the main factor influencing the behavior of the model lies in its formulation, that is amplitude-velocity versus amplitude-flux form, enhanced models giving the same results as Peregrine or Abbott equations. This fact has been demonstrated analytically by the study of the propagation of higher harmonics in section 1.7.3, following Madsen et Schaffer [1998], and numerically with tests involving shoaling in genuinely nonlinear regimes. While in the linear case we have as many models as the number of linear dispersion relations and linear shoaling coefficients, in the nonlinear case, only two types of behaviors

are observed. Since weakly nonlinear and weakly dispersive models are widely used in the scientific and engineering community, and often used outside their range of validity, this result has important consequences, *e.g.* on the way in which wave breaking conditions are applied to these models, as well as on the way in which wave breaking dissipation is included. Clearly, breaking criteria should not be the same for the two family of models, and perhaps even the amount of dissipation in breaking regions necessary in the two cases should be different. This result has pushed us toward genuinely nonlinear models, and in particular Green-Naghdi type systems. We have thus considered and studied the enhanced GN equations proposed by Bonneton *et al.* [2011b]; Chazel *et al.* [2011], which couples the genuinely nonlinear properties of the original GN system with the improved linear dispersive properties of the enhanced weakly nonlinear BT models. The last model taken into account has been the constant diagonal eGNd model proposed by Lannes et Marche [2015], which, despite belonging to the same asymptotic of the GN and eGN model, has displayed a different behaviour in the nonlinear shoaling test performed, showing a large phase lag in time respect to the experimental data. The results presented seem, however, to be influenced by the initial setup of the test (*i.e.* initial still water level, amplitude of the solitary wave) and therefore deserve further investigations.

Discretization in one-dimension:

The second part of the thesis was devoted to the study of a flexible and unsplit strategy, which allows to enhance a (hyperbolic) Shallow Water code, by a purely algebraic correction to the discrete momentum equation with, both the fully-nonlinear weakly dispersive eGN effects and wave breaking. This correction can be computed from the solution of a stationary elliptic problem. To evaluate the potential of this enhancement technique, we have investigated hybrid discretizations in which different methods are used in the two different phases (elliptic solver, hyperbolic evolution step). Several methods are thus tested both in space and in time, involving both finite element and finite volume methods in space, and both multi-stage and multi-step methods in time. In particular, we have focused on the use of a C^0 Galerkin approximation of the variational form of the elliptic problem, and on the use of both upwind finite volumes (*cf.* Nikolos et Delis [2009]; Kazolea *et al.* [2014]), Galerkin and stabilized Galerkin finite elements (*cf.* Bacigaluppi *et al.* [2014a]; Ricchiuto et Filippini [2014]) in the hyperbolic part. All the schemes implemented are endowed with robustness and stability properties such as positivity, well-balancing and wet/dry interfaces treatment.
Time continuous dispersion analysis of the schemes has shown several important facts. Firstly, the behavior obtained when coupling the continuous

Galerkin elliptic solver with different hyperbolic methods is quite similar, confirming the flexibility of the approach proposed. Then, an essential role is played by the approximation of the third order derivatives in the right hand side of the elliptic equation. Evaluating this term by exact integration allows to recover, for all the combinations considered, dispersion errors which are of the same order, or smaller, than those provided by fourth order finite differencing. Lastly, we find that the use of a properly designed second order accurate discretization for the elliptic phase is enough to achieve such low levels of dispersion errors, provided that at least third order of accuracy is guaranteed for the hyperbolic component. This is true for all the different combinations of the elliptic–hyperbolic methods considered. This result generalizes previous findings and constructions in the finite difference context (*cf.* Wei et Kirby [1995]). The analysis shows that this approach allows enough flexibility to enhance many of the existing Shallow Water codes based on finite element and finite volume discretizations.
The fourth order Adams Bashforth - Adams Moulton method Wei et Kirby [1995]; Roeber *et al.* [2010], the three stages third order SSP Runge-Kutta scheme Gottlieb *et al.* [2001] and the third order explicit backward differencing method Hundsdorfer *et al.* [2003] have been used for the integration in time in one-dimension. The results have shown little influence to this choice.
The method proposed has been thoroughly verified on a large number of benchmarks involving both simple analytical solutions, and complex flows with wave propagation and breaking, as well as run-up and overtopping. The results show monotone shock-capturing performances and accuracy close to third order for all the schemes discussed.

Discretization in two-dimensions:

In chapter 4 we have discussed the extension to the two-dimensional case of the hybrid FE-FV scheme, which uses the C^0 continuous Galerkin method for the elliptic part, coupled with a third order finite volume scheme with MUSCL reconstruction for the hyperbolic phase. The efficiency of the two dimensional scheme has been improved by exploiting the coercivity property of the elliptic operator $(I+\alpha T)$. In particular, we have shown that, solving for ψ the elliptic phase, and recomputing ϕ in a second time by the definition $\phi = h\psi$, allows to work always with SPD matrices. Moreover, the MUSCL reconstruction has been corrected in order to respect the conservation of the mean property also in the case of very stretched meshes. The only SSP Runge-Kutta scheme has been used in 2D for the integration in time, as a consequence of the small influence of the time scheme (if higher-order) on the results, shown in 1D. The SSP-RK scheme has been implemented in the form of Chertock *et al.* [2015], which allows to increase the efficiency of the friction treatment and to avoid

losing the order of the scheme when friction becomes dominant (typically in run-up processes). The results performed on academic benchmarks confirms, also in 2D, the good performances of the proposed scheme also on non-uniform triangulations.

Wave breaking:

For the management of wave breaking, the hybrid scheme presented in Kazolea *et al.* [2014] have been successfully applied in the context of fully nonlinear models in both one and two dimensions. The strategy proposed, dividing the original system in its elliptic and hyperbolic parts, has revealed particularly adapted for the implementation of a hybrid technique, since the effects of dispersion can be easily switched off when breaking is detected by simply imposing $\phi = 0$. A preliminary study on two different formulations on the treatment of the hybrid breaking technique have been performed in the one-dimensional case (*cf.* section 2.9.3 and 3.9), in the hope of reducing spurious oscillations arising form the coupling of GN and NLSW equations in breaking regions, as pointed out by many in the past Tonelli et Petti [2011]; Tissier *et al.* [2012]; Kazolea et Delis [2013]; Kazolea *et al.* [2014]. Embedding the breaking in the elliptic phase is shown to reduce considerably spurious oscillations in the proximities of the breaking region. However, it does not resolve issues related to the intermittency of the breaking detection and, unfortunately, still leaves open the problem of obtaining fully mesh converged solutions for the coupled model.

The numerical schemes have been validated against standard one and two-dimensional benchmarks of non-breaking and breaking wave propagation over variable topographies, using arbitrary unstructured meshes, with emphasis to comparisons with experimental results. In all test cases, on meshes similar to those used in the reference literature, the performed results were in good agreement with experimental data and previously solutions by other authors, proving the potential of this approach.

Estuarine dynamics:

In the last part of this work, under the hypotheses of constant bathymetry and negligible river discharge, we have used the Saint-Venant system of equations to numerically investigate the bore occurrence in convergent alluvial estuaries of idealized geometry. The scaling of the equations shows that estuarine dynamics is fully controlled by three dimensionless parameters entirely dependent on the estuary geometrical properties and tidal forcing: the nonlinearity ϵ_0, the convergence parameter δ_0 and the friction parameter ϕ_0, defined by (6.4).

Taking a constant value of $\delta_0 = 2$, we have numerically explored the plane (ϕ_0, ϵ_0), ensuring that the results provided are independent from the scheme chosen for the investigation, and that they can be considered as mesh converged. By means of a bore detection criterion, we have traced the critical line $\epsilon_c(\phi_0)$ dividing estuaries into displaying or not a tidal bore. This curve is in good agreement with real estuaries data, despite the several assumptions made (figure 6.2), and provides the necessary conditions for tidal bore formation. These conditions are a result of a complex equilibrium between nonlinear distortion and tidal range damping/amplification processes both driven by the dissipation parameter $D_i^* \propto \epsilon_0\phi_0$ multiplying the friction, the dominant nonlinear term for this class of estuaries. The particular shape of $\epsilon_c(\phi_0)$ shows that, for low values of ϕ_0 (indicatively $1 < \phi_0 \leq \sim 20$), bore formation depends almost exclusively on the nonlinear parameter ϵ_0, while being, instead, mainly disciplined by the dissipation, related to the value of ϕ_0, for $\phi_0 \geq \sim 20$.
The critical curve intersects the computed marginal curve of amplification, dividing the plane into four main areas. Estuaries will thus experience tidal range amplification or damping, tidal bore formation or not, depending on which region in the plane they belong to. The existence of a sector characterized by tidal bore generation and tidal range damping shows that tidal range amplification along the estuary is not a necessary condition for tidal bore occurrence, as it is instead commonly assumed in the literature Chanson [2012].
We have studied the effect of river discharge for estuaries characterized by $\delta_0 = 2$ and $\phi_0 = 18$ (which are close to the values displayed by the Gironde/Garonne estuary). We have shown that for low Q_0 (i.e. $Q_0 < 4.16 \times 10^{-3}$), corresponding to the dry season, the effect of river discharge on tidal wave dynamics and on bore formation can be neglected.
The above findings are based on several simplifying assumptions, that have allowed a clear understanding of the bore inception mechanism.

Future works and further developments:

We consider that the results obtained show that the approach proposed has enormous potential as a non-intrusive enhancement technique for existing Shallow Water solvers. The work done highlights several issues still open and provides many research avenues.

Modeling wave propagation: The analysis on the two different nonlinear shoaling behaviours of weakly nonlinear BT models suggests that different results should be expected when coupling of the BT models considered with physical breaking criteria, as those used *e.g.* in Bacigaluppi *et al.* [2014a]; Kazolea *et al.* [2014]; Tonelli et Petti [2011]; Tissier *et al.* [2012] and references therein. This should be argument of future analysis.
Moreover, we found the constant diagonal eGNd model of Lannes et Marche

[2015] very promising, since it sensibly reduces the cost of the solution of the elliptic part of the system without affecting the linear properties of the original model. However, as the nonlinear shoaling test of chapter 1 shows, some more understanding of the basic properties of this model is required. This is the object of ongoing studies.

Modeling wave breaking: The implementation of the breaking criterion inside the elliptic phase has been shown to sensibly reduce the numerical perturbations appearing at the breaking interface in the hybrid approach. This approach should thus be preferred and used also in 2D. Note that this formulation has the additional advantage of leaving all additional the physical modeling in the elliptic phase, the shallow water solver being completely unaware of the dispersive and breaking effects, all lumped into the computation of the source phi. Clearly, some efforts are required to improve this coupling as mesh converged results still are not obtainable with this method. This may hinder the use of local mesh adaptation to capture efficiently these regions. The well-posedness of the overall procedure should be investigated in the future.
Alternative approaches to model wave breaking, based on the use of turbulence models to improve dissipation or based on an eddy viscosity should also be explored (*cf.* Nwogu [1996]; Briganti *et al.* [2004]; Demirbilek *et al.* [2007]; Kazolea et Ricchiuto [2016]). Also, more general flagging techniques to detect breaking fronts should be developed in order to handle genuinely multidimensional wave dynamics.

Efficiency of the implementation: The exploitation of the coercivity of the elliptic operator $(I+\alpha T)$ has simplified the formulation of the elliptic step by making it completely symmetric. However, remarking that the dispersive correction is only computed in smooth areas and the use of the conservative form of the problem does not bring anything to the implementation, the fully non-conservative form of the elliptic phase could be now considered:

$$\begin{aligned} (I+\alpha\mathcal{T})\,\boldsymbol{\psi} &= \mathcal{T}(g\nabla\eta) - \mathcal{Q}_1(\mathbf{u})\ , \\ h_t + \nabla\cdot\mathbf{q} &= 0\ , \\ \mathbf{q}_t + \nabla\cdot\left(\frac{\mathbf{q}\otimes\mathbf{q}}{h}\right) + gh\nabla\eta &= h\boldsymbol{\psi}\ , \end{aligned} \tag{6.10}$$

with $\mathcal{T}$ and $\mathcal{Q}_1$ the differential operators of the non-conservative GN formulation, respectively defined by (1.113) and (1.114).
This would have the same cost of a splitting approach and, in particular, it would reduce the requirements on the quadrature formulas used to evaluated the finite element matrices, and of the right hand side, by one degree of accu-

racy. This is currently object of investigations.
Moreover, the use of a direct method for matrix inversion is not well suited for the algorithm proposed here. This is due to the fact that most matrices change at each time step (or sub-stage for the Runge-Kutta schemes). This requires a re-factorization of the new matrix after each assembly, which is too costly. Other techniques should be exploited, taking also advantage from the SPD form of the matrix (*e.g.* iterative matrix free methods or conjugate gradients). This has to be coupled with a parallelization of the algorithm implemented for an additional increase of performance.

Numerical discretization: This work is based on a low order approximation of the non-hydrostatic terms of the eGN equations. A first numerical issue would be the comparison of the gains in dispersion accuracy when enhancing the elliptic solver from second to higher order. Moreover, the dispersion analysis and optimization of the schemes could be repeated by optimizing (with respect to the linear Airy theory) the dispersion relation of the discrete equations instead of that of the continuous one. This may allow to further gain some accuracy on coarser meshes. The objective, here, is to reduce as much as possible the overhead of the elliptic phase, by devising what the minimal accuracy requirements are for this step.
In the hybrid FE/FV scheme proposed, the non-hydrostatic correction ϕ has been added to the hyperbolic part exactly integrating over the computational cells the piecewise linear polynomial ϕ_{h}. The use of polynomial reconstruction techniques for this quantity may be an interesting alternative to a costly high order finite element discretization of the elliptic step, and will be explored in the future.
Other future directions involve the application of the flexible approach proposed to other discretization techniques. For instance, the coupling of continuous finite elements for the elliptic phase with discontinuous Galerkin methods for the hyperbolic one, possibly with a lower order continuous approximation for the elliptic phase to further reduce the algebraic costs. The use of dynamic unstructured mesh adaptation techniques can also be investigated, coupled with implicit or local time stepping, to compensate for the reduction in time step brought by the adaptation process.

Tidal bore conditions: The study of the occurrence of tidal bores should be enhanced by considering other effects influencing the spatial location of bore development that have been so far ignored, as the variable bathymetry, river banks and meanders. In particular, it would be important to extend the scaling analysis presented, taking into account large variations of the estuary water depth.
Our approach has been validated from both field observations and numerical simulations. However, an accurate estuarine classification would require new

quantitative field measurements for estuaries having contrasting characteristics. Furthermore, addressing alluvial estuaries with nonlinear parameter ε_0 close to $\varepsilon_c(\phi)$ would allow a more accurate determination of the critical curve between tidal-bore and no-tidal-bore estuaries.
Moreover, very energetic phenomena, such as the tsunami-tide interaction, can propagate the bore far upstream (*cf.* Chanson [2012]). The analysis of the interaction between impulsive and periodic waves in complex scenarios is the subject of current investigations. The consideration of such effects will require significant attention, but will provide a more thorough comprehension when approaching the analysis of real natural estuaries.

Appendix A

FD formulations of the schemes

We report here the finite difference expressions of the one-dimensional schemes analyzed in chapter 2 when applied to the linearized equations (1.124). All the derivation is done by assuming an equally spaced mesh of size h $= \Delta x$; $c^2 = gh_0$ denotes the square of the linearized Shallow Water celerity (*cf.* (1.61)).

Second order central finite differences:

$$\begin{aligned}
&\frac{d\eta_i}{dt} + \frac{h_0}{2\Delta x}\left(u_{i+1} - u_{i-1}\right) = 0 \ , \\
&\frac{du_i}{dt} + \frac{g}{2\Delta x}\left(\eta_{i+1} - \eta_{i-1}\right) - \frac{\phi_i}{h_0} = 0 \ , \\
&\phi_i - \frac{\alpha h_0^2}{3\Delta x^2}\left(\phi_{i+1} - 2\phi_i + \phi_{i-1}\right) = \\
&\qquad\qquad = \frac{gh_0^3}{6\Delta x^3}\left(-\eta_{i+2} + 2\eta_{i+1} - 2\eta_{i-1} + \eta_{i-2}\right) \ .
\end{aligned} \tag{A.1}$$

Fourth order central finite differences:

$$\begin{aligned}
&\frac{d\eta_i}{dt} + \frac{h_0}{12\Delta x}\left(-u_{i+2} + 8u_{i+1} - 8u_{i-1} + u_{i-2}\right) = 0 \ , \\
&\frac{du_i}{dt} + \frac{g}{12\Delta x}\left(-\eta_{i+2} + 8\eta_{i+1} - 8\eta_{i-1} + \eta_{i-2}\right) - \frac{\phi_i}{h_0} = 0 \ , \\
&\phi_i - \frac{\alpha h_0^2}{36\Delta x^2}\left(-\phi_{i+2} + 16\phi_{i+1} - 30\phi_i + 16\phi_{i-1} - \phi_{i-2}\right) = \\
&\qquad = \frac{gh_0^3}{24\Delta x^3}\left(-\eta_{i+3} + 8\eta_{i+2} - 13\eta_{i+1} + 13\eta_{i-1} - 8\eta_{i-2} + \eta_{i-3}\right) \ .
\end{aligned} \tag{A.2}$$

Continuous Galerkin scheme:

$$\begin{aligned}
&\frac{\Delta x}{6}\left(\frac{d\eta_{i+1}}{dt}+4\frac{d\eta_i}{dt}+\frac{d\eta_{i-1}}{dt}\right)+\frac{h_0}{2}\left(u_{i+1}-u_{i-1}\right)=0\ ,\\
&\frac{\Delta x}{6}\left(\frac{du_{i+1}}{dt}+4\frac{du_i}{dt}+\frac{du_{i-1}}{dt}\right)+\frac{g}{2}\left(\eta_{i+1}-\eta_{i-1}\right)\ +\\
&\qquad\qquad-\frac{\Delta x}{6h_0}\left(\phi_{i+1}+4\phi_i+\phi_{i-1}\right)=0\ ,\\
&\frac{\Delta x}{6}\left(\phi_{i+1}+4\phi_i+\phi_{i-1}\right)-\frac{\alpha h_0^2}{3\Delta x}\left(\phi_{i+1}-2\phi_i+\phi_{i-1}\right)=\\
&\qquad\qquad=\frac{gh_0^3}{6\Delta x^2}\left(-\eta_{i+2}+2\eta_{i+1}-2\eta_{i-1}+\eta_{i-2}\right)\ .
\end{aligned}\tag{A.3}$$

SUPG scheme: In the linearized case, the matrix associated to the Shallow Water quasi-linear form is:

$$A_0=\begin{bmatrix}0 & h_0\\ g & 0\end{bmatrix}$$

Straightforward eigenvalue decomposition show that the sign of this matrix can be written as:

$$\operatorname{sign}(A_0)=\begin{bmatrix}0 & c/g\\ g/c & 0\end{bmatrix}$$

Using this expression we can deduce the form of the SUPG scheme (2.26) applied to system (1.124):

$$\begin{aligned}
&\frac{\Delta x}{6}\left(\frac{d\eta_{i+1}}{dt}+4\frac{d\eta_i}{dt}+\frac{d\eta_{i-1}}{dt}\right)+\frac{h_0}{2}\left(u_{i+1}-u_{i-1}\right)-\frac{c}{2g}\left[\frac{\Delta x}{2}\left(\frac{du_{i+1}}{dt}-\frac{du_{i-1}}{dt}\right)+\right.\\
&\qquad\left.+g(\eta_{i+1}-2\eta_i+\eta_{i-1})-\frac{\Delta x}{2h_0}\left(\phi_{i+1}-\phi_{i-1}\right)\right]=0\ ,\\
&\frac{\Delta x}{6}\left(\frac{du_{i+1}}{dt}+4\frac{du_i}{dt}+\frac{du_{i-1}}{dt}\right)+\frac{g}{2}\left(\eta_{i+1}-\eta_{i-1}\right)-\frac{\Delta x}{6h_0}\left(\phi_{i+1}+4\phi_i+\phi_{i-1}\right)\ +\\
&\qquad-\frac{g}{2c}\left[\frac{\Delta x}{2}\left(\frac{d\eta_{i+1}}{dt}-\frac{d\eta_{i-1}}{dt}\right)+h_0(u_{i+1}-2u_i+u_{i-1})\right]=0\ ,\\
&\frac{\Delta x}{6}\left(\phi_{i+1}+4\phi_i+\phi_{i-1}\right)-\frac{\alpha h_0^2}{3\Delta x}\left(\phi_{i+1}-2\phi_i+\phi_{i-1}\right)=\\
&\qquad\qquad=\frac{gh_0^3}{6\Delta x^2}\left(-\eta_{i+2}+2\eta_{i+1}-2\eta_{i-1}+\eta_{i-2}\right)\ .
\end{aligned}\tag{A.4}$$

Finite Volume scheme:

$$\begin{aligned}
&\frac{d\eta_i}{dt} + \frac{h_0}{2\Delta x}\left(-\frac{1}{6}u_{i+2} + \frac{4}{3}u_{i+1} - \frac{4}{3}u_{i-1} + \frac{1}{6}u_{i-2}\right) + \\
&\qquad - \frac{c}{2\Delta x}\left(-\frac{1}{6}\eta_{i+2} + \frac{2}{3}\eta_{i+1} - \eta_i + \frac{2}{3}\eta_{i-1} - \frac{1}{6}\eta_{i-2}\right) = 0 \ , \\
&\frac{du_i}{dt} + \frac{g}{2\Delta x}\left(-\frac{1}{6}\eta_{i+2} + \frac{4}{3}\eta_{i+1} - \frac{4}{3}\eta_{i-1} + \frac{1}{6}\eta_{i-2}\right) + \\
&\qquad - \frac{c}{2\Delta x}\left(-\frac{1}{6}u_{i+2} + \frac{2}{3}u_{i+1} - u_i + \frac{2}{3}u_{i-1} - \frac{1}{6}u_{i-2}\right) + \\
&\qquad\qquad - \frac{1}{h_0}\left(\phi_{i+1} + 6\phi_i + \phi_{i-1}\right) = 0 \ , \\
&\frac{\Delta x}{6}\left(\phi_{i+1} + 4\phi_i + \phi_{i-1}\right) - \frac{\alpha h_0^2}{3\Delta x}\left(\phi_{i+1} - 2\phi_i + \phi_{i-1}\right) = \\
&\qquad\qquad = \frac{g h_0^3}{6\Delta x^2}\left(-\eta_{i+2} + 2\eta_{i+1} - 2\eta_{i-1} + \eta_{i-2}\right) \ .
\end{aligned} \tag{A.5}$$

Appendix B

Dispersion error

We report here the definitions of the several quantities called in section 2.7.2 and involved in the analysis of the dispersion properties of the schemes. Moreover, the paragraph contains the expressions of the dispersion relation formulae of the FD2 and FD4 schemes used as comparison in figures from 2.3 to 2.8 and the description of the several configurations (from 1 to 4) taken into account for the elliptic problem discretization.

cG scheme: The quantities involved in the dispersion analysis are easily computed from the finite difference form of the schemes, reported in appendix (A), and read:

- the Galerkin mass matrix: $\tilde{\mathrm{M}}^{\mathrm{G}} = \frac{1}{6}\Big(4 + 2\cos\bar{\mu}\Big)$;

- the solution of the elliptic problem:

$$\tilde{\Phi}_{LIN} = -\frac{gh_0^3}{3}\tilde{\mathrm{T}}^{\mathrm{G}}\Big(\tilde{\mathrm{M}}^{\mathrm{G}}\Big)^{-1}\Big(\tilde{\mathrm{M}}^{\mathrm{G}} - \frac{\alpha h_0^2}{3}\tilde{\mathrm{S}}^{\mathrm{G}}\Big)^{-1}$$

and the Galerkin discretization of:

- the first order space derivatives $\partial_x(\cdot)$: $\tilde{\mathrm{F}}^{\mathrm{G}} = j\frac{k}{2\bar{\mu}}\Big(2\sin\bar{\mu}\Big)$;

- the second order space derivatives $\partial_{xx}(\cdot)$: $\tilde{\mathrm{S}}^{\mathrm{G}} = \frac{k^2}{\bar{\mu}^2}\Big(2\cos\bar{\mu} - 2\Big)$;

- the third order space derivatives $\partial_{xxx}(\cdot)$: $\tilde{\mathrm{T}}^{\mathrm{G}} = j\frac{k^3}{2\bar{\mu}^3}\Big(2\sin 2\bar{\mu} - 4\sin\bar{\mu}\Big)$;

where $\bar{\mu} = k\Delta x$ and k represents the wavenumber associated to the Fourier mode.

For the Galerkin scheme, the phase resulting from the condition that the matrix of system (2.47) has zero determinant is:

$$\left(\omega_{\Delta x}^{\mathrm{G}}\right)^2 = \frac{g h_0 \left(\tilde{\mathrm{F}}^{\mathrm{G}}\right)^2 - \tilde{\mathrm{F}}^{\mathrm{G}} \tilde{\mathrm{M}}^{\mathrm{G}} \tilde{\Phi}_{LIN}}{\left(\tilde{\mathrm{M}}^{\mathrm{G}}\right)^2} \ . \tag{B.1}$$

The amplification rate is found to be identically equal to zero (no dumping or amplification).

SUPG scheme: The analysis is more complex for the SUPG scheme. Discretizing system (2.44)-(2.45) by means of the SUPG scheme will now lead to:

$$\left(\tilde{\mathrm{M}}^{\mathrm{G}} - \frac{\alpha h_0^2}{3} \tilde{\mathrm{S}}^{\mathrm{G}}\right) \phi_i = -\frac{g h_0^3}{3} \tilde{\mathrm{T}}^{\mathrm{G}} \left(\tilde{\mathrm{M}}^{\mathrm{G}}\right)^{-1} \eta_i \ , \tag{B.2}$$

$$\tilde{\mathrm{M}}^{\mathrm{G}} \nu_{\Delta x} \eta_i + h_0 \tilde{\mathrm{F}}^{\mathrm{G}} u_i - \frac{c}{2g} \left[\tilde{\mathrm{M}}^{\mathrm{UFE}} \nu_{\Delta x} u_i + g \tilde{\mathrm{F}}^{\mathrm{UFE}} \eta_i - \frac{1}{h_0} \tilde{\mathrm{M}}^{\mathrm{UFE}} \phi_i\right] = 0 \ , \tag{B.3}$$

$$\tilde{\mathrm{M}}^{\mathrm{G}} \nu_{\Delta x} u_i + g \tilde{\mathrm{F}}^{\mathrm{G}} \eta_i - \frac{g}{2c} \left[\tilde{\mathrm{M}}^{\mathrm{UFE}} \nu_{\Delta x} \eta_i + h_0 \tilde{\mathrm{F}}^{\mathrm{UFE}} u_i\right] = \frac{1}{h_0} \tilde{\mathrm{M}}^{\mathrm{G}} \phi_i \ ,$$

the two quantities $\tilde{\mathrm{M}}^{\mathrm{UPE}}$ and $\tilde{\mathrm{F}}^{\mathrm{UPE}}$ derive from the FE discretization of the upwind flux and have the following form:

- $\tilde{\mathrm{M}}^{\mathrm{UFE}} = j \sin \bar{\mu}$;
- $\tilde{\mathrm{F}}^{\mathrm{UFE}} = \frac{k}{\bar{\mu}} \left(2 \cos \bar{\mu} - 2\right)$.

The writing of the Jacobian matrix of the system (B.3) and of its characteristic polynomial lead to a complex algebraic equation, whose solution in the real part can be written in the form:

$$\left(\omega_{\Delta x}^{\mathrm{SU}}\right)^2 = \frac{\mathrm{A}_S^{\mathrm{SU}}}{\mathrm{A}_{\nu^2}^{\mathrm{SU}}} - \left(\frac{\mathrm{A}_\nu^{\mathrm{SU}}}{2\mathrm{A}_{\nu^2}^{\mathrm{SU}}}\right)^2 \ , \tag{B.4}$$

where $\mathrm{A}_{\nu^2}^{\mathrm{SU}}$, $\mathrm{A}_\nu^{\mathrm{SU}}$ and $\mathrm{A}_S^{\mathrm{SU}}$ are functions of the just defined quantities $\tilde{\mathrm{M}}^{\mathrm{G}}$, $\tilde{\mathrm{F}}^{\mathrm{G}}$, $\tilde{\mathrm{M}}^{\mathrm{UPE}}$, $\tilde{\mathrm{F}}^{\mathrm{UPE}}$ and $\tilde{\Phi}_{LIN}$.

FV scheme: Concerning the FV scheme, using the linearized equations (2.45) and the third order MUSCL reconstruction, described in section 2.3, we get for the following system of equations:

$$\left(\tilde{\mathrm{M}}^{\mathrm{G}} - \frac{\alpha h_0^2}{3}\tilde{\mathrm{S}}^{\mathrm{G}}\right)\phi_i = -\frac{g h_0^3}{3}\tilde{\mathrm{T}}^{\mathrm{G}}\left(\tilde{\mathrm{M}}^{\mathrm{G}}\right)^{-1}\eta_i \,, \tag{B.5}$$

$$\nu_{\Delta x}\eta_i + h_0\tilde{\mathrm{F}}^{\mathrm{FV}}u_i - c\tilde{\mathrm{F}}^{\mathrm{UFV}}\eta_i = 0 \,, \tag{B.6}$$

$$\nu_{\Delta x}u_i + g\tilde{\mathrm{F}}^{\mathrm{FV}}\eta_i - c\tilde{\mathrm{F}}^{\mathrm{UFV}}u_i = \frac{1}{h_0}\tilde{\mathrm{M}}^{\mathrm{FV}}\phi_i \,,$$

which, by means of the procedure already described above for the SUPG scheme, lead to the final form of the dispersion relation:

$$\left(\omega_{\Delta x}^{\mathrm{FV}}\right)^2 = \frac{\mathrm{A}_S^{\mathrm{FV}}}{\mathrm{A}_{\nu^2}^{\mathrm{FV}}} - \left(\frac{\mathrm{A}_\nu^{\mathrm{FV}}}{2\mathrm{A}_{\nu^2}^{\mathrm{FV}}}\right)^2 \,. \tag{B.7}$$

being $\mathrm{A}_{\nu^2}^{\mathrm{FV}}$, $\mathrm{A}_\nu^{\mathrm{FV}}$ and $\mathrm{A}_S^{\mathrm{FV}}$ functions of the quantities $\tilde{\mathrm{M}}^{\mathrm{FV}}$, $\tilde{\mathrm{F}}^{\mathrm{FV}}$, $\tilde{\mathrm{F}}^{\mathrm{UFV}}$ and $\tilde{\Phi}_{LIN}$, whose expressions comes from the discretization of the:

- elliptic term $\overline{\mathbf{\Phi}}$: $\tilde{\mathrm{M}}^{\mathrm{FV}} = \frac{1}{8}\left(6 + 2\cos\bar{\mu}\right)$;
- centered fluxes: $\tilde{\mathrm{F}}^{\mathrm{FV}} = j\frac{k}{2\bar{\mu}}\left(\frac{8}{3}\sin\bar{\mu} - \frac{1}{3}\sin 2\bar{\mu}\right)$;
- upwind fluxes: $\tilde{\mathrm{F}}^{\mathrm{UFV}} = \frac{k}{2\bar{\mu}}\left(\frac{4}{3}\cos\bar{\mu} - \frac{1}{3}\cos 2\bar{\mu} - 1\right)$.

FD2 and FD4 schemes: Figures from 2.3 to 2.8 show the dispersion errors of the several schemes with respect to the analytical dispersion relation of the model given by (1.15). The comparison is made for low and high values of the parameter kh_0 with respect to the errors provided by the FD2 and FD4 discretization schemes, whose dispersion relations are respectively:

$$\left(\omega_{\Delta x}^{\mathrm{FD2}}\right)^2 = gh_0\left(\tilde{\mathrm{F}}^{\mathrm{FD2}}\right)^2 - \tilde{\mathrm{F}}^{\mathrm{FD2}}\tilde{\Phi}_{LIN}^{(FD2)} \,, \tag{B.8}$$

$$\left(\omega_{\Delta x}^{\mathrm{FD4}}\right)^2 = gh_0\left(\tilde{\mathrm{F}}^{\mathrm{FD4}}\right)^2 - \tilde{\mathrm{F}}^{\mathrm{FD4}}\tilde{\Phi}_{LIN}^{(FD4)} \,, \tag{B.9}$$

where the introduced tensors are defined in the following and come from the second order finite difference:

- discretization of the first order space derivatives $\partial_x(\cdot)$: $\tilde{\mathrm{F}}^{\mathrm{FD2}} = \tilde{\mathrm{F}}^{\mathrm{G}}$;
- discretization of the second order space derivatives $\partial_{xx}(\cdot)$: $\tilde{\mathrm{S}}^{\mathrm{FD2}} = \tilde{\mathrm{S}}^{\mathrm{G}}$;
- discretization of the first order space derivatives $\partial_{xxx}(\cdot)$: $\tilde{\mathrm{T}}^{\mathrm{FD2}} = \tilde{\mathrm{T}}^{\mathrm{G}}$;
- solution of the elliptic problem: $\tilde{\Phi}_{LIN}^{(FD2)} = -\dfrac{gh_0^3}{3}\tilde{\mathrm{T}}^{\mathrm{FD2}}\Big(1 - \dfrac{\alpha h_0^2}{3}\tilde{\mathrm{S}}^{\mathrm{FD2}}\Big)^{-1}$;

and from the fourth order finite difference:

- discretization of the first order space derivatives $\partial_x(\cdot)$:

$$\tilde{\mathrm{F}}^{\mathrm{FD4}} = j\frac{k}{12\bar{\mu}}\Big(-2\sin 2\bar{\mu} + 16\sin\bar{\mu}\Big)\ ;$$

- discretization of the second order space derivatives $\partial_{xx}(\cdot)$:

$$\tilde{\mathrm{S}}^{\mathrm{FD4}} = \frac{k^2}{12\bar{\mu}^2}\Big(-2\cos 2\bar{\mu} + 32\cos\bar{\mu} - 30\Big)\ ;$$

- discretization of the first order space derivatives $\partial_{xxx}(\cdot)$:

$$\tilde{\mathrm{T}}^{\mathrm{FD4}} = j\frac{k^3}{8\bar{\mu}^3}\Big(-2\sin 3\bar{\mu} + 16\sin 2\bar{\mu} - 26\sin\bar{\mu}\Big)\ ;$$

- solution of the elliptic problem: $\tilde{\Phi}_{LIN}^{(FD4)} = -\dfrac{gh_0^3}{3}\tilde{\mathrm{T}}^{\mathrm{FD4}}\Big(1 - \dfrac{\alpha h_0^2}{3}\tilde{\mathrm{S}}^{\mathrm{FD4}}\Big)^{-1}$.

Elliptic configuration analysis: Finally, we give in the following the descriptions of the four different configurations studied for the discretization of the elliptic equation (2.46), whose dispersion errors are compared each other on figures 2.4, 2.6 and 2.8.

1). it stands for the choice to lump both the mass matrices of the equations (2.4) and (2.10). The equation (2.46) thus becomes $\Big(1 - \dfrac{\alpha h_0^2}{3}\tilde{\mathrm{S}}^{\mathrm{G}}\Big)\phi_i = -\dfrac{gh_0^3}{3}\tilde{\mathrm{T}}^{\mathrm{G}}\eta_i$ and the related $\tilde{\Phi}_{LIN}$ takes the form:

$$\tilde{\Phi}_{LIN}^{(1)} = -\frac{gh_0^3}{3}\tilde{\mathrm{T}}^{\mathrm{G}}\Big(1 - \frac{\alpha h_0^2}{3}\tilde{\mathrm{S}}^{\mathrm{G}}\Big)^{-1}\ ;$$

2). it stands for the choice to lump only the mass matrix of equation (2.10). The equation (2.46) thus becomes $\left(\tilde{\mathrm{M}}^{\mathrm{G}} - \frac{\alpha h_0^2}{3}\tilde{\mathrm{S}}^{\mathrm{G}}\right)\phi_i = -\frac{g h_0^3}{3}\tilde{\mathrm{T}}^{\mathrm{G}}\eta_i$ and the related $\tilde{\Phi}_{LIN}$ takes the form:

$$\tilde{\Phi}^{(2)}_{LIN} = -\frac{g h_0^3}{3}\tilde{\mathrm{T}}^{\mathrm{G}}\left(\tilde{\mathrm{M}}^{\mathrm{G}} - \frac{\alpha h_0^2}{3}\tilde{\mathrm{S}}^{\mathrm{G}}\right)^{-1};$$

3). it stands for the choice to lump only the mass matrix of equation (2.4). The equation (2.46) thus becomes $\left(1 - \frac{\alpha h_0^2}{3}\tilde{\mathrm{S}}^{\mathrm{G}}\right)\phi_i = -\frac{g h_0^3}{3}\tilde{\mathrm{T}}^{\mathrm{G}}\left(\tilde{\mathrm{M}}^{\mathrm{G}}\right)^{-1}\eta_i$ and the related $\tilde{\Phi}_{LIN}$ takes the form:

$$\tilde{\Phi}^{(3)}_{LIN} = -\frac{g h_0^3}{3}\tilde{\mathrm{T}}^{\mathrm{G}}\left(\tilde{\mathrm{M}}^{\mathrm{G}}\right)^{-1}\left(1 - \frac{\alpha h_0^2}{3}\tilde{\mathrm{S}}^{\mathrm{G}}\right)^{-1};$$

4). it stands for the choice not to lump any mass matrix. The equation (2.46) thus dont changes and the related $\tilde{\Phi}_{LIN}$ is given by:

$$\tilde{\Phi}^{(4)}_{LIN} = -\frac{g h_0^3}{3}\tilde{\mathrm{T}}^{\mathrm{G}}\left(\tilde{\mathrm{M}}^{\mathrm{G}}\right)^{-1}\left(\tilde{\mathrm{M}}^{\mathrm{G}} - \frac{\alpha h_0^2}{3}\tilde{\mathrm{S}}^{\mathrm{G}}\right)^{-1}.$$

Appendix C

Real Estuaries Data

Index	Estuaries	Tidal bore	$h_0[m]$	$L_B[km]$	$a_0[m]$	C_{f0}	ϵ_0	δ_0	ϕ_0	D_i^*
1	Chao Phya	no	7.2	109	1.2	0.0039	0.167	0.548	32.343	9.84
2	Columbia	no	10	25	1.0	0.0031	0.1	2.815	21.814	0.775
3	Conwy	no	3	6.3	2.4	0.0051	0.8	6.118	65.522	8.568
4	Corantijin	no	6.5	48	1.0	0.0032	0.154	1.182	27.93	3.645
5	Daly	yes	10	27	3.0	0.0025	0.3	2.606	17.592	2.025
6	Delaware	no	5.8	40	0.64	0.0021	0.11	1.34	19.404	1.598
7	Elbe	no	10	42	2.0	0.0025	0.2	1.675	17.592	2.1
8	Gironde	yes	10	43	2.3	0.0025	0.23	1.636	17.592	2.4725
9	Hooghly	yes	6	25	2.15	0.0015	0.358	2.18	13.627	2.24
10	Humber	yes	12	25	3.2	0.0031	0.267	3.083	19.914	1.722
11	Limpopo	no	7	50	0.55	0.0027	0.079	1.177	22.709	1.515
12	Loire	no	13	21	2.5	0.0024	0.192	3.82	14.812	0.746
13	Mae Klong	no	5.2	155	1.0	0.0035	0.192	0.327	34.154	20.063
14	Maputo	no	3.6	16	1.4	0.0027	0.389	2.639	31.666	4.667
15	Ord	yes	4	15.2	2.5	0.0024	0.625	2.928	26.703	5.7
16	Pungue	yes	4	17	3.2	0.0031	0.8	2.618	34.491	10.54
17	Qiantang	yes	10	40	3.1	0.0015	0.31	1.759	10.555	1.86
18	Scheldt	no	10.5	28	2.0	0.0023	0.19	2.575	15.795	1.168
19	Severn	yes	15	41	3.75	0.0025	0.25	2.102	14.364	1.708
20	Tha Chin	no	5.3	87	1.35	0.0048	0.255	0.589	46.396	20.07
21	Thames	no	8.5	25	2.0	0.0050	0.235	2.595	38.163	3.46

Table C.1: Tidal and geometric properties of convergent alluvial estuaries. h_0, water depth; L_B, convergence length; a_0, mean spring tidal amplitude at the estuary mouth; C_{f0}, friction coefficient. Sources: Savenije [2012] for estuaries 1, 4, 11, 13, 14, 18, 20; Lanzoni et Seminara [1998] for 2, 3, 6, 7, 15, 19, 21; Bonneton *et al.* [2015] for 8, 9, 10, 16, 17 where we substituted the mean spring tidal amplitude for the maximum spring tidal amplitude; Wolanski *et al.* [2006] for 5; Winterwerp *et al.* [2013] for 12. We consider that for these 21 estuaries the dominant tidal period T_0 is semi-diurnal.

Bibliography

Abbott, M. B., Petersen, H. M. et Skovgaard, O., 1978. Computations of short waves in shallow water. *Coast.Eng.*

Abgrall, R., 2006. Essentially non oscillatory residual distribution schemes for hyperbolic problems. *J.Comp.Phys.*, 214:773–808.

Abgrall, R., Baurin, G., Krust, A., De Santis, D. et Ricchiuto, M., 2013. Numerical approximation of parabolic problems by residual distribution schemes. *International Journal for Numerical Methods in Fluids*, 71:1191–1206.

Abgrall, R., De Santis, D. et Ricchiuto, M., 2012a. Construction of a high order residual distribution scheme for complex viscous flows. Dans *Seventh International Conference on Computational Fluid Dynamics (ICCFD7)*. Big Island, Hawaii, USA.

Abgrall, R., De Santis, D. et Ricchiuto, M., 2012b. High order preserving residual distribution schemes for advection-diffusion scalar problems on arbitrary grids. Research Report RR-8157, INRIA.

Abgrall, R. et Roe, P. L., 2003. High-order fluctuation schemes on triangular meshes. *J.Sci.Comput.*, 19:3–36.

Alvarez-Samaniego, B. et Lannes, D., 2008. A nash-moser theorem for singular evolution equations. Applications to the serre and green-naghdi equations. *Indiana Univ.Math.J.*, 57(1).

Ambrosi, D., 1995. Approximation of shallow water equations by Roe's Riemann solver. *Int.J.Numer.Meth.Fluids*, 20(2):157–168.

Amestoy, P., Duff, I.S., L'Excellent, J.-Y. et Koster, J., 2001. A fully asynchronous multifrontal solver using distributed dynamic scheduling. *SIAM J. Matrix Anal. Appl.*, 23(1):15–41. doi:10.1137/S0895479899358194. URL http://dx.doi.org/10.1137/S0895479899358194

Amestoy, P., Guermouche, A., L'Excellent, J.-Y. et Pralet, S., 2006. Hybrid scheduling for the parallel solution of linear systems. *Parallel Computing*, 32(2):136–156.

Antunes do Carmo, J. S., Seabra-Santos, F. J. et Almeida, A. B, 1993. Numerical solution of the generalized Serre equations with the MacCormack finite-difference scheme. *Int.J.Numer.Meth.Fluids*, 16:725–738.

Arpaia, L., Filippini, A. G., Bonneton, P. et Ricchiuto, M., 2016. Modelling analysis of tidal bore formation in convergent estuaries. *submitted to Ocean Modelling*.

Bacigaluppi, P., Ricchiuto, M. et Bonneton, P., 2014a. A 1D stabilized finite element model for non-hydrostatic wave breaking and run-up. Dans *Finite Volumes for Complex Applications VII-Elliptic, Parabolic and Hyperbolic Problems*, tome 78, pages 779–790. Springer.

Bacigaluppi, P., Ricchiuto, M. et Bonneton, P., 2014b. Upwind stabilized finite element modelling of non-hydrostatic wave breaking and run-up. Rapport technique RR-8536, INRIA.

Barth, T. J., 1992. Aspects of unstructured grids and finite volume solvers for the euler and navier-stokes equations. AGARD report 787.

Barth, T. J., 1998. Numerical Methods for Gasdynamic Systems on Unstructured Meshes. Dans Kroner, Ohlberger et Rohde, rédacteurs, *An introduction to recent developments in theory and numerics for conservation laws*, tome 5 de *Lecture Notes in Computational Science and Engineering*, pages 195–285. Springer-Verlag, Heidelberg.

Barth, T. J., 2003. *Numerical methods and error estimation for conservation laws on structured and unstructured meshes.*

Barth, T. J. et C., Jespersen, 1989. The design and application of upwind schemes on unstructured meshes. *AIAA paper 89-0366.*

Barth, T. J. et M., Ohlberger, 2004. *Finite volume methods: fundation and analysis.* John Wiley & Sons, Ltd.

Bartsch-Winkler, S. et Lynch, D. K., 1988. *Catalog of worldwide tidal bore occurrences and characteristics.* US Government Printing Office.

Beji, S. et Battjes, J. A., 1994. Numerical simulations of nonlinear-wave propagation over a bar. *Coast.Eng.*, 23.

Beji, S. et Nadaoka, K., 1996. A formal derivation and numerical modeling of the improved Boussinesq equations for varying depth. *Ocean Eng.*, 23:1–16.

Bellec, S. et Colin, M., 2014. On the existence of solitary waves for Boussinesq type equations and a new conservative model. *Submitted to*.

Berger, M. J. et Leveque, R. J., 1998. Adaptive mesh refinement using wave-propagation algorithms for hyperbolic systems. *SIAM J. Numer. Anal.*, 35.

Berkhoff, J. C. W., Booy, N. et Radder, A. C., 1982. Verification of numerical wave propagation models for simple harmonic linear water waves. *Coast.Eng.*, 6:255–279.

Berman, A. et Plemmons, R.J., 1979. Nonnegative matrices in the mathematical science. *Academic press*.

Bermudez, A. et Vazquez, M. E., 1994. Upwind methods for hyperbolic conservation laws with source terms. *Computers & Fluids*, 23(8):1049–1071.

Besse, C., Noble, P. et Sanchez, D., 2016. Discrete transparent boundary conditions for the mixed kdv-bbm equation. Submitted.

Bonetton, P., 2004. Wave celerity in the inner surf zone. Dans *29th International Conference on Coastal Engineering*, tome 1, pages 392–401.

Bonetton, P., 2007. Modelling of periodic wave transformation in the inner surf zone. *Ocean Eng.*, 34:1459–1471.

Bonneton, N., Bonneton, P., Parisot, J. P., Sottolicchio, A. et Detandt, G., 2012. Tidal bore and mascaret - example of garonne and seine rivers. *Comptes Rendus Geosci.*, 344:508–515.

Bonneton, P., Barthelemy, E., Carter, J. D., Chazel, F. et Cien, S. T., 2011a. Fully nonlinear weakly dispersive modelling of wave transformation, breaking and runup. *Preprint submitted to European Journal of Mechanics - B/Fluids*.

Bonneton, P., Bonneton, N., Parisot, J. P. et Castelle, B., 2015. Tidal bore dynamics in funnel-shaped estuaries. *J.Geophys.Res.*, 120:923–941.

Bonneton, P., Chazel, F., Lannes, D., Marche, F. et Tissier, M., 2011b. A splitting approach for the fully nonlinear and weakly dispersive Green-Naghdi model. *J.Comp.Phys.*, 230(4):1479–1498.

Bonneton, P., Filippini, A. G., Arpaia, L., Bonneton, N. et Ricchiuto, M., 2016. Conditions for tidal bore formation in convergent alluvial estuaries. *Estuar.Coast.Shelf S.*, 172:121–127.

Bonneton, P., Van de Loock, J., Parisot, J. P., Bonneton, N., Sottolicchio, A., Detandt, G., Castelle, B., Marieu, V. et Pochon, N., 2011c. On the occurrence of tidal bores - the garonne river case. *J.Coast.Res.*, SI 64:11462–11466.

Borthwick, A. G. L., Ford, M., Weston, B. P., Taylor, P. H. et Stansby, P. K., 2006. Solitary wave transformation, breaking and run-up at a beach. *Maritime Engineering*, 159:97–105.

Boussinesq, J., 1872. Théorie des ondes et des remous qui se propagent le long d'un canal rectangulaire horizontal, en communiquant au liquide contenu dans ce canal des vitesses sensiblement pareilles de la surface au fond. *J.Math.Pures Appl.*, 17(55).

Briganti, R., Musumeci, R., Bellotti, R. E., Brocchini, M. et Foti, E., 2004. Boussinesq modeling of breaking waves: description of turbulence. *J.Geophys.Res.*, 109.

Brocchini, M., 2014. A reasoned overview on Boussinesq-type models: the interplay between physics, mathematics and numerics. *Proc.Royal Soc.A*, 469:20130496.

Brocchini, M. et Dodd, N., 2008. Nonlinear shallow water equations modeling for coastal engineering. *J.Waterw.Port.Coast.Ocean Eng.*, 134:104.

Brufau, P. et Garcia-Navarro, P., 2003. Unsteady free surface flow simulation over complex topography with a multidimensional upwind technique. *J.Comp.Phys.*, 186(2):503–526.

Brufau, P., García-Navarro, P. et Vázquez-Cendón, M. E., 2004. Zero mass error using unsteady wetting-drying coditions in shallow flows over dry irregular topography. *Int.J.Numer.Meth.Fluids*, 45:1047–1082.

Brufau, P., Vázquez-Cendón, M. E. et García-Navarro, P., 2002. A numerical model for the flooding and drying of irregular domains. *Int.J.Numer.Meth.Fluids*, 39:247–275.

Burman, E., 2010. Consistent SUPG-method for transient transport problems: Stability and convergence. *Comp.Meth.Appl.Mech.Engrg.*, 199:1114–1123.

Cai, H., Savenije, H. H. G. et Toffolon, M., 2014. Linking the river to the estuary: influence of river discharge on tidal damping. *Hydrol.Earth Syst.Sci.*, 18:287–304.

Castro, M. J., Ferreiro, A. M., García-Rodriguez, J. A., González-Vida, J. M., Macías, J., Parés, C. et Vázquez-Cendón, M. E., 2005. The numerical treatment of wet/dry fronts in shallow flows: application to one-layer and two-layer systems. *Mathematical and Computer Modelling*, 42:419–439.

Chanson, H., 2012. *Tidal Bores, Aegir, Aegir, Eagre, Mascaret, Pororoca: Theory and Observations*. World Scientific, Singapore.

Chazel, F., Lannes, D. et Marche, F., 2011. Numerical simulation of strongly nonlinear and dispersive waves using a Green–Naghdi model. *J.Sci.Comput.*, 48(3).

Chertock, A., Cui, S., Kurganov, A. et Wu, T., 2015. Steady state and sign preserving semi-implicit Runge-Kutta methods for ODEs with stiff damping term. *SIAM Journal on Numerical Analysis*, 53:2008–2029.

Cienfuegos, R., Barthélemy, E. et Bonneton, P., 2006. A fourth-order compact finite volume scheme for fully nonlinear and weakly dispersive Boussinesq-type equations. Part I: Model development and analysis. *Int.J.Numer.Methods Fluids*, 51:1217–1253.

Cienfuegos, R., Barthelemy, E. et Bonneton, P., 2007. A fourth-order compact finite volume scheme for fully nonlinear and weakly dispersive Boussinesq-type equations. part II: Boundary conditions and validation. *Int.J.Numer.Meth.Fluids*, 53:1423–1455.

Cienfuegos, R., Barthélemy, E. et Bonneton, P., 2010. Wave-breaking model for Boussinesq-type equations including roller effects in the mass conservation equation. *J.Waterw.Port Coast.Ocean Engrg.*, 136:10–26.

Cox, D. T., 1995. *Experimental and numerical modelling of surf zone hydrodynamics*. Thèse de doctorat, University of Delaware.

D'Alessandro, F. et Tomasicchio, G., 2008. The bci criterion for the initiation of breaking process in Boussinesq-type equations wave models. *Coast.Eng.*, 55:1174–1184.

Davies, G. et Woodroffe, C. D., 2010. Tidal estuary width convergence: Theory and form in North Australian estuaries. *Earth Surf Process Landforms*, 35. 737749.doi: 10.1002/esp.1864.

Deconinck, H. et Ricchiuto, M., 2007. *Encyclopedia of Computational Mechanics: Residual Distribution schemes: foundation and analysis*. John Wiley & Sons, Ltd. DOI: 10.1002/0470091355.ecm054.

Deconinck, H., Ricchiuto, M. et Sermeus, K., 2003. Introduction to residual distribution schemes and stabilized finite elements. *VKI LS 2003-05, 33rd Computational Fluid dynamics Course, von Karman Institute for Fluid Dynamics.*

Delestre, O., Lucas, C., Ksinant, P. A., Darboux, F., Laguerre, C., Tuoi Vo, T. N., James, F. et Cordier, S., 2013. Swashes: a compilation of shallow water analytic solutions for hydraulic and environmental studies. *Int.J.Numer.Meth.Fluids.*

Delis, A. I. et Kazolea, M., 2011. Finite volume simulations of waves formed by sliding masses. *Communications in Numerical Methods in Engineering*, 18(57).

Delis, A. I., Nikolos, I. K. et Kazolea, M., 2011. Performance and comparison of cell-centered and node-centered unstructured finite volume discretizations for shallow water free surface flows. *Archives of Computational Methods in Engineering*, 18:57–118.

Demirbilek, Z., Zundel, A. et Nwogu, O., 2007. Boussinesq modeling of wave propagation and runup over fringing coral reefs, model evaluation report. Rapport technique Coastal and Hydraulics Laboratory Technical Note CHLTR0712, U.S. Army Engineer Research and Development Center, Vicksbourg.

Dingemans, M. W., 1997. *Water wave propagation over uneven bottoms.* Advanced Series Ocean Eng. World Scientific.

Duran, A. et Marche, F, 2014. Discontinuous-Galerkin discretization of a new class of Green-Naghdi equations. *Communications in Computational Physics, Global Science Press*, page 130.

Duran, A. et Marche, F, 2016. A discontinuous galerkin method for a new class of Green-Naghdi equations on simplicial unstructured meshes. ArXiv:1604.05227.

Engsig-Karup, A. P., Hesthaven, J. S., Bingham, H. B. et Madsen, P. A., 2006. Nodal DG-FEM sollution of high order Boussinesq-type equations. *J.Eng.Math.*, 56.

Eskilsson, C. et Sherwin, S. J., 2003. An hp/spectral element model for efficient long-time integration of Boussinesq-type equations. *J. of Coastal Engineering*, 45.

Eskilsson, C. et Sherwin, S. J., 2006. Spectral/HP discontinuous galerkin methods for modelling 2D Boussinsq equations. *J.Comp.Phys.*, 210.

Eskilsson, C., Sherwin, S. J. et Bergdhal, L., 2006. An unstructured spectral hp element model for enhanced Boussinesq-type euations. *Coast.Eng.*, 53.

Filippini, A. G., Bellec, S., Colin, M. et Ricchiuto, M., 2015. On the nonlinear behavior of Boussinesq type models: amplitude-velocity vs amplitude-flux forms. *Coast.Eng.*, 99:109–123.

Filippini, A. G., Kazolea, M. et Ricchiuto, M., 2016. A flexible genuinely nonlinear approach for nonlinear wave propagation, breaking and run-up. *J.Comp.Phys.*, 310:381–417.

Filippini, A. G., Kazolea, M. et Ricchiuto, M., 2017. A fully nonlinear and weakly dispersive approach for wave propagation, breaking and run-up on unstructured meshes. *In preparation.*

Friedrichs, C. T. et Aubrey, D. G., 1994. Tidal propagation in strongly convergent channels. *J.Geophys.Res.*, 99(C2). 33213336.doi: 10.1029/93JC03219.

Fuhrman, D. R. et Bingham, H. B, 2004. Numerical solution of fully nonlinear and highly dispersive boussinesq equations in two horizontal dimensions. *Int.J.Numer.Meth.Fluids*, 44.

Furgerot, L., 2014. *Propriètè hydrodynamiques du mascaret et de son influence sur la dynamique sédimentaire. Une approche couplée en canal et in situ (estuaire de la Sée, Baie du Mont Saint Michel).* Thèse de doctorat, University of Caen.

Furgerot, L., Mouaze, D., Tessier, B., Perez, L. et Haquin, S., 2013. Suspended sediment concentration in relation to the passage of a tidal bore (Sée river estuary, mont saint michel bay). *Proc.Coast.Dyn.*, pages 671–682.

Gooch, C. O., Nejat, A. et Michalak, K., 2009. On obtaining high-order finite-volume solutions to the Euler equations on unstructured meshes. *AIAA J.*., 47. DOI: 10.2514/1.40585.

Gooch, C. O. et Van Altena, M., 2002. A high-order accurate unstructured mesh finite-volume scheme for the advection-diffusion equation. *J.Comp.Phys.*, 181:729–752.

Gottlieb, S., Shu, C.-W. et Tadmor, E., 2001. Strong stability preserving high-order time discretization methods. *SIAM review*, 43:89–112.

Green, A. E. et Naghdi, P. M., 1976. A derivation of equations for wave propagation in water of variable depth. *J.Fluid Mech.*, 78:237–246.

Grilli, S. T., Subramanya, R., Svendsen, I. A. et Veeramony, J., 1994. Shoaling of solitary waves on plane beaches. *J.Waterw.Port.C.-ASCE*, 120:609–628.

Harten, A., 1983. High resolution cchemes for hyperbolic conservation laws. *J.Comput.Phys.*, 135:260–278.

Harten, A. et Hyman, J. M., 1983. Self-adjusting grid methods for one-dimensional hyperbolic conservation laws. *J.Comput.Phys.*, 50(2).

Hartmann, R. et Houston, P., 2009. Error estimation and adaptive mesh refinement for aerodynamic flows. Dans H. Deconinck, rédacteur, *VKI LS 2010-01: 36th CFD/ADIGMA course on hp-adaptive and hp-multigrid methods, Oct. 26-30, 2009*. Von Karman Institute for Fluid Dynamics, Rhode Saint Genèse, Belgium.

Hauke, G., 1998. A symmetric formulation for computing transient shallow water flows. *Comp.Meth.Appl.Mech.Engrg.*, 163:111–122.

Horrevoets, A. C., Savenije, H. H. G., Schuurman, J. N. et Graas, S., 2004. The influence of river discharge on tidal damping in alluvial estuaries. *J.Hydrol.*, 294:213–228.

Hubbard, M. E. et Dodd, N., 2002. A 2D numerical model of wave runup and overtopping. *Coast.Eng.*, 47:1–26.

Hubbard, M. E. et García-Navarro, P., 2000. Flux difference splitting and the balancing of source terms and flux gradients. *J.Comp.Phys.*, 165:89–125.

Hughes, T. J. R. et Brook, A., 1982. Streamline upwind Petrov-Galerkin formulations for convection dominated flows with particular emphasis on the incompressible Navier-Stokes equations. *Comp.Meth.Appl.Mech.Engrg.*, 32:199–259.

Hughes, T. J. R., Scovazzi, G. et Tezduyar, T., 2010. Stabilized methods for compressible flows. *J.Sci.Comp.*, 43:343–368.

Hundsdorfer, W., Ruuth, S. J. et Spiteri, R. J., 2003. Monotonicity-preserving linear multistep methods. *SIAM Journal on Numerical Analysis*, 41(2):605–623.

Hundsdorfer, W. et Verwer, J. G, 2003. Numerical solution of time-dependent advection-diffusion-reaction equations. Dans H. Yeh, P. Liu et R. C Synolakis, rédacteurs, *Springer Series in Comput. Math.* Springer.

Jay, D. A., 1991. Green's law revisited: tidal long wave propagation in channels with strong topography. *J.Geophys.Res.Oceans*, 96(11):20585–20598.

Kazolea, M., 2013. *Mathematical and computational modeling for the generation and propagation of waves in marine and coastal environments*. Thèse de doctorat, Technical University of Crete.

Kazolea, M. et Delis, A. I., 2013. A well-balanced shock-capturing hybrid finite volume-finite difference numerical scheme for extended 1D Boussinesq models. *Applied Numerical Mathematics*, 67:167–186.

Kazolea, M., Delis, A. I. et Nikolos, I. K. and, 2012. An unstructured finite volume numerical scheme for extended 2D Boussinesq-type equations. *Coast.Eng.*, 69:42–66.

Kazolea, M., Delis, A. I. et Synolakis, C., 2014. Numerical treatment of wave breaking on unstructured finite volume approximations for extended Boussinesq type equations. *J.Comput.Phys.*, 271:281–305.

Kazolea, M. et Ricchiuto, M., 2016. Wave breaking for Boussinesq-type models using a turbulence kinetic energy model. Rapport technique RR-8781, INRIA.

Kennedy, A., Chen, Q., Kirby, J. et Dalrymple, R., 2000. Boussinesq modeling of wave transformation, breaking, and runup. *J.Waterw.Port Coast.Ocean Engrg.* DOI: 10.1061/(ASCE)0733-950X(2000)126:1(39).

Kermani, M. J., Geber, A. G. et Stockie, J. M., 2003. Thermodynamically based moisture prediction using Roe's scheme. Dans *The 4th Conference of Iranian AeroSpace Society*. Amir Kabir University of Technology, Tehran, Iran.

Kirby, J. T., Wei, G. et Chen, Q., 1998. FUNWAVE 1.0, Fully Nonlinear Boussinesq Wave Model Documentation and User's Manual. Rapport technique CACR-98-06, University of Delaware.

Klosa, J., 2012. Extrapolated BDF residual distribution schemes for the shallow water equations. Master thesis.

Koobus, B., Wornom, S., Camarri, S., Salvetti, M. V. et Dervieux, A., 2008. Nonlinear v6 schemes for compressible flow. Rapport technique RR-6433, INRIA.

Lannes, D., 2013. *The water waves problem. Mathematical analysis and asymptotics*. Mathematical Surveys and Monographs. Americal Mathematical Society.

Lannes, D. et Bonneton, P., 2009. Derivation of asymptotic two-dimensional time-dependent equations for surface water wave propagation. *Physics of Fluids*, 21. 016601 doi:10.1063/1.3053183.

Lannes, D. et Marche, F., 2015. A new class of fully nonlinear and weakly dispersive Green-Naghdi models for efficient 2D simulations. *J.Comp.Phys.*, 282:238–268.

Lanzoni, S. et Seminara, G., 1998. On tide propagation in convergent estuaries. *J.Geophys.Res.*, 103:30793–30812.

Lee, C., Cho, Y. S. et Yoon, S. B., 2003. A note on linear dispersion and shoaling properties in extended Boussinesq equations. *Ocean Eng.*, 30:1849–1867.

LeVeque, R. J., 2002. *Finite Volume Methods for Hyperbolic Problems*. Cambridge University Press.

Li, M., Guyenne, P., Li, F. et Xu, L., 2014. High-order well-balanced CDG-FE methods for shallow water waves by a Green-Naghdi model. *J.Comput.Phys.*, 257:169–192.

Liang, Q. et Borthwick, A. G. L., 2009. Adaptive quadtree simulation of shallow flows with wet/dry front over complex topography. *Comput.Fluids*, 38:221–234.

Lynch, D. K., 1982. Tidal bores. 242.

Lynett, P. J., Wu, T. R. et Liu, P. L. F., 2002. Modeling wave runup with depth-integrated equations. *Coast.Eng.*, 46:89–107.

Madsen, P. A., Fuhrman, D. R. et Schaffer, H. A, 2008. On the solitary wave paradigm for tsunamis. *J.Geophys.Res.*, 113. DOI: 10.1029/2008JC004932.

Madsen, P. A. et Schaffer, H. A., 1998. Higher-order Boussinesq-type equations for surface gravity waves: derivation and analysis. *Phil.Trans.R.Soc.Lond.A*, 356:3123–3184.

Madsen, P. A., Simonsen, H. J. et Pan, C. H., 2005. Numerical simulation of tidal bores and hydraulic jumps. *Coast.Eng.*, 52:409–433.

Madsen, P. A. et Sørensen, O. R., 1992. A new form of the Boussinesq equations with improved dispersion characteristics. Part 2: A slowing varying bathymetry. *Coast.Eng.*, 18:183–204.

Marche, F., Bonneton, P., Fabrie, P. et Seguin, N., 2007. Evaluation of well-balanced bore-capturing schemes for 2d wetting and drying processes. *Int.J.Num.Meth.Fluids*, 53:867–894.

MARCHE, F. et LANNES, D., 2015. A new class of fully nonlinear and weakly dispersive Green-Naghdi models for efficient 2D simulations. *sumbitted to J.Comp.Phys.*

MITSOTAKIS, D. E., ILAN, B. et DUTYKH, D., 2014. On the Galerkin/finite-element method for the Serre equations. *J.Sci.Comp.*, 61:166–215.

MUNCHOW, A. et GARVIN, R. W., 1991. Nonlinear barotropic tides and bores in estuaries. *Tellus*, 43:246–256.

MURILLO, J., GARCIA-NAVARRO, P. et BURGUETE, J., 2009. Time step restrictions for well-balanced shallow water solutions in non-zero velocity steady states. *Int.J.Num.Meth.Fluids*, 60:1351.

MURILLO, J., GARCIA-NAVARRO, P., BURGUETE, J. et BRUFAU, P., 2007. The influence of source terms on stability, accuracy and conservation in two-dimensional shallow flow simulation using triangular finite volumes. *Int.J.Num.Meth.Fluids*, 54:543.

NIKOLOS, I. K. et DELIS, A. I., 2009. An unstructured node-centered finite volume scheme for shallow water flows with wet/dry fronts over complex topography. *Comput.Methods Appl.Mech.Engrg*, 198:3723–3750.

NWOGU, O., 1994. An alternative form of the Boussinesq equations for near-shore wave propagation. *J.Waterw.Port.C.-ASCE*, 119:618–638.

NWOGU, O., 1996. Numerical prediction of breaking waves and currents with a Boussinesq model. Dans *25th International Conference on Coastal Engineering*.

ORSZAGHOVA, J., BORTHWICK, A. G. L. et TAYLOR, P. H., 2012. From the paddle to the beach - a Boussinesq shallow water numerical wave tank based on madsen and sørensen's equations. *J.Comput.Phys.*, 231:328–344.

PAN, C. H. et LU, H., 2010. 2d numerical simulation of tidal bore on Qiantang river using KFVS scheme. Dans *Proceedings of the 32nd International Conference on Coastal Engineering*. Lynett.

PEREGRINE, D. H., 1967. Long waves on a beach. *J.Fluid.Mech.*, 27.

PRANDLE, D., 2003. Relationships between tidal dynamics and bathymetry in strongly convergent estuaries. *J.Phys.Oceanogr.*, 33(12):2738–2750.

RICCHIUTO, M., 2011. On the C-property and generalized C-property of residual distribution for the shallow water equations. *J.Sci.Comp.*, 48:304–318.

RICCHIUTO, M., 2015. An explicit residual based approach for shallow water flows. *J.Comput.Phys.*, 280:306–344.

Ricchiuto, M., Abgrall, R. et Deconinck, H., 2007. Application of conservative residual distribution schemes to the solution of the shallow water equations on unstructured meshes. *J.Comp.Phys.*, 222(1):287–331.

Ricchiuto, M. et Bollermann, A., 2009. Stabilized residual distribution for shallow water simulations. *J.Comp.Phys.*, 228(4):1071–1115.

Ricchiuto, M. et Filippini, A. G., 2014. Upwind residual discretization of enhanced Boussinesq equations for wave propagation over complex bathymetries. *J.Comput.Phys.*, 271:306–341.

Roe, P. L., 1981. Approximate Riemann solvers, parameter vectors, and difference schemes. *J.Comp.Phys.*, 43:357–372.

Roeber, V. et Cheung, K. F., 2012. Boussinesq-type model for energetic breaking waves in fringing reef environments. *Coast.Eng.*, 70:1–20.

Roeber, V., Cheung, K. F. et Kobayashi, M. H., 2010. Shock-capturing Boussinesq-type model for nearshore wave processes. *Coast.Eng.*, 57:407–423.

Roy, C. J., Nelson, C. C., Smith, T. M. et Ober, C. C., 2004. Verification of euler/navier–stokes codes using the method of manufactured solutions. *Int.J.Numer.Methods Fluids*, 44:599–620.

Saad, Y., 1996. *Iterative Methods for Sparse Linear Systems*. PWS.

Salari, K. et Patrick, K., 2000. Code verification by the method of manufactured solutions. Rapport technique SAND2000-1444, SANDIA.

Savenije, H. H. G., 2001. A simple analytical expression to describe tidal damping or amplification. *J.Hydrol.*, 243:205–215.

Savenije, H. H. G.., 2012. *Salinity and tides in alluvial estuaries*. 2nd revised, open access édition.

Savenije, H. H. G., Toffolon, M., Haas, J. et Veling, M., 2008. Analytical description of tidal dynamics in convergent estuaries. *J.Geophys.Res.*, 113:1–18.

Savenije, H. H. G. et Veling, E. J. M., 2005. Relation between tidal damping and wave celerity in estuaries. *J.Geophys.Res.*, 101. Doi:10.1029/2004JC002278.

Schaffer, H. A., Madsen, P. A. et Deigaard, R., 1993. A Boussinesq model for waves breaking in shallow water. *Coast.Eng.*, 20(3-4):185–202.

Seaid, M., 2004. Non-oscillatory relaxation methods for the shallow-water equations in one and two space dimensions. *Int.J.Numer.Meth.Fluids*, 46(5):457–484.

Sebra-Santos, F. J., Renouard, D. P. et Temperville, A. M, 1987. Numerical and experimental study of the transformation of a solitary wave over a self or isolated obstacle. *J.Fluid Mech.*, 185:523–545.

Serre, F., 1953. Contribution à l'étude des écoulements permanents et variables dans les canaux. *Houille Blanche*, 8:374–388.

Shi, F., Kirby, J. T., Harris, J. C., Geiman, J. D. et Grilli, S. T., 2012. A high-order adaptive time-stepping TVD solver for Boussinesq modeling of breaking waves and coastal inundation. *Ocean Modelling*, 43-44:36–51.

Simpson, J. H., Fisher, N. R. et Wiles, P., 2004. Reynolds stress and tke production in an estuary with a tidal bore. *Estuar.Coast.Shelf Sci.*, 60(4):619–627.

Sorensen, O. R., Schaffer, H. et Sorensen, L., 2004. Boussinesq-type modelling using an unstructured finite element technique. *Coast.Eng.*, 50.

Sørensen, O. R., Schäffer, H. A. et Madsen, P. A., 1998. Surf zone dynamics simulated by a Boussinesq type model: Part III. Wave-induced horizontal nearshore circulations. *Coast.Eng.*, 33:155–176.

Stoker, J. J., 1992. *Water Waves: The Mathematical Theory with Applications*. John Wiley & Sons, Ltd.

Strang, G., 1968. On the construction and comparison of difference schemes. *SIAM Journal on Numerical Analysis*, 5:506–517.

Swigler, D. et Lynett, P. J., 2011. Laboratory study of the three-dimensional turbulence and kinematic properties associated with a solitary wave travelling over an alongshore-variable, shallow shelf. *submitted for pubblication.*

Synolakis, C. E., 1987. The run up of solitary waves. *J.Fluid Mech.*, 185:532–545.

Synolakis, C. E., Bernard, E. N., Titov, V. V., Kanoglu, U. et Gonzalez, F. I., 2007. Standards, criteria, and procedures for NOAA evaluation of tsunami numerical models. NOAA Tech. Memo. OAR PMEL-135, NOAA/Pacific Marine Environmental Laboratory, Seattle, WA.

Thacker, W. C., 1981. Some exact solutions to the nonlinear shallow-water wave equations. *J.Fluid Mech.*, 107:499–508.

Ting, F. C. K. et Kirby, J. T., 1996. Dynamics of surf-zone turbulence in a spilling breaker. *Coast.Eng.*, 27:131–160.

Tissier, M., Bonneton, P., Marche, F., Chazel, F. et Lannes, D., 2011. Nearshore dynamics of tsunami-like undular bores using a fully nonlinear Boussinesq model. *J.Coast.Res.*, 64:603–607.

Tissier, M., Bonneton, P., Marche, F., Chazel, F. et Lannes, D., 2012. A new approach to handle wave breaking in fully nonlinear Boussinesq models. *Coast.Eng.*, 67:54–66.

Titov, V. V. et Synolakis, C. E., 1998. Numerical modelling of tidal wave runup. *J.Waterw.Port Coast.Ocean Engrg.*, 124:157–171.

Toffolon, M., 2002. *Hydrodynamics and morphodynamics of tidal channels*. Thèse de doctorat, Università degli studi di Trento.

Toffolon, M., Vignoli, G. et Tubino, M., 2006. Relevant parameters and finite amplitude effects in estuarine hydrodynamics. *J.Geophys.Res.*, 111:1–17.

Tonelli, M. et Petti, M., 2009. Hybrid finite volume - finite difference scheme for 2DH improved Boussinesq equations. *Coast.Eng.*, 56.

Tonelli, M. et Petti, M., 2010. Finite volume scheme for the solution of 2D extended Boussinesq equations in the surf zone. *Ocean.Eng.*, 37:567–582.

Tonelli, M. et Petti, M., 2011. Simulation of wave breaking over complex bathymetries by a Boussinesq model. *J.Hydraulic Res.*, 49:473–486.

Tonelli, M. et Petti, M., 2012. Shock-capaturing Boussinesq model for irregular wave propagation. *Coast.Eng.*, 61:8–19.

Toro, E. F., 2001. *Shock-Capturing Methods for Free-Surface Shallow Flows*. John Wiley & Sons, Ltd.

Toro, E. F., 2009. *Riemann Solvers and Numerical Methods for Fluid Dynamic*. Springer.

Turing, Alan Mathison, 1936. On computable numbers, with an application to the Entscheidungsproblem. *Proceedings of the London Mathematical Society*, 2(42):230–265.
URL http://plms.oxfordjournals.org/content/s2-42/1/230.full.pdf

Van Leer, B., 1979. Towards the ultimate conservative difference scheme v. a second order sequel to godunov's method. *J.Comput.Phys*, 32(101).

VEERAMONY, J. et SVENDSEN, I. A., 2000. The flow in surf zone waves. *Coast.Eng.*, 39(2-4):93–122.

VENKATAKRISHAN, V., 1993. On the accuracy of limiters and convergence to steady state solutions. *AIAA paper 1993-0880.*

VIGNOLI, G., TOFFOLON, M. et TUBINO, M., 2003. Non-linear frictional residual effects on tide propagation. *Proceedings of XXX IAHR Congress*, A:291–298.

WALKLEY, M. A., 1999. *A numerical method for extended Boussinesq shallow-water wave equations.* Thèse de doctorat, University of Leeds.

WALKLEY, M. A. et BERZINS, M., 2002. A finite element method for the two-dimensional extended Boussinesq equations. *Int.J.Numer.Meth.Fluids*, 39:865–886.

WATERSON, N.P. et DECONINCK, H., 2007. Design principles for bounded higher-order convection schemes: a unified approach. *J.Comput.Phys.*, 224(1):182–207.

WEI, G. et KIRBY, J. T., 1995. A time-dependent numerical code for extended Boussinesq equations. *J.Waterw.Port.C.-ASCE*, 120:251–261.

WEI, G., KIRBY, J. T. et SINHA, A., 1999. Generation of waves in Boussinesq models using a source function method. *Coast.Eng.*, 36:271–299.

WHALIN, R. W., 1971. The limit of applicability of linear wave refraction theory in a convergence zone. Res.Rep.H-71-3, USACE,Waterways Expt.Station, Vicksburg, MS.

WINCKLER, P. et LIU, P. L. F, 2015. Long waves in a straight channel with non-uniform cross-section. *J.Fluid Mech.*, 770:156–188. 10.1017/jfm.2015.147.

WINTERWERP, J. C., WANG, Z. B., VAN BRAECKEL, A., VAN HOLLAND, G. et KOSTERS, F., 2013. Man-induced regime shifts in small estuaries II: a comparison of rivers. *Ocean Dynamics*, 63(11-12):1293–1306.

WOLANSKI, E., WILLIAMS, D. et HANERT, E., 2006. The sediment trapping efficiency of the macro-tidal Daly Estuary, tropical Australia. *Estuar.Coast. Shelf Sci.*, 69(1):291–298.

WOLANSKI, E., WILLIAMS, D., SPAGNOL, S. et CHANSON, H., 2004. Undular tidal bore dynamics in the daily estuary, northern australia. *Estuar.Coast. Shelf Sci.*, 60(4):629–636.

Wright, L. D., Coleman, J. M. et C., Thom B., 1973. Processes of channel development in a high-tide-range environment: Cambridge Gulf-Ord river Delta, Western Australia. *J.Geol.*, 81:15–41.

Xing, Y., Zhang, X. et Shu, C.-W., 2010. Positivity-preserving high order well-balanced discontinuous Galerkin methods for the shallow water equations. *Advances in Water Resources*, 33(12):1476–1493.

Zelt, J. A., 1991. The run-up of nonbreaking and breaking solitary waves. *Coast.Eng.*, 15(3):205–246.

Zhang, X., Xia, Y. et Shu, C.-W., 2012. Maximum-principle-satisfying and positivity-preserving high order discontinuous Galerkin schemes for conservation laws on triangular meshes. *J.Sci.Comp.*, 50:29–62.

Zhang, Y., Kennedy, A. B., Panda, N., Dawson, C. et Westerink, J. J., 2014. Generating-absorbing sponge layers for phase-resolving wave models. *Coast.Eng.*, 84:1–9.